1290

UNIVERSIDADE Ð COIMBRA

Bruno Alexandre Silva Pedrosa

Fatigue Assessment
of
Resin-Injected
Bolted Shear Connections
From Material to Structural Detail

Maio de 2023

Faculdade de Ciências e Tecnologia da Universidade de Coimbra
Departamento de Engenharia Civil

FATIGUE ASSESSMENT
OF
RESIN-INJECTED
BOLTED SHEAR CONNECTIONS
FROM MATERIAL TO STRUCTURAL DETAIL

BRUNO ALEXANDRE SILVA PEDROSA

Thesis submitted in fulfilment of the requirements for the degree of Doctor of Philosophy on Steel and Composite Construction, supervised by Professor Carlos Alberto da Silva Rebelo, Professor José António Fonseca de Oliveira Correia and Professor Milan Veljkovic

May 2023

1 2 9 0

UNIVERSIDADE Ð
COIMBRA

ABSTRACT

Construction of metallic bridges started to spread throughout the world during the 19th and 20th century and a significant number of these structures are still on service, therefore it is essential not only to assess their structural integrity but also to develop strengthening solutions aiming to improve its adaptability to face higher frequency of extreme weather phenomena (climate change influence) and traffic level variations (higher load and frequency). The most common evidence of damage is the presence of corroded metallic elements and cracks in structural details due to the fatigue phenomenon. In fact, recent investigations showed that fatigue is the most frequent cause of damage in steel bridges. Furthermore, many cases were found in which fatigue cracks were detected in connections.

Different strategies can be implemented for repairing and strengthening operations of steel bridges. However, the use of injection bolts has been considered as an alternative with important advantages not only to replace faulty rivets but also to connect new plates. In this sense, the study described in this thesis intends to be a contribution to the scientific knowledge about the fatigue behaviour of bolted shear connections using injection bolts.

Considering the local nature of fatigue phenomenon, material characterization is essential for any structural integrity study. One example of puddled iron extracted from a Portuguese centenary bridge still on service and two structural steels used in new constructions were selected to be investigated concerning its metallographic and mechanical properties. Several fatigue models were used to describe the cyclic and fatigue behaviour of each material aiming to define mean and characteristic parameters. Fatigue crack propagation was also studied, mainly based on an experimental approach. In fact, the scientific knowledge about the behaviour of a fatigue crack is fundamental to define reliable methods and strategies to mitigate the propagation of a crack. In this sense, an analytical model was developed to describe crack propagation on two non-alloy structural steels which consider the crack closure effects. The proposed model was based on the UniGrow approach.

Fatigue assessment was then performed at the level of the metallic plate by conducting experimental fatigue tests whose results allowed to evaluate the influence of hole execution method, presence of protection layer and metallic material. Global and local approaches were implemented to analyse fatigue data which enable to assess the advantages and disadvantages of each methodology.

In what concerns the adhesives used in resin-injected bolted connections to fill the gap between the bolt shank and the hole of the plate, it is essential to characterize its behaviour under the same conditions that are created in a bolted connection assembly. In this sense, this study was based on experimental and numerical approaches to assess the compressive behaviour of an epoxy resin and a steel reinforced resin solution under confined conditions aiming to, not only propose reliable material parameters, but also to compare different structural adhesive solutions.

Finally, an experimental campaign was conducted to assess the fatigue strength of preloaded injection bolts and establish a comparison with preloaded standard bolts. Specimens were prepared aiming to be representative of a bridge strengthening scenario. Experimental results showed that injection bolts contribute not only to decrease the scatter in fatigue life but also to increase the fatigue strength of bolted connections specially in those fatigue regimes which are more relevant in the design of bridges (high-cycle fatigue regime).

Keywords:

 Fatigue | Metallic materials | Crack propagation | Resins | Connections | Injection bolts

RESUMO

A construção de pontes metálicas teve uma grande expansão por todo o mundo durante os séculos 19 e 20 sendo que, uma parte significativa destas estruturas encontram-se ainda em serviço. É essencial não só avaliar a sua integridade estrutural, mas também desenvolver soluções de reforço com o objetivo de aumentar a sua capacidade estrutural tendo em vista uma maior frequência de fenómenos climáticos extremos (influência das alterações climáticas) e variações no nível de tráfego (aumento de cargas e sua frequência). A evidência mais comum de danos estruturais são a presença de elementos metálicos corroídos e fissuras em detalhes estruturais devido ao fenómeno de fadiga. De facto, investigações recentes têm mostrado que a fadiga é o dano estrutural mais frequente em pontes de aço e que, na maioria dos casos, estes danos de fadiga são detetados nas ligações.

Poderão ser implementadas múltiplas estratégias em operações de reparação e reforço estrutural de pontes em aço. Contudo, o uso de parafusos injetados tem sido considerado uma alternativa com importantes vantagens não apenas para substituição de rebites defeituosos, mas também para ligação de novas chapas de reforço. Neste sentido, o estudo descrito nesta tese tem como objetivo ser um contributo para o conhecimento científico sobre o comportamento à fadiga de ligações aparafusadas ao corte utilizando parafusos injetados.

Tendo em consideração a natureza local do fenómeno de fadiga, caracterizar os materiais é essencial em qualquer estudo de integridade estrutural. Neste sentido, foram selecionados três materiais metálicos com vista à sua caracterização metalográfica e mecânica: ferro pudlado extraído de elementos estruturais de uma ponte portuguesa com mais de cem anos e dois aços estruturais usados frequentemente em construções novas. O comportamento cíclico e de fadiga de cada um destes materiais foi descrito por diferentes modelos com o intuito de definir valores médios e característicos para os parâmetros de cada modelo. Adicionalmente, a propagação de fenda de fadiga em cada um destes materiais foi também analisada tendo como base uma abordagem essencialmente experimental. De facto, o conhecimento científico sobre o fenómeno da propagação de fenda é fundamental para definir métodos e estratégias seguras para o seu controlo e mitigação. Neste sentido, foi desenvolvido um modelo analítico que

descreve o comportamento de uma fenda de fadiga na fase de propagação em dois aços estruturais considerando os efeitos do fecho de fenda. O modelo proposto tem como base a abordagem UniGrow.

De seguida, a avaliação do fenómeno de fadiga foi efetuada ao nível das chapas metálicas através da execução de ensaios experimentais cujos resultados permitiram avaliar aspetos como a influência do método de execução do furo, a presença de uma camada de proteção anti corrosão e o material metálico que compõe a chapa. A análise dos dados de fadiga foi efetuada considerando abordagens globais e locais por forma a avaliar as vantagens e desvantagens de cada metodologia.

No que diz respeito aos adesivos para preenchimento do espaço entre o perno do parafuso e o furo das chapas nas ligações aparafusas com parafusos injetados, é essencial caracterizar o seu comportamento considerando as mesmas condições que são criadas na ligação. Assim, a avaliação do comportamento à compressão de uma solução à base de resina epóxi e de uma solução à base de resina epóxi reforçada com esferas de aço foi efetuada através de abordagens experimentais e numéricas com o objetivo de não só apresentar valores seguros para parâmetros do material, mas também estabelecer uma comparação entre diferentes soluções para adesivos estruturais.

For fim, é descrita uma companha experimental conduzida com o objetivo de avaliar a resistência à fadiga de parafusos injetados pré-esforçados e estabelecer uma comparação com parafusos convencionais pré-esforçados. Os provetes foram preparados tendo em consideração um cenário de efetivo reforço estrutural de uma ponte metálica. Dos resultados experimentais foi possível concluir que o uso de parafusos injetados contribui não só para diminuir a dispersão na vida à fadiga, mas também para um aumento da resistência das ligações parafusadas, especialmente para os regimes de fadiga que são mais relevantes para o dimensionamento de pontes metálicas (regime de fadiga de elevado número de ciclos).

Palavras-chave:

  Fadiga | Materiais metálicos | Propagação de fenda | Resinas | Ligações | Parafusos injetados
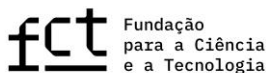
ACKNOWLEDGEMENTS

Institutional

Personal

This PhD thesis is the final step of a long but grateful journey in my life. Even if this thesis is the results of my work during the last years, this achievement would be impossible to reach only by myself. In this sense, I would like to express my gratitude to my supervising team, Prof. Carlos Rebelo, Prof. José Correia and Prof. Milan Veljkovic for their support and guidance during these years. Besides scientific knowledge, during this journey I was granted not only with enriching challenges but also with new friends that change my personality for good. I am deeply grateful for all the support that I received from my colleagues and friends.

Quero também deixar um agradecimento especial aos meus pais e aos meus irmãos por todo o amor que me deram, mas em especial à minha mãe pela força e coragem que me transmite através do seu exemplo de vida e que é a minha grande inspiração. A ela dedico este trabalho.

Se eu pudesse escolher qual foi a melhor coisa que me aconteceu ao longo do meu doutoramento, não teria dúvidas em dizer que foi o amor que encontrei na Sara. Esta caminhada foi muito mais fácil com o seu apoio.

CONTENTS

SYMBOLOGY

Latin Symbols

a	Crack length
a_0	Side dimension of dog-bone specimen for monotonic tests
$a_{crystal}$	Unit cell edge length – crystal structure
a_i	Initial crack length
a_{inv}	Third invariant of deviatoric stress
a_f	Final crack length
a_{FT}	Crack length measured in FCG test of plate with hole specimen
A	Slope for linear regression analysis
A_0, A_1	Constants of linear equation to reproduce F-v_c curve
A_b	Gross cross-section area of bolt
A_f	Percentage of elongation after fracture
A_{gross}	Gross cross-section area
A_J	Domain enclosed by the contour $C_J + C_J^+ + \Gamma + C_J^-$
A_{HV}	Area of indentation in hardness test
A_{net}	Net cross-section area
A_s	Tensile stress area of bolt
b	Fatigue strength exponent using Coffin-Manson-Basquin model
b_0	Side dimension of dog-bone specimen for monotonic tests
B	Intersection with ordinate axis for linear regression analysis
B_0, B_1, B_2	Constants of non-linear equation to reproduce F-v_c curve
B_{CT}	Thickness of CT specimen
$b_{Huffman}$	Fatigue strength exponent using Huffman model
b_{Morrow}	Fatigue strength exponent using Morrow model
b_{SWT}	Fatigue strength exponent using SWT model
$\vec{b}$	Burger's vector
c	Fatigue ductility exponent using Coffin-Manson-Basquin model
C	Intersection of fatigue curve with ordinate axis

$C_0, \ldots, C_5$	Coefficients used in compliance method to calculate crack length
C_{eff}	Intersection of fatigue curve with ordinate axis for ΔK_{eff}
C_{el}	Intersection with ordinate axis for elastic FCG curve
C_J, C_J^+, C_J^-	Contour for J-integral
C_{pl}	Intersection with ordinate axis for plastic FCG curve
$c_{Huffman}$	Fatigue ductility exponent using Huffman model
c_{MC}	Material cohesion for Mohr-Coulomb criterion
c_{Morrow}	Fatigue ductility exponent using Morrow model
c_{SWT}	Fatigue ductility exponent using SWT model
d	Diameter of bolt
d_0	Diameter of hole
$d\,(\ )$	Derivative
da/dN	Fatigue crack growth rate
d_c	Material cohesion for Drucker-Prager model
$d\varepsilon^{pl}$	Plastic strain increment
$d\bar{\varepsilon}^{pl}$	Equivalent plastic strain increment
d_{hkl}	Interplanar distance
D	Crystallite size
D_d	Cumulative damage
D_{max}	Crystallite size – maximum value
D_{min}	Crystallite size – minimum value
D_M	Width of monotonic specimen
D_μ	Crystallite size – average value
D_σ	Crystallite size – standard deviation
$e_{2,min}$	Minimum edge distance of hole
$e_{2,plate}$	Edge distance of hole in the plate
E	Young's modulus
$\bar{E}$	Elastic striffness
$E_{conf,i}$	Stiffness under confined conditions at cycle i
E_Z	Young's modulus in Z direction

f	Frequency
$f\,(\,)$	Function to compute equivalent plastic strain
$f_{b,resin}$	Bearing strength of the resin
f_J	Body force per unit volume
$f_R\,(\,)$	Stress ratio normalization function
f_u	Ultimate strength
f_{ub}	Ultimate strength of bolt
f_y	Yield strength
$f_{y,c}$	Compressive yield stress
$f_{y,t}$	Tensile yield stress
F	Applied force
$F_{b,Rd}$	Design bearing resistance of plates
$F_{b,Rd,resin}$	Design bearing resistance of resin
F_{cl}	Crack closure force
F_j	Applied force at iteration j
F_{HV}	Applied force in hardness test
F_{max}	Maximum applied force
F_{min}	Minimum applied force
$F_{net,Rd}$	Design plastic resistance to normal forces of the net cross-section
$F_{p,C}$	Bolt preload force
$F_{pl,Rd}$	Design plastic resistance to normal forces of the gross cross-section
F_s	Slip load
$F_{s,Rd}$	Design slip resistance
$F_{s,Rd,ser}$	Design slip resistance per bolt for service limit state
F_u	Ultimate resistance
$F_{v,Rd}$	Design shear resistance of the bolt
$F_{v,Sd,ser}$	Service load range per bolt
F_y	Yield force
G	ASTM grain size number
G_f	Flow potential

h	Miller indices
H	Variable to compute J integral
HV	Hardness
i	Cycle number in quasi-static resin and steel-reinforced resin confined tests
j	Iteration variable
J	J integral
k	Miller indices
k_b	Correlation coefficient for bolt preload
k_D	Scherrer constant
$k_{p,1-\alpha_n,v_{dg}}$	One-sided tolerance limit
k_s	Hole size parameter
k_t	Limit state parameter
K	Stress intensity factor
K'	Cyclic strength coefficient
K_I	Stress intensity factor in Mode I
K_c	Fracture toughness
K_{cl}	Stress intensity factor at crack closure
K_{max}	Maximum stress intensity factor
K_{max}^{eff}	Maximum effective stress intensity factor
K_{min}	Minimum stress intensity factor
K_r	Residual stress intensity factor
$K_{r,j}$	Residual stress intensity factor at iteration j computed experimentally
$\widehat{K}_{r,j}$	Residual stress intensity factor at iteration j computed analytically
K_t	Stress concentration factor
K_{tc}	Ratio between triaxial tension and compression yield stresses
l	Miller indices
$\bar{l}$	Mean line intercept
L	Total length of lines for grain size measurement
$L\,(\ )$	Maximum likelihood function of Weibull distribution
L_{diag}	Indentation diagonal
L_0	Original gauge length

L_c	Parallel length
L_t	Total length of test piece
L_R, L_{SRR}	Length of specimens: resin and steel-reinforced resin
m	Slope of fatigue curve
$m\,(\,)$	Weight function
m_{eff}	Slope of fatigue curve for ΔK_{eff}
m_{el}	Slope for elastic FCG curve of Peeker and Niemi model
m_J	Outward normal vector for J-integral calculations
m_{pl}	Slope for plastic FCG curve of Peeker and Niemi model
n	Sample size
n'	Cyclic strain-hardening exponent
n_b	Number of bolt rows
n_{Ei}	Number of cycles associated with the stress range $\gamma_{Ff}\Delta\sigma_i$
n_J	Normal vector to contour Γ
n_p	Number of slip planes
M	Magnification
M_1, M_2	Population moments for Method of Moments
M_b	Bolt torque
$M_{w,1}, M_{w,2}, M_{w,3}$	Geometry factors for weight function
N	Number of fatigue cycles
N_{block}	Number of fatigue cycles to reach failure within the process block size
N_i	Number of fatigue cycles for crack initiation phase
N_f	Number of fatigue cycles at failure
N_p	Number of fatigue cycles for crack propagation phase
N_{Ri}	Endurance number of fatigue cycles for stress field i
N_t	Number of fatigue cycles at transition between elastic and plastic domains
p	Hydrostatic pressure
$P(\,)$	Probability density function
$\bar{P}_j$	Total number of intersections
$\bar{P}_L$	Number of intersections per length of test line
q	Vector that indicates the direction of the crack growth

$\bar{q}$	Weighting function
q_{eq}	von Mises equivalent stress
r	Radial distance to the crack tip – polar coordinate
r_M	Radial distance to the crack tip – polar coordinate
R^2	Coefficient of determination
R_{eH}	Upper yield strength
R_m	Tensile strength
R_p	Reversed plastic zone ahead of the crack tip for Ellyin and Kujawski model
R_y	Monotonic plastic zone ahead of the crack tip for Ellyin and Kujawski model
R_σ	Stress ratio
R_ε	Strain ratio
S	Applied remote stress
S_{max}	Applied remote stress – maximum value
S_{min}	Applied remote stress – minimum value
SWT^e	Smith-Watson-Topper model – elastic component
SWT^p	Smith-Watson-Topper model – plastic component
SWT_{block}	Fatigue damage within the process block size
t	Thickness of dog-bone specimen for monotonic tests
t_1, t_2	Thickness of plates in resin-injected bolted connection
$t_{b,resin}$	Effective bearing thickness of the resin
t_D	Deviatoric stress
u	Displacement
u_x	Independent variable used in compliance method
U	Crack closure level
U_d	Dislocation strain energy
U_e	Elastic strain energy density
U_p^*	Complementary plastic strain energy density
U_x, U_y, U_z	Computational displacement in Cartesian coordinates
U_r	Radial displacement
UR_x, UR_y, UR_z	Computational rotation in Cartesian coordinates
v_c	Crack opening displacement

$v_{c,max}$	Maximum value of crack opening displacement
$v_{c,min}$	Minimum value of crack opening displacement
v_{dg}	Degrees of freedom for normal distribution function
v_j	Crack opening displacement at applied force F_j
v_L	Linear component of F-v_c curve
v_Q	Non-linear component of F-v_c curve
W	Elastic strain energy
W_{CT}	Width of CT specimen
W_p	Width of plate
w	Fitting parameter for Walker strain-life expression (Hurley and Evans model)
w_j	Polynomial weight function for WLLSM
x, y, z	Coordinates from Cartesian system
X	Independent variable for linear regression analysis
$\bar{X}$	Mean value of X_j
X_j	Value of the independent variable for specimen j
Y	Dependent variable for linear regression analysis
Y_K	Normalized value of stress intensity factor
$\bar{Y}$	Mean value of Y_j
Y_j	Value of the dependent variable for specimen j

Greek Symbols

α	Ratio of crack length
α_n	Variable to compute the confidence level
α_v	Bolt class parameter
α_W	Scale parameter for Weibull distribution
β	Geometry factor for stress intensity factor
β_{EK}	Parameter of Ellyin and Kujawski model
β_D	Full width and half maximum
β_f	Material angle of friction
β_{resin}	Thickness ratio coefficient

β_W	Shape parameter for Weibull distribution
γ_{Ff}	Partial factor for fatigue loads
γ_{M0}	Partial factor for resistance of cross-sections whatever the class is
γ_{M2}	partial factor for resistance of cross-sections in tension to fracture
γ_{M4}	Partial safety factor for the bearing resistance of an injection bolt
γ_{Mf}	Partial safety factor for fatigue strength
$\Gamma\,(\,)$	Gama function for Method of Moments
Γ	Contour that surrounds crack tip
Δd	Displacement range
ΔF	Applied force range
$\Delta F_{v,Sd,ser,max}$	Maximum service load range per bolt
ΔJ	Strain energy release range
ΔK	Stress intensity factor range
ΔK_{app}	Applied stress intensity factor range
ΔK_{eff}	Effective stress intensity factor range
ΔK_{th}	Threshold of stress intensity factor range
ΔN	Range of fatigue cycles
ΔW^p	Strain energy range per cycle – plastic component
$\Delta \varepsilon$	Strain range
$\Delta \varepsilon^p$	Strain range – plastic component
$\Delta \varepsilon_{eq}^p$	Equivalent strain range – plastic component (Ellyin and Kujawski model)
$\Delta \sigma$	Stress range
$\Delta \sigma_1, \ldots, \Delta \sigma_5$	Stress range levels
$\Delta \sigma_C$	Detail category
$\Delta \sigma_D$	Constant amplitude fatigue limit
$\Delta \sigma_{eq}$	Equivalent stress range for Ellyin and Kujawski model
$\Delta \sigma_{gross}$	Stress range using gross cross-section
$\Delta \sigma_{gross,norm.}$	Stress range using gross cross-section (normalized value)
$\Delta \sigma_i$	Stress range for stress field i
$\Delta \sigma_L$	Fatigue cut-off limit
$\Delta \sigma_{norm}$	Stress range (normalized value)

$\Delta\sigma_{net}$	Stress range using net cross-section
$\Delta\sigma_{net,norm.}$	Stress range using net cross-section (normalized value)
δ	Process zone for Peeker and Niemi model
δ_D	Dislocation density
δ_p	Process block size
δ^*	Process zone for Ellyin and Kujawski model
ε_a	Strain amplitude
ε_a^e	Strain amplitude – elastic component
$\varepsilon_{a,x}^e, \varepsilon_{a,y}^e, \varepsilon_{axy}^e$	Elastic strain amplitude ahead of the crack tip
ε_a^p	Strain amplitude – plastic component
$\varepsilon_{a,block}^{eff}$	Effective strain amplitude over the process block size
ε_f'	Fatigue ductility coefficient using Coffin-Manson-Basquin model
$\varepsilon_{f,Huffman}'$	Fatigue ductility coefficient using Huffman model
$\varepsilon_{f,Morrow}'$	Fatigue ductility coefficient using Morrow model
$\varepsilon_{f,SWT}'$	Fatigue ductility coefficient using SWT model
ε_{max}	Maximum strain
$\varepsilon_{max,x}^e, \varepsilon_{max,y}^e$	Maximum elastic strain ahead of the crack tip
ε_{mean}	Mean strain
ε_{min}	Minimum strain
ε_w	Walker strain
$\varepsilon_x, \varepsilon_y, \varepsilon_z$	Strain in Cartesian coordinates
$\varepsilon_{y,a}$	Strain amplitude in Y direction
$\varepsilon_{y,max}$	Maximum strain in Y direction
$\varepsilon_{y,F_{max}}$	Strain in Y direction at maximum applied load
$\varepsilon_{y,F_{min}}$	Strain in Y direction at minimum applied load
$\varepsilon_x^e, \varepsilon_y^e$	Elastic strain in Cartesian coordinates
$\varepsilon_x^{e-p}, \varepsilon_y^{e-p}, \varepsilon_z^{e-p}$	Elastoplastic strain in Cartesian coordinates
ε_{xy}^e	Elastic shear strain ahead of the crack tip
$\varepsilon_{z_0}^{\,f}$	Nominal fracture initiation strain
$\varepsilon_{z_0}^{\,f}$	Nominal fracture ultimate strain

$\varepsilon_{z,pl}$	Nominal plastic strain
$\varepsilon_{z,r}$	Nominal residual strain
$\varepsilon_{z,r,i}$	Nominal residual strain at cycle i
$\varepsilon_{z,r,pl}$	Nominal residual plastic strain
$\varepsilon_{z,r,pl,i}$	Nominal residual plastic strain at cycle i
$\varepsilon_{z,r,visc}$	Nominal residual viscoelastic strain
$\varepsilon_{z,r,visc,i}$	Nominal residual viscoelastic strain at cycle i
ξ	Residual sum of squares
θ	Angle of the crack tip – polar coordinate
θ_D	Interception angle of particle beam in X-ray diffraction
λ	Wavelength
μ	Mean for normal distribution function
μ_e	Static friction coefficient
μ_k	Sampling moments for Method of Moments
$\emptyset$	Diameter
φ	Material friction angle for Mohr-Coulomb criterion
ρ_c	Dislocation density – critical value
ρ^*	Crack tip radius
σ	Applied remote normal stress
$\hat{\sigma}$	Standard deviation
σ'_0	Cyclic yield stress
σ_1, σ_2	Nominal stress on plates in a resin-injected bolted connection
σ_a	Normal stress amplitude
$\sigma^e_{a,x}, \sigma^e_{a,y}$	Elastic normal stress amplitude ahead of the crack tip
σ^{e-p}_{eq}	Elastoplastic equivalente normal stress
σ'_f	Fatigue strength coefficient using Coffin-Manson-Basquin model
$\sigma'_{f,Huffman}$	Fatigue strength coefficient using Huffman model
$\sigma'_{f,Morrow}$	Fatigue strength coefficient using Morrow model
$\sigma'_{f,SWT}$	Fatigue strength coefficient using SWT model
σ_{max}	Maximum normal stress

$\sigma^e_{max,x}$, $\sigma^e_{max,y}$	Maximum elastic normal stresses ahead of the crack tip
$\sigma^{eff}_{max,block}$	Maximum effective stress over the block size
σ_{mean}	Mean normal stress
σ_{min}	Minimum normal stress
$\sigma_{MC,1},\ldots,\sigma_{MC,3}$	Principal stresses for Mohr-Coulomb criterion
σ_{net}	Normal nominal stress at net cross-section
σ_r	Residual normal stress
σ_x, σ_y, σ_z	Stress on principal directions
$\sigma_{y,max}$	Maximum stress on y direction
$\sigma_{y,F_{max}}$	Stress on y direction at maximum applied force
σ^e_x, σ^e_y	Elastic stress on principal directions
σ^{e-p}_x, σ^{e-p}_y	Elastoplastic stress on principal directions
$\sigma^{e-p}_{y,max}$	Elastoplastic stress on y direction – maximum value
$\sigma^{e-p}_{y,a}$	Elastoplastic stress on y direction – amplitude value
σ_{yield}	Yield normal stress
$\sigma_{z,true}$	True normal stress in Z direction
$\tau^e_{a,xy}$	Elastic tangential stress amplitude on xy direction
τ_{xy}	Tangential stress on xy direction
$\tau^e_{max,xy}$	Elastic tangential stress on xy direction – maximum value
τ_{yz}	Tangential stress on yz direction
τ_{xz}	Tangential stress on xz direction
ν	Poisson's ratio
χ^2	χ-Squared goodness-of-fit test
ψ	Dilatation angle
Ψ	Function that defines the analytical plastic field

xxii

ACRONYMS

AD	Anderson-Darling goodness-of-fit test
AASHTO	American Association of State Highway and Transportation Officials
ASTM	American Society for Testing and Materials
BCC	Body-Centred Cubic
BCIB	Bolted connections with injection bolts
BMR	Bernard Median Rank
BS	British Standard
CCT	Central Crack
CMB	Coffin-Manson-Basquin model
COD	Crack Opening Displacement
CT	Compact Tension
DIC	Digital Image Correlation
DNV-GL-RP	Det Norske Veritas – Germanischer Lloyd – Recommended Practice
ECCS	European Convention for Constructional Steelwork
EDM	Electrical Discharge Machining
EIFS	Equivalent initial flaw size
EN	European Standard
EPFM	Elastic Plastic Fracture Mechanics
ISO	International Organization for Standardization
FCC	Face-Centred Cubic
FCG	Fatigue crack growth
FMA	Fracture Mechanics Approach
FRP	Fiber Reinforced Polymer
FWHM	Full Width Half Maximum
HSFG	High strength friction grip
JSSC	Japanese Society of Steel Construction
KS	Kolmogorov-Smirnov goodness-of-fit test
LCF	Low-Cycle Fatigue
LEFM	Linear Elastic Fracture Mechanics

LLSM	Linear Least Squares Method
MLM	Maximum Likelihood Method
MM	Method of Moments
NDI	Non-destructive inspection
RSS	Residual Sum of Squares
SEM	Scanning Electron Microscope
SIF	Stress Intensity Factor
SWT	Smith-Watson-Topper
WLLSM	Weighted Linear Least Squares Method
WWII	World War II
XRD	X-Ray Diffraction

LIST OF FIGURES

LIST OF TABLES

1   INTRODUCTION

1.1   Motivation

In the second half of the 19th and turn of the 20th century, new materials have widely spread throughout the world allowing for an exponential growth of metallic constructions, namely steel bridges, many of which are still in service nowadays [1]. In Portugal, there are also a large number of centenary steel bridges requiring maintenance and rehabilitation [2]. Through the years, these structures have been subjected to a constant increase of traffic level, not only in terms of vehicle gross weight but also in terms of their frequencies. Consequently, governmental authorities need to implement and study innovative methods aiming to maintain their safety levels since their replacement in short period of time will be too costly. The most common evidences of damages in these structures are the presence of corroded metallic elements and cracks in structural details due to the fatigue phenomenon [3]. At the time that these structures were designed, there was only a rough understanding on the fatigue phenomenon, since it only has been intensively investigated in the second half of the 20th century. Consequently, fatigue assessment of old riveted bridges has been a major concern [4,5]. Concerning steel structures, Oehme [3] made a study focused on the major causes of damage and type of structure. It was found that the most frequent cause of structural damage in bridges (combining railway and roadway) is fatigue.

Table 1.1. Main causes of damages of steel structures [3].

Damage cause	Buildings		Bridges		Conveyors		Total	
	No.	%	No.	%	No.	%	No.	%
Fatigue	8	2.6	49	38.3	35	31.5	92	16.9
Static strength	102	33.6	19	14.8	40	36	161	29.7
Stability (local or global)	62	20.4	11	8.6	14	12.6	87	16
Rigid body movement	25	8.2	2	1.6	17	15.3	44	8.1
Elastic deformation	14	4.6	1	0.8	0	0	15	2.8
Brittle fracture	9	3	5	3.9	1	0.9	15	2.8
Environment	59	19.4	41	32	1	0.9	101	18.6
Thermal loads	23	7.6	0	0	0	0	23	4.2
Others	2	0.7	0	0	3	2.7	5	0.9
Sum	304	100	128	100	111	100	543	100

More recently, Imam and Chryssanthopoulos [6] found that the most frequently encountered modes of metallic bridge failure are scour of piers/foundations (17%), buckling (16%), fatigue

(13%), impact (13%) and fracture (9%). Furthermore, fatigue damage is dominant cause of non-collapsing failure modes (67%).

Several European Union scientific projects have been funded aiming to improve the state of knowledge about the fatigue phenomenon on steel bridges, for example, PROLIFE [7–10], BRiFaG [11] and Sustainable Bridges [12]. An extensive collection of data about fatigue damages on steel and composite bridges performed within the BRiFag project [11] showed that the most common types of fatigue damage are: a) in the connections between diaphragms and cross-bracings; b) in the connections between stringers and cross beams; c) in the connections between cross beams and the main load-carrying members. In Figure 1.1a) is presented an example of a fatigue crack found in the outstanding leg of the connections angle in a cross-bracing element. Mechanically fastened stringer-to-cross-beam connections are also prone to develop fatigue damage. Many cases were found in which fatigue cracks were detected in the connection angles. Furthermore, rivet failures are also very common leading to total separation of the riveted head – see Figure 1.1b). In Figure 1.1c) is illustrated an example of a typical fatigue crack growing from the hole of the plate found in structural elements of Eiffel bridge, in Viana do Castelo.

a)   b)   c)
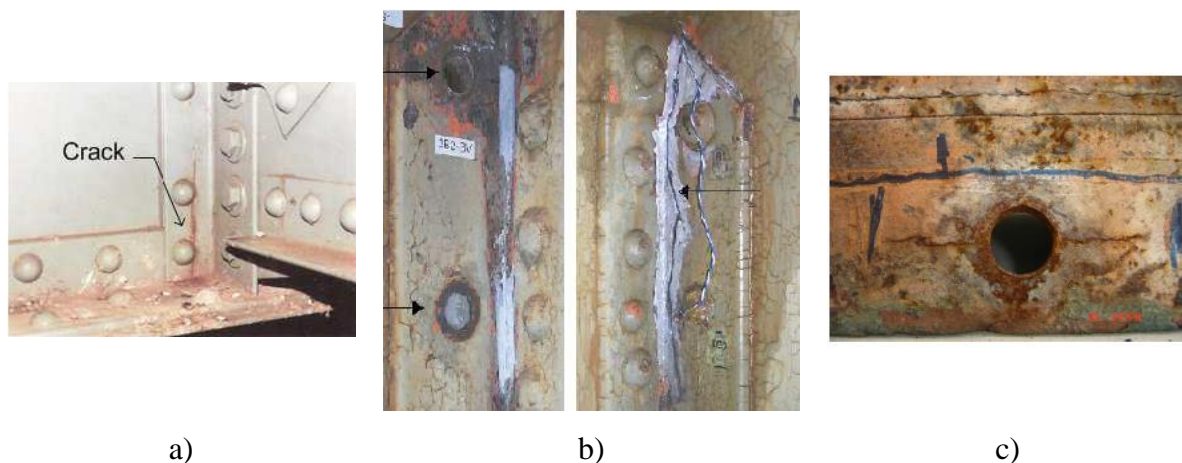
Figure 1.1. Fatigue cracks: a) in riveted connection between cross-bracing elements [11]; b) in stringer-to-cross-beam connections [11]; c) growing from a rivet hole [13].

There are significant differences between those metallic bridges that were built at the beginning of the 20th century and those that are built nowadays. One main difference is related to the metallic material that is used. The first metallic bridge structures were mainly based on cast

iron. With significant improvements on production technological procedures and scientific researches, cast iron was first replaced by puddled iron, latter by non-alloy structural steels and finally by high strength steels [14]. In this sense, any fatigue damage assessment on bridge structures must rely on a comprehensive study about the exact properties of the materials considering its variability and the period of production. Furthermore, many fatigue damage models have been created to describe fatigue mechanisms based on material properties which not only strengthen the importance of material detailed assessment but also creates the need to analyse material properties based on a probabilistic approach.

The common procedure to assess the fatigue life on civil engineering structures is based on global methods using nominal stresses and linear damage accumulation. For example, fatigue design of steel structures based on EN 1993-1-9 [15], AASHTO [16] and JSSC [17] is based on fatigue strength S-N curves assigned for a catalogue of constructional details. Its application is simple, however there are several limitations related to the accuracy to address complex geometries, stress computation and material properties. Considering the evolution of technological and computation efficiency in the last decades, local approaches for fatigue assessment have been considered as a reliable alternative in which finite element method is the basis to obtain local fatigue damage parameters used to derive fatigue life. Furthermore, these local approaches allow to establish a clear distinction between initiation and propagation phases which is not possible if global approaches are used. This separation is essential to establish fatigue life predictions avoiding expensive experimental campaigns on structural details in real scale.

Fatigue cracks in metallic structures can be acceptable when they do not have significant safety or economic consequences. However, in this scenario not only periodic inspections have to be considered but also the knowledge concerning fatigue crack growth is essential. The mechanisms and the velocity of a fatigue crack growth process deserve especial attention to set timely inspection periods. In this sense, experimental tests and new analytical models are required to strengthen the scientific knowledge about general fatigue crack growth and specific mechanisms like crack closure phenomenon. Furthermore, in what concerns fatigue damages in riveted/bolted shear connections, it is essential to properly acknowledge fatigue crack propagation mechanisms to establish reliable predictions about the behaviour of the crack. This

aspect is especially relevant for cracks that emerge in invisible areas as, for example, in the region of the plates covered by bolt head, nut and washers, as presented in Figure 1.1c).

Different strategies can be implemented for repairing and strengthening operations of bridges with long period in service. To preserve their original architecture, riveting might be used, however this process is no longer a common practice. The use of welding may not be appropriate since old metallic materials are characterized by their poor weldability properties. Another possibility is using high-strength friction grip (HSFG) bolts, but their good performance is dependent on the friction behaviour between the connected plates and on long term preload forces. Concerning the use of fitted bolts, their application requires an expensive preparation of the holes. Therefore, implementing injection bolts might be the most appropriate solution [18]. The structural performance of resin-injected bolted connectors is mainly dependent on the adhesive that surrounds the shank of the bolt. Its selection should consider mechanical, technological, and structural requirements.

Resin-injected shear connectors have already been applied successfully in reparation of old bridges [19]. For example, when the rehabilitation of an old riveted steel bridge in Oranienburg, connecting The Netherlands to Germany, were studied, the decision was using injection bolts to connect new plates in corroded areas of its structural elements [20]. Even in Portugal, the use of injection bolts has been reported [21]. However, the fatigue behaviour of this structural solution has not been widely studied [22].

1.2   Framework and objectives

The research work described in this thesis aims to present a comprehensive study on the fatigue performance of resin-injected bolted shear connections. Due to the local nature of fatigue damages, this goal can only be achieved by performing specific studies on the different elements that compose this connection: injection material, metallic plates, and connectors. With the knowledge acquired from the study of each component, the global assessment of the fatigue performance of resin-injected bolted connections was also conducted. A schematic representation of the content framework of this thesis is presented in Figure 1.2.
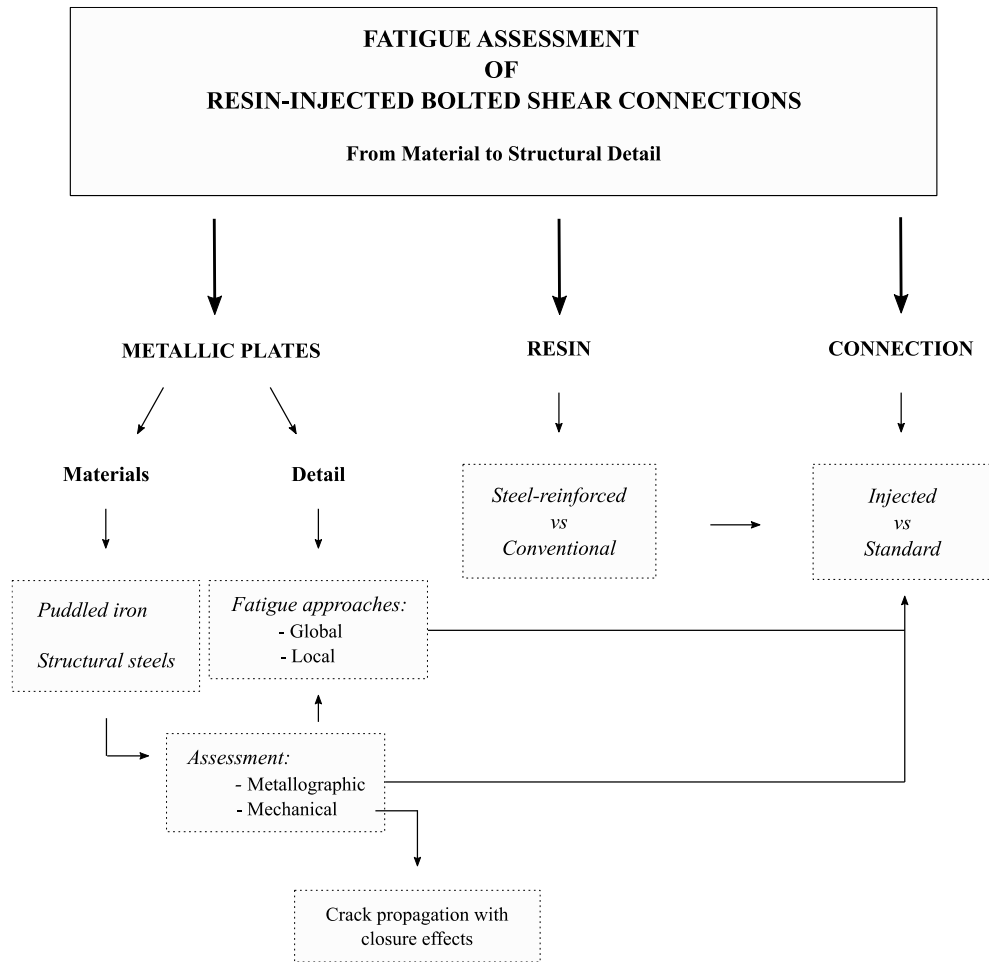
Figure 1.2. Schematic representation of PhD thesis content framework.

The first approach to the topic is based on establishing a full characterization of materials that compose the metallic plates of the connection. Three relevant materials within the field of metallic bridge structural elements were selected including not only modern steels but also a representative material from long time operating bridges. The goal is to compare these materials concerning their micro and nano-structural properties and to characterize their monotonic, fatigue and fracture performance. Furthermore, several fatigue damage models are implemented to describe the fatigue performance of each material. This material mechanical assessment is complemented with a statistical approach.

Fatigue crack growth (FCG) of selected modern steels deserve special attention. Generally, fatigue damages start by local cyclic plastic deformation and then a fatigue crack emerges. It is essential to understand the behaviour of the crack and how material properties influence it, to

be able to establish reliable predictions. The general approach is to analyse fatigue crack growth using global parameters such as nominal stress, crack length and geometry. However, the effect of residual stresses induced by reversed plastic deformation is neglected (crack closure phenomenon). In this sense, fatigue crack growth of selected materials is studied by means of experimental, numerical, and analytical characterization of the stress-strain field formed ahead of the crack tip. The objective is to propose an analytical approach based on Unigrow model that leads to reliable predictions of FCG behaviour considering plasticity induced crack-closure materialized in residual stresses formed ahead of the crack tip.

The most common location of fatigue damage in bolted connections is in the plates. When the load is transferred by shear through the shank of the bolt to the plate, there is a high level of stress concentration around the hole of the plate that can lead to fatigue damage. In this sense, it is intended to characterize the fatigue behaviour of bolt hole details by means of experimental and numerical approaches. The influence of hole execution method, protection layers (galvanization) and material properties on the fatigue behaviour is investigated. It is also important to analyse the fatigue life of this detail to evaluate the moment when the crack would become visible, considering it as an element of a bolted/riveted assembly. Besides global approaches to fatigue, several fatigue local models are implemented aiming to assess the advantages and disadvantages of each damage criterion. Additionally, a more comprehensive study concerning fatigue crack growth in bolt holes is essential to analyse the relative weight of initiation and propagation phases in the total fatigue life.

In what concerns the characterization of injection materials to implement in bolted connections, it is essential to determine material parameters to describe its behaviour considering, as close as possible, the conditions faced in the assembly. In this sense, experimental and numerical approaches are implemented to fully characterize different resin materials.

Finally, at the connection level, double and single bolted shear connections are studied to characterize the fatigue behaviour when using injection bolts in comparison to standard bolts. Specimens connect new steel to old metallic material obtained from structural elements extracted from the Eiffel bridge in Viana do Castelo aiming to reproduce as close as possible

the real situation of strengthening techniques. Experimental results are compared with the European standard for fatigue design of steel structures – EN 1993-1-9.

1.3 Structure of the thesis

This thesis is divided in eight chapters, as shown in Figure 1.3. In the first chapter, INTRODUCTION, a general perspective of the research topic is presented including motivations and objectives.
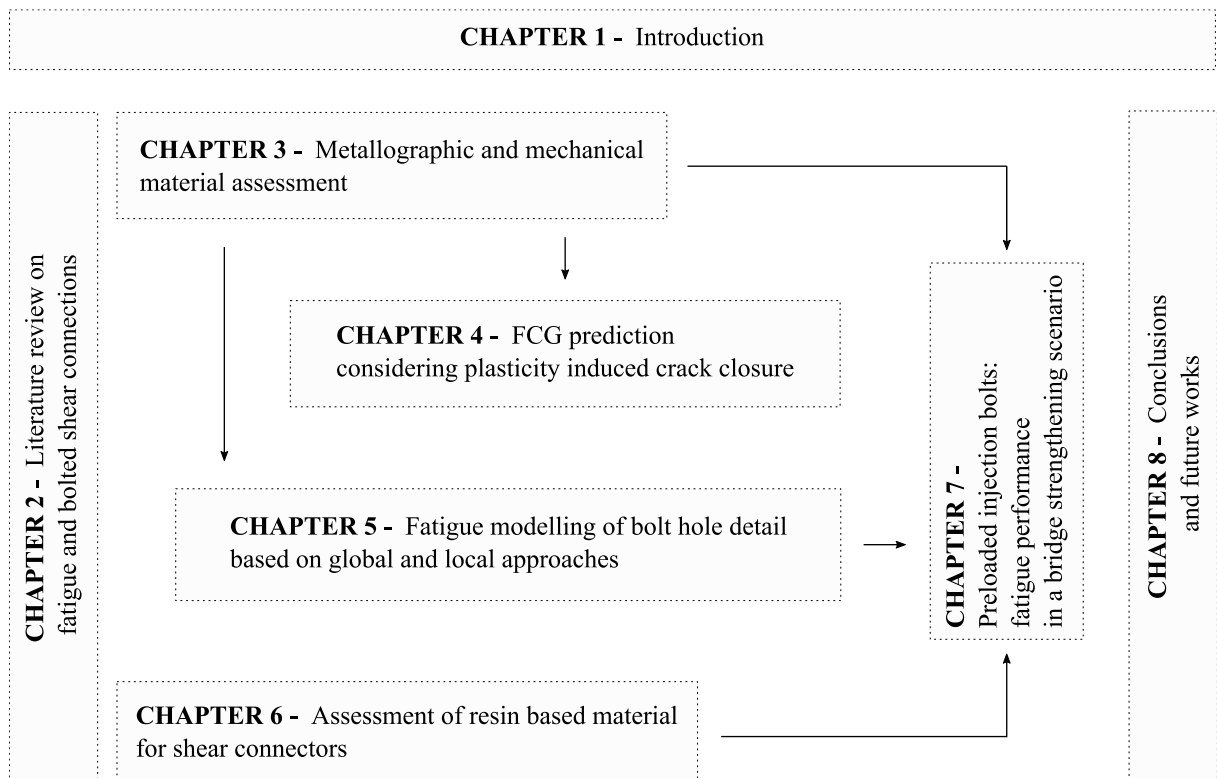
Figure 1.3. Schematic representation of thesis structure.

The next chapter is entitled LITERATURE REVIEW ON FATIGUE AND BOLTED SHEAR CONNECTIONS in which a general characterization of the fatigue phenomenon is presented showing the differences between initiation and propagation phases and the main factors that influence each part. Then, the most relevant fatigue life prediction models are described including global and local approaches. This chapter is complemented with a literature review on the fatigue behaviour of bolted connections. The distinction between bearing and friction-type connections is described as well as the effects of load eccentricity in the case of single lap joints. Fatigue design recommendations were reviewed as well as scientific studies on the

fatigue behaviour of bolted connections using puddled iron plates. Finally, the statistical methods used to analyse experimental data are described. They are based on normal and Weibull distribution functions.

In Chapter 3, entitled METALLOGRAPHIC AND MECHANICAL MATERIAL ASSESSMENT, three metallic materials were selected for a comprehensive study which includes a metallographic analysis and a mechanical study with monotonic, fatigue and fracture characterization. The metallographic analysis comprises the study of the microstructure and the evaluation of the grain size. For modern metallic materials, it also included a study on the nanostructure of each material, namely concerning its crystallite size aiming to assess the dislocation density. In what concerns mechanical assessment, the hardness of each material was evaluated as well as the monotonic tensile behaviour. Fatigue performance was studied using a collection of experimental data from literature and three damage parameters were implemented: strain, SWT and strain energy. Finally, FCG behaviour of each material was evaluated by means of experimental tests. Statistical analysis allowed to define FCG parameters for each material and establish a comparison with recommendations in standards.

In the next chapter, number 4, intitled FATIGUE CRACK GROWTH PREDICTION CONSIDERING PLASTICITY INDUCED CRACK-CLOSURE, an analytical approach to model FCG is developed based on UniGrow model. The effective stress intensity factor range is used to study the fatigue crack growth of two modern steels. The residual stress field caused by crack-closure effect is considered by means of experimental, numerical and analytical approaches.

Then, in chapter 5, entitled FATIGUE MODELLING OF BOLT HOLE DETAIL BASED ON GLOBAL AND LOCAL APPROACHES, fatigue assessment is focused on the plates that compose a bolted connection. Fatigue experimental tests were conducted to characterize the fatigue behaviour of this detail and fatigue predictions were established using global and local fatigue models. Specific fatigue crack growth tests were also conducted aiming to fully characterize the fatigue crack growth process when a crack is emerging from a hole.

In chapter 6, intitled ASSESSMENT OF RESIN BASED MATERIAL FOR SHEAR CONNECTORS, injection materials for shear connectors are studied. Experimental and numerical approaches are implemented to propose a material model that can represent the material behaviour in the conditions that are found in bolted connection assemblies.

In chapter 7, intitled INJECTION BOLTS – FATIGUE PERFORMANCE IN A METALLIC BRIDGE STRENGTHENING SCENARIO, an experimental campaign is detailed. Single and double bolted shear connections were tested under fatigue loading conditions aiming to compare the fatigue strength of injection and standard bolts. Specimens were defined aiming to be as close as possible to a bridge strengthening scenario, thus they are composed of modern and old metallic materials.

Finally, in chapter 8, the overall conclusions are addressed, and the main contributions are summarized. Future research topics are also proposed.

2   LITERATURE REVIEW ON FATIGUE AND BOLTED SHEAR CONNECTIONS

2.1   Introduction

The study of fatigue and fracture of materials was initiated in the 19th century, when the German mining administrator, Wilhelm Albert, published the first known results about fatigue failure in metallic components. Furthermore, with the development of metallic materials and its use in civil engineering structures, specifically in highway and railway bridges, the study of fatigue phenomenon began to be investigated more frequently [23].

August Wöhler stood out for his engineering research on fatigue. He understood that a repeated load could induce a complete failure, even with a magnitude far below the static strength of a structure. He also introduced the concept of fatigue limit along with fatigue phenomenon characterization using stress-life curves, which became known as Wöhler curves or *S-N* curves. Later in the 20th century, investigations proved that repeated loads (service loads) can start a fatigue fracture mechanism in the material, beginning from nucleation of micro-cracks, which can evolve with a crack growing process leading to complete failure [23].

Fatigue prediction models began in the first half of the 20th century with Palmgren and Miner who proposed the linear damage accumulation theory, known as Miner's rule [24]. Later, Coffin and Mason performed scientific investigations in order to describe cyclic plastic behaviour of metallic materials leading to the empiric Coffin-Mason relation [25,26]. Fracture Mechanics approaches, which comprise the fatigue crack propagation study, were firstly developed by Griffith in 1920 [27].

In what concerns fatigue damages on civil engineering structures, they occur mainly in connections. Depending on the type of connection and its design, a significant stress concentration can occur, and fatigue cracks can be initiated. In this chapter, a general characterization on the fatigue phenomenon on metallic materials is presented as well as a literature review on the most relevant fatigue life prediction models. Fatigue mechanisms in bolted connections will be also addressed with emphasis on resin-injected bolted connections. In the last section, statistical approaches to analyse fatigue experimental data are described.

2.2   General characterization on the fatigue phenomenon

2.2.1   Fatigue life phases

Fatigue phenomenon normally starts at a microscopic scale, although it can evolve significantly and cause specimen failure or irreversible damage of structures. This fatigue behaviour needs to be properly acknowledged and the best way to do so is by dividing it in two parts: crack initiation period and crack growth period [23].

This distinction is important because each phase of the fatigue phenomenon is influenced by different aspects. While some surface conditions, namely surface roughness (a texture indicator), do affect the crack initiation period, it has a negligible influence on the crack propagation period. Therefore, fatigue prediction models are also distinct for these two periods. In fatigue prediction models for crack initiation, the general procedure is to consider the stress concentration factor, K_t, which is a parameter that characterizes the severity of stress distribution around a notch. Nevertheless, when the notch evolves into a crack, this parameter is meaningless. A crack differs from a notch specially in geometry – a notch typically has a circular or elliptical form and can be defined by two main axes. However, it turns into a crack when the dimension along one axis becomes much bigger than the other. Consequently, to define crack growth period, typical procedures are based on the stress intensity factor, K, which characterizes the stress field around the crack. When the stress intensity factor reaches a critical value, there is a sudden fracture and complete failure occurs. This final moment of the fatigue life is defined by the fracture toughness of the material, K_c [23]. A schematic representation of the various steps of fatigue life and its important parameters is presented in Figure 2.1.
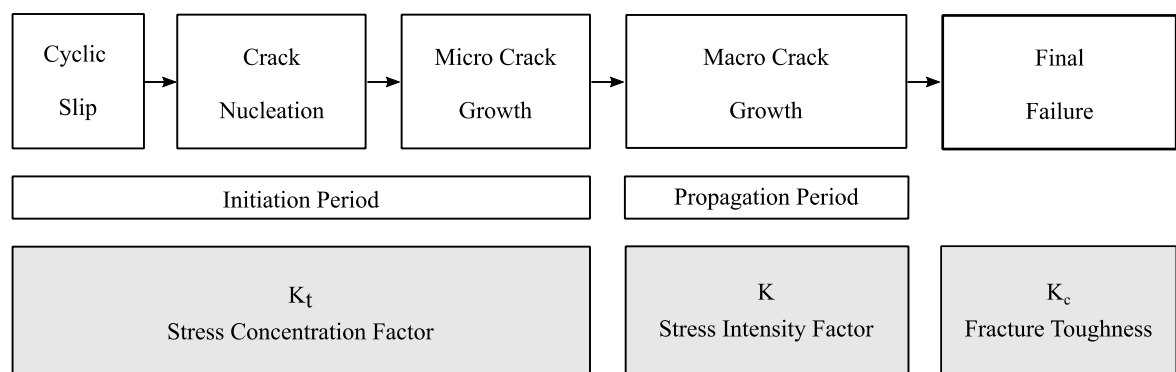
Figure 2.1. Characterization of fatigue life phases.

Fatigue life of a structural element is the total number of load cycles, N_f, endured in the two processes mentioned before, being N_i referred to the initiation period, and N_p, to the propagation period, as shown in the following equation:

$$N_f = N_i + N_p \qquad (2.1)$$

Previous investigations on laboratory specimens have shown that invisible micro cracks remain in most part of the total fatigue life. When those fatigue cracks become visible, only a small percentage remains of the total life of the detail. However, in real structures such as ships, aircraft and bridges, this remaining life may be much longer than the investigations carried out in laboratory specimens [28]. Fatigue crack initiation implies some amount of cyclic plastic deformation, and it normally occurs at stress amplitudes below the yield stress. Therewith, this plastic deformation is restricted to small and specific grains in the material surface. These grains are the most vulnerable because the surrounding material is present on one side only. In fact, crack initiation period is mainly influenced by surface conditions. Thus, stress concentration on the surface, due to a notch effect or some other geometric discontinuity, roughness or corrosion pits are aspects to consider. Crack initiation period also includes initial micro-crack growth. Previous studies showed that it starts with a relatively high crack growth rate and then slows down or even stops due to material structural barriers [23].

There is no easy way to define the transition from the initiation period to the crack propagation period in quantitative terms because the transition depends on microstructural barriers (grain boundaries) that are not the same in all materials. However, it can be established that when micro crack growth has occurred away from the nucleation site, it is the beginning of the real crack growth period. At this stage, surface conditions are no longer relevant parameters, and crack growing resistance depends on the material as a bulk property. There is a general tendency in the crack growing process to develop in a direction perpendicular to the load [23].

2.2.2 Cyclic parameters

Within the scientific community, it is widely accepted that fatigue damage is related to stresses or strains varying in time. Fatigue cyclic load can be divided in three different categories: constant amplitude loading spectrums, variable amplitude loading spectrums defined by

constant amplitude blocks and variable amplitude loading spectrums, randomly defined. In order to characterize constant amplitude stress cycles, Figure 2.2 shows the different parameters that should be established, such as the maximum and minimum stresses, σ_{max} and σ_{min}, the stress range, $\Delta\sigma = \sigma_{max} - \sigma_{min}$, the stress amplitude, $\sigma_a = (\sigma_{max} - \sigma_{min})/2$, the mean stress, $\sigma_{mean} = (\sigma_{max} + \sigma_{min})/2$, and the stress ratio, $R_\sigma = \sigma_{min}/\sigma_{max}$. The most common values for stress ratio are $R_\sigma = 0$ (pulsating load) and $R_\sigma = -1$ (alternating load).
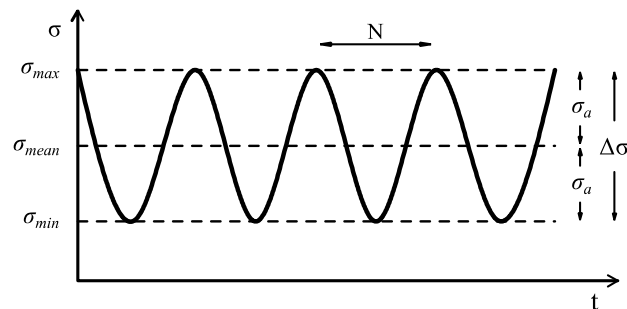
Figure 2.2. Cyclic parameters for constant amplitude fatigue loading.

In the same way, similar expressions can be obtained if load magnitude is controlled by strain: for strain range $\Delta\varepsilon = \varepsilon_{max} - \varepsilon_{min}$, for strain amplitude $\varepsilon_a = (\varepsilon_{max} - \varepsilon_{min})/2$, for mean strain $\varepsilon_{mean} = (\varepsilon_{max} + \varepsilon_{min})/2$ and for strain ratio $R_\varepsilon = \varepsilon_{min}/\varepsilon_{max}$.

2.3   Fatigue life prediction models

2.3.1   Introduction

This section deals with the most relevant fatigue life prediction models in literature. These models can be based on several distinct methods, such as global and local approaches.

Global analysis is directly dependent on the applied forces or on nominal stresses with the purpose of relating global failure of the components to loading (or stress) values. As far as local approaches are concerned, it aims to describe local damage phenomena using parameters obtained from stress or strain local analysis. Some prediction models make use of local approaches (especially strain-based models) together with fracture mechanics analysis.

2.3.2   Global models

Fatigue problems in structural elements are not easily understandable once several parameters, which are not always independent, command the structural response to cyclic loading. Therefore, empirical procedures are commonly used to define and model fatigue response [29].

Experimental campaigns are usually performed to overcome this problem and establish a reliable prediction of the fatigue life. The most typical way to represent fatigue damage for mechanical components or structural details is to use S-N curves, also called Wöhler curves. These curves relate remote stress amplitude with the number of cycles to failure. Generally, in fatigue tests is almost impossible to establish the division between crack initiation and propagation phases, hence S-N curves usually represent only the total fatigue life [30].

An S-N curve is obtained with experimental results from fatigue tests performed at different stress levels. Figure 2.3 shows a schematic representation of typical experimental data and S-N curve. It is preferable to adopt a logarithmic scale on both axes to establish a linear relation between $log\,\Delta\sigma$ and $log\,N_f$ for most results. This linear relation can be mathematically expressed by the Basquin relation [31] as Eq. (2.2) demonstrates. The slope of the straight line is equal to $-1/m$ [23].

$$\Delta\sigma^m N_f = constant \qquad\qquad (2.2)$$

If maximum stress, σ_{max}, reaches the ultimate resistance of the detail, the specimen will obviously fail in the first loading cycle. In this sense, the static strength defines the upper limit of the S-N curve. It may also present a flat zone for large number of cycles representing a stress level below which fatigue failure will not occur. Between these limits, two regions may be defined in S-N curves. While fatigue failure at high stress amplitudes with corresponding short lives is called low-cycle fatigue, low stress amplitudes applied for a long number of cycles is referred to as high-cycle fatigue. There is no way to define in which number of cycles the transition between these two regions takes place, however their main difference is that low-cycle fatigue is associated with plastic deformation in every cycle and high-cycle fatigue is characterized by predominantly elastic behaviour [23].
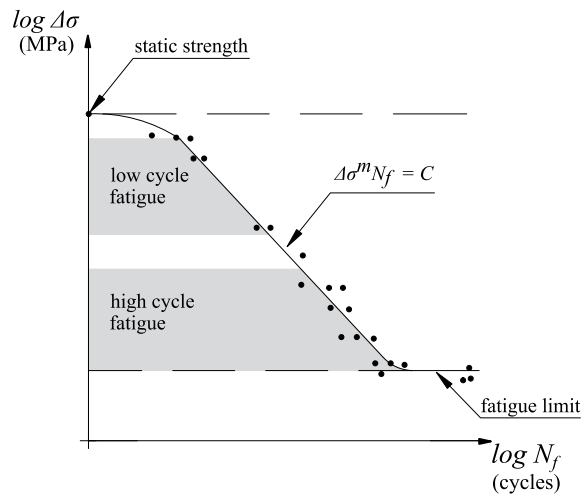
Figure 2.3. S-N schematic representation. Adapted from Schijve [23].

A given S-N curve is only valid for the specific conditions under which it was tested, which means that to generalize results, the effects of member geometry, scaling, chemical environment, load frequency, temperature and mean stress must be properly acknowledged [30]. In what concerns the effect of mean stress level (stress ratio, R_σ), it can be considered by computing a normalized stress range value, $\Delta\sigma_{norm}$. Taras and Greiner [32] proposed the procedure presented in Eq. (2.3) in which $\Delta\sigma$ is the remote stress range applied during the experimental test and $f(R_\sigma)$ is a normalization function to consider stress ratio effects.

$$\Delta\sigma_{norm} = \frac{\Delta\sigma}{f(R_\sigma)} \tag{2.3}$$

This function depends on the material that compose the detail. For puddled iron and non-alloy structural steel manufactured before 1900, $f(R_\sigma)$ is defined as:

$$
\begin{aligned}
f(R_\sigma) &= \frac{1 - R_\sigma}{1 - 0.7 \cdot R_\sigma} \ if \ -1 \leq R_\sigma \leq 0 \\
f(R_\sigma) &= \frac{1 - R_\sigma}{1 - 0.75 \cdot R_\sigma} \ if \ R_\sigma > 0
\end{aligned}
\tag{2.4}
$$

For non-alloy structural steel after 1900 (S235, S275 and S355), the following normalization function is proposed:

$$f(R_\sigma) = \frac{1 - R_\sigma}{1 - 0.4 \cdot R_\sigma} \ if \ -1 \leq R_\sigma \leq 0$$

$$f(R_\sigma) = \frac{1 - R_\sigma}{1 - 0.6 \cdot R_\sigma} \ if \ R_\sigma > 0$$

(2.5)

2.3.3   Local models for crack initiation

2.3.3.1   Introduction

Local approaches focus particularly on crack initiation period, and they use local fatigue damage parameters to correlate fatigue test results. Predictions on fatigue life can be performed using different fatigue damage functions: stress, strain and energy. In this section, three types of local models are described: local models based on strain functions, local models based on stress-strain functions and local models based on strain-energy functions.

2.3.3.2   Models based on strain functions

Local models based on strains are widely used in fatigue analysis, especially for calculation of fatigue crack initiation. These models differ from global approaches because they consider that plastic deformation may occur in specific areas where fatigue crack initiates. Strain-based models consider that the material that surrounds highly strained areas (at a geometric discontinuity, for example) behaves in a similar way to the material in a smooth specimen, tested under cyclic strain-controlled loading [33]. Fatigue tests under strain-controlled conditions can be performed following the recommendations of ASTM E 606 [34].

Stress-strain relations obtained for a metallic material under cyclic plastic conditions are different from those relations obtained under monotonic loading conditions. In Figure 2.4 are presented the two most typical types of cyclic behaviour. When the strain cycle requires an increasing stress amplitude, it is named cyclic strain hardening. On the other hand, if the strain cycle is maintained with a decreasing stress amplitude it is referred as cyclic strain softening. Generally, they both stabilize to a constant level after a certain number of cycles. For materials obtained by a heat treatment (e.g. high-strength materials), this stabilization process occurs almost immediately, while for soft materials or materials strain-hardened by a deformation process (e.g. rolling) the stabilization process is less predictable [23].

Independent Variable | Dependent Variable | Hysteresis Loop
(input) | (output) |
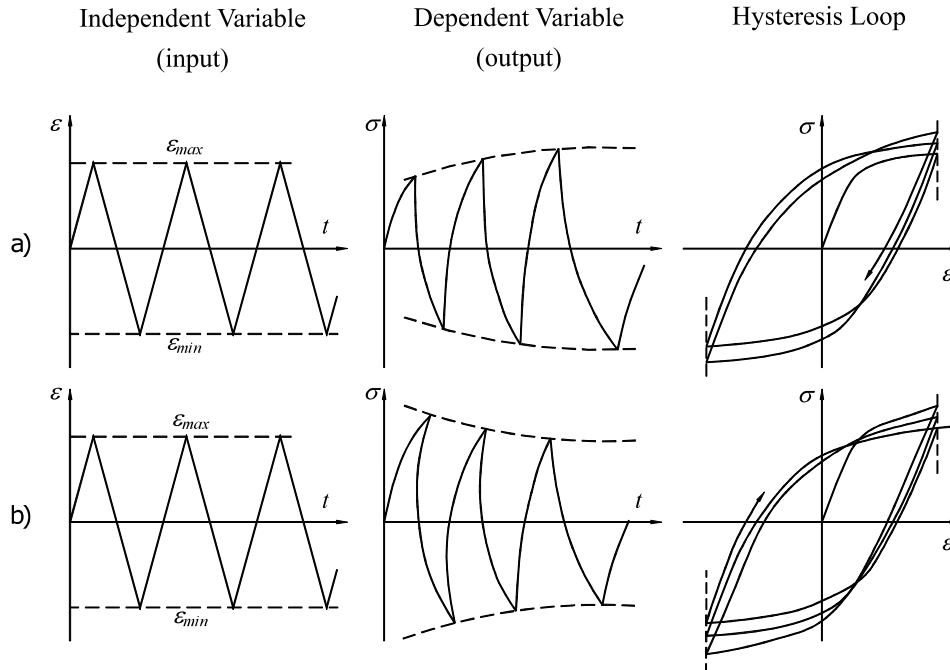
Figure 2.4. Typical cyclic behaviour: a) cyclic strain hardening; b) cyclic strain softening.

Generally, the stabilized cyclic behaviour is described by a cyclic curve relating stresses and strains. This curve can be determined by joining several hysteresis loops for different strain amplitudes, as is presented in Figure 2.5. This curve can be expressed by Eq. (2.6) proposed by Ramberg-Osgood [35], where E is Young's modulus, K' is the cyclic strength coefficient and n' is the cyclic strain-hardening exponent.

$$\varepsilon_a = \frac{\sigma_a}{E} + \left(\frac{\sigma_a}{K'}\right)^{\frac{1}{n'}} \tag{2.6}$$

The relation proposed by Coffin [25] and Manson [26], expressed in Eq. (2.7), is used to represent low-cycle fatigue behaviour, considering that it relates the plastic component of strain amplitude, ε_a^p, with the number of cycles to failure, N_f. Parameters ε_f' and c (determined experimentally) are the fatigue ductility coefficient and exponent, respectively.

$$\varepsilon_a^p = \varepsilon_f'\left(2N_f\right)^c \tag{2.7}$$

To describe the behaviour in high-cycle fatigue domains, the relation proposed by Basquin [31] can be used as described in Eq. (2.8). It establishes a relation between elastic strain amplitude ε_a^e and the number of cycles to failure, N_f, where σ_f' is the fatigue strength coefficient, b is the fatigue strength exponent and E is Young's modulus.

$$\varepsilon_a^e = \frac{\sigma_f'}{E}\left(2N_f\right)^b \tag{2.8}$$
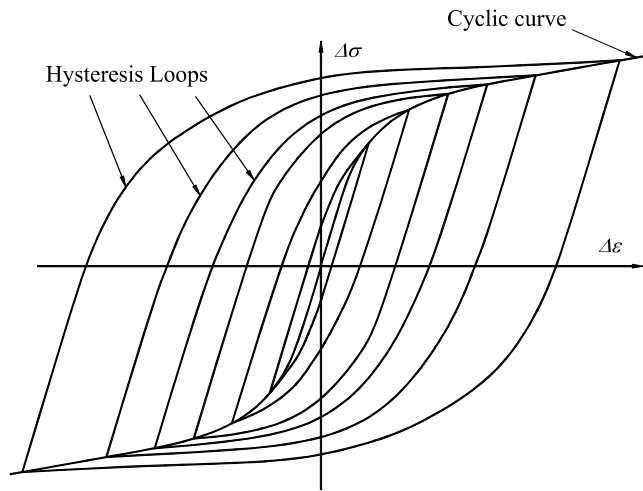
Figure 2.5. Typical cyclic curve.

As illustrated in Figure 2.6, the number of cycles corresponding to the transition, N_t, between low and high-cycle fatigue regimes is established when the total strain amplitude is composed of equal components of elastic and plastic strain amplitudes. Therefore, while fatigue life below this transition value is ruled by ductility properties, above it, elastic properties rule. The algebraic sum of the two previous equations, as presented in Eq. (2.9), is designated as Coffin-Manson-Basquin (CMB) model which stands as a general equation, valid for both low and high-cycle fatigue regimes.

$$\varepsilon_a = \varepsilon_a^e + \varepsilon_a^p = \frac{\sigma_f'}{E}\left(2N_f\right)^b + \varepsilon_f'\left(2N_f\right)^c \tag{2.9}$$

Mean stress effect can also be considered in this model by implementing Eq. (2.10) as suggested by Morrow [36].

$$\varepsilon_a = \frac{\sigma'_{f,Morrow} - \sigma_{mean}}{E} \left(2N_f\right)^{b_{Morrow}} + \varepsilon'_{f,Morrow}\left(2N_f\right)^{c_{Morrow}} \tag{2.10}$$
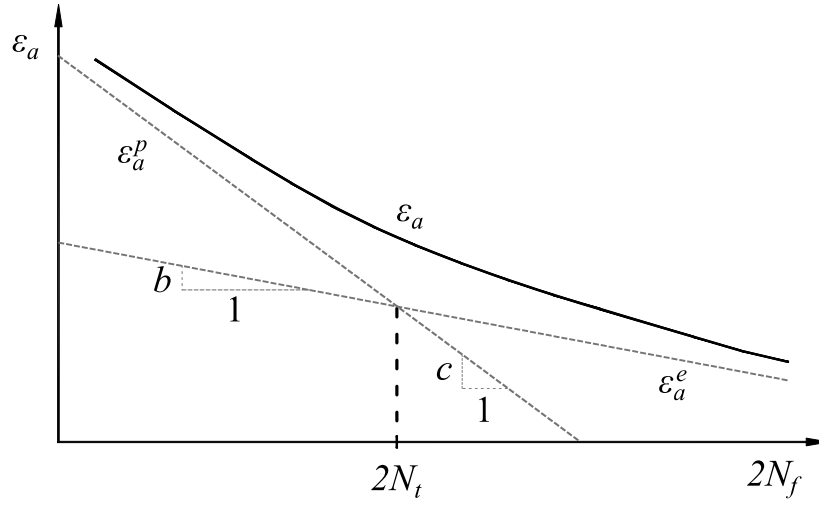
Figure 2.6. Schematic representation of elastic, plastic and total strain amplitudes *versus* reversals to failure (logarithmic scale).

2.3.3.3   Models based on stress-strain functions

A stress-strain function to describe fatigue life of metallic materials was proposed by K. Smith, P. Watson and T. Topper [37]. It has been designated as SWT fatigue damage model. It considers that the fatigue life of any level of mean stress is related to the product of the maximum stress, σ_{max}, and strain amplitude, ε_a, as expressed in Eq. (2.11).

$$SWT = \sigma_{max}\varepsilon_a = \frac{\left(\sigma'_{f,SWT}\right)^2}{E}\left(2N_f\right)^{2b_{SWT}} + \sigma'_{f,SWT}\,\varepsilon'_{f,SWT}\left(2N_f\right)^{b_{SWT}+c_{SWT}} \tag{2.11}$$

2.3.3.4   Models based on strain-energy functions

Fatigue life predictions can be based on strain-energy density functions. This is the case for the fatigue damage model proposed by Huffman [38]. This model has the advantage of establishing a prediction for the strain-life behaviour based only in cyclic stress-strain properties and dislocation density. The Huffman damage model is defined as presented in Eq. (2.12) where U_e is the tensile elastic strain energy density computed from σ_{max}, U_p^* is the complementary plastic strain energy density computed from $\Delta\sigma$, ρ_c is the critical dislocation density and U_d is the

dislocation strain energy obtained by Eq. (2.13) where E is the Young's modulus, v is the Poisson's ratio and $\vec{b}$ is the Burger's vector.

$$\left(\frac{U_e}{U_d\rho_c}\right)\left(\frac{U_p^*}{U_d\rho_c}\right) = \frac{2N}{2N_f} \tag{2.12}$$

$$U_d = \left(\frac{E}{2(1+v)}\right)|\vec{b}|^2 \tag{2.13}$$

The value of the Burger's vector for irons and steels is equal to 2.52×10^{-10} m as recommended by Huffman [38]. The strain energy densities U_e and U_p^* can be obtained by integrating the cyclic stress-strain equation leading to Eq. (2.14) and Eq. (2.15), respectively.

$$U_e = \frac{\sigma_{max}^2}{2E} \tag{2.14}$$

$$U_p^* = 4\left(\frac{n'}{1+n'}\right)\left(\frac{1}{K'}\right)^{\frac{1}{n'}}(\sigma_a)^{\left(\frac{1+n'}{n'}\right)} \tag{2.15}$$

In this sense, the damage equation can be reformulated using the parameters of Ramberg-Osgood relation as follows:

$$\left(\frac{2}{U_d^2\rho_c^2}\right)\left(\frac{n'}{1+n'}\right)\left(\frac{1}{K'}\right)(\sigma_{max}^2)(\sigma_a)^{\left(\frac{1+n'}{n'}\right)} = \frac{1}{2N_f} \tag{2.16}$$

Furthermore, this damage equation can also be expressed using a strain-life relation as presented in Eq. (2.17) whose parameters can be determined using Equations (2.18), (2.19), (2.20) and (2.21).

$$\varepsilon_a = \frac{\sigma'_{f,Huffman}}{E}(2N_f)^{b_{Huffman}} + \varepsilon'_{f,Huffman}(2N_f)^{c_{Huffman}} \tag{2.17}$$

$$\sigma'_{f,Huffman} = E\left(\left(\frac{2}{U_d^2\rho_c^2}\right)\left(\frac{n'}{1+n'}\right)\left(\frac{1}{K'}\right)^{\left(\frac{1}{n'}\right)}E^{\left(\frac{1+2n'}{n'}\right)}\right)^{\left(\frac{-n'}{1+3n'}\right)} \tag{2.18}$$

$$b_{Huffman} = \frac{-n'}{1 + 3n'} \tag{2.19}$$

$$\varepsilon'_{f,Huffman} = E\left(\left(\frac{2(K')^3}{U_d^2\rho_c^2E}\right)\left(\frac{n'}{1 + n'}\right)\right)^{\left(\frac{-n'}{1+3n'}\right)} \tag{2.20}$$

$$c_{Huffman} = \frac{-1}{1 + 3n'} \tag{2.21}$$

Huffman [38] proposes that the value of the critical dislocation density can be found by fitting the resultant strain-life curve to low-cycle strain-life data by solving Eq. (2.16) for ρ_c leading to Eq. (2.22).

$$\rho_c = \sqrt{\left(\frac{2(2N_f)}{U_d^2EN}\right)\left(\frac{n'}{1 + n'}\right)\left(\frac{1}{K'}\right)^{\left(\frac{1}{n'}\right)}(\sigma_{max}^2)(\sigma_a)^{\left(\frac{1+n'}{n'}\right)}} \tag{2.22}$$

2.3.4   Fracture mechanics concepts

2.3.4.1   Stress intensity factor

Fatigue phenomenon can be observed in structural details of metallic bridges, namely in riveted, bolted, or welded connections. The presence of an incipient fatigue crack not always lead to structural collapse. Generally, there is a stable crack growth period from this initial state until the critical crack length which can lead to failure, eventually.

There are three main types of crack opening modes – see Figure 2.7. The most typical type of fatigue crack growth is observed in a direction perpendicular to the tensile stress oriented to open the crack. This type of crack propagation is designated as Mode I. The other two modes are essentially shear modes characterized by shear loading in the plane of the crack – Mode II – and by shear loading in the transverse direction – Mode III. It is also possible to observe fatigue crack growth resulting from a combination of these three modes [23]. Irwin [39] developed the concept of stress intensity factor to analyse and predict fatigue crack growth of materials which is normally referred as Linear Elastic Fracture Mechanics (LEFM). The magnitude of the crack tip stress field is related to the stress intensity factor as shown in Eq. (2.23) in the case of Mode I loading. In this equation, β is a parameter which depends on

the geometry of the detail, σ is the remote stress and a is the crack length. Stress intensity factor can be determined either by analytical, numerical or experimental methods [40]. In literature, it is possible to find recommended values for this parameter for a significant variety of details [41,42].

$$K_I = \beta \sigma \sqrt{\pi a} \qquad (2.23)$$
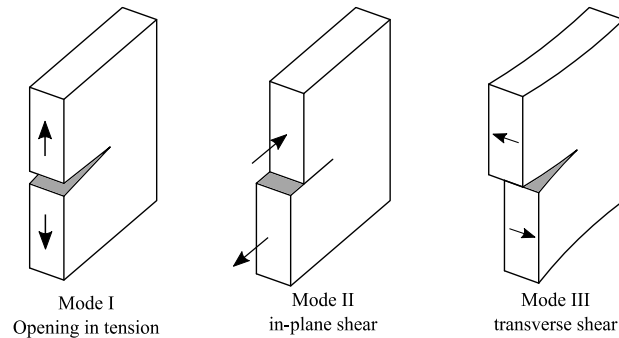
Figure 2.7. Fatigue crack opening modes.

If a Mode I fatigue crack is considered in an infinite plate composed of isotropic material with linear elastic behaviour – see Figure 2.8 – stresses at the surroundings of the crack tip can be obtained by the system of equations presented in Eq. (2.24) [43]. It is noticed that stresses around the crack tip depend on the coordinates r and θ as well as the stress intensity factor (geometry factor β is equal to 1 for infinite sheets). For values of r close to zero, stresses became infinite for each value of θ which means that in practice there is plastic deformation in the crack tip. LEFM principles are valid until the dimension of this plastic deformation zone remain smaller when compared to the crack dimension [23].
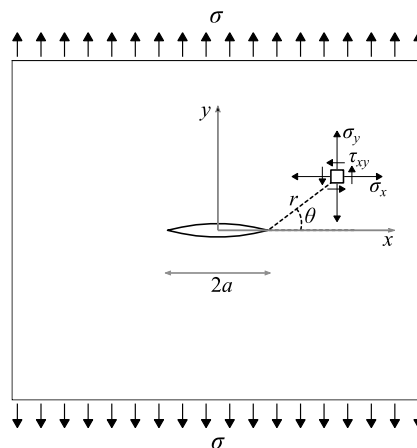
Figure 2.8. Infinite plate with a Mode I crack.

$$\begin{cases} \sigma_x = \dfrac{K_I}{\sqrt{2\pi r}} cos\left(\dfrac{\theta}{2}\right)\left[1 - sin\left(\dfrac{\theta}{2}\right) sin\left(\dfrac{3\theta}{2}\right)\right] \\[3mm] \sigma_y = \dfrac{K_I}{\sqrt{2\pi r}} cos\left(\dfrac{\theta}{2}\right)\left[1 + sin\left(\dfrac{\theta}{2}\right) sin\left(\dfrac{3\theta}{2}\right)\right] \\[3mm] \sigma_z = \begin{cases} 0, & plane\ stress \\ v\left(\sigma_x + \sigma_y\right), & plane\ strain \end{cases} \\[3mm] \tau_{xy} = \dfrac{K_I}{\sqrt{2\pi r}} cos\left(\dfrac{\theta}{2}\right) sin\left(\dfrac{\theta}{2}\right) sin\left(\dfrac{3\theta}{2}\right) \\[3mm] \tau_{xz} = \tau_{yz} = 0 \end{cases} \tag{2.24}$$

2.3.4.2 Fatigue crack growth analysis

Fatigue crack growth rate can be analysed by specific tests performed with indications on ASTM E 647 [44]. In Figure 2.9 is presented the relation between the crack length (from initial crack length, a_i, until its critical value, a_f) and the number of cycles to failure. It displays results from different stress levels, $\sigma_1, \sigma_2, \sigma_3$ with $\sigma_1 > \sigma_2 > \sigma_3$. It is observed that for a certain crack length, a, the crack propagation rate given by the slope of the curve is higher for higher stress amplitude levels. Furthermore, the number of cycles and the crack length at failure is lower when higher stress amplitudes are considered. The crack growth rate, da/dN, is expressed in meters per cycle, generally [23].
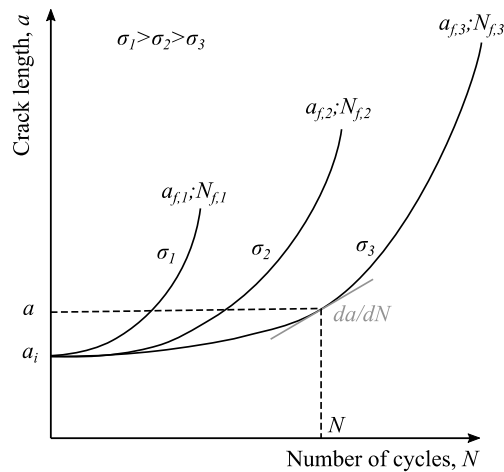
Figure 2.9. Crack length evolution for different stress levels.

The same way that cyclic stress varies between σ_{max} and σ_{min}, the corresponding stress intensity factor varies between K_{max} and K_{min}. Thus, the same stress ratio, R_σ, is obtained from cyclic stress and from the cyclic K values as shown in Eq. (2.25) [23].

$$R_\sigma = \frac{\sigma_{min}}{\sigma_{max}} = \frac{K_{min}}{K_{max}} \qquad (2.25)$$

Figure 2.10 presents a schematic representation of the three fatigue crack growth regions in a double logarithmic scale. It shows two vertical asymptotes. The one on the left, at $\Delta K = \Delta K_{th}$, indicates that ΔK values below this threshold level are too low to cause macro crack growth while the right asymptote occurs for a ΔK cycle with $K_{max} = K_c$. It is a critical value for K_{max} which leads to complete failure of the specimen. These three regions can be named as: I – the threshold ΔK-region; II – the Paris ΔK-region; III - the stable tearing crack growth region [23].
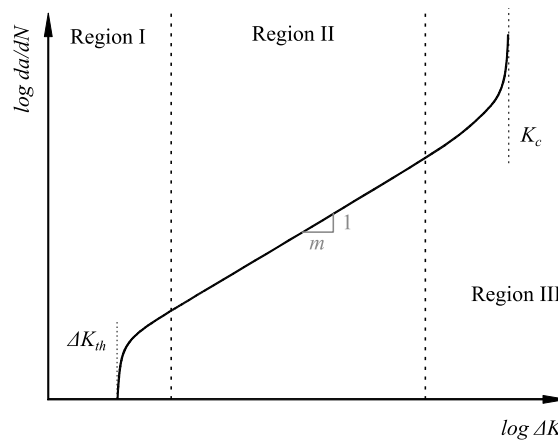
Figure 2.10. Crack growth rate regions.

Th stress intensity factor range can be decreased until nearly zero crack growth is obtained, and the lowest value reached is the threshold level, ΔK_{th}. Evidence has shown that ΔK_{th} is not a single material constant because it depends on stress ratio. Furthermore, this region is largely influenced by the microstructure of the material (grain size), the mean stress of the applied load, the operating temperature and the environmental conditions [30]. Recommendations on ASTM E 647 [44] establish that crack growth comes to a stop when it is in the order of 10^{-10} m/cycle which implies a crack extension of just 1 mm in 10^7 cycles.

The Paris region was named due to the research work carried out by Paris and Erdogan [45]. In this region, the use of LEFM concepts is acceptable because experimental data follows a linear relation when using a logarithmic scale, as shown in Figure 2.10. Paris and Erdogan [45]

established a power function – Eq. (2.26) – to describe the relation between da/dN and ΔK, where C and m are material constants.

$$\frac{da}{dN} = C\,\Delta K^m \tag{2.26}$$

The previous equation provides a linear relation: $log\left(\frac{da}{dN}\right) = log(C) + m\,log\,(\Delta K)$ with m as the slope. Nevertheless, it does not account for the R_σ effect on crack growth, neither for the asymptotic behaviour in regions I and II.

In the stable-tearing crack growth region, crack growth rate is high, around 0.01mm/cycle or higher. Fatigue crack growth life in this region is relatively short, which implies that its engineering significance is limited. It seems easy to predict the occurrence of failure because it should occur when $K_{max} = K_c$. However, K_c (the stress intensity factor that causes final failure) for structural materials is not usually a constant material property [23].

The above presented relations belong to LEFM because they make use of linear parameter ΔK. This means that those relations are formulated to be applicable for cracks with limited plasticity ahead of the crack tip. Consequently, several proposals have been made to correlate fatigue crack growth for generalized elastoplastic conditions with Elastoplastic Fracture Mechanics (EPFM) parameters. One example is the case of using the J-Integral instead of ΔK, as proposed by Dowling and Begley [46] – see Eq. (2.27). It can be applied in situations of large-scale yielding.

$$\frac{da}{dN} = C\,\Delta J^m \tag{2.27}$$

In 1970, Elber [47,48] introduced the concept of crack closure. He stated that a fatigue crack propagating under tensile loading may be partially or completely closed at minimum load level. Stress distribution on the fracture surfaces show compressive stresses higher than the yield stress of the material which influence the fatigue crack growth. Therefore, he proposed that an effective load cycle must be considered to derive the growth of a fatigue crack which should correspond to the load cycle when the crack is fully open. In this sense, the concept of an

effective stress intensity factor range emerged, which can be obtained by affecting the applied stress intensity factor range by the U parameter, as presented in Eq. (2.28) where K_{max}, K_{min} and K_{cl} are the maximum, minimum and crack closing stress intensity factors, respectively. Paris law can then be rewritten as Eq. (2.29) presents to consider crack closure effects.

$$\Delta K_{eff} = U \cdot \Delta K_{app} = \frac{K_{max} - K_{cl}}{K_{max} - K_{min}} \Delta K_{app} \qquad (2.28)$$

$$\frac{da}{dN} = C_{eff} \, \Delta K_{eff}{}^{m_{eff}} \qquad (2.29)$$

This approach requires the accurate definition of K_{cl} for specific materials, loading types and fatigue crack growth region.

2.3.4.3 Fatigue modelling

The reliability of fatigue life predictions of mechanical components or structural details based on Fracture Mechanics is largely dependent on the availability of accurate fatigue crack propagation laws. Normally, the use of Fracture Mechanics based on fatigue propagation models consists in residual fatigue life assessment of mechanical components or structural details containing initially known defects acting as cracks. Thereby, crack propagation laws should be integrated as indicated by Eq. (2.30), where a_i is the initial crack size and a_f is the final crack size.

$$\frac{da}{dN} = f(\Delta K, R_\sigma \dots) \Rightarrow N_f = \int_{a_i}^{a_f} \frac{da}{f(\Delta K, R_\sigma, \dots)} \qquad (2.30)$$

The integration of fatigue crack growth relations can also be used for total fatigue life assessment of components, thus neglecting crack initiation, and considering fatigue life as a process of fatigue crack propagation. However, the determination of the initial crack size, a_i, for the crack growth analysis is the main difficulty of this approach. It is possible to find proposals in literature for empirical assumed crack lengths, such as $0.1 - 1$ mm [49,50].

Furthermore, some authors complement this approach by computing the number of cycles to initiate a crack with local strain-based models [51,52].

Alternatively, non-destructive inspection (NDI) techniques can be used to measure the size of an initial defect [53]. There are several NDI techniques, such as, acoustic emission, liquid penetrant or ultrasonic testing that can give good results however they can fail to detect a crack if it is below the detection capacity of the NDI technique.

The other possibility is to determine an equivalent initial flaw size (EIFS) aiming to estimate the initial crack size for fatigue life predictions based on fracture mechanics [54]. This approach is based on a back-extrapolation method that uses fatigue crack growth with an assumed initial crack geometry and size to match fatigue data (stress-life) using a trial-and-error method. This back-extrapolation technique was applied by several authors [55–57]. However, Moreira *et al.* [58] showed that using back-extrapolation method to obtain EIFS resulted in stress level dependent results. To avoid this problem and other uncertainties of EIFS such as, the inherent variability of fatigue crack growth data, Liu and Mahadevan [54] propose the application of a probabilistic EIFS calculation methodology based on the Kitagawa-Takahashi.

2.3.5   Local models for crack propagation

Several authors have studied the possibility of using local approaches to fatigue, typically applied for fatigue crack initiation phase, to model also fatigue crack propagation [59–66]. Crack growing is assumed to be a process of continuous crack re-initiations in which local approaches are implemented to analyse the plastic zone ahead of the crack tip. In other words, stress-strain field ahead of the crack tip is estimated by means of local approaches to apply a failure criterion to model fatigue crack growth. The differences between the approach of each author are based on the methodology to define the geometry of the crack, equations used to compute local stress-strain field, the damage model, and the distance ahead of the crack tip in which the damage is computed.

In 1985, Glinka [60] published a study about modelling fatigue crack growth using a notch stress-strain analysis approach. Crack was modelled as a notch with a finite tip radius, ρ^*, which is also used to divide the region ahead of the crack into elementary blocks – see Figure 2.11. It

is assumed that crack growth is associated with the failure of successive elementary blocks ahead of the crack tip and crack growth rate is defined as presented in Eq. (2.31) where N_{block} is the number of cycles to obtain failure in the first elementary block.
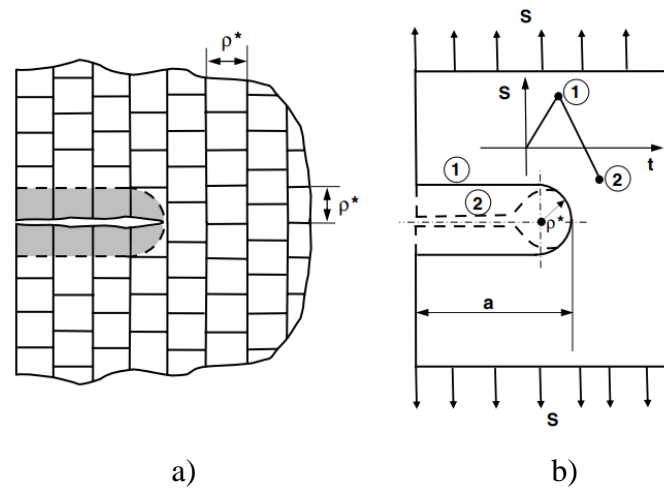
Figure 2.11. Glinka discrete material model (a) and crack tip geometry at maximum and minimum load (b) [63].

$$\frac{da}{dN} = \frac{\rho^*}{N_{block}}$$
(2.31)

In this approach, material behaviour is based on Ramberg-Osgood cyclic stress-strain curve and damage is determined by means of SWT-life model. Elastoplastic stress-strain field is computed based on the elastic solution for a blunt crack using the effective stress range to consider the crack closure effects. Both region I and region II of fatigue crack propagation regimes can be correlated. This approach was later improved by Noroozi, Lambert and Mikheevskiy [62–65] following the same assumptions as the original work presented by Glinka but using a different procedure to determine elastoplastic stress-strain field in the representative material element. In this case, crack closure effect was considered as compressive residual stresses generated by cyclic elastoplastic behaviour. In this way, the correction of the stress intensity factor range is done with these compressive residual stresses leading to a net stress intensity factor range which is used to compute elastoplastic stress-strain field ahead of the crack tip. It was also demonstrated that this approach can be applied not only in constant but also in variable amplitude loading scenarios.

Around the same period that Glinka published his work, Ellyin and Kujawski [67] developed, in 1986, a low-cycle fatigue-based model for crack propagation. Three different regions were defined ahead of the crack tip as presented in Figure 2.12. Region III is the biggest and it corresponds to the monotonic plastic zone, the intermediate region is region II which is related with cyclic plastic zone and the smallest zone ahead of the crack tip, region I, is designated as process zone and it is identified as δ^*. The damage is computed with an energetic parameter defined by Ellyin and Kujawski, described as $\Delta\sigma\Delta\varepsilon^p$.
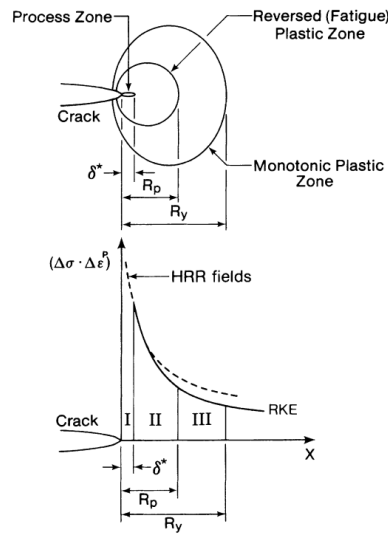
Figure 2.12. Fatigue crack growth modelling proposed by Ellyin and Kujawski [67].

This fatigue crack growth model uses the hysteretic energy in front of the crack as a criterion for the crack advance. The stable hysteresis energy per cycle and per unit volume is determined with Eq. (2.32), where n' is the strain hardening exponent, E is the Young's modulus, ΔK is the stress intensity factor range, r and θ are the polar coordinates with origin in the crack tip and Ψ is the function that defines the analytical plastic field ahead of the crack tip.

$$\Delta W^p = \left(\frac{1-n'}{1+n'}\right)\Delta\sigma_{eq}\Delta\varepsilon_{eq}^p = \left(\frac{1-n'}{1+n'}\right)\frac{\Delta K^2}{Er\Psi(n',\theta)} \tag{2.32}$$

If crack propagates throughout the x axis, it results in $\theta = 0$ and $r = x$. The crack blunting, ρ^*, is attained in the computation of the damage parameter resulting in Eq. (2.33).

$$\Delta W^p = \left(\frac{1-n'}{1+n'}\right)\frac{\Delta K^2}{E\Psi(n',0)(\delta^* + \rho^*)} \tag{2.33}$$

The damage parameter is then related with the number of cycles to failure using Basquin [31] and Coffin-Manson [25,26] relations resulting in Eq. (2.34)

$$\Delta W^p = 4\left(\frac{1-n'}{1+n'}\right)\varepsilon_f'\sigma_f'\left(2N_f\right)^{b+c} \tag{2.34}$$

Relating the size of the process zone, δ^*, and the number of cycles increment ΔN, the following equation is obtained where $\beta_{EK} = -(b+c)$.

$$\frac{da}{dN} = \frac{\delta^*}{\Delta N} = \frac{\Delta K^2}{4E\varepsilon_f'\sigma_f'\Psi(n')}\frac{(2\Delta N)^{\beta_{EK}}}{\Delta N} - \frac{\rho^*}{\Delta N} \tag{2.35}$$

The critical blunting radius, ρ^*, is found using the threshold value of the stress intensity factor range, ΔK_{th}, and $da/dN = 0$. The final expression for fatigue crack propagation rate is shown in Eq. (2.36). According to the authors, the process zone size is associated with microstructure and/or micro failure mechanisms [59].

$$\frac{da}{dN} = 2\delta^*\left[\frac{\Delta K^2 - \Delta K_{th}^2}{4E\varepsilon_f'\sigma_f'\delta^*\Psi(n')}\right]^{\frac{1}{\beta_{EK}}} \tag{2.36}$$

Later on 1999, Peeker and Niemi [61] proposed a different approach to model fatigue crack propagation based on local strain analysis. Crack path is discretized in equally sized elements with dimension, δ, as presented in Figure 2.13, and the damage in each element is computed using the Morrow strain-life equation [33]. Elastoplastic stress-strain field is computed using Ramberg-Osgood relation together with the equivalent strain energy density approach developed by Molski and Glinka [68].

The possibility of simultaneous damaging of elements was considered using linear summation damage rule and the concept of a fictitious stress intensity factor range for notches was proposed

to consider the same stress field as resulting from the stress concentration factor. Crack closure effects were also considered using the effective stress intensity factor range.
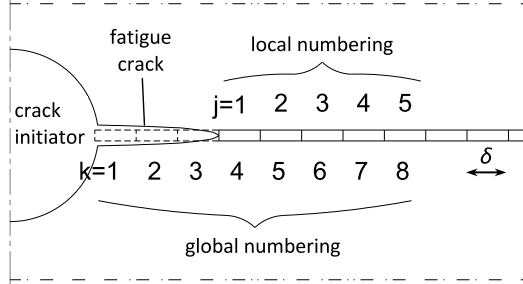
Figure 2.13. Elements along the crack propagation path and their numbering (by Peeker and Niemi model) [61].

The model proposed by Peeker and Niemi [61] allowed the distinction between near threshold fatigue crack propagation and stable crack growth. In the first case, it is assumed that the elastic strain ranges at the crack tip are much higher than the plastic strain ranges then only the elastic parts of the Ramberg-Osgood equation and strain-life relation is used leading to the fatigue crack propagation rate presented in Eq. (2.37).

$$\frac{da}{dN} = C_{el}\Delta K^{m_{el}} \tag{2.37}$$

$$C_{el} = 2\delta\left[(\sigma_f' - \sigma_{mean})\sqrt{2\pi\delta}\right]^{\frac{1}{b}} \tag{2.38}$$

$$m_{el} = -\frac{1}{b} \tag{2.39}$$

For the stable crack growth regime, the plastic strain ranges at the crack tip are larger than the elastic strain ranges, therefore only the plastic parts of Ramberg-Osgood equation and strain-life relation is used leading to the fatigue crack propagation rate presented in Eq. (2.40).

$$\frac{da}{dN} = C_{pl}\Delta K^{m_{pl}} \tag{2.40}$$

$$C_{pl} = 2\delta\left[\varepsilon_f'\left(\frac{4\pi\delta K'E}{n'+1}\right)^{\frac{1}{n'+1}}\right]^{\frac{1}{c}} \tag{2.41}$$

$$m_{pl} = -\frac{2}{c(n'+1)} \tag{2.42}$$

According to the authors, the size of the elements considered for FCG computation, δ, must be large enough to represent the local properties by their mean value through continuous variables and it should be related to material micro-structural parameters, such as the material grain-size. Authors propose an average element size for structural steel as $\delta = 0.1$ mm [61].

More recently, Hurley and Evans [66] presented a methodology for prediction of fatigue crack growth rates in titanium material based on the assumption that a similar number of cycles is required to propagate a crack through the cyclic plastic zone as to initiate a crack in a plain strain controlled specimen where an equivalent stress-strain field exists. The damage state within the cyclic plastic zone is determined using a Walker strain-life relation and the elastoplastic stress-strain field at the crack tip is computed by means of a non-linear finite element analysis. The Walker strain parameter, defined in Eq. (2.43), was correlated directly with fatigue life using a power law. The fitting parameter, w, vary between 0 and 1.

$$\varepsilon_w = \frac{\sigma_{max}}{E}\left(\frac{\Delta\varepsilon E}{\sigma_{max}}\right)^w \tag{2.43}$$

The size of the cyclic plastic zone, which is assumed as the same as the process damage zone under plain strain conditions is described in Eq. (2.44) where σ_0' is the cyclic yield stress and ΔK is the stress intensity factor range computed from numerical model.

$$a_i = \frac{1}{3\pi}\left(\frac{\Delta K}{2\sigma_0'}\right)^2 \tag{2.44}$$

2.4   Bolted shear connections

2.4.1   Bearing and friction-type

The behaviour of bolted connections under cyclic loading conditions is dependent on the type of load transfer. It can be obtained either by friction on contact surfaces, by shear and bearing

of bolts, or by both depending on the magnitude of the clamping force, the conditions of the faying surfaces and the possible occurrence of major slip. Furthermore, the failure pattern under cyclic loading can differ depending on the load transfer mechanism [69].

For bolted connections designed as bearing-type, fatigue crack initiates at the edge of the hole and grows in the region of the net cross-section where there is a geometric discontinuity of the cross-section area of plates – see Figure 2.14a). This is typical for bolted connections where the applied load exceeds the slip resistance of the faying surfaces. These two types of failure have been observed in experimental tests and it is often that they occur simultaneously in the same connection [69].

In what concerns the fatigue behaviour of preloaded bolted connections, stress concentration is present in the geometric discontinuity between the outer and inner plates and between the washers and the outer plates as presented in Figure 2.14b). This type of fatigue failure is governed by the fretting corrosion mechanism and it is obtained at the gross cross-section of the plates [70,71].

Stress Concentration

Stress Concentration

a)   b)
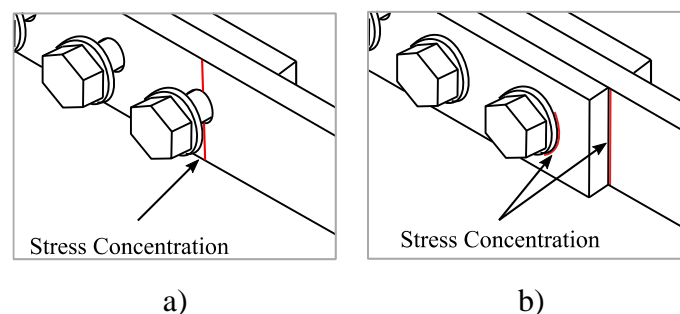
Figure 2.14. Typical position of stress concentration on: a) bearing-type bolted connections; b) friction-type bolted connections.

This fretting corrosion phenomenon can occur in a structural detail under cyclic loading if there is a clamping force between the components. If Figure 2.15a) is considered as an example of a flat element clamped at one end and loaded in tension at the other end, load is transferred by frictional forces along the contact surfaces $\overline{AB}$. In the free part of the tensioned element, a positive tensile strain occurs, $\varepsilon_x = S/E$, as well as lateral contraction, $\varepsilon_y = -\nu S/E$ due to the Poisson's effect leading to a thickness reduction of the tension element at section A-A. Inside

the clamping area, tensile stress (S) reduces to zero at section B-B. This means that the lateral contraction varies between full contraction at A and no contraction at B. Under cyclic loading, a cyclic change of contact between the bar and the clamping area occurs near point A leading to cyclic slip between the mating surfaces. This slip is large enough to cause fritting damage by rubbing between the two materials as shown in Figure 2.15b) [23].

The influence of preload magnitude on fatigue life of bolted connections was assessed by Jiménez-Peña *et al.* [71] by means of experimental and numerical investigations. Results showed that higher fatigue performance can be obtained with higher preload forces. Furthermore, Fernando *et al.* [72] focused on the fatigue behaviour of aluminium alloy preloaded bolted connections and found that the high contact pressure generated by the preload force contributes to increase the fatigue life of the detail due to crack closure effect. In fact, the beneficial effect of preload has been proven by several authors [73–75].

a)   b)
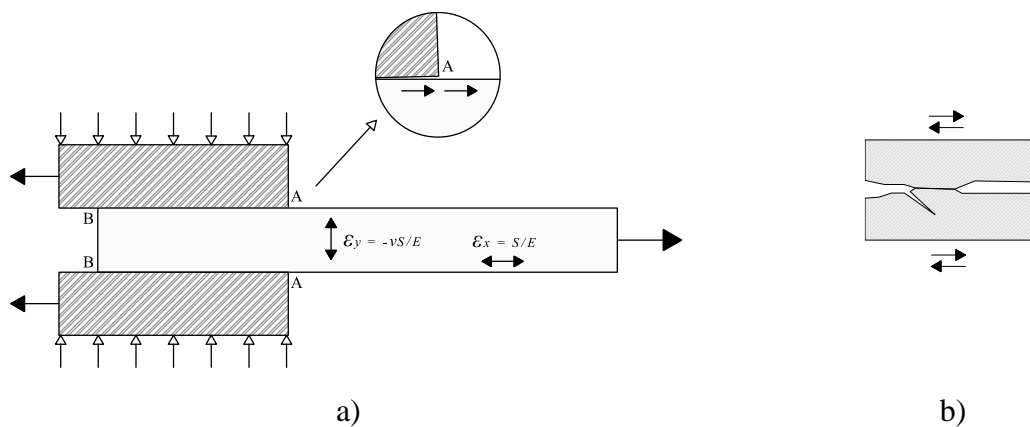
Figure 2.15. Fretting corrosion mechanism: a) detailed analysis of clamped surfaces; b) crack initiation by shear.

Experimental fatigue data has been correlated with net cross-section and gross cross-section stresses. A comparison was made with experimental data from friction-type bolted connections. Nearly all specimens failed through the gross cross-section and major slip did not occur. Three different cross-section ratios (A_{gross}/A_{net}) were used: 0.83, 0.66 and 0.50. It was observed that using gross cross-section area to compute stress range decreases the scatter in the results – see Figure 2.16.

a)   b)
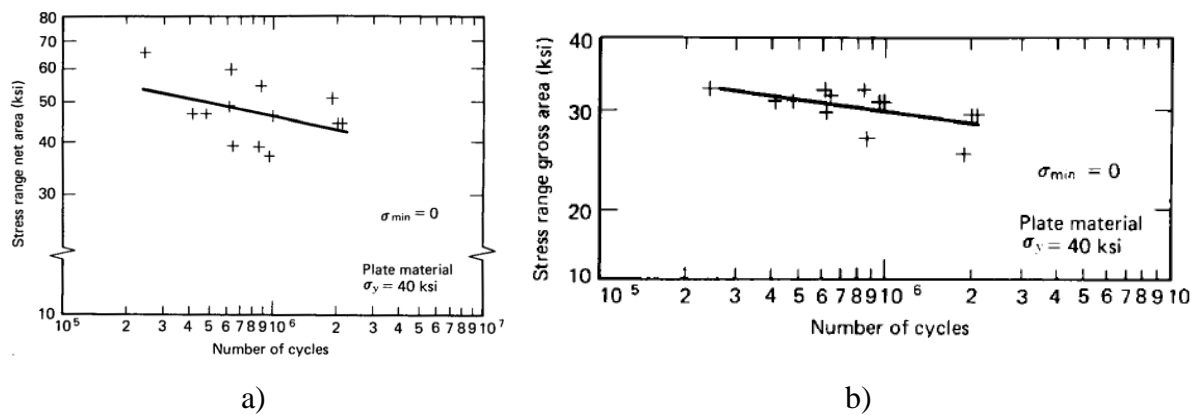
Figure 2.16. Experimental *S-N* data from friction-type connections – stress range based on:
a) net cross-section area; b) gross cross-section area [69].

In what concerns the loss of bolt tension, it has been observed that the initial bolt relaxation which occurs almost immediately after installation and the additional relaxation observed during cyclic loading was rarely more than 10%. Another important aspect to consider is the influence that the yield stress of the material has on the fatigue experimental data. Scientific investigations showed that this parameter does not have a significant influence in the fatigue behaviour of bolted connections [69].

2.4.2   Influence of load eccentricity

Single lap joints are characterized by the eccentricity in the neutral line. The main differences between connections with and without eccentricities are:

-   The eccentricity produces a tensile load which causes bending on the plates. Maximum bending stresses occur at the fasteners rows and extra stress concentration will be produced. This effect caused by the tensile load is referred as secondary bending – see Figure 2.17;

-   The eccentricity produces asymmetric loading conditions in the fastener – see Figure 2.18 – leading to an inhomogeneous bearing pressure along the hole.
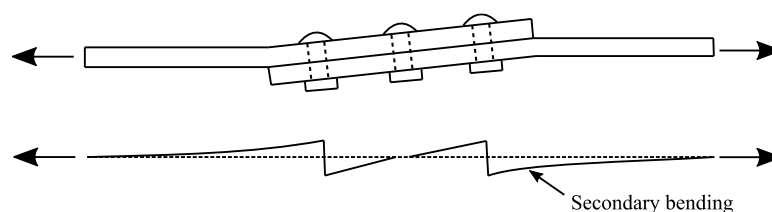
Figure 2.17. Secondary bending in a fastened single lap joint under tensile loading [23].
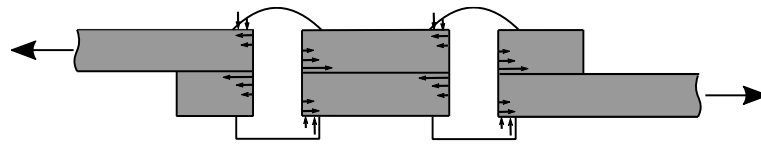
Figure 2.18. Asymmetric loading on fasteners as a result of the eccentricity in a lap joint [23].

2.4.3   Design guidelines

Reference standards propose *S-N* fatigue strength curves mainly based on experimental fatigue results, and they are normally defined by the detail category which represents the fatigue strength at 2 million cycles. However, some differences may be found between the curves proposed in standards. For example, AASHTO [16], EN 1993-1-9 [15] and JSSC [17] indicate S-N curves with a slope of $m = 3$ while the German standard DS 804 [76] for railway structures proposes $m = 5$.

Concerning bolted connections, AASHTO [16] proposes:

-   Curve B – Detail Category 125 – for bolted connections connected by high strength bolts satisfying all requirements for slip-critical connections (crack initiating in the gross cross-section).
-   Curve D – Detail Category 71 – for bolted connections in hot dipped galvanized members (crack initiating in the net cross-section).

In the case of EN 1993-1-9 [15], the following S-N curves are proposed:

-   Detail Category 112 should be used for double covered symmetrical joints with preloaded high strength bolts or preloaded injection bolts (stress computed at gross cross-section);
-   Detail Category 90 should be used for double covered joints with fitted bolts or non-preloaded injection bolts (stress computed at net cross-section) and one-sided connections with preloaded high strength bolts or preloaded injection bolts (stress computed at gross cross-section);
-   Detail Category 80 should be used for one-sided connections with fitted bolts or non-preloaded injection bolts (stress computed at net cross-section);
-   Detail Category 50 for one sided or double covered symmetrical connections with non-preloaded bolts in normal clearance holes (stress computed at net cross-section).

With respect to the fatigue design curves prescribed in EN 1993-1-9 [15], a slope of $m = 3$ is used until the constant amplitude fatigue limit $\Delta\sigma_D$ at 5 million cycles and then a slope of $m = 5$ is used until the horizontal limit defined as the cut-off limit $\Delta\sigma_L$ at 100 million cycles. Each curve is defined by the detail category $\Delta\sigma_C$. S-N curves proposed in EN 1993-1-9 [15] for bolted connections are presented in Figure 2.19.
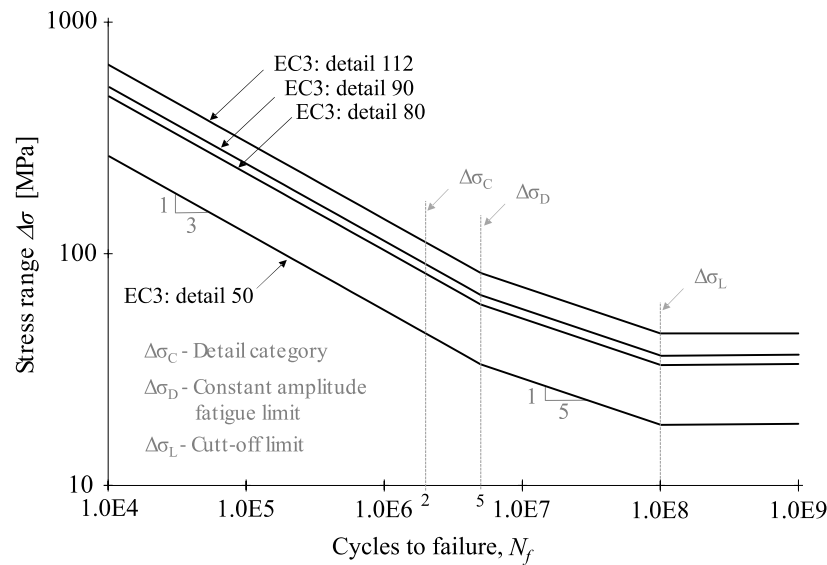
Figure 2.19. S-N fatigue curves for bolted connections in EN 1993-1-9 [15].

The Japanese standard [17] propose:

- For base plates of friction type bolted connections with the number of bolt rows, $n_b \leq 4$, joint detail B (detail category 155) should be used, for $5 \leq n_b \leq 15$, joint detail C (detail category 125) should be used and for $n_b \geq 16$ joint detail D (detail category 100) should be used;

- For base plates of bearing type bolted connections joint detail B (detail category 155) should be used.

2.4.4   Research with material extracted from existing bridges

An experimental campaign on bolted connections composed of metallic plates extracted from structural elements of a centenary Portuguese bridge named Fão bridge was performed by Jesus *et al*. [77]. Fatigue tests were conducted under null stress ratio and test frequencies ranged between 2.5 and 12 Hz. Two types of specimens were analysed: non-preloaded and preloaded

bolted connections. Although the level of preload force is low, the beneficial effect on the fatigue life was noticeable. However, when the obtained data is compared with the *S-N* curves proposed in the EN 1993-1-9 [15] it is observed that more than half of the data have lower fatigue strength. This fact can be explained by the lower preload level and by the inadaptability of this European standard to represent the fatigue behaviour of old metallic materials.

2.4.5   Resin-injected bolted connections

2.4.5.1   Introduction

Injection bolts can be produced from standard bolts adapting them for the resin injection process as mentioned in Annex K of EN 1090-2 [78]. As shown in Figure 2.20, connections with injection bolts are characterized by filling the gap between the plates and the bolt with a structural resin. The filling process is usually carried out through an injection hole in the bolt's head. Regarding washer preparation, a groove should be machined in the bottom washer (under the nut) to enable the air to escape while the top washer (under the bolt's head) must be prepared to ensure a smooth passage and uniform resin distribution.
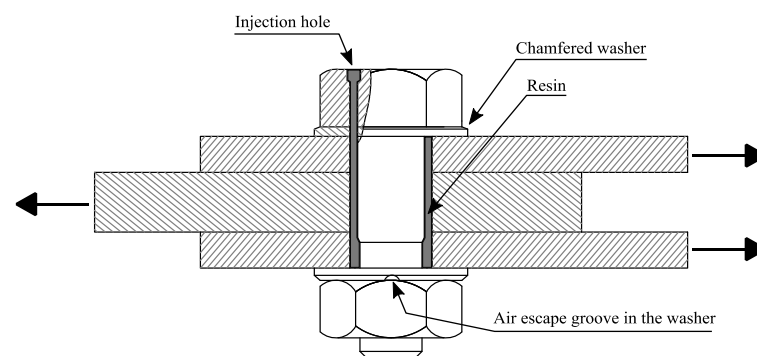
Figure 2.20. Injection bolt configuration.

After resin develops its finest mechanical properties at the end of the curing process, it is intended to obtain a slip resistant connection. Environmental temperature during injection should be a concern because it influences two important parameters of the resin: the viscosity level and the curing time. Concerning the viscosity level of the resin, it should have such a magnitude which eases the injection process even for small clearances. Manufacturer's indications must be followed to obtain the optimum injection temperature. It is also important

that the workability time of the resin (potlife) will be such that allows its injection. In Annex K of EN 1090-2 [78] a potlife of at least 15 minutes is recommended.

2.4.5.2   Structural performance and applications

Different strategies can be implemented for repairing old riveted steel bridges. Generally, these old structures present advanced corrosion damage and, due to the poor weldability properties of old materials, repairing by welding additional plates is not considered.

Riveting tends to be preferred when preservation of the original architecture of the bridge is priority. However, this option is risky and requires a time-consuming process since rivets must be heated to high temperatures. Another disadvantage of using rivets is the uncontrolled clamping stress that is created (considerable variation in clamping forces is observed [69]). For injection bolts, the design bearing resistance of the connection is usually quite sufficient to replace faulty rivets [20].

Another possibility that is excluded is using high strength friction grip (HSFG) bolts because it requires a good friction coefficient between contact surfaces. Slip can be avoided with no special treatment on the contact surfaces when using non-preloaded injection bolts, while for HSFG bolts, good friction behaviour has to be secured in order to obtain a satisfactory slip factor [19]. After injection and curing of the resin, injection bolts have a structural behaviour like fitted bolts in what concerns their slip resistance. However, the use of fitted bolts may not guarantee a good fatigue behaviour.

Since the static design resistance of a preloaded injection bolt is obtained by adding the bearing resistance of the resin to the slip resistance, when the desired load transfer per bolt is high (e.g. lack of available space for bolts in small connections), preloaded injection bolts offer a more compact connection (fewer bolts) when compared to HSFG bolts.

Additionally, overloads can produce slip in preloaded bolted connections with standard bolts. Implementing preloaded injection bolts prevents the occurrence of sudden slip. Furthermore, provided that the overload is only temporary, creep deformation will be negligible [19].

Another advantage of implementing injection bolts in a structure is the protection against internal corrosion when the resin is used [19].

Nevertheless, there are some disadvantages when injection bolts are used. As mentioned before, bolts and washers must be adapted to enable the injection process which increases the cost of bolts and washers themselves. Another disadvantage is the additional time spent in preparing the resin and its injection in the cavity. Weather conditions may also be a concern because holes must be dry during the injection. Using injection bolts can also create some difficulties if the dismantling process is required [19].

Material costs for bolted connections with injection bolts (BCIB) are related to the purchase of the bolts themselves (duly adapted for the injection process) and the structural resin. Injection equipment is cheap and although resin is an expensive material, the amount required per bolt is reduced. Bearing in mind that for BCIB the number of bolts can be reduced, final costs can be lower than in other solutions mentioned. The execution of this type of connection depends on the number of bolts, its accessibility and cleaning of the hole. The labour time for injection varies roughly between one and two minutes per bolt [20].

Repairing and strengthening operations in old riveted construction have been implemented using injection bolts. *ECCS Publication no. 79* [19] states: "Since 1970 it has been standard practice in The Netherlands to repair old railway bridges and road bridges in this way. […] No failures with injection bolts have been reported.". A specific case study of a riveted bridge in Rotterdam is described where injection bolts were used to replace faulty rivets. However, this solution can also be considered for new constructions. Such was the case in the new football stadium for AJAX Amsterdam, where injection bolts were used in the steel structure of the movable roof. This solution ensures that no slip will occur [79].

In Germany, the first application of injection bolts to repair steel bridges is described in Gresnight *et al*. [20]. Due to the advanced corrosion state of several structural elements, it was decided to apply injection bolts to connect new plates at the corroded areas of the webs of the main girders, as shown in Figure 2.21. The paper mentioned before also describes the long duration creep tests in bolted connections with injection bolts requested by German authorities. Results showed that this solution stands as a good alternative when no slip is allowed.

Figure 2.21. Strengthening operations of the web in the main girder using injection bolts [20].

In Portugal, the first known application of injection bolts was in the steel structure of the bridge originally designed by Edgar Cardoso, in Figueira da Foz, over the Mondego River, in 1980. Although this solution was not stated in the tender documents, the construction company performed a series of monotonic tests in order to prove the good behaviour of such connections in serviceability state and thus justify its application [21].

2.4.5.3   Design recommendations

Concerning European standards, EN 1993-1-8 [80] indicates the procedure to design this type of connections under static loading while EN 1993-1-9 [15] should be used for design under fatigue loading conditions.

According to EN 1993-1-8 [80], for connections defined as Category A (bearing type), the design shear load shall not exceed the design shear resistance of the bolt $F_{v,Rd}$ nor the design bearing resistance of the resin, $F_{b,Rd,resin}$ given by the following equation:

$$F_{b,Rd,resin} = \frac{k_t \, k_s \, d \, t_{b,resin} \, \beta_{resin} \, f_{b,resin}}{\gamma_{M4}} \qquad (2.45)$$

with:

k_t 1.0 for serviceability limit state (long duration) and 1.2 for ultimate limit state;

k_s 1.0 for holes with normal clearances or $(1-0.1m)$ for oversized hole where m is
              the difference between the normal and oversized hole dimensions;

d bolt diameter;

$t_{b,resin}$ effective bearing thickness of the resin given in Table 2.1;

β_{resin} coefficient depending on the thickness ratio of the connected plates as given in
            Table 2.1;

$f_{b,resin}$ bearing strength of the resin determined according to EN 1090-2 [78];

γ_{M4} partial safety factor for the bearing resistance of an injection bolt.

Table 2.1. Values for β_{resin} and $t_{b,resin}$ [80].

t_1/t_2	β_{resin}	$t_{b,resin}$
≥ 2	1.00	$2t_2 \leq 1.5\,d$
$1.0 < t_1/t_2 < 2.0$	$1.66 - 0.33\,t_1/t_2$	$t_1 \leq 1.5\,d$
≤ 1.0	1.33	$t_1 \leq 1.5\,d$
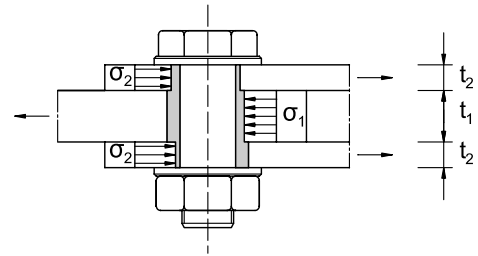
Figure 2.22. Thicknesses of plates.

According to ECCS recommendations for bolted connections with injection bolts [19], the bearing resistance of the resin, $f_{b,resin}$, is the long duration bearing resistance where the displacement due to creep is not greater than 0.3 mm. It should be determined similarly to the procedure for extended creep tests described in EN 1090-2 [78].

According to EN 1993-1-8 [80], for connections defined as Category B or Category C (slip-resistant type), the design static resistance is the sum of the design slip resistance $F_{s,Rd}$ due to the clamping force and the design bearing resistance of the resin $F_{b,Rd,resin}$. It should also not exceed the design shear resistance of the bolt $F_{v,Rd}$ nor the design bearing resistance of the steel plates $F_{b,Rd}$.

In what concerns fatigue design, in *ECCS Publication no. 79* [19] is mentioned that for non-preloaded connections, fatigue verifications must be implemented considering three different failure modes:

- through net section of the connected plates;
- shear of bolt;
- bearing of resin.

A fatigue *S-N* strength curve should be used for each failure mode. Concerning net cross-section of the connected plates, EN 1993-1-9 [15] indicates detail category 90 for double

lap and detail category 80 for single lap joints with the stress range computed with the net cross-section area. Shear of bolts should be verified for both single and double lap joints with detail category 100 ($m = 5$) with the stress range computed on the shank of the bolt.

For resin failure verification, the detail category follows from fatigue tests on BCIB performed with different bearing stress ranges (0.90, 0.60 and 0.30) of the characteristic bearing resistance of the resin, $f_{b,resin}$. These tests should be conducted under stress ratio $R_\sigma = 0.1$. The fatigue life is obtained when the total displacement exceeds the static requirement (0.3 mm), or the displacement during one cycle is greater than 0.1 mm. The lowest result determines the detail category.

Regarding preloaded connections, ECCS recommendation lists two failure modes to be verified:

- through gross cross-section of connected plates;
- maximum load range per bolt.

In this case, the fatigue S-N strength curve defined in EN 1993-1-9 [15] for fatigue verification in the connected plates is defined by the detail category 112 for double lap and detail category 90 for single lap.

The load range per bolt should fulfil the requirement presented in Eq. (2.46). $\Delta F_{v,Sd,ser,max}$ refers to the maximum applied load range per bolt and $F_{s,Rd,ser}$ is the design slip resistance per bolt, both determined at serviceability limit state.

$$\frac{\gamma_{Ff} \ \Delta F_{v,Sd,ser,max}}{2 \ F_{s,Rd,ser} \ / \ \gamma_{Mf}} \leq 1.0 \qquad\qquad (2.46)$$

For each failure mode, either in non-preloaded or preload connections, with the applied stress range, $\Delta\sigma_i$, properly increased by the partial factor for fatigue loads γ_{Ff} (the recommended value in EN 1993-2 [81] is 1.0) and fatigue strength values acquired from fatigue strength curves divided by the partial safety factor for fatigue strength γ_{Mf} (obtained in Table 2.2), the endurance value (in cycles), N_{Ri}, for each band in the load spectrum is obtained.

Table 2.2. Recommended values for partial factor for fatigue strength, γ_{Mf} [15].

Assessment method	Consequence of failure	
	Low consequence	High consequence
Damage tolerant	1.00	1.15
Safe life	1.15	1.35

Cumulative damage, D_d, during the design life should be calculated from Eq. (2.47), where n_{Ei} is the number of cycles associated with the stress range $\gamma_{Ff}\Delta\sigma_i$ for band i in the load spectrum. This fatigue assessment based on damage accumulation should meet the criterion: $D_d \leq 1.0$.

$$D_d = \sum_{i}^{n} \frac{n_{Ei}}{N_{Ri}} \tag{2.47}$$

Fatigue strength curves proposed in EN 1993-1-9 [15] for preloaded and non-preloaded bolted connections with injections bolts are compared to the fatigue strength curves for preloaded and non-preloaded bolted connections with standard bolts in Table 2.3. According to EN 1993-1-9 [15] design recommendations, the fatigue strength of bolted connections with injection bolts is higher than bolted connections with standard bolts for non-preloaded connection type. However, the same detail category is assigned for preloaded connections with injection bolts and standard bolts.

Table 2.3. Detail categories for bolted connections given in EN 1993-1-9 [15].

		Bolted connections		Detail Category	m	Stresses are calculated with the…
Plates verification	Non-preloaded	Double lap	Injection Bolts	90	3	Net cross-section area of plates
			Standard Bolts	50	3	
		Single lap	Injection Bolts	80	3	
			Standard Bolts	50	3	
	Preloaded	Double lap	Injection Bolts	112	3	Gross cross-section area of plates
			Standard Bolts	112	3	
		Single lap	Injection Bolts	90	3	
			Standard Bolts	90	3	
Bolt verification	Single and double lap			100	5	Shank cross-section area of the bolt

2.4.5.4 Research on fatigue performance of injections bolts

There is limited scientific research about the fatigue behaviour of injection bolts. An experimental investigation on bolted connections with injection bolts under fatigue loading

conditions was conducted by Jesus *et al.* [22]. Single shear specimens were designed with steel plates manufactured from structural elements of Trezoi bridge (constructed in 1956) while double shear specimens were designed with steel plates manufactured from structural elements of Fão bridge (1892). For all specimens, bolts were tightened with a torque of 80 N.m. This level of preload indicates that these connections can be considered as bearing-type connections which means that load transfer occurs through the resin, bolt shank and the hole of the plates. The adhesive chosen for injection bolts was the epoxy-based resin Sikadur®-30 which can be considered as a grout material.

It was found that all specimens presented higher fatigue strength compared to the *S-N* curves prescribed in EN 1993-1-9 [15] but specimens with injection bolts showed lower fatigue strength compared to standard bolts. Concerning fatigue experimental data from double shear specimens, injection bolts also led to lower fatigue strength when compared to standard bolts. It can be concluded that the grout epoxy-based resin Sikadur®-30 is not adequate to be implemented in resin-injected bolted connections.

The level of scatter in this case is significantly higher compared to single shear specimens. Furthermore, while for single shear specimen, mean *S-N* curves have a slope like the slope of the standard curves, for double shear connections, mean *S-N* curves are no longer parallel. These observations can be explained by the fact that single shear specimens were produced with plates of current steel material, but double shear specimens are composed of puddled iron plates which is a material with many heterogeneities, responsible for significant scatter in material properties.

2.5   Statistical methods to analyse fatigue data

2.5.1   Introduction

There are multiple sources of scatter in fatigue, not only on laboratory test series, but specially on structures in service. Within the aspects to be consider on laboratory experimental campaign, there is the material source (single batch of material or different batches), the production (specimen production and surface treatment) and the load (accuracy of test equipment). However, statistical methods should be used to overcome this matter and establish practical

solutions to analyse the obtained data [23]. Considering the most common way to describe fatigue endurance for civil engineering structures (S-N curves), it is observed from experimental results that scatter increases for longer fatigue lives as shown in Figure 2.23.
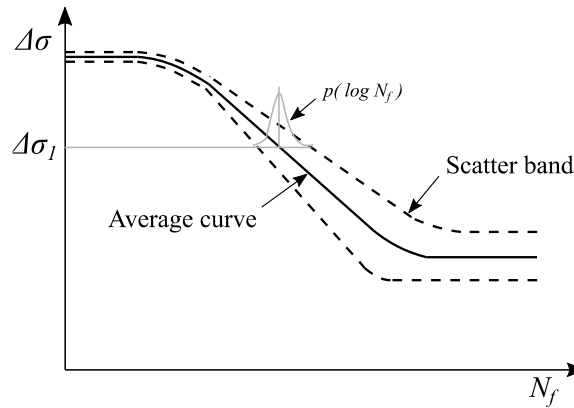
Figure 2.23. Typical scatter distribution for S-N curves.

Linear regression analysis can be applied in multiple fatigue assessments to establish a representative model of experimental data. As presented in Eq. (2.48), this linear method relies on a dependent variable, Y, on an independent variable, X, on the slope, A, and on constant B.

$$Y = AX + B \tag{2.48}$$

For the estimation of B constant and slope A, Eq. (2.49) and Eq. (2.50) should be used, where $\bar{Y}$ and $\bar{X}$ are the mean values of each variable and n is the sample size.

$$B = \frac{\sum_{j=1}^{n}(X_j - \bar{X})(Y_j - \bar{Y})}{\sum_{j=1}^{n}(X_j - \bar{X})^2} \tag{2.49}$$

$$A = \bar{Y} - B\bar{X} \tag{2.50}$$

The quality of this statistical approach can be evaluated with the coefficient of determination, R^2, which enables to assess the adjustment level of the data to a linear model. The highest level of adjustment is obtained with $R^2 = 1$ and the lowest with $R^2 = 0$. Its computation was made with Eq. (2.51). Unfortunately, the distribution function to determine characteristic S-N curves cannot be derived based on physical arguments. In general, it is simply assumed or adjusted to

experimental data of large test series. Two popular distributions are the normal or Gaussian distribution and the Weibull distribution [23].

$$R^2 = 1 - \frac{\sum_{j=1}^{n}[Y_j - Y(X_j)]^2}{\sum_{j=1}^{n}[Y_j - \bar{Y}]^2} \tag{2.51}$$

2.5.2   Normal distribution

The well-known normal distribution function is presented in Eq. (2.52) where μ is the mean value and $\hat{\sigma}$ is the standard deviation which can be assessed by Eq. (2.53) and Eq. (2.54), respectively. The variable of interest, y, is the logarithm of the fatigue life, generally. Standard deviation, $\hat{\sigma}$, depends on the number of degrees of freedom, v_{dg}, which are computed as $n - 2$ with n as the sample size.

$$P(y) = \frac{1}{\hat{\sigma}\sqrt{2\pi}} \int_{-\infty}^{y} e^{-\frac{1}{2}\left[\frac{y-\mu}{\sigma}\right]^2} dy \tag{2.52}$$

$$\mu = \frac{1}{n} \sum_{j=1}^{n} y_j \tag{2.53}$$

$$\hat{\sigma} = \sqrt{\frac{\sum_{j=1}^{n}(y_j - \mu)^2}{v_{dg}}} \tag{2.54}$$

Combining a linear model with normal distribution function, the estimation of lower and upper limits are made using recommendations of ISO 12107 [82] as presented in Eq. (2.55) where $k_{p,1-\alpha_n,v_{dg}}$ is the one-sided tolerance limit for a normal distribution. This parameter was computed in the software MATLAB® using the function developed by Viktor Witkovsky [83] and it depends on the probability p, confidence level (1 - α_n) and the number of degrees of freedom, v_{dg}, used for standard deviation. Characteristic values of variables based on normal distribution function presented in this thesis were determined assuming a probability of not reaching Y_j equal to p = 5% and a confidence level equal to (1 - α_n) = 75% which are the values recommended in the design code EN 1993-1-9 [15].

$$Y \ = \ AX \ + \ B \ \pm \ k_{p,1-\alpha_n, v_{dg}} \ \hat{\sigma} \tag{2.55}$$

2.5.3   Weibull distribution

The alternative approach is to implement the Weibull distribution function which is often used to represent skewed distributions [84]. The description of the cumulative probability function with two parameters is given in Eq. (2.56) where α_w and β_w are the scale and shape parameters, respectively.

$$P(y) \ = \ 1 - e^{-\left[\frac{y}{\alpha_w}\right]^{\beta_w}} \tag{2.56}$$

Weibull distribution parameters can be estimated with different methods. In this thesis, four estimation methods were applied to determine their most accurate values: Maximum Likelihood Method (MLM), Method of Moments (MM), Linear Least Squares Method (LLSM) and Weighted Linear Least Squares Method (WLLSM).

- Maximum Likelihood Method

This method is popular within the scientific community mainly because it is versatile and reliable. The likelihood function of the Weibull distribution [85] is given by Eq. (2.57) where n is the sample size.

$$
\begin{aligned}
L(\alpha_w, \beta_w | y) \ &= \ \prod_{j=1}^{n} f(y_j | \alpha_w, \beta_w) \\
&= \ \prod_{j=1}^{n} \left[\frac{\beta_w}{\alpha_w^{\beta_w}} y_j^{(\beta_w-1)} exp\left\{ -\left(\frac{y_j}{\alpha_w}\right)^{\beta_w} \right\} \right] \\
&= \ \left(\frac{\beta_w}{\alpha_w^{\beta_w}}\right)^n \prod_{j=1}^{n} \left[y_j^{(\beta_w-1)} exp\left\{ -\left(\frac{\sum y_j}{\alpha_w}\right)^{\beta_w} \right\} \right]
\end{aligned}
\tag{2.57}
$$

The estimation of Weibull parameters is obtained with the log-likelihood function. They are computed by maximizing the logarithmic function by means of interactive numerical methods.

- Method of Moments

The moment method is one of the oldest estimation methods [86]. The estimation of distribution parameters relies on matching sampling moments to the experimental data. Sampling moments are determined using Eq. (2.58).

$$\mu_k = \frac{1}{n} \sum_{j=1}^{n} y_j^k \tag{2.58}$$

For y as independent and identically distributed variable, the first two population moments (M_1, M_2) are enough to estimate Weibull distribution parameters. These moments are computed with Eq. (2.59) and Eq. (2.60) in which Γ is the gamma function.

$$M_1 = \alpha_w \Gamma \left(1 + \frac{1}{\beta_w} \right) \tag{2.59}$$

$$M_2 = \alpha_w{}^2 \Gamma \left(1 + \frac{2}{\beta_w} \right) \tag{2.60}$$

Using mathematical operations, it is possible to relate these equations resulting in Eq. (2.61). It corresponds to the coefficient of variation of the sample, and it is dependent only on the shape parameter, β_w. The solution can be found using Newton-Raphson method. Ben-Israel [87] detailed the application of this method.

$$\frac{\mu_2}{\mu_1^2} = \frac{\Gamma \left(1 + \frac{2}{\beta_w} \right)}{\Gamma^2 \left(1 + \frac{1}{\beta_w} \right)} \tag{2.61}$$

- Linear Least Squares Method

The application of logarithm in Eq. (2.56) allows to establish a linear model as presented in Eq. (2.62) in which $X_j = ln(y_j)$ and $Y_j = ln(-ln(1 - P(y_j)))$.

$$ln\big(-ln\big(1 - P(y_j)\big)\big) = \alpha_w \, ln\big(y_j\big) - \alpha_w \, ln(\beta_w) \tag{2.62}$$

The estimation of Weibull parameters is then computed with simple linear regression [88]. The optimization method is applied using the following equation.

$$min\,QQ = \sum_{j=1}^{n}\big[Y_j - \big(\alpha_w X_j - \alpha_w \, ln(\beta_w)\big)\big]^2 \tag{2.63}$$

Finally, the estimation of Weibull parameters is performed with the partial derivatives of QQ, as presented below.

$$\alpha_w = \frac{n \sum_{j=1}^{n} X_j Y_j - \sum_{j=1}^{n} X_j \sum_{j=1}^{n} Y_j}{n \sum_{j=1}^{n} X_j^2 - \big(\sum_{j=1}^{n} X_j\big)^2} \tag{2.64}$$

$$\beta_w = exp\left(\frac{\sum_{j=1}^{n} Y_j - \alpha_w \sum_{j=1}^{n} X_j}{n \, \alpha_w}\right) \tag{2.65}$$

- Weighted Linear Least Squares Method

The weighted linear least squares estimation method assigns different relevance for each element of the data set [89]. The approximation of weights, w_j, is modelled with a polynomial function dependent on the estimated values of the accumulated probability function $P(y_j)$ as presented in Eq. (2.66) [88].

$$w_j = -0.076 + 3.610P(y_j) - 6.867P(y_j)^2 + 13.54P(y_j)^3$$
$$-9.231P(y_j)^4 \tag{2.66}$$

The optimization method follows the same strategy as in linear least square method – Eq. (2.63). In this case, the values of scale and shape parameters of Weibull distribution are obtained with Eq. (2.67) and Eq. (2.68), respectively. The evaluation of each method is performed by three different goodness-of-fit statistic tests between the estimative values for each method and the estimative values using Bernard's median rank [90] presented in Eq. (2.69) where j is the order number and n is the sample size.

$$\alpha_w = \frac{\sum_{j=1}^{n} w_j \sum_{j=1}^{n} w_j X_j Y_j - \sum_{j=1}^{n} w_j X_j \sum_{j=1}^{n} w_j Y_j}{\sum_{j=1}^{n} w_j \sum_{j=1}^{n} w_j X_j^2 - \left(\sum_{j=1}^{n} w_j X_j\right)^2} \tag{2.67}$$

$$\beta_w = exp\left(\frac{\sum_{j=1}^{n} w_j Y_j - \alpha_w \sum_{j=1}^{n} w_j X_j}{\alpha_w \sum_{j=1}^{n} w_j}\right) \tag{2.68}$$

$$P(y_j) = \frac{j - 0.3}{n + 0.4} \tag{2.69}$$

The goodness-of-fit tests implemented in this thesis were: Kolmogorov-Smirnov described in Eq. (2.70), Anderson-Darling described in Eq. (2.71) and χ-Squared test described in Eq. (2.72).

$$KS = sup \left| P(y_j) - P(y_j)_{est.method} \right| \tag{2.70}$$

$$AD = -n - \frac{1}{n}\sum_{j=1}^{n} \left\{ (2j - 1)\left(log\left(P(y_j)_{est.method}\right) + log\left(1 - P(y_{n+1-j})_{est.method}\right)\right)\right\} \tag{2.71}$$

$$\chi^2 = \frac{\left(P(y_j)_{est.method} - P(y_j)\right)^2}{P(y_j)} \tag{2.72}$$

This evaluation enables to determine the most accurate estimation method for each study case and choose the values for Weibull distribution function parameters.

Combining a linear model with Weibull distribution function, it is necessary to consider that the values of the scale parameter and the shape parameter are constants for all values of the dependent variable. Therefore, experimental data is normalized by dividing it by the estimated values [91]. After the determination of Weibull distribution parameters, the estimation of lower and upper limits is made using Eq. (2.73) where p is the probability. In this thesis the probability used to compute characteristic values was $p = 5\%$.

$$Y = [AX + B]\, \beta_w [-\ln(1 - p)]^{\alpha_w} \tag{2.73}$$

3   METALLOGRAPHIC AND MECHANICAL MATERIAL ASSESSMENT

3.1   Introduction

The scientific research presented in this thesis is focused on structural details composed of metallic components that are commonly used in civil engineering structures subjected to fatigue loading, such as bridges. It is essential to note that, a fully comprehensive study on the fatigue behaviour of these details requires an accurate characterization at material level and, therefore, this chapter presents a metallographic and mechanical assessment of three selected metallic materials: Eiffel bridge material, S235 and S355. These are the metallic materials that compose the structural details studied in this thesis.

The first material, which can be categorized as puddled iron, was extracted from the web of the main girders of a centenary Portuguese bridge named Eiffel bridge – see Figure 3.1. It was inaugurated in 1886 and was built in puddled iron, which is a material with many heterogeneities responsible for significant scatter in its properties [52]. The other two materials selected for this characterization are modern non-alloy structural steels: S235 and S355.

Figure 3.1. Eiffel bridge – Viana do Castelo, Portugal [92].

As it is represented in Figure 3.2, this material assessment includes metallographic and mechanical approaches. It is intended to fully characterize these materials aiming to understand the relation between metallographic properties (microstructural composition, grain and crystallite sizes, dislocation density and chemical composition) and mechanical performance (hardness, monotonic, fatigue and crack growth behaviour). A literature review on low-cycle and fatigue crack growth (FCG) experimental results from these materials was conducted but also new FCG tests were performed aiming to establish reliable material laws. This goal was

achieved by implementing a statistical analysis based on normal and Weibull distribution functions to define characteristic values of fatigue parameters. Standard recommendations based on DNV-RP-C-208 [93] for cyclic and fatigue behaviour and BS 7910 [94] for fatigue crack growth were compared with statistical analysis of experimental results. Fatigue behaviour was assessed based on three distinct damage parameters: strain, SWT and strain energy.

METALLOGRAPHIC AND MECHANICAL MATERIAL ASSESSMENT
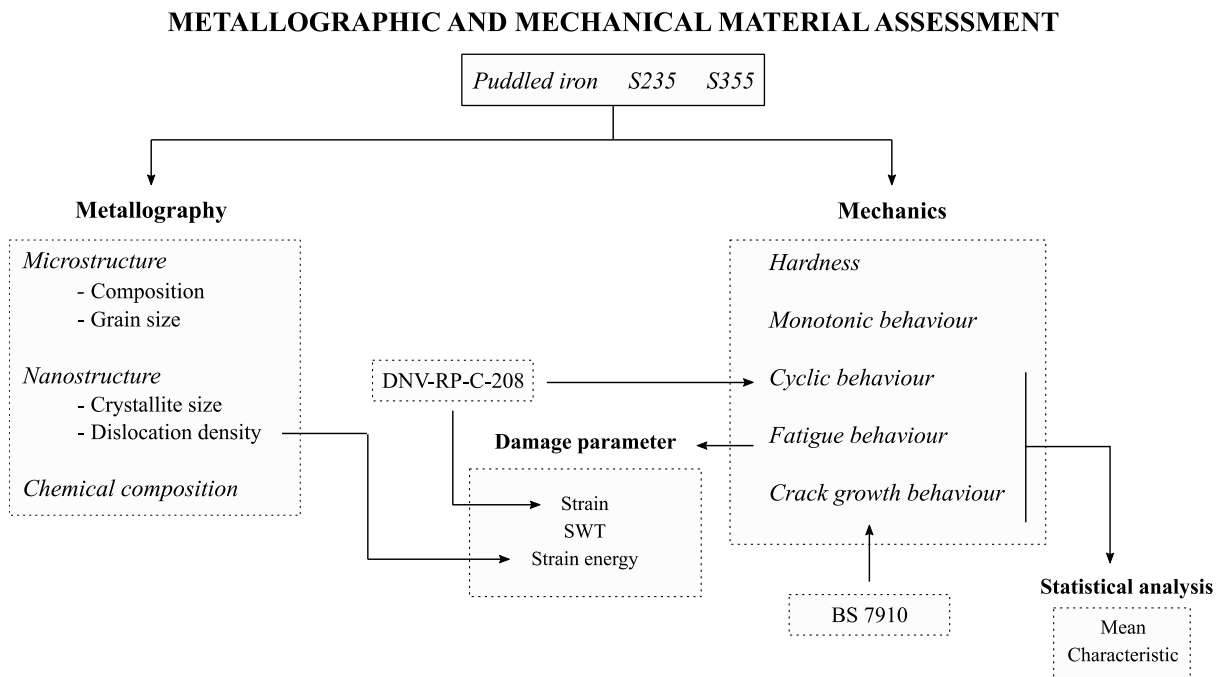
Figure 3.2. Schematic representation about the content of Chapter 3.

3.2   Metallography

3.2.1   Microstructure

3.2.1.1   Composition

Small samples with 20x10xthickness (mm) were prepared for each material. The preparation of these samples included the removal of the external oxidation layer and polishing the surface to obtain an area without dust and scratches in which the grains and its boundaries could be visible in an optical microscope. In this sense, each sample was embedded in a resin using a Struers® thermal press (see Figure 3.3a) to facilitate the sanding procedure. The Struers® rotating desk presented in Figure 3.3b) was used for sanding each sample with sandpaper from P100 to P1200 grit size and polishing with two diamond papers (6 and 1 μm). Grain boundaries

became visible after etching the surface with Nital (a solution of nitric acid, HNO_3, and ethanol C_2H_6O).

a)   b)
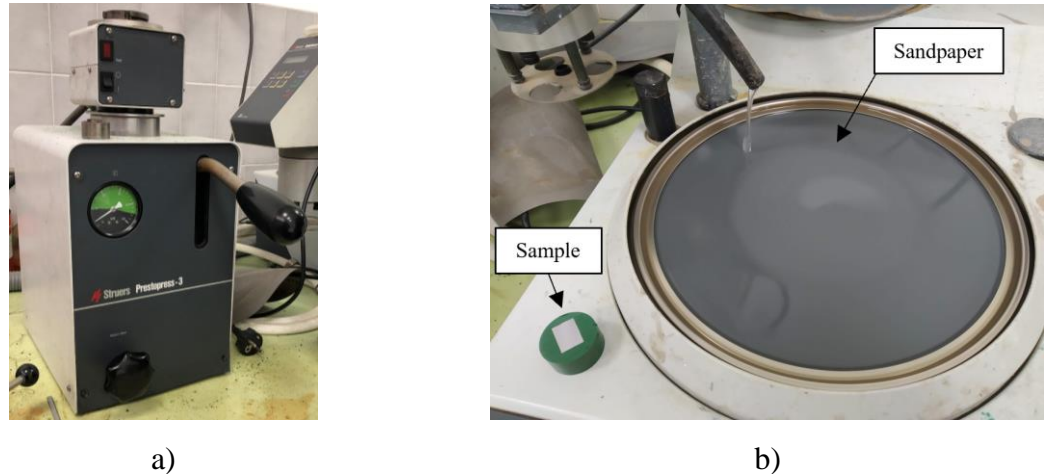
Figure 3.3. Preparation of samples: a) thermal press; b) rotating desk.

Observations in the optical microscope for these materials are presented in Figure 3.4. The image obtained from the Eiffel bridge material shows a typical microstructure of 19th century puddled iron [95] with abundant presence of slags (generally silica slags [96]) and non-metallic inclusions (A) aligned with the direction of lamination and mainly present in the boundaries of the ferritic grains (B) which are visible in an irregular and elongated structure. A layered cross section is visible which is directly related with rolling production process. This characteristic contributes to highly scattered material properties and a material response closer to an anisotropic behaviour.

S235 and S355 structural steels have a typical ferrite-pearlite (pearlite areas are identified with letter C in Figure 3.4) microstructure and there are no visible slags or non-metallic inclusions. Ferrite is associated with soften material properties while higher quantity of perlite indicates higher strength. Comparing Figure 3.4a) and Figure 3.4 b), it is visible that the presence of perlite is higher in S355. It is also noticed that there is no visible preferential orientation of the matrix as was also confirmed by Neslušan *et al*. [97] for S235 steel. This characteristic contributes to homogeneous and low scattered material properties as well as a material response closer to an isotropic behaviour. An image from Scanning Electron Microscope (SEM) FEI QUANTA - 400 was obtained for S235 steel sample – see Figure 3.5 – in which the ferrite matrix is visible as well as perlite areas.

a)

b)

c)
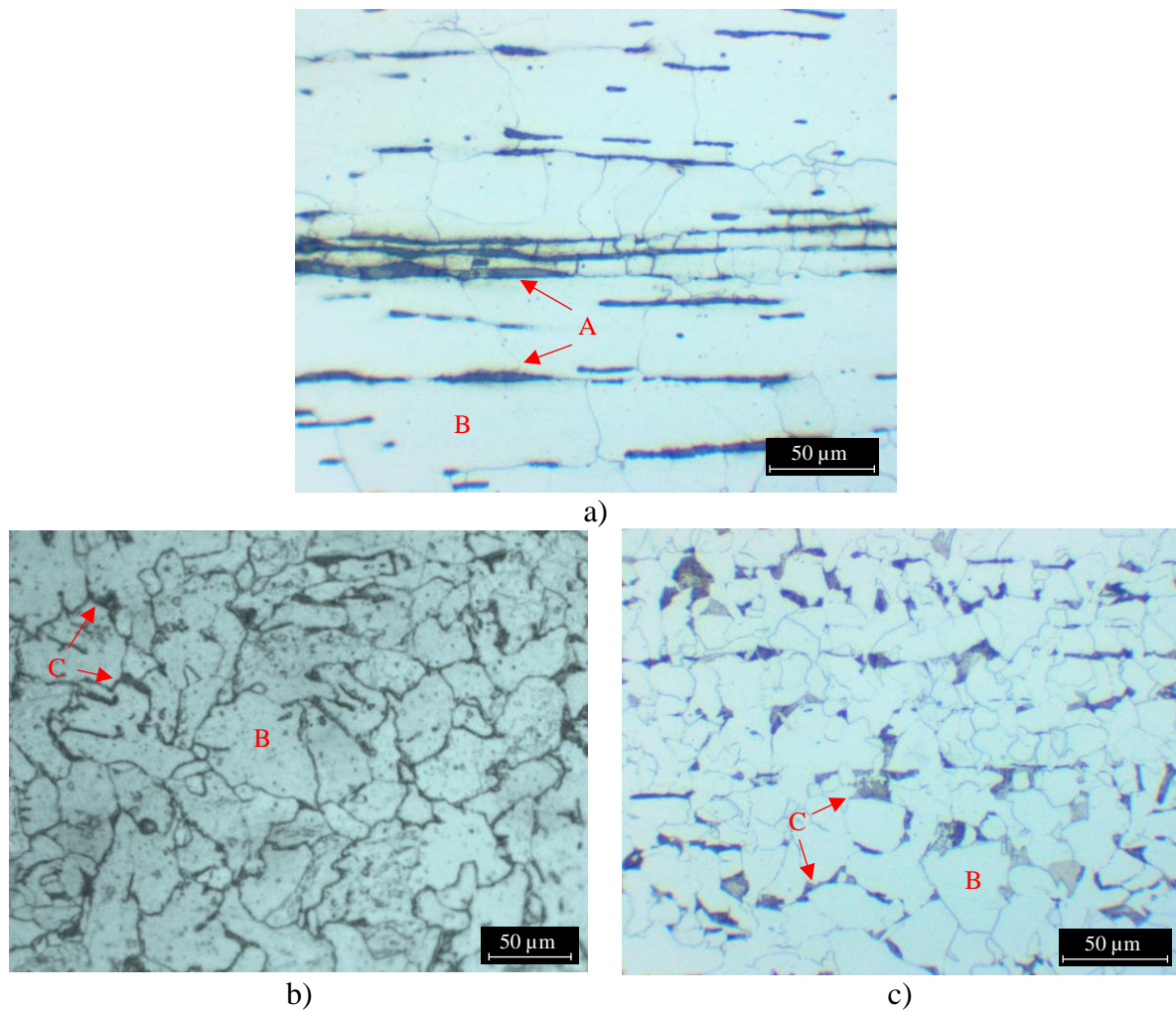
Figure 3.4. Microstructure observations on optical microscope: a) material from the Eiffel bridge (Magn. 400x); b) S235 steel (Magn. 500x); c) S355 steel (Magn. 400x).
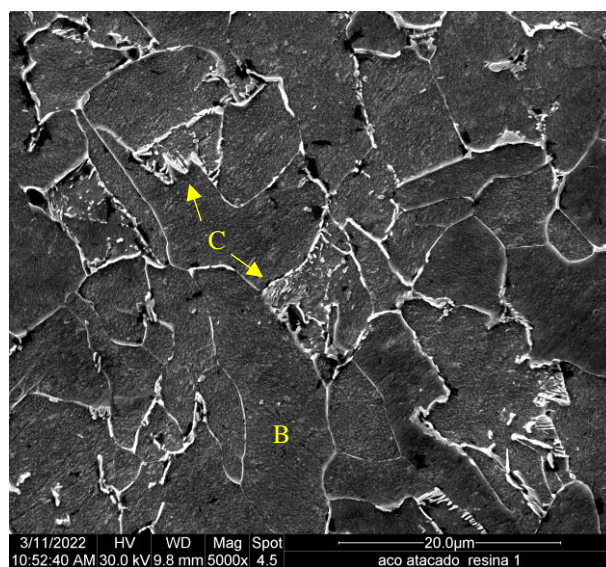
Figure 3.5. Microstructure observations of S235 obtained with SEM.

3.2.1.2 Grain size

The grain size is an important parameter to be determined because it has a high influence on the mechanical performance. Using a series of microstructural observations obtained with SEM, grain size was measured using the Abrams Three-Circle Intercept Procedure described in ASTM E112 [98] by means of the software *Image J* [99]. The test pattern consists of two crossed lines and three concentric circles. For each material, four images were used in which three measurements were made for each image. An example is presented in Figure 3.6.
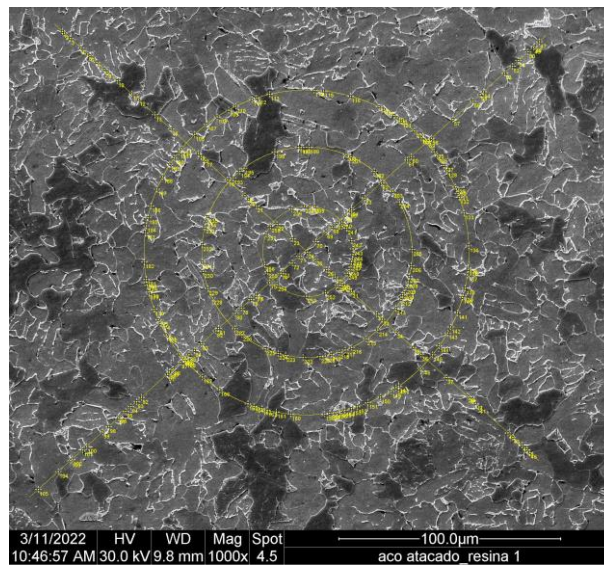
Figure 3.6. Grain size measurement example using a SEM image on a S235 sample.

The number of intersections (point where a test line crosses a grain boundary) per length of test line (and circle), $\bar{P}_L$, is calculated as presented in Eq. (3.1) in which $\bar{P}_j$ is the total number of intersections, L is the total length of test line (and circle) and M is the magnification.

$$\bar{P}_L = \frac{\bar{P}_j}{L/M} \tag{3.1}$$

The mean line intercept, $\bar{l}$, is then computed as:

$$\bar{l} = \frac{1}{\bar{P}_L} \tag{3.2}$$

Furthermore, the ASTM grain size number is obtained as:

$$G = -3.2877 - 6.6439 \cdot log_{10}(\bar{l})$$

(3.3)

The analysis of the grain size for these three materials led to the results presented in Table 3.1. There is a significant difference between the value of the mean line intercept, $\bar{l}$, obtained for Eiffel bridge material and the value obtained for modern steels, since it is approximately 6 times bigger than S235 and 15 times bigger when compared to S355. Experimental results obtained by Oliveira [100] on puddled iron from a Brazilian bridge built in 1865 are in line with the values found for Eiffel bridge material. Regarding the values of grain size obtained for modern steels, it is verified that higher yield strength is associated with lower values of grain size, since from S235 to S355, a reduction on the mean line intercept value is obtained.

Table 3.1. Results from grain size analyses of Eiffel bridge material, S235 and S355.

Material	Magnification	$\bar{P}_L$ [µm]			$\bar{l}$ [µm]	G [-]
		Max.	Min.	Average		
Eiffel bridge (1878)	400x	12.9	8.1	9.4	106.1	3.2
Barão de Juparanã bridge (1865) [100]	400x	-	-	-	-	5.1
	1410x	-	-	-	-	6.5
S235	500x	87.8	53.0	60.7	16.5	8.6
S355	400x	164.7	108.3	136.3	7.3	10.9

3.2.2   Nanostructure

3.2.2.1   Crystallite size

Crystalline materials are characterized by a periodic and repetitive arrangement of atoms. It means that atoms are positioned in a three-dimensional repetitive pattern. The description of a crystal structure is made using solid spheres as presented in Figure 3.7a) that can be divided in unit cells as presented in Figure 3.7b) which are considered the basic nano structural unit. They are defined by its geometry and position of atoms. The crystal structure of iron is body-centred cubic (BCC), and the atomic ratio is 0.1241 nm. It has atoms in the vertices and at the centre of the cube. The atomic bond in metals is non-directional which means that there are few restrictions in terms of quantity and location of neighbouring atoms leading to compact crystal structures [101]. The characterization of material's crystal structure has been made using X-ray

diffraction (XRD), therefore an explanation of the diffraction phenomenon is presented in the following paragraphs.

<p align="center">a)   b)</p>
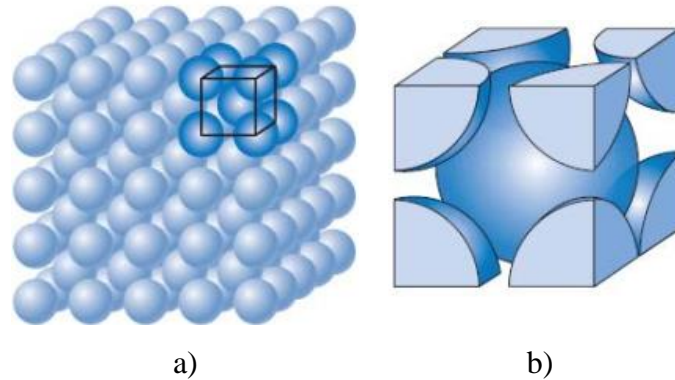
Figure 3.7. Rigid spheres schematic representation of: a) BCC crystal structure and b) unit cell [101].

Diffraction occurs when a wave intercepts a series of regularly spaced obstacles, and the result is a wave with a wave length like the space between the obstacles. It is also related with specific phase relations between two or more waves that were scattered by obstacles [102]. Considering that two waves with the same wavelength (λ) and in phase at point OO' are scattered to different trajectories by the obstacles, one possible result is that these two waves continue with the same phase – constructive interference – and a diffracted wave is created, see Figure 3.8a). Other phase relationships are possible between scattered waves that will not lead to this mutual reinforcement. The other possible extreme situation can be found when these two waves are not in phase as the example represented in Figure 3.8b) – destructive interference – in which waves cancel each other after scattering event.

X-rays are an electromagnetic radiation with high energy and small wave lengths (like the atomic distances in solids). When a particle beam of X-ray hits a solid material, a portion of this beam is scattered in all directions by electrons in the atoms that are in the path of the particle beam. Figure 3.9 presents two atomic parallel planes (A-A' and B-B') with the same Miller indices (h,k and l) and separated by an interplanar distance d_{hkl}. A particle beam of parallel, monochromatic, and coherent (in phase) X-rays with wavelength λ hits these two planes at an angle θ_D. Two rays in this beam, labelled 1 and 2, are scattered by atoms P and Q. If the path length difference between 1-P-1' and 2-Q-2' (which means $\overline{SQ} + \overline{QT}$) is equal to a multiple, n,

of wavelength, there is a constructive interference of the scattered X-rays 1' and 2' at an angle θ_D. Mathematically, it can be expressed with the Bragg law – Eq. (3.4) – relating the wavelength, the interatomic distance, and the diffraction angle for a constructive interference. If the Bragg law is not followed, the interference will be non-constructive and the diffracted beam will have very low intensity [102].

$$n\lambda = \overline{SQ} + \overline{QT} = 2d_{hkl}\ sen\ \theta_D \tag{3.4}$$
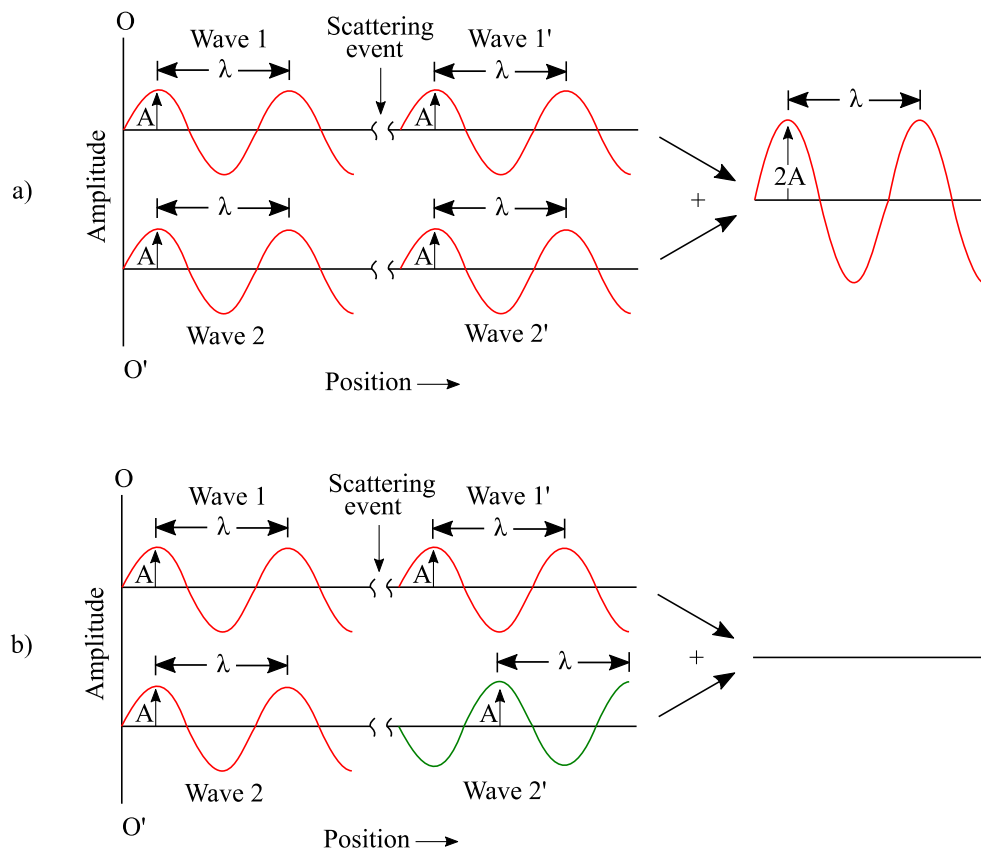
Figure 3.8. Schematic representation of scattering events on waves: a) diffracted waves continue synchronized; b) diffracted waves are desynchronized. Adapted from [102].

The interplanar distance d_{hkl} is a function of the Miller indices and the parameters of the crystal structure. For crystal structures with cubic symmetry, the interplanar distance is computed as presented in Eq. (3.5) in which $a_{crystal}$ is the parameter that defines the crystal structure (unit cell edge length).

$$d_{hkl} = \frac{a_{crystal}}{\sqrt{h^2 + k^2 + l^2}} \tag{3.5}$$
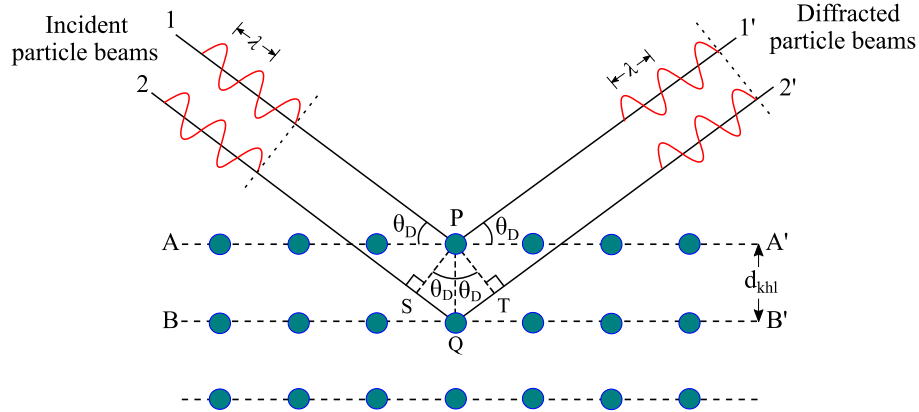
Figure 3.9. XRD for atoms planes (A-A' and B-B'). Adapted from [102].

Bragg law specifies the diffraction in unit cells with atoms in the vertices. However, the other atoms of the cell act as additional scattering elements which can produce out-of-phase scattering in several Bragg angles resulting in missing some diffracted particle beams which should be present. The crystallographic planes that do not origin diffracted particle beams depend on crystal structure. In the case of BCC crystal structure, the sum $h + k + l$ should be even to generate diffraction while for face-centred cubic (FCC), the Miller indices should be all even or all odd as described in Table 3.2.

Table 3.2. Reflection planes for XRD for different crystal structures [102].

Crystal structure	Reflections	Miller index for the first six planes
BCC	$(h + k + l)$ even	110, 200, 211, 220, 310, 222
FCC	h, k, and l are all even or all odd	111, 200, 220, 311, 222, 400
Primitive cubic	All	100, 110, 111, 200, 210, 211

Generally, diffraction techniques are based on exposing a sample to a monochromatic X-ray. The diffractometer is a device that measures the diffraction angles as presented in Figure 3.10. The sample, S, is positioned to rotate around the axis O. The monochromatic X-ray is generated in point T and the intensity of diffracted beams is detected with a device positioned in letter C. The sample, the source and the receiving device are all in the same plane. The receiving device is placed in a rotating platform around the axis O. During the procedure, the rotation angle of

the sample, θ_D, is followed by a rotation angle of $2\theta_D$ from the receiving device to ensure that incident and reflection angles are equal.
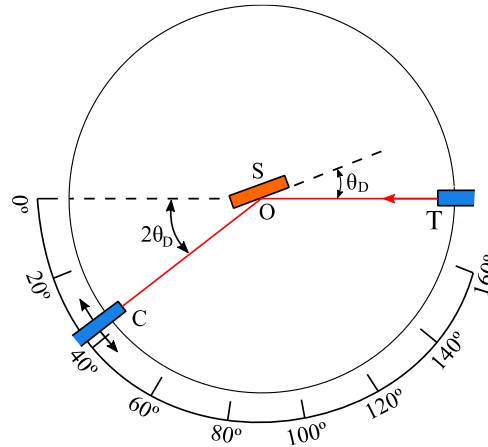
Figure 3.10. Schematic representation of an X-ray diffractometer: T – X-ray source; S – sample; C – detecting device; O – rotating axis. Adapted from [102].

While the receiving device is moving with a constant angular speed, the intensity of the diffracted particle beam is recorded as a function of $2\theta_D$ (diffraction angle). An example of a diffractogram obtained with XRD for a lead sample is presented in Figure 3.11. The high intensity peaks occur when Bragg diffraction condition is satisfied for a set of crystallographic planes. The size and geometry of the unit cell can be obtained from the angular positions in the diffraction peaks, while the arrangement of atoms within the interior of the cell is associated with the intensity of those peaks.
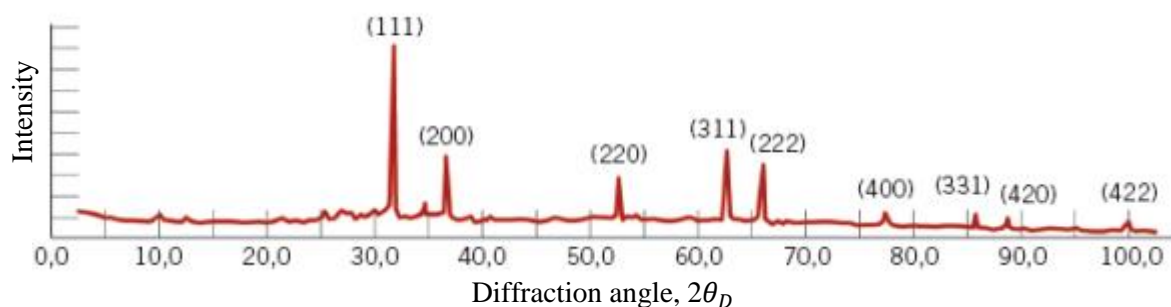
Figure 3.11. Example of a X-ray diffractogram obtained for a lead sample [101].

A small sample (similar to those used for microstructural characterization) was used for both S235 and S355 materials to characterize its crystal structure. Eiffel bridge material was

excluded from this study due to its high level of heterogeneity. The obtained data from XRD was collected at room temperature by PANalytical X'Pert Pro diffractometer – see Figure 3.12. The measurement was made using a standard sample holder, at 40 kV and 30 mA, 100 s/step, within a range of diffraction angle $2\theta_D$ varying between 30º and 120°.

Figure 3.12. X-ray diffraction equipment used in this study.

The obtained spectrum for S235 and S355 is presented in Figure 3.13. It is evident that these two materials have the same crystal structure (BCC). Five peaks were identified for each sample with nearly coincident diffraction angles. Crystallite size, D, was computed for S235 and S355 considering this diffractogram obtained with XRD using the Scherrer equation described in Eq. (3.6).

$$D = \frac{k_D \lambda}{\beta_D \cos \theta_D} \qquad (3.6)$$

The Scherrer constant, k_D, depends on the reflection and crystal form and it varies between 0.62 and 2.08. The value adopted for Scherrer constant was 0.89, following the recommendations made by He *et al.* [103]. The parameter λ is the X-ray wavelength (in this case it was used Cu which has $\lambda = 1.5406\mathring{A} = 0.15406nm$) and β_D is the full width and half maximum (FWHM) of each peak which was determined using OriginPro® software. The analysis of each peak obtained from the diffractogram led to the results presented in Table 3.3.
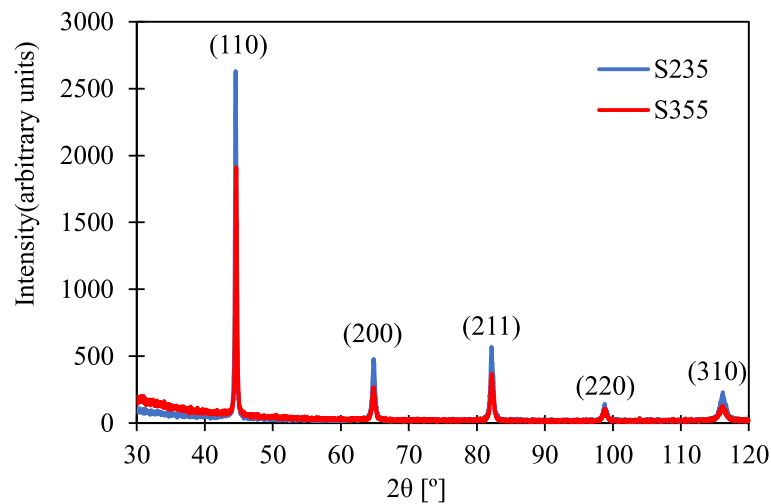
Figure 3.13. Diffractogram obtained for S235 and S355 samples.

Table 3.3. Crystallite size obtained from XRD for S235 and S355 samples.

Material	Peak	Diffraction angle $2\theta_D$ [°]	FWHM β_D [rad]	Crystallite Size D [nm]
S235	1	44.5	0.308	27.6
	2	64.8	0.501	18.6
	3	82.2	0.547	19.1
	4	98.8	0.586	20.6
	5	116.2	0.981	15.1
S355	1	44.6	0.274	31.0
	2	64.8	0.565	16.5
	3	82.2	0.526	19.8
	4	98.8	0.605	20.0
	5	116.1	1.184	12.5

The values obtained for crystallite size of S235 and S355 are analysed in terms of maximum, minimum and mean values and results are shown in Table 3.4. It is evident that there is no significant difference when the comparison is established with the mean value, however, maximum and minimum values of crystallite size differ between these two materials. The range of crystallite size values is wider for S355.

Table 3.4. Comparison of crystallite size between S235 and S355.

Material	S235	S355
D_{max} [nm]	27.6	31.0
D_{min} [nm]	15.1	12.5
D_μ [nm]	20.2	20.0
D_σ [nm]	2.3	3.4

3.2.2.2 Dislocation density

A dislocation is a linear or unidirectional defect around which misaligned atoms can be found. One type of dislocation is called the edge dislocation represented in Figure 3.14a). It is formed by an extra plane or semi-plane of atoms that ends in the interior of the crystal structure. In the region of the dislocation line there is a distortion of the crystal structure: the atoms above the dislocation line are squeezed and the atoms below the dislocation line are pulled apart. This defect leads to bending of the vertical planes, especially those that are closer to the dislocation. Another type of dislocation is the screw dislocation which is formed by a shear stress – see Figure 3.14b). One part of the crystal is moved one atomic distance relatively to the other part. The atomic distortion associated with screw dislocation is also linear and it is localized within the line AB. However, the majority of dislocations found in crystalline materials are not pure edge neither pure screw dislocations but a mixture of both, they are called mixed dislocations – see Figure 3.14c) [102].
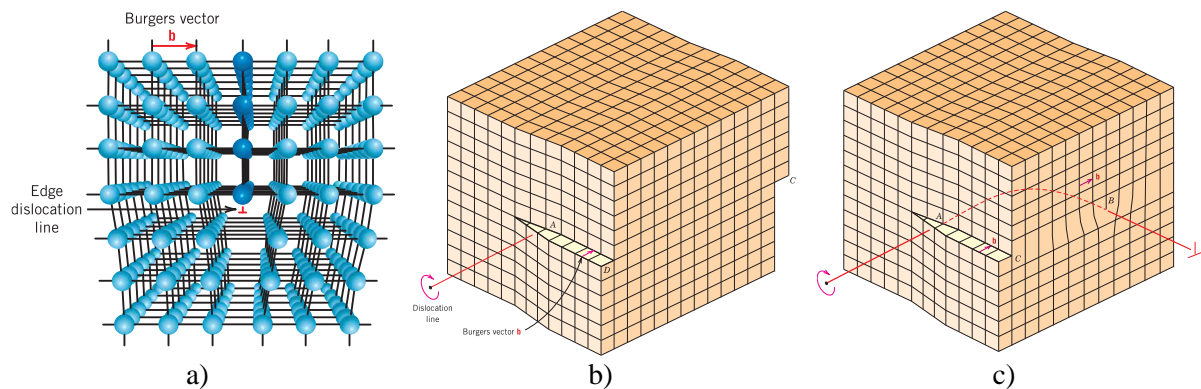
a)   b)   c)
Figure 3.14. Types of dislocations: a) edge; b) screw; c) mixed [102].

The direction and magnitude of crystal structure distortion associated with the dislocation is expressed by the Burgers vector, represented by $\vec{b}$. For metallic materials, the Burger's vector for a dislocation is oriented to a compact crystallographic direction and the magnitude is equal to the interatomic distance [102].

All metals and alloys have dislocations introduced during solidification, plastic deformation or as a consequence of thermic stresses resulting from the cooling process. The number of dislocations is determined by the dislocation density which is the total dislocation length per unit volume. For carefully solidified metal crystals, dislocation density is as low as 10^{-9} nm^{-2},

generally. For highly deformed metals, this parameter may run up to 10^{-3} and 10^{-2} nm^{-2}, generally. [101] The dislocation density can be determined using the following expression:

$$\delta_D = \frac{1}{D^2} \qquad (3.7)$$

Considering the crystallite size computed in previous section for S235 and S355, it was possible to estimate the dislocation density induced by the manufacture process. As it is presented in Table 3.5, results are within the range of the values found in literature for highly deformed metals.

Table 3.5. Dislocation density obtained by XRD for S235 and S355.

| Peak | Dislocation density, δ_D [nm⁻²] | |
	S235	S355
1	1.3E-03	1.0E-03
2	2.9E-03	3.7E-03
3	2.7E-03	2.5E-03
4	2.4E-03	2.5E-03
5	4.4E-03	6.4E-03
Max	4.4E-03	6.4E-03
Min	1.3E-03	1.0E-03
Average	2.7E-03	3.2E-03
Strd. Dev.	5.5E-04	9.9E-04

3.2.3   Chemical composition

A collection of data from literature was made to characterize the chemical composition of selected materials. Results are presented in Table 3.6. Jesus *et al*. [104] showed that Eiffel bridge material fit within the typical chemical composition values for puddled iron established by Helmerich [96]. Comparison is done with the standard chemical composition of S235 and S355 (non-alloy steel) materials defined by EN 10025-2 [105]. The term non-alloy steel refers to steels that do not contain alloy elements like chromium, nickel or molybdenum and the alloy elements that they have, such as manganese, silicon or carbon are present in less than 5% by weight. One significant difference between puddled iron and modern steel materials is related to the amount of phosphorus whose presence is associated with lower mechanical performance. The presence of manganese in modern steels turns the material harder, with improved

mechanical properties, and better weldability [96]. In what concerns carbon content, it influences not only the strength of the material but also the ductility, in the sense that, higher carbon percentages increases the strength but the ductility is reduced [106].

Table 3.6. Chemical composition of selected materials in wt.% (weight percentage).

Material	Carbon	Silicon	Manganese	Phosphorus	Sulphur	Nitrogen	Copper
Eiffel bridge [104]	0.03	0.13	0.02	0.46	0.06	-	-
Typical values for puddled iron [96]	[0.0032, 0.15]	[0.0030, 0.42]	[0.054, 0.11]	[0.011, 0.39]	[0.0034, 0.018]	[0.0037, 0.04]	-
S235 JR [105]	< 0.19	-	< 1.5	< 0.045	< 0.045	< 0.014	< 0.60
S355 JR [105]	< 0.27	< 0.60	< 1.7	< 0.045	< 0.045	< 0.014	< 0.60

3.3 Mechanics

3.3.1 Hardness

The hardness of the three selected materials was measured using Vickers hardness test. This parameter is related to the material's ability to resist plastic deformation under a standard mechanical indentation. The relation between the applied force, F_{HV}, and the area of the indentation, A_{HV}, (determined as a function of the average length of the indentation diagonal, L_{diag}) gives the value of the hardness as described in Eq. (3.8). A total of 10 measurements were performed for each material sample. A summary of results from Vickers hardness test is presented in Table 3.7 and an image of the S235 sample after hardness measurement is presented in Figure 3.15.

$$HV = \frac{F_{HV}}{A_{HV}} = \frac{2 \cdot F_{HV} \cdot sin\left(\frac{136}{2}\right)}{L_{diag}^2} = 1.8544 \frac{F_{HV}}{L_{diag}^2} \tag{3.8}$$

Results show that puddled iron material extracted from Eiffel bridge is harder when compared to modern steels which means that ductility properties differ significantly. The level of scatter is also higher for this old metallic material which is related to its heterogeneous microstructure and abundant presence of non-metallic inclusions. S235 and S355 are within the same level of hardness and the standard deviation is small for both materials, however, S355 presents a higher

level of hardness showing that higher mechanical performance is associated with lower ductility in this case.

Figure 3.15. S235 sample used in hardness test.

Table 3.7. Summary of results from Vickers hardness test.

Material	F_{HV}	Time	HV	
	[kgf]	[s]	μ	σ
Eiffel bridge	1	20	212.5	5.2
S235	10	20	130.0	1.6
S355	1	20	186.7	1.0

3.3.2 Monotonic behaviour

The monotonic behaviour of Eiffel bridge material, S235 and S355 was characterized by means of experimental tests following the recommendations on ISO 6892-1 [107]. Three dog-bone specimens were produced for each material with the geometry described in Figure 3.16. Specimens used to characterize the monotonic properties of Eiffel bridge material were extracted from main structural elements of the bridge, namely the web of the girders, and loading direction is coincident with the rolling direction.

Tests were conducted under displacement control with a loading rate of 0.02 mm/s on a Servo Hydraulic Machine rated to 200 kN. Dog-bone specimens after the test are shown in Figure 3.17. A closer look on the fracture surface of puddled iron specimens, which can be observed in Figure 3.17b), reveals the heterogeneity of this material and a layered composition. In the case of S235 and S355, the fracture surface presented a homogeneous structure.
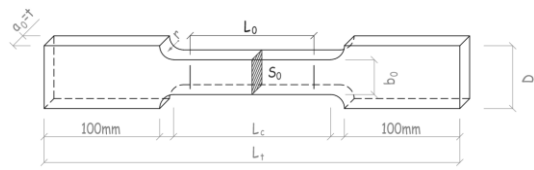
Material	a_0	b_0	L_0	L_c	L_t	D	r
Eiffel bridge	5	5	30	40	265	30	12.5
S235	4	5	25	30	150	21	12.0
S355	8	8	45	125	350	32	12.5

Dimensions in mm

Figure 3.16. Geometric parameters of dog-bone specimens used to characterize the monotonic behaviour of metallic materials.

a)

b)

c)

d)

Figure 3.17. Specimens after monotonic tensile testing: a) and b) Eiffel bridge material; c) S235; d) S355.

Stress-strain data was recorded to determine the Young's modulus E, the upper yield strength, R_{eH}, the tensile strength, R_m, and the percentage elongation after fracture A_f, as presented in Table 3.8. There are no significant changes in what concerns the Young's modulus of these three materials, since the average value is similar. However, it should be stated that the level of scatter for Eiffel bridge material is higher when compared to the other two materials. For yield and ultimate strength, it was verified that Eiffel bridge material is not significantly different when compared to S235, since slightly lower values were obtained. The most significant difference between puddled iron material and the two modern steels analysed in this study is in the value of the percentage elongation after fracture. While S235 and S355 presented values higher than 20%, Eiffel bridge material stand on 5%. This fact evidences the difference between

these materials in terms of ductility which was already observed from hardness tests. In fact, the microstructure heterogeneity, the significant presence of phosphorus in the chemical composition and the abundance of non-metallic inclusions originate a significant reduction on the deformation capacity of this material. When the results from S235 and S355 are compared with each other, it is observed that S355 has higher strength values but lower ductility capacity which results from the higher carbon percentage in the chemical composition.

Table 3.8. Experimental results from monotonic tensile tests.

Material	Specimen	E [GPa]	R_{eH} [MPa]	R_m [MPa]	A_f [%]
Puddled iron (Eiffel bridge)	1	181.5	302.0	351.8	4.0
	2	205.2	314.0	387.2	8.7
	3	227.0	303.0	345.6	3.3
	Average	204.6	306.3	361.5	5.4
S235	1	204.3	328.1	421.8	37.3
	2	205.8	321.8	434.3	34.7
	3	215.4	319.8	432.0	35.0
	Average	208.5	323.2	429.4	35.7
S355	1	203.3	452.7	608.4	20.5
	2	215.6	404.8	583.4	19.2
	3	199.4	398.2	592.3	22.2
	Average	206.1	418.6	594.7	20.6

3.3.3 Cyclic and fatigue behaviour

In this section, a data collection of low-cycle fatigue (LCF) tests performed with Eiffel bridge material, S235 and S355 is presented. The main goal is to characterize the cyclic stress-stress behaviour of these materials and analyse the fatigue performance using several damage parameters.

A statistical analysis of experimental data is implemented to present mean and characteristic values of relevant parameters aiming to establish reliable material models. Normal and Weibull distribution functions described in Section 2.5 were implemented to compute characteristic values considering a probability of failure of 5% and a confidence level of 75%.

3.3.3.1 Data collection

There is a set of experimental results in literature related to the characterization of cyclic elastoplastic behaviour of Eiffel bridge material, S235 and S355. This data was collected from Jesus *et al*. [104] for Eiffel bridge material, Carvalho *et al*. [108] for S235 and Jesus *et al*. [109] and Carvalho [110] for S355. All these experimental programmes were based on LCF tests with smooth specimens conducted according to ASTM E606 [34] recommendations under strain controlled conditions. Strain ratio was set to -1 and strain rate to 0.8%/s. The data collected from these experimental campaigns is presented in Table 3.9 showing the parameters of the stabilized cyclic curve for each specimen as well as the number of cyclic reversals when failure is achieved.

Table 3.9. Data collection from LCF tests on Eiffel bridge material, S235 and S355.

Material	Source	Specimen N°	ε_a [%]	ε_a^e [%]	ε_a^p [%]	σ_a [MPa]	σ_{max} [MPa]	$2N_f$
		1	0.500	0.188	0.31166	358.1	333.6	100
		2	0.400	0.184	0.21617	331.0	316.9	290
		3	0.375	0.188	0.18703	350.2	346.2	328
		4	0.375	0.194	0.18117	363.2	358.5	306
		5	0.350	0.182	0.16771	324.9	305.5	1 518
		6	0.300	0.182	0.11802	350.1	340.8	814
		7	0.250	0.179	0.07053	330.2	318.3	5 690
		8	0.250	0.179	0.07149	345.5	344.6	1 844
		9	0.250	0.180	0.07014	345.2	338.9	1 074
		10	0.250	0.170	0.07987	323.5	309.4	6 024
		11	0.200	0.170	0.02975	328.4	324.2	5 368
Puddled iron (Eiffel bridge)	Jesus *et al*. [104]	12	0.200	0.164	0.03650	316.4	303.5	1 162
		13	0.200	0.167	0.03268	318.7	310.0	11 394
		14	0.200	0.170	0.03006	319.5	322.0	8 308
		15	0.150	0.141	0.00862	281.3	270.8	160 562
		16	0.150	0.143	0.00684	289.2	293.4	98 920
		17	0.150	0.145	0.00512	267.9	255.8	160 240
		18	0.150	0.141	0.00946	274.0	275.1	40 020
		19	0.128	0.125	0.00310	233.4	233.0	137 004
		20	0.125	0.122	0.00332	231.9	231.6	137 822
		21	0.101	0.101	0.00019	208.6	208.5	1 368 228
		22	0.100	0.099	0.00117	204.2	230.9	1 708 192
		23	0.098	0.097	0.00078	192.8	193.2	385 588
		24	0.100	0.099	0.00149	199.8	183.7	2 000 000*
		25	0.094	0.094	0.00065	183.8	184.7	1 969 598
		26	0.094	0.093	0.00079	184.7	269.7	1 829 792

		27	0.083	0.083	0.00001	161.3	161.1	10 000 000*
S235	Carvalho *et al.* [108]	1	1.000	0.227	0.773	360.2	360.9	1 324
		2	1.000	0.214	0.786	416.7	417.0	528
		3	0.500	0.187	0.313	368.3	368.6	3 644
		4	0.500	0.173	0.327	353.5	354.8	6 044
		5	0.250	0.149	0.101	300.8	303.2	54 426
		6	0.250	0.155	0.095	297.2	300.2	38 792
		7	0.200	0.160	0.040	313.1	317.2	47 332
		8	0.200	0.143	0.057	275.0	313.7	15 250
		9	0.200	0.143	0.057	292.1	294.5	46 714
		10	0.150	0.129	0.021	262.6	287.7	104 402
		11	0.150	0.136	0.014	282.2	284.6	135 634
		12	0.125	0.123	0.002	250.9	251.2	3 031 488
S355	Carvalho [110]	1	1.000	0.235	0.765	419.6	420.4	882
		2	1.000	0.235	0.765	428.6	429.6	798
		3	0.500	0.200	0.300	365.7	367.7	5 684
		4	0.500	0.190	0.310	371.2	373.5	6 282
		5	0.375	0.175	0.200	342.2	344.9	21 840
		6	0.375	0.175	0.200	336.7	336.8	15 606
		7	0.250	0.145	0.105	292.0	293.4	73 208
		8	0.250	0.150	0.100	292.0	292.2	56 504
		9	0.200	0.130	0.070	284.2	287.9	29 912
		10	0.200	0.135	0.065	272.3	273.5	79 152
		11	0.150	0.120	0.030	261.7	280.2	162 036
		12	0.125	0.115	0.010	240.7	245.8	2 777 354
	Jesus *et al.* [109]	13	1.000	0.279	0.722	487.7	497.4	672
		14	1.000	0.287	0.714	484.1	482.4	1 084
		15	0.500	0.215	0.285	408.7	409.5	9 610
		16	0.500	0.182	0.319	331.8	329.8	4 018
		17	0.250	0.141	0.110	284.8	282.9	32 350
		18	0.200	0.154	0.047	307.7	311.1	59 002
		19	0.200	0.164	0.036	330.6	376.5	128 488
		20	0.175	0.150	0.026	290.8	292.7	556 486
		21	0.150	0.140	0.011	268.2	253.3	1 722 608

*Run-out

3.3.3.2   Cyclic behaviour

Cyclic stress-strain curve was defined using the Ramberg-Osgood expression described in Eq. (3.9) which relates strain and stress amplitude, ε_a and σ_a, respectively. Elastic and plastic strain amplitudes are identified as ε_a^e and ε_a^p, respectively. The strength coefficient K' and the strain-hardening exponent n' are found by means of a statistical analysis on the collected

stress-strain data. Results obtained for S235 and S355 will be compared with the values recommended in DNV-RP-C208 [93].

$$\varepsilon_a = \varepsilon_a^e + \varepsilon_a^p = \frac{\sigma_a}{E} + \left(\frac{\sigma_a}{K'}\right)^{\frac{1}{n'}} \tag{3.9}$$

The determination of strain hardening coefficient and exponent was made considering the stress amplitude and plastic strain amplitude of the stabilized curve for each test. By means of a linear regression analysis based on Eq. (3.10) using σ_a as dependent variable and ε_a^p as independent variable, mean curve was defined for each material – see Figure 3.19 – and strain hardening parameters are presented in Table 3.11. The coefficient of determination, R^2, for mean curves was found as 0.90, 0.80 and 0.78 for Eiffel bridge material, S235 and S355, respectively. These values are all close to one which means that the quality of this statistical analysis is high.

$$\sigma_a = K'\left(\varepsilon_a^p\right)^{n'} \tag{3.10}$$

Normal distribution function was applied to determine the upper and lower boundaries for strain hardening parameters – see results in Table 3.11. The one-sided tolerance limit $k_{5,75,v_{dg}}$ and the standard deviation $\hat{\sigma}$ are also presented.

Regarding the application of the two-parameter Weibull distribution, the relation between the cumulative probability, $P(Y)$, obtained for each data point with Bernard median rank (BMR) and the cumulative probability obtained with Weibull distribution using the estimation methods is presented in Figure 3.18. The values of the Weibull distribution parameters are presented in Table 3.10, as well as the values for each goodness-of-fit statistic test for each estimation method. Results shown that WLLSM is the best estimation method for Eiffel bridge material and S355 while LLSM is the best for S235.

In this sense, upper and lower boundary curves using Weibull distribution were defined based on the scale and shape parameters obtained with WLLSM method for Eiffel bridge material and S355 and with the scale and shape parameters obtained with LLSM for S235 – see Table 3.11.

Characteristic stress-strain curves based on normal and Weibull distribution functions are represented in Figure 3.19.

Table 3.10. Parameters of Weibull distribution and goodness-of-fit statistics of cyclic stress-strain data to determine **strain hardening parameters**.

Material	Method		LLSM	WLLSM	MLM	MM
Eiffel bridge	α_w		14.90	13.29	15.21	15.33
	β_w		1.04	1.04	1.04	1.04
	Goodness-of-fit	KS	0.078	0.068	0.084	0.086
		AD	0.333	0.321	0.357	0.368
		χ^2	0.192	0.257	0.197	0.200
S235	α_w		15.74	13.21	16.37	16.71
	β_w		1.03	1.03	1.03	1.03
	Goodness-of-fit	KS	0.161	0.109	0.169	0.177
		AD	0.371	0.381	0.397	0.421
		χ^2	0.190	0.307	0.190	0.196
S355	α_w		11.57	9.27	11.12	12.80
	β_w		1.05	1.04	1.05	1.05
	Goodness-of-fit	KS	0.142	0.140	0.139	0.145
		AD	0.724	0.624	0.658	1.013
		χ^2	0.425	0.873	0.451	0.411

Mean and characteristic stabilized cyclic stress-strain curves for Eiffel bridge material, S235 and S355 obtained from statistical analysis are presented in Figure 3.20, as well as the cyclic curve using the parameters proposed in DNV-RP-C208 [93] for S235 and S355 – see parameters in Table 3.11. For Eiffel bridge material, both normal and Weibull characteristic curves represent a consistent approach but a higher distance from experimental data is observed using Weibull distribution function. In this sense, the use of normal distribution function is recommended.

In what concerns results for S235 presented in Figure 3.20b), it is observed that characteristic curves using normal and Weibull distributions lead to very similar results. In this case, either normal or Weibull characteristic values of strain hardening parameter can be used as a reliable approach to predict the cyclic behaviour of this material. The curve proposed in the standard shows very distinct results from experimental evidences with significantly lower performance.

From Figure 3.20c) corresponding to S355, it can be stated that strain hardening parameters using normal distribution function should be implemented to obtain a reliable characteristic curve since Weibull distribution function led to lower compliance with experimental evidences. In the other hand, the proposal established in DNV-RP-C208 [93] represents a prediction similar to mean curve.

The values of the cyclic yield strength, σ_0', for these materials are also presented in Table 3.11 for mean, characteristic and standard curves. It was computed considering a strain amplitude of 0.2%.

a)

b)

c)
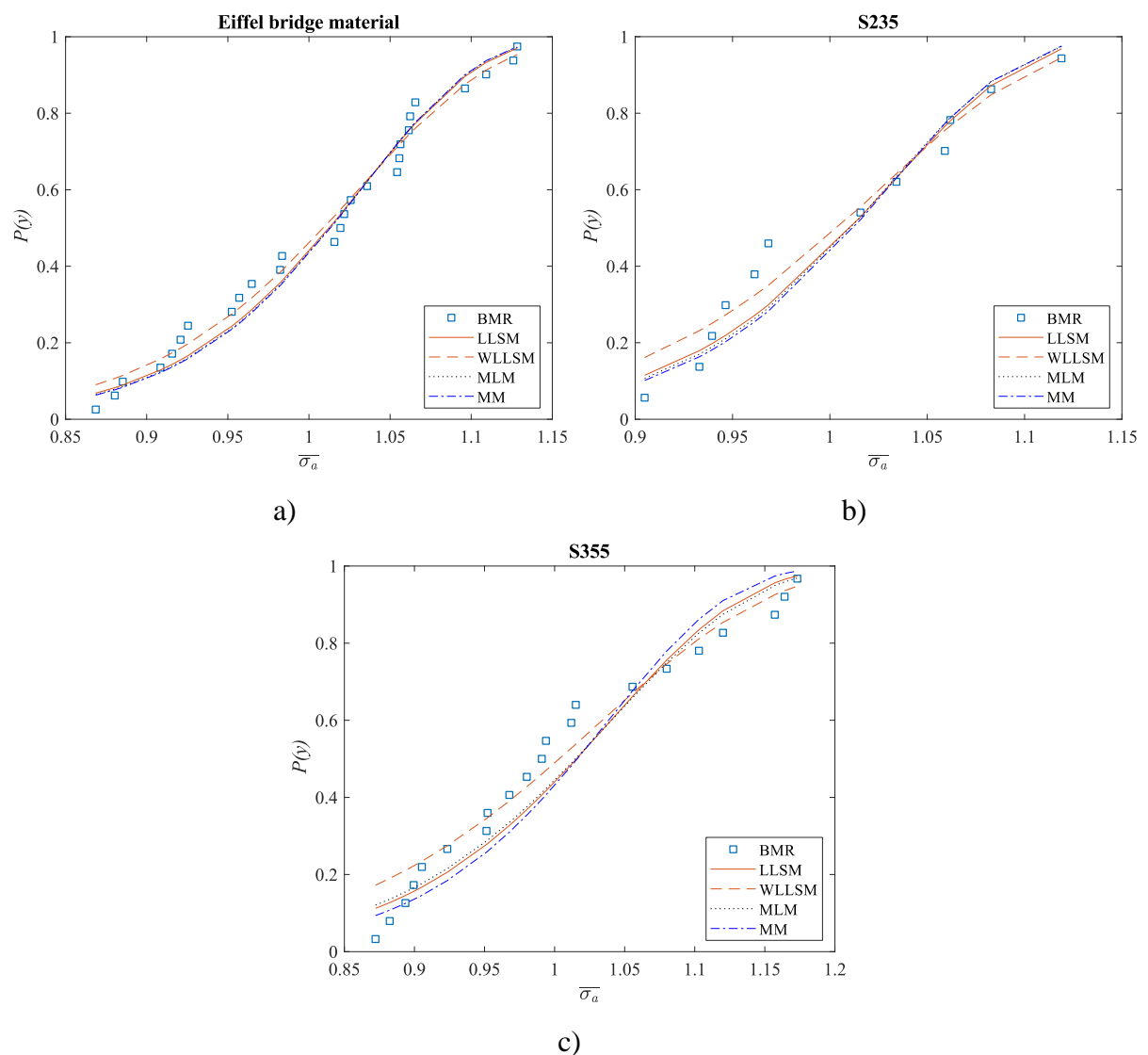
Figure 3.18. Comparison of cumulative Weibull distribution function of cyclic stress-strain data to determine **strain hardening parameters**: a) Eiffel bridge material; b) S235; c) S355.
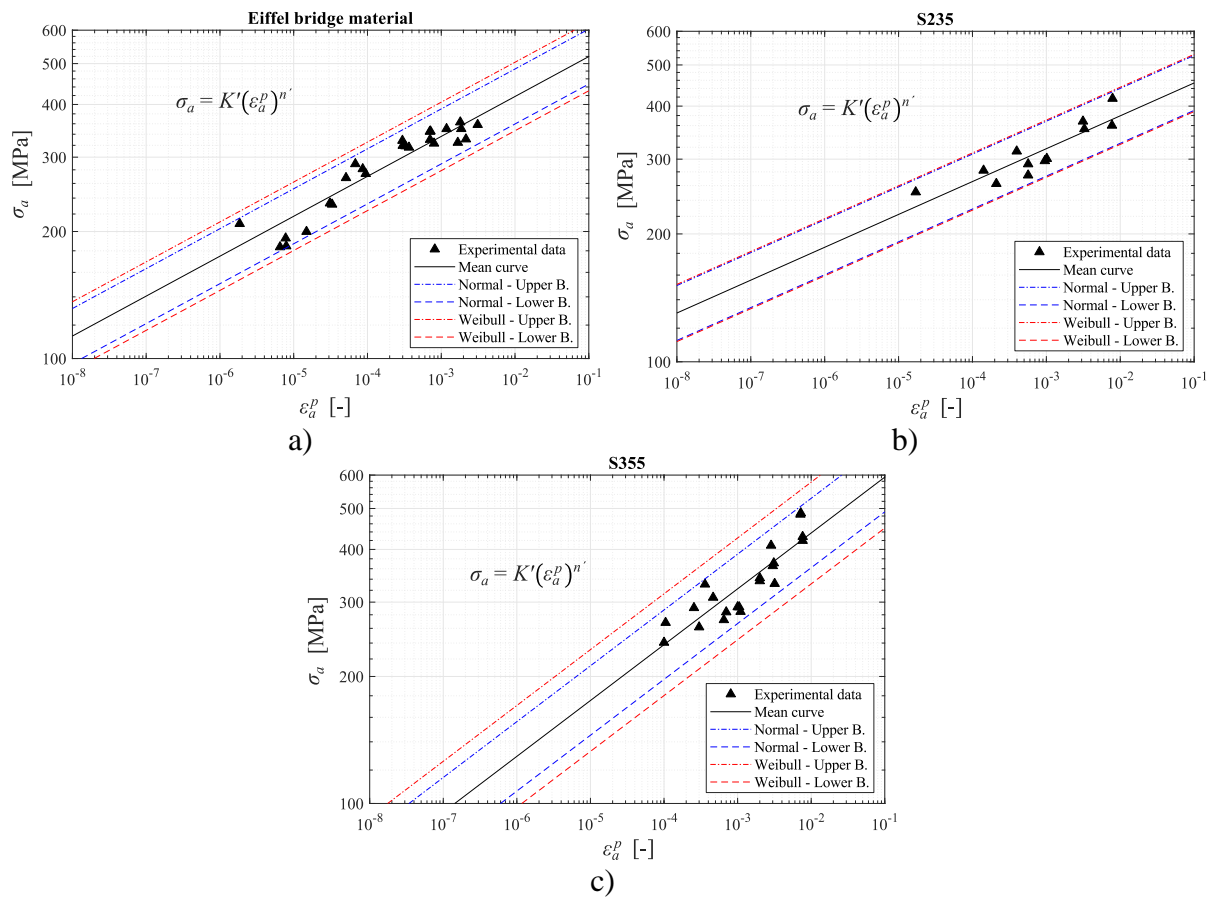
Figure 3.19. Statistical analysis of cyclic stress-strain data to determine **strain hardening parameters**: a) Eiffel bridge material; b) S235; c) S355.

Table 3.11. Strain hardening parameters for Eiffel bridge material, S235 and S355.

Material	Approach		σ'_0 [MPa]	K' [MPa]	n' [-]	R^2 [-]	$k_{5,75,v_{dg}}$ [-]	$\hat{\sigma}$ [-]	α_W [-]	β_W [-]
Eiffel bridge	Mean		314.8	645.9		0.90	-	-	-	-
	Normal	Upper B.	354.3	750.5	0.0946	-	1.89	0.035	-	-
		Lower B.	278.6	555.9						
	Weibull	Upper B.	359.9	778.6		-	-	-	13.29	1.04
		Lower B.	270.0	535.8						
S235	Mean		303.4	541.9		0.80	-	-	-	-
	Normal	Upper B.	341.5	628.9	0.0774	-	2.07	0.031	-	-
		Lower B.	267.0	466.9						
	Weibull	Upper B.	343.1	632.8		-	-	-	15.74	1.03
		Lower B.	265.5	464.0						
	DNV-RP-C208		275.4	410.0	0.1000	-	-	-	-	-
S355	Mean		299.7	804.6		0.78	-	-		
	Normal	Upper B.	342.0	972.4	0.1323	-	1.93	0.043	-	-
		Lower B.	257.9	665.8						
	Weibull	Upper B.	360.4	1062.1		-	-	-	9.27	1.04
		Lower B.	239.5	605.8						
	DNV-RP-C208		287.2	600.0	0.1000	-	-	-	-	-
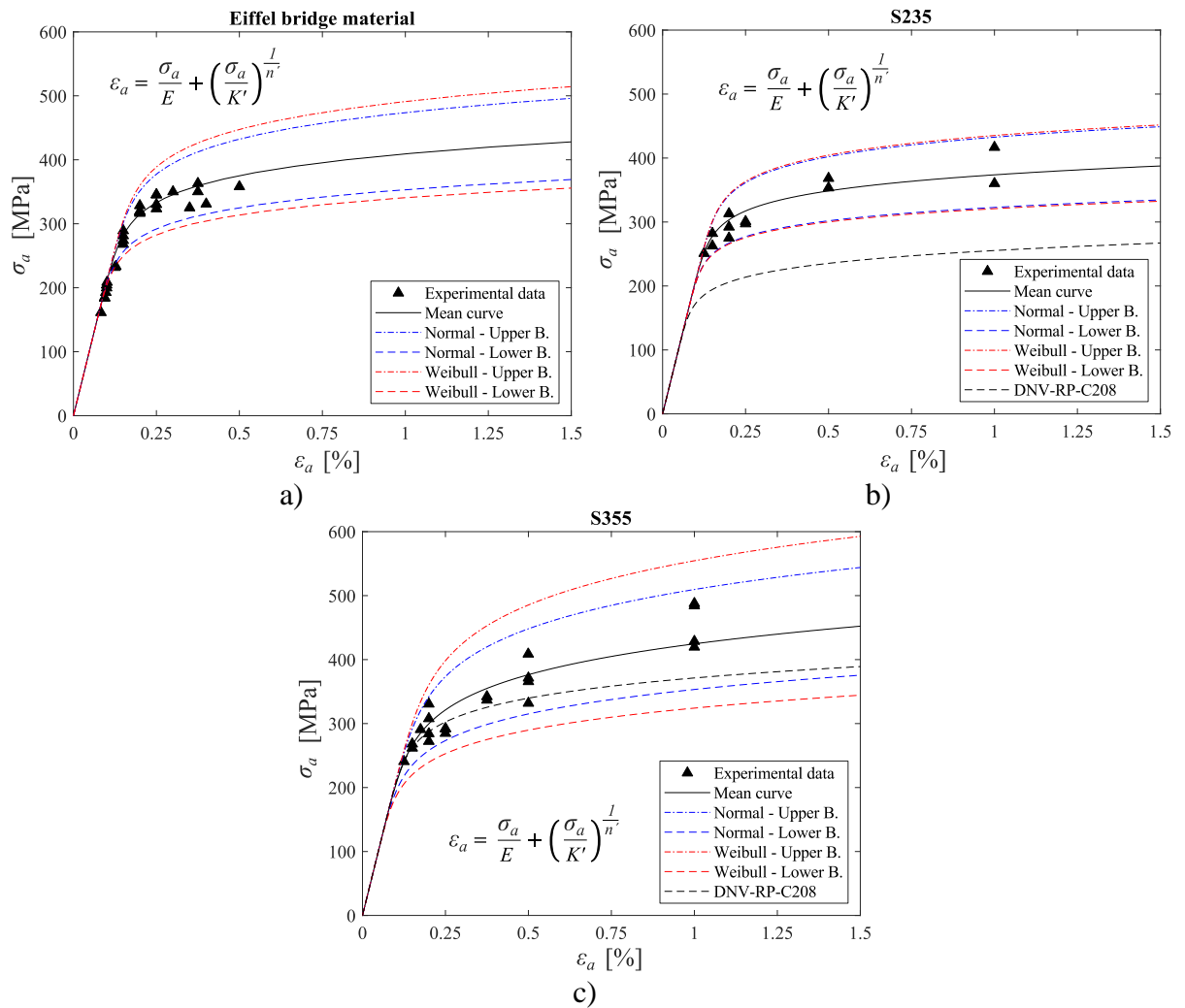
Figure 3.20. Mean and characteristic stabilized cyclic stress-strain curves: a) S235; b) S355; c) Eiffel bridge material.

Mean curves obtained for each material are now compared in Figure 3.21. It is verified that Eiffel bridge material has a superior performance for lower strain amplitudes when compared to the other two materials. It should be stated that the sample size for Eiffel bridge material is higher when compared to S235 and S355. Moreover, in this comparison the number of cycles to reach failure is not considered and, therefore, even if Eiffel bridge material present similar cyclic stress-strain curve when compared to modern steels, the number of cycles is considerably lower. LCF tests for Eiffel bridge material were performed for lower strain amplitudes when compared with values used in LCF tests for S235 and S355. There is a higher number of LCF tests for Eiffel bridge material performed with very small plastic strain amplitude. The highest strain amplitude used in LCF tests with Eiffel bridge material was $\varepsilon_a = 0.5\%$ in which the number of cycles at failure was $2N_f = 100$ while for S235 and S355 highest strain amplitude

was ε_a = 1.0% in which the minimum number of cycles at failure was $2N_f$ = 528. The elastoplastic cyclic behaviour of S355 is generally superior to S235, especially for higher values of strain amplitudes. This means that better monotonic performance is associated with improved cyclic stress-strain behaviour.

$$\varepsilon_a = \frac{\sigma_a}{E} + \left(\frac{\sigma_a}{K'}\right)^{\frac{1}{n'}}$$
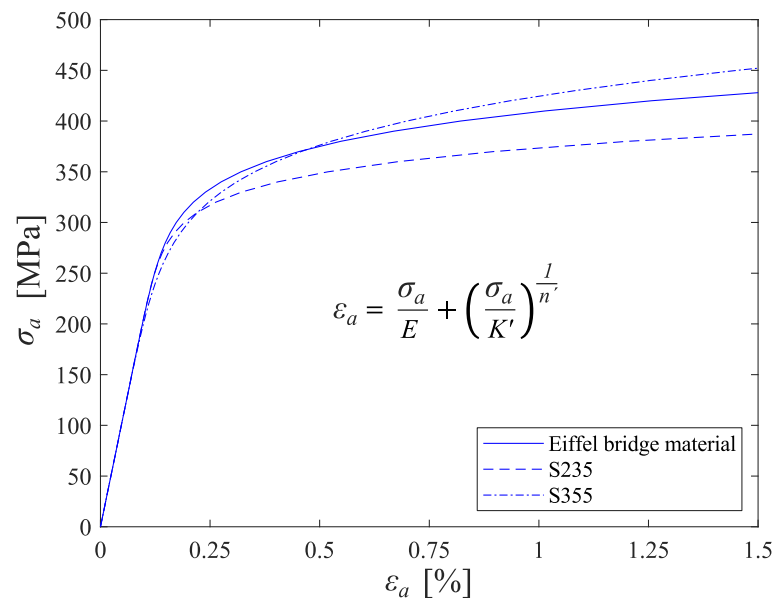
Figure 3.21. Comparison between mean cyclic stress-strain curves defined for Eiffel bridge material, S235 and S355.

3.3.3.3 Fatigue behaviour

Fatigue experimental data obtained for the three materials under study is now analysed in terms of fatigue life performance. Three types of fatigue damages are used: strain, strain energy (Huffman model) and SWT. Normal and Weibull distribution functions are implemented to determine characteristic fatigue life curves based on 5% probability of failure and 75% confidence level. Results obtained for strain-life damage parameter are compared with recommendations in DNV-RP-C208 [93]. This standard proposes a unique strain-life equation valid for both structural steels S235 and S355.

1) Strain-life damage parameter

In the following paragraphs, LCF experimental data obtained for Eiffel bridge material, S235 and S355 is analysed statistically to obtain mean and characteristic values of CMB strain-life fatigue model described in Section 2.3.3.2 and expressed in Eq. (3.11).

$$\varepsilon_a = \varepsilon_a^e + \varepsilon_a^p = \frac{\sigma_f'}{E}\left(2N_f\right)^b + \varepsilon_f'\left(2N_f\right)^c \qquad (3.11)$$

1.a) Elastic strain-life

The determination of fatigue strength coefficient, σ_f', and exponent, b, was made using the elastic component of the strain amplitude, ε_a^e, for each test. By means of a linear regression analysis based on Eq. (3.12) using ε_a^e as independent variable and $2N_f$ as dependent variable, mean curve for Eiffel bridge material, S235 and S355 was defined – see Figure 3.23 – and fatigue strength parameters are presented in Table 3.13. The coefficient of determination for mean curve was found as 0.87, 0.82 and 0.76 for Eiffel bridge material, S235 and S355, respectively.

$$\varepsilon_a^e = \frac{\sigma_f'}{E}\left(2N_f\right)^b \qquad (3.12)$$

Normal distribution function was applied to determine the characteristic values of the fatigue strength parameters – see Table 3.13. The one-sided tolerance limit $k_{5,75,v_{dg}}$ and the standard deviation $\hat{\sigma}$ are also presented.

The relation between the cumulative probability, $P(Y)$, obtained for each data point with BMR and the cumulative probability obtained with Weibull distribution function using estimation methods is presented in Figure 3.22. Considering these results, goodness-of-fit statistic tests were implemented, and results are shown in Table 3.12.

The estimation method that was used to determine the Weibull distribution parameters for Eiffel bridge material, S235 and S355 was the MLM method, since it is the estimation method that leads to higher correlation of BMR results. Fatigue strength parameters obtained with Weibull distribution are presented in Table 3.13. The characteristic curve using normal distribution function and the characteristic curve using Weibull distribution function were defined and the result is presented in Figure 3.23.

Table 3.12. Parameters of Weibull distribution and goodness-of-fit statistics of elastic strain-life data to determine **fatigue strength parameters**.

Material	Method		LLSM	WLLSM	MLM	MM
Eiffel bridge	α_w		1.05	0.90	0.98	0.90
	β_w		1.69	1.64	1.72	1.65
	Goodness-of-fit	KS	0.107	0.080	0.105	0.082
		AD	0.401	0.360	0.354	0.359
		χ^2	0.139	0.267	0.161	0.264
S235	α_w		1.11	0.94	1.06	0.92
	β_w		1.61	1.53	1.61	1.51
	Goodness-of-fit	KS	0.121	0.137	0.110	0.143
		AD	0.404	0.415	0.390	0.428
		χ^2	0.146	0.274	0.159	0.301
S355	α_w		0.93	0.72	0.82	0.69
	β_w		1.80	1.63	1.83	1.62
	Goodness-of-fit	KS	0.186	0.155	0.171	0.167
		AD	1.005	0.918	0.870	0.988
		χ^2	0.445	1.092	0.587	1.277
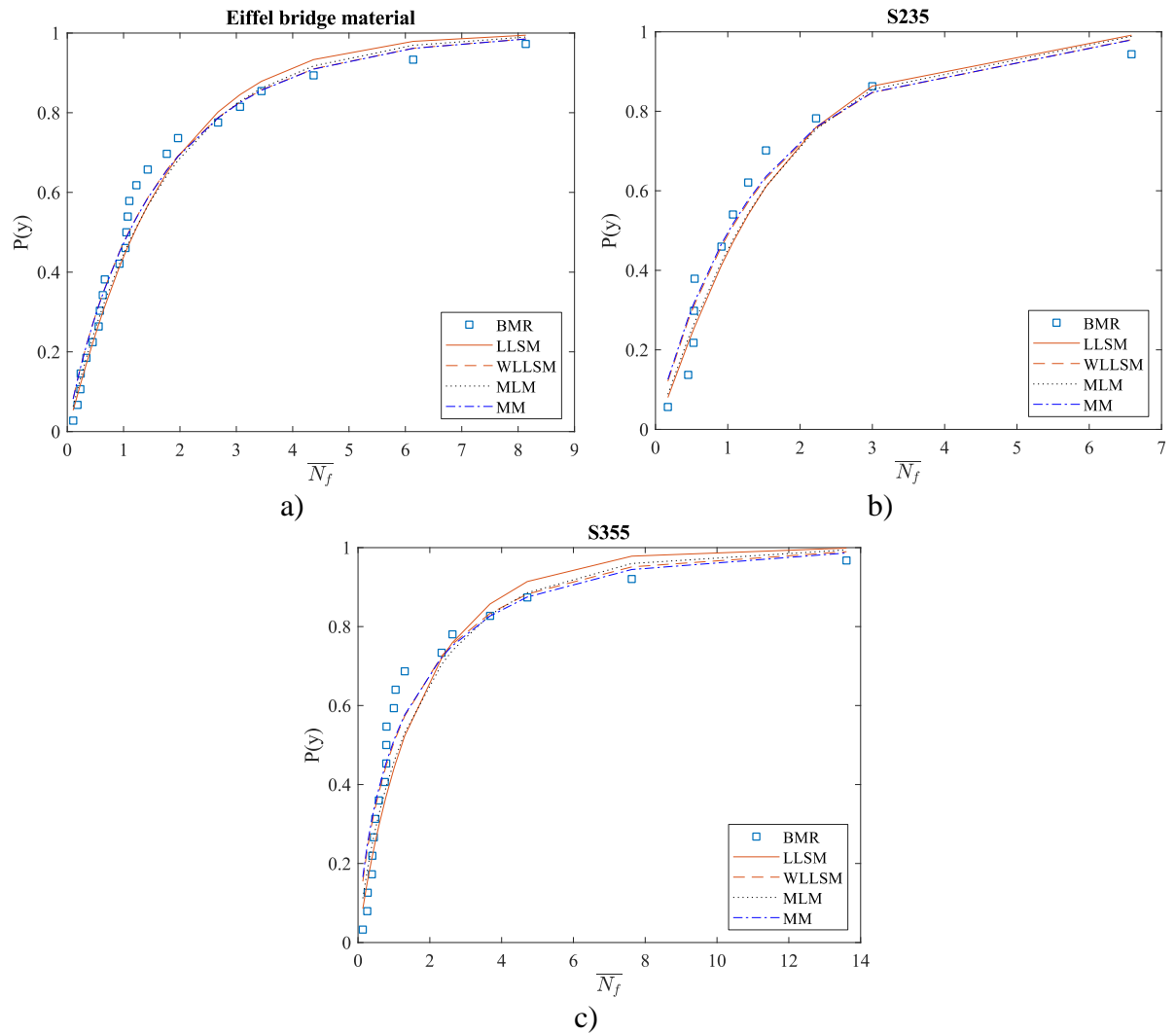
Figure 3.22. Comparison of cumulative Weibull distribution function of elastic strain-life data to determine **fatigue strength parameters**: a) Eiffel bridge material; b) S235; c) S355.
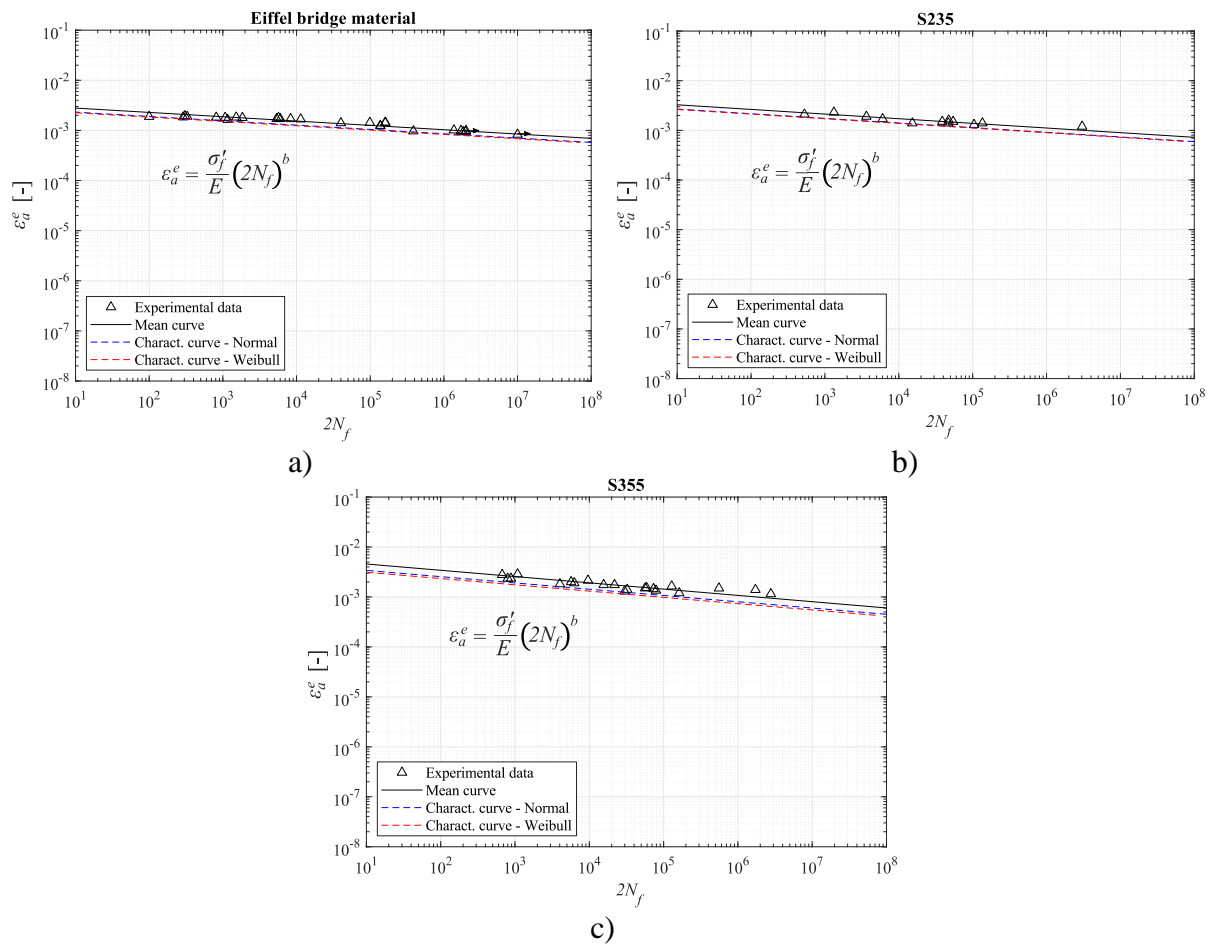
Figure 3.23. Statistical analysis of elastic strain-life data to determine **fatigue strength parameters**: a) Eiffel bridge material; b) S235; c) S355.

Table 3.13. Fatigue strength parameters for Eiffel bridge material, S235 and S355.

Material	Approach	σ'_f [MPa]	b [-]	R^2 [-]	$k_{5,75,v_{dg}}$ [-]	$\hat{\sigma}$ [-]	α_W [-]	β_W [-]
Eiffel bridge	Mean	714.6		0.87	-	-	-	-
	Charact. Normal	592.2	-0.086	-	1.90	0.49	-	-
	Charact. Weibull	576.1		-	-	-	0.98	1.72
S235	Mean	854.2		0.82	-	-	-	-
	Charact. Normal	696.9	-0.094	-	2.07	0.45	-	-
	Charact. Weibull	687.6		-	-	-	1.06	1.61
	DNV-RP-C208	175.0	-0.100	-	-	-	-	-
S355	Mean	1282.0		0.76	-	-		
	Charact. Normal	952.4	-0.126	-	1.93	0.53	-	-
	Charact. Weibull	876.2		-	-	-	0.82	1.83
	DNV-RP-C208	175.0	-0.100	-	-	-	-	-

1.b) Plastic strain-life

The determination of the fatigue ductility coefficient, ε'_f, and exponent, c, was made using the plastic component of the strain amplitude, ε^p_a, for each test. By means of a linear regression

analysis based on Eq. (3.13) using ε_a^p as independent variable and $2N_f$ as dependent variable, mean curve for Eiffel bridge material, S235 and S355 was defined – see Figure 3.25 – and fatigue strength parameters are presented in Table 3.15. The coefficient of determination, R^2, for mean curve was found as 0.93, 0.93 and 0.96 for Eiffel bridge material, S235 and S355, respectively, which is very close to one and assures that the quality of this statistical analysis is high. Normal distribution was applied to determine the characteristic values of the strain hardening parameters – see Table 3.15. The one-sided tolerance limit $k_{5,75,v_{dg}}$ and the standard deviation $\hat{\sigma}$ were also computed for each material.

$$\varepsilon_a^p = \varepsilon_f'\left(2N_f\right)^c \tag{3.13}$$

The relation between the cumulative probability, $P(Y)$, obtained for each data point with BMR and the cumulative probability obtained with Weibull distribution using the selected estimation methods is presented in Figure 3.24. The values of Weibull distribution parameters are presented in Table 3.14, as well as the values for each goodness-of-fit statistic test for each estimation method. It is verified from Table 3.14 that MM is the estimation method that led to more accurate results and, therefore, the characteristic curve for Weibull distribution function was defined using MM parameters. Final characteristic curves based on normal and Weibull distribution functions are presented in Figure 3.25.

Table 3.14. Parameters of Weibull distribution and goodness-of-fit statistics of plastic strain-life data to determine **fatigue ductility parameters**.

Material	Method		LLSM	WLLSM	MLM	MM
Eiffel bridge	α_w		1.40	1.25	1.39	1.35
	β_w		1.48	1.47	1.49	1.48
	Goodness-of-fit	KS	0.094	0.070	0.095	0.085
		AD	0.219	0.203	0.217	0.195
		χ^2	0.087	0.116	0.088	0.082
S235	α_w		1.81	1.51	1.72	1.61
	β_w		1.34	1.29	1.34	1.32
	Goodness-of-fit	KS	0.163	0.116	0.155	0.138
		AD	0.458	0.464	0.439	0.431
		χ^2	0.158	0.319	0.176	0.221
S355	α_w		2.45	2.16	2.43	2.4
	β_w		1.25	1.24	1.25	1.25
	Goodness-of-fit	KS	0.101	0.081	0.102	0.098
		AD	0.259	0.254	0.257	0.247
		χ^2	0.124	0.191	0.125	0.124
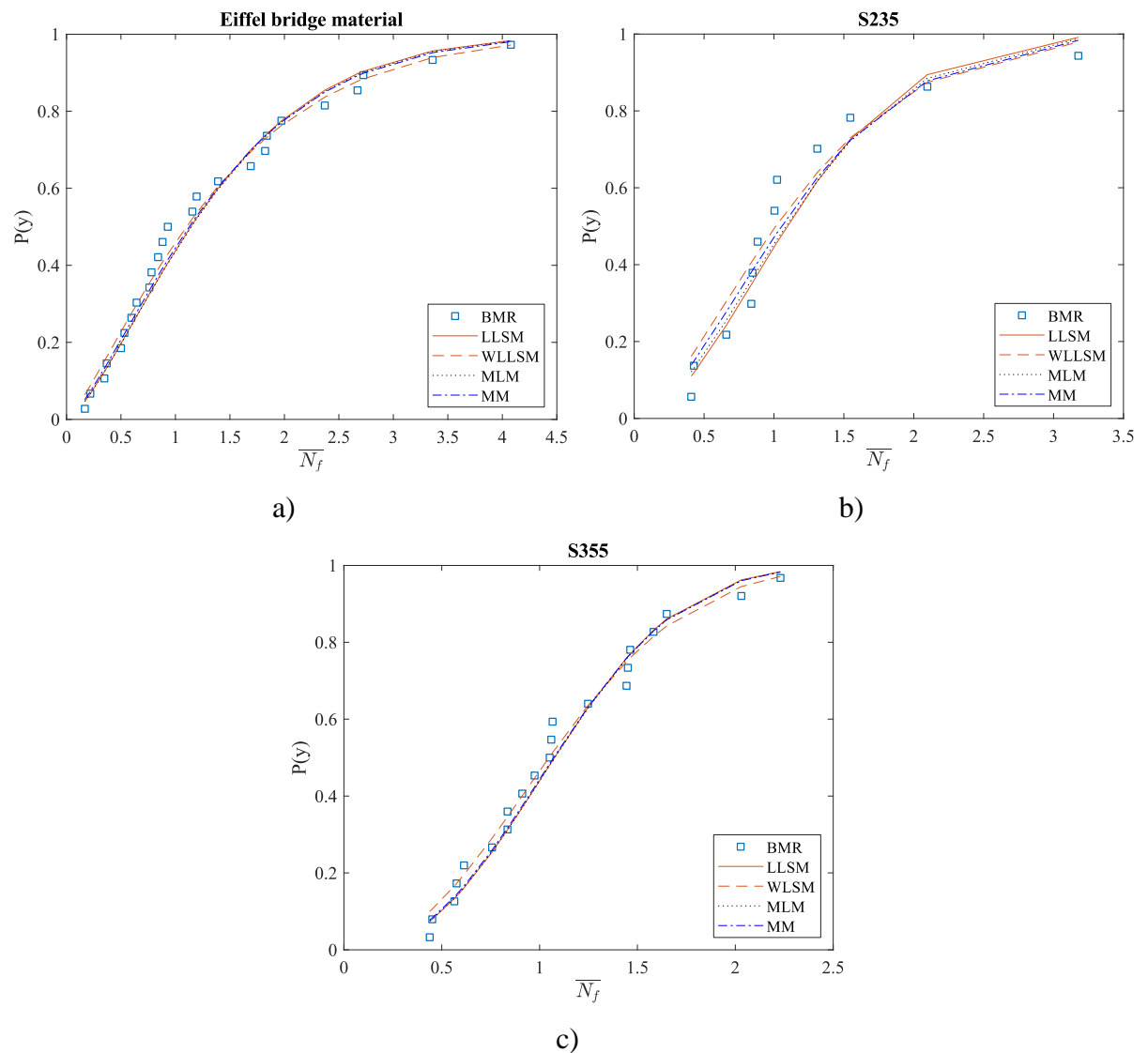
Figure 3.24. Comparison of cumulative Weibull distribution function of plastic strain-life data to determine **fatigue ductility parameters**: a) Eiffel bridge material; b) S235; c) S355.

Table 3.15. Fatigue ductility parameters for Eiffel bridge material, S235 and S355.

Material	Approach	ε'_f [-]	c [-]	R^2 [-]	$k_{5,75,v_{dg}}$ [-]	$\hat{\sigma}$ [-]	α_W [-]	β_W [-]
Eiffel bridge	Mean	0.177		0.93	-	-	-	-
	Charact. Normal	0.054	-0.721	-	1.90	0.37	-	-
	Charact. Weibull	0.048		-	-	-	1.35	1.48
S235	Mean	2.295		0.93	-	-	-	-
	Charact. Normal	0.804	-0.792	-	2.07	0.27	-	-
	Charact. Weibull	0.667		-	-	-	1.61	1.32
	DNV-RP-C208	0.091	-0.430	-	-	-	-	-
S355	Mean	0.426		0.96	-	-	-	-
	Charact. Normal	0.247	-0.578	-	1.93	0.21	-	-
	Charact. Weibull	0.236		-	-	-	2.41	1.25
	DNV-RP-C208	0.091	-0.430	-	-	-	-	-
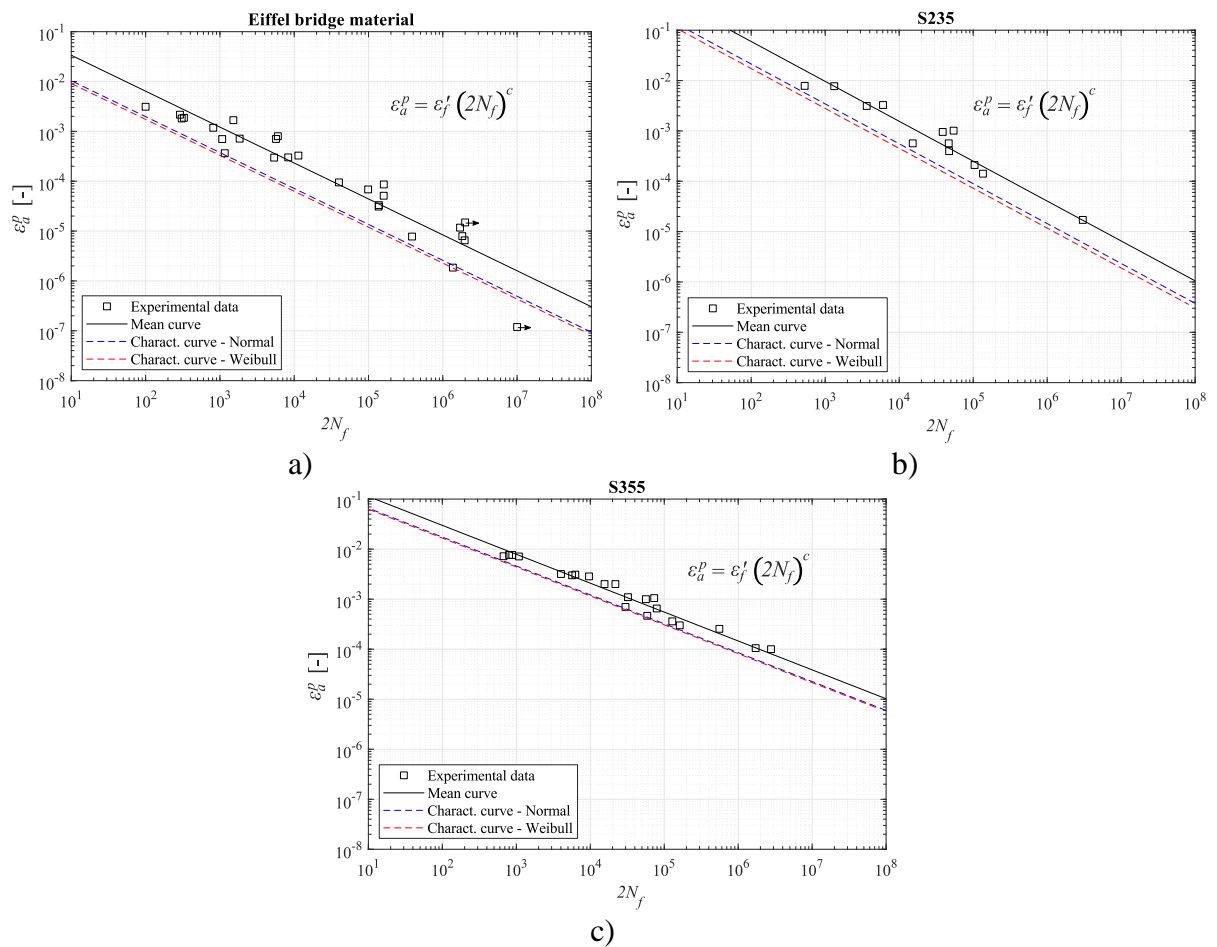
Figure 3.25. Statistical analysis of plastic strain-life data to determine **fatigue ductility parameters**: a) Eiffel bridge material; b) S235; c) S355.

1.c) Total strain-life

Total strain-life curve for Eiffel bridge material was computed using mean and characteristic values, as presented in Figure 3.26a). The transition point between elastic and plastic regimes is at $2N_f = 505$ considering the mean curve. It is evident that most of tests were performed under the main influence of elastic properties. If characteristic curves are considered, the transition point is at $2N_f = 105$ and $2N_f = 91$ for normal and Weibull distribution functions, respectively. Both statistical methods can be implemented, however using normal distribution function leads to results with a closer relation with experimental evidence.

Figure 3.26b) presents total strain-life curve obtained for S235 for both mean and characteristic values. For this material, the transition between elastic and plastic regimes occurs for $2N_f = 8\ 656$ in the mean curve (considerably higher when compared to the value found for Eiffel bridge material) and for characteristic curves $2N_f = 2\ 014$ and $2N_f = 1\ 501$ for normal

and Weibull distribution functions, respectively. Both normal and Weibull characteristic curves can be used as a reliable design prediction, however normal distribution function leads to higher strain-life performance, especially in plastic strain domain. The proposal made in DNV-RP-C208 [93] for strain-life of S235 whose parameters are presented in Table 3.15 is also compared with experimental data in Figure 3.26b). It is observed that it can be considered as a good design approach, specially until $2N_f = 10^5$ cycles. From this point beyond, it represents a very conservative method. In this standard curve, the transition between elastic and plastic strain domains occurs at $2N_f = 1\,501\,173$ cycles which is very distinct from the value obtained in experimental data.

a)   b)

c)
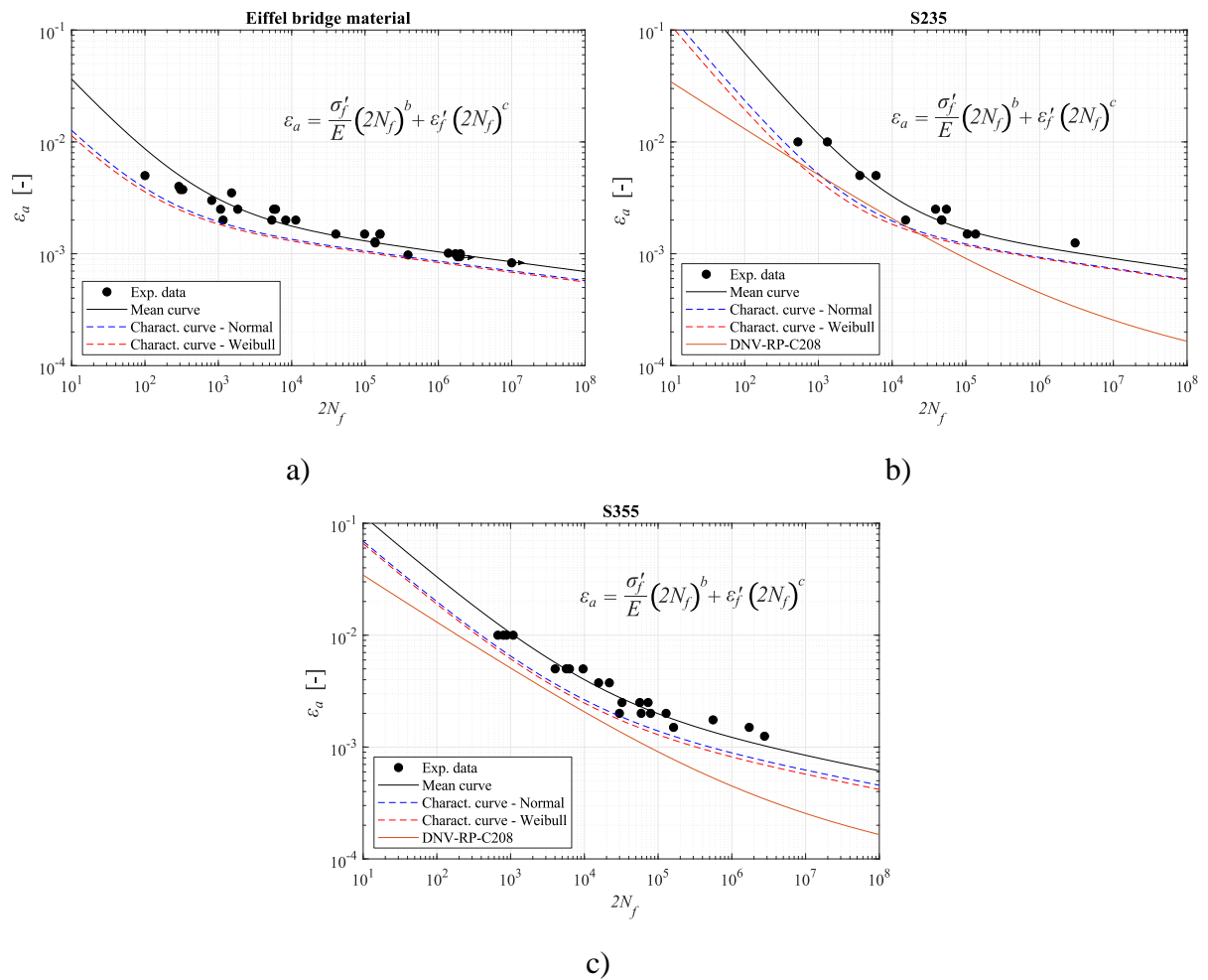
Figure 3.26. Mean and characteristic values for strain-life curves: a) Eiffel bridge material; b) S235; c) S355

Total strain-life curve for S355 was computed using mean and characteristic values, as presented in Figure 3.26c). Normal and Weibull distribution functions were implemented, and both can be considered as reliable design approaches, however the characteristic curve based in normal distribution function is recommended because it leads to a higher strain-life performance. The transition between elastic and plastic strain domain occurs at $2N_f = 12\ 022$ which means that both domains were relevant for this curve. This transition occurs at $2N_f = 6\ 958$ and $2N_f = 7\ 645$ for characteristic curves obtained with normal and Weibull distribution functions, respectively. Strain-life curve obtained with the parameters recommended in DNV [93] stands as a very conservative approach for S355.

1.d) Comparison

Characteristic curves obtained for each material are now compared in Figure 3.27. It is verified that strain-life performance of Eiffel bridge material is considerably inferior when compared to modern steels, especially for fatigue regimes under plastic domain. Strain-life behaviour of S355 is generally better when compared to S235 within the range of strain amplitude implemented in experimental tests. This fact indicates that improved fatigue life performance is achieved for materials with higher monotonic yield strength.
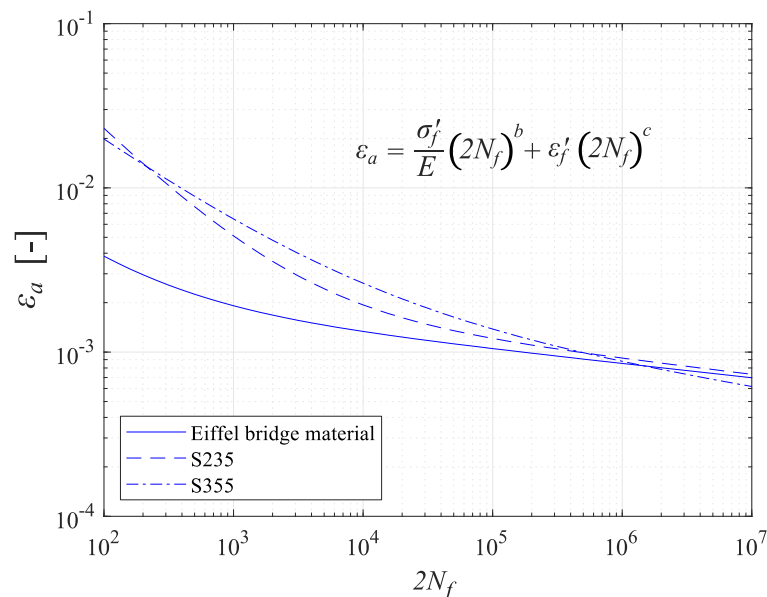
Figure 3.27. Comparison between characteristic strain-life curves defined for Eiffel bridge material, S235 and S355.

2) SWT-life damage parameter

Experimental LCF data was correlated with the SWT model [37] that uses the maximum stress σ_{max} and strain amplitude ε_a as damage parameters as described in the following equation. The parameters of this model were determined using a linear regression analysis on elastic and plastic components of strain amplitude.

$$SWT = \varepsilon_a \sigma_{max} = \frac{\left(\sigma'_{f,SWT}\right)^2}{E}\left(2N_f\right)^{2b_{SWT}} + \sigma'_{f,SWT}\varepsilon'_{f,SWT}\left(2N_f\right)^{b_{SWT}+c_{SWT}} \quad (3.14)$$

2.a) Elastic SWT-life

The determination of elastic SWT parameters was made using the elastic component of the strain amplitude, ε_a^e, and the maximum stress, σ_{max}, for each test. By means of a linear regression analysis based on Eq. (3.15) using $2N_f$ as dependent variable and SWT^e as independent variable, the mean curve for Eiffel bridge material, S235 and S355 was defined – see Figure 3.29 – and elastic SWT parameters are presented in Table 3.17. The coefficient of determination for mean curve, R^2, was found as 0.86, 0.91 and 0.77 for Eiffel bridge material, S235 and S355, respectively.

$$SWT^e = \varepsilon_a^e \sigma_{max} = \frac{\left(\sigma'_{f,SWT}\right)^2}{E}\left(2N_f\right)^{2b_{SWT}} \quad (3.15)$$

Normal distribution was applied to determine the characteristic values of elastic SWT-life parameters. The one-sided tolerance limit $k_{5,75,v_{dg}}$ and the standard deviation $\hat{\sigma}$ were also computed. For the application of Weibull distribution, the relation between the cumulative probability, $P(Y)$, obtained for each data point with BMR and the cumulative probability obtained with different estimation methods was computed as presented in Figure 3.28. Parameters of Weibull distribution are presented in Table 3.16, as well as the values for each goodness-of-fit statistic test for each estimation method. It was found that MM estimation method led to more accurate results for Eiffel bridge material and S355 while MLM estimation method was the best for S235. Characteristic curves using normal and Weibull distribution functions were defined and the result is presented in Figure 3.29 whose parameters are presented in Table 3.17.

Table 3.16. Parameters of Weibull distribution and goodness-of-fit statistics of **elastic SWT-life** data.

Material	Method		LLSM	WLLSM	MLM	MM
Eiffel bridge	α_w		0.99	0.88	0.98	0.95
	β_w		1.74	1.72	1.76	1.74
	Goodness-of-fit	KS	0.094	0.064	0.093	0.085
		AD	0.271	0.246	0.257	0.238
		χ^2	0.103	0.157	0.104	0.102
S235	α_w		1.54	1.26	1.40	1.21
	β_w		1.41	1.33	1.41	1.35
	Goodness-of-fit	KS	0.162	0.155	0.147	0.153
		AD	0.699	0.714	0.679	0.743
		χ^2	0.186	0.398	0.236	0.430
S355	α_w		0.95	0.73	0.88	0.82
	β_w		1.78	1.64	1.79	1.74
	Goodness-of-fit	KS	0.188	0.143	0.174	0.151
		AD	1.083	0.933	0.942	0.865
		χ^2	0.479	1.114	0.539	0.663
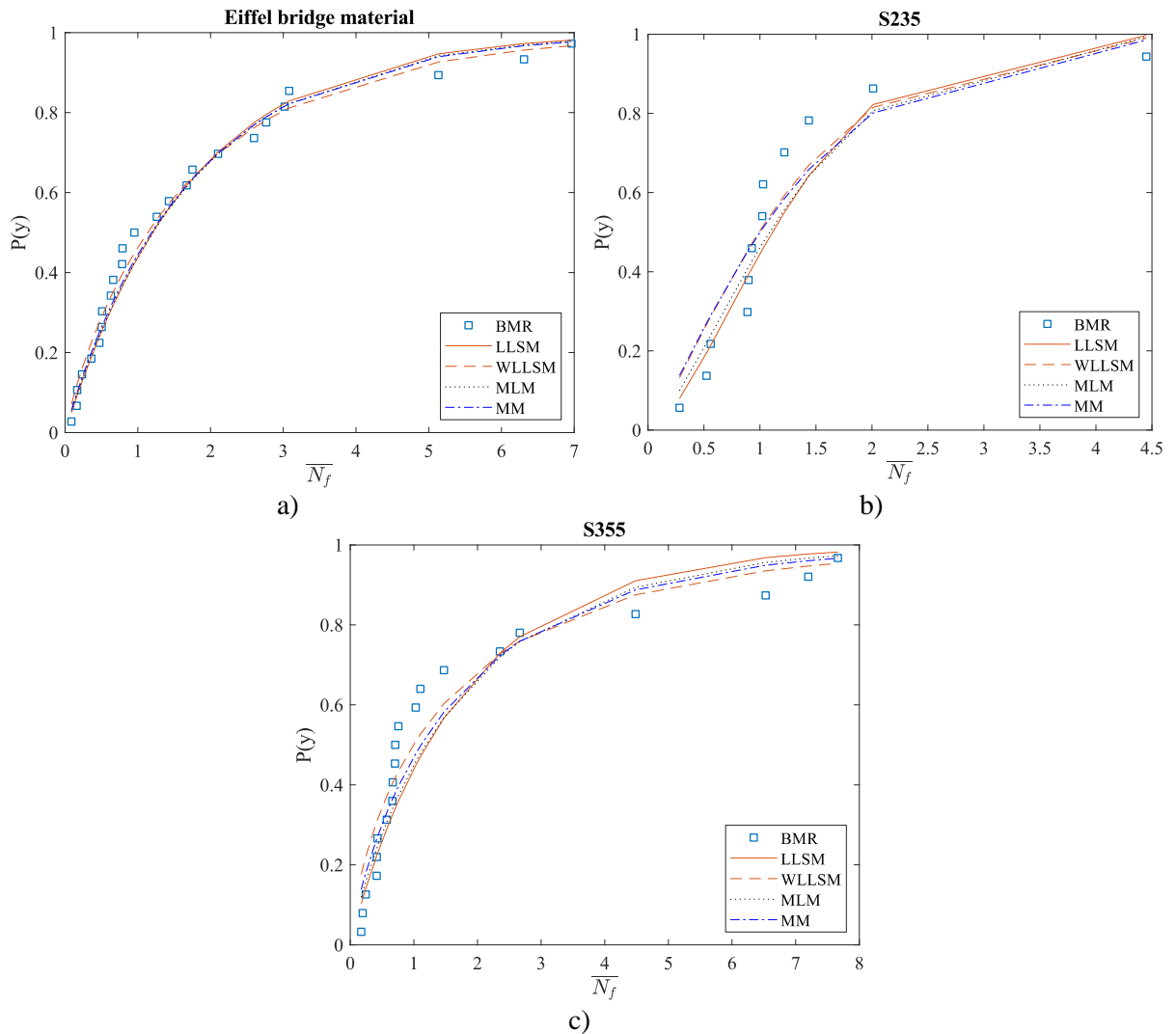
Figure 3.28. Comparison of cumulative Weibull distribution function of **elastic SWT-life** data: a) Eiffel bridge material; b) S235; c) S355.
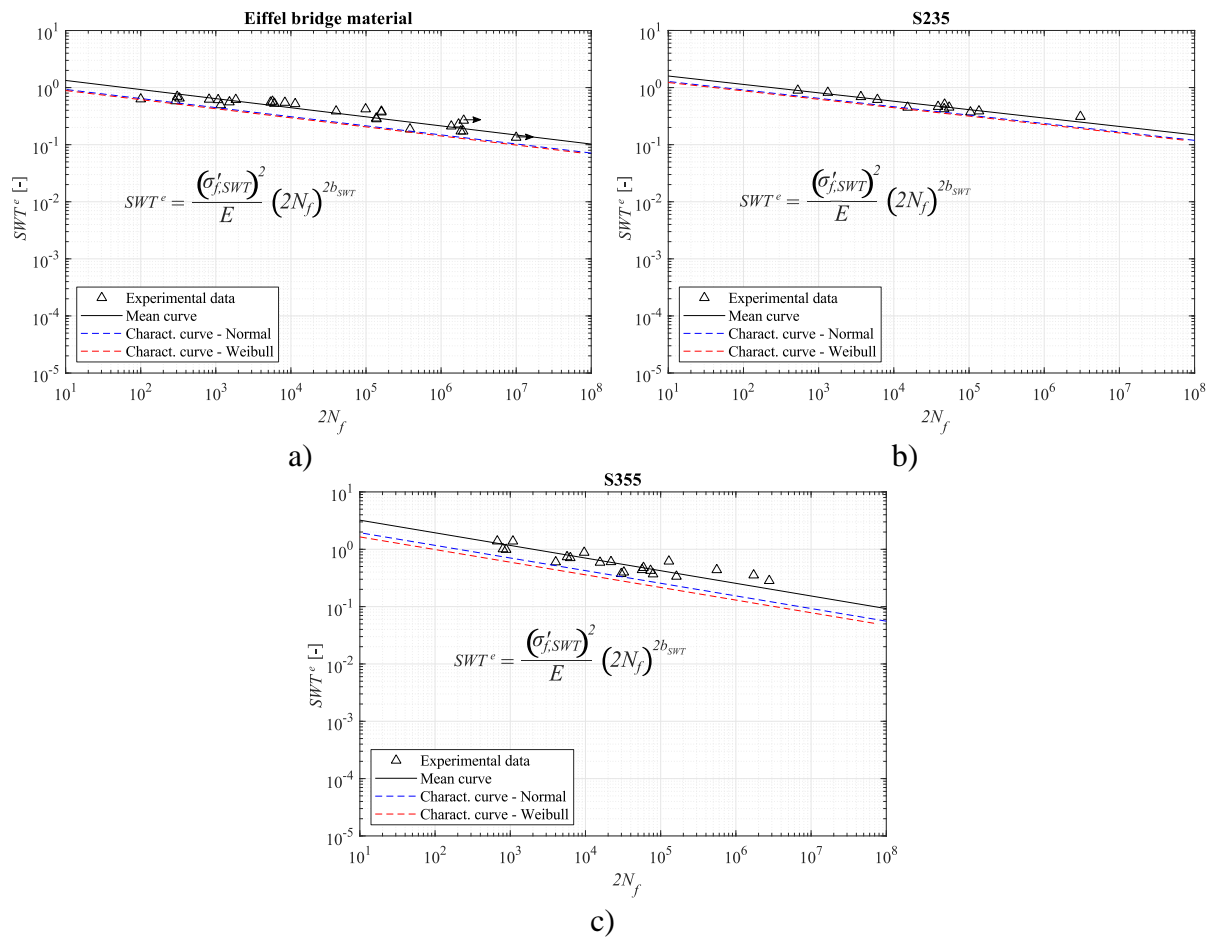
Figure 3.29. Statistical analysis of **elastic SWT-life** data: a) Eiffel bridge material; b) S235; c) S355.

Table 3.17. Elastic SWT-life parameters for Eiffel bridge material, S235 and S355.

Material	Approach	$\sigma'_{f,SWT}$ [MPa]	b_{SWT} [-]	R^2 [-]	$k_{5,75,v_{dg}}$ [-]	$\hat{\sigma}$ [-]	α_W [-]	β_W [-]
Eiffel bridge	Mean	635.5		0.86	-	-	-	-
	Charact. Normal	529.0	-0.080	-	0.13	0.52	-	-
	Charact. Weibull	518.4		-	-	-	0.95	1.74
S235	Mean	685.8		0.91	-	-	-	-
	Charact. Normal	613.8	-0.074	-	2.07	0.32	-	-
	Charact. Weibull	601.7		-	-	-	1.40	1.41
S355	Mean	1058.8		0.77	-	-	-	-
	Charact. Normal	823.1	-0.110	-	1.93	0.51	-	-
	Charact. Weibull	756.7		-	-	-	0.82	1.74

2.b) Plastic SWT-life

The determination of plastic SWT parameters was made using the plastic component of the strain amplitude, ε_a^p, and the maximum stress, σ_{max}, for each test. By means of a linear regression analysis based on Eq. (3.16), the mean curve for Eiffel bridge material, S235 and

S355 was defined – see Figure 3.31 – and plastic SWT parameters are presented in Table 3.19. The coefficient of determination for mean curve, R^2, was found as 0.93, 0.94 and 0.97 for Eiffel bridge material, S235 and S355, respectively. These values guarantee that the quality of this statistical analysis is high.

$$SWT^p = \varepsilon_a^p \sigma_{max} = \sigma'_{f,SWT} \varepsilon'_{f,SWT} \left(2N_f\right)^{b_{SWT}+c_{SWT}} \tag{3.16}$$

Normal distribution was applied to determine the characteristic values of plastic SWT parameters. The one-sided tolerance limit $k_{5,75,\nu_{dg}}$ and the standard deviation $\hat{\sigma}$ were also computed. The relation between the cumulative probability, $P(Y)$, obtained for each data point with BMR and the cumulative probability obtained with Weibull distribution using estimation methods is presented in Figure 3.30. The values of the Weibull distribution parameters are presented in Table 3.18, as well as the values for each goodness-of-fit statistic test for each estimation method. It was verified that MM estimation method should be used for Eiffel bridge material and S235 while WLLSM presented the best results for S355.

The characteristic curve obtained with normal and two-parameter Weibull distribution was then applied to the experimental data of Eiffel bridge material, S235 and S355 and the result is presented in Figure 3.31 whose parameters are shown in Table 3.19.

Table 3.18. Parameters of Weibull distribution and goodness-of-fit statistics of **plastic SWT-life** data.

Material	Method		LLSM	WLLSM	MLM	MM
Eiffel bridge	α_w		1.39	1.24	1.38	1.34
	β_w		1.48	1.47	1.49	1.48
	Goodness-of-fit	KS	0.077	0.066	0.077	0.066
		AD	0.257	0.242	0.253	0.229
		χ^2	0.118	0.169	0.120	0.118
S235	α_w		1.96	1.64	1.86	1.77
	β_w		1.31	1.27	1.31	1.30
	Goodness-of-fit	KS	0.1465	0.103	0.140	0.127
		AD	0.4379	0.444	0.420	0.412
		χ^2	0.1388	0.285	0.157	0.186
S355	α_w		2.61	2.32	2.63	2.61
	β_w		1.23	1.23	1.24	1.23
	Goodness-of-fit	KS	0.081	0.061	0.084	0.080
		AD	0.277	0.257	0.286	0.276
		χ^2	0.077	0.113	0.081	0.076

a)

b)

c)
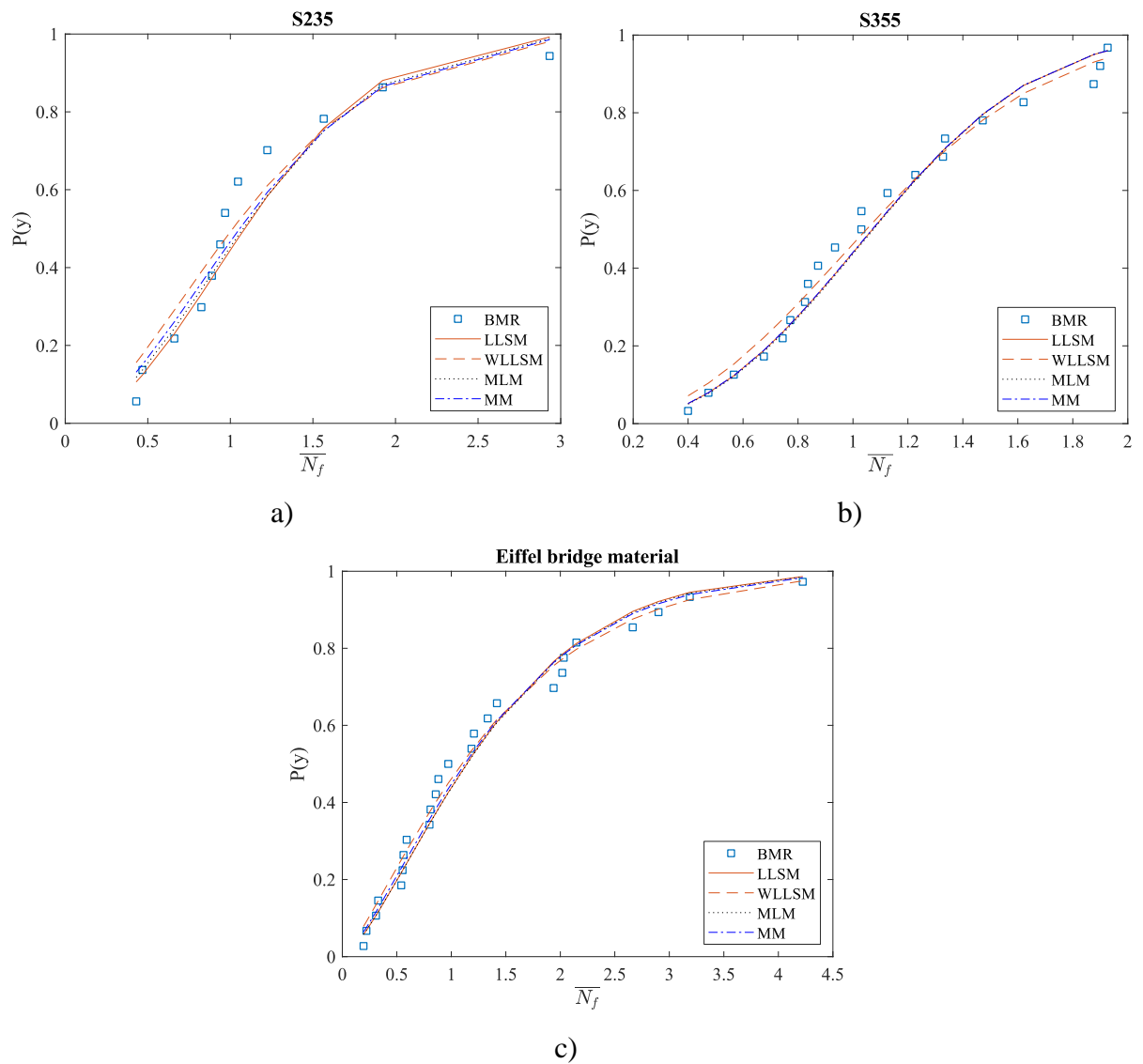
Figure 3.30. Comparison of cumulative Weibull distribution function of **plastic SWT-life data**: a) Eiffel bridge material; b) S235; c) S355.

Table 3.19. Plastic SWT-life parameters for Eiffel bridge material, S235 and S355.

Material	**Approach**	$\varepsilon'_{f,SWT}$ [-]	c_{SWT} [-]	R^2 [-]	$k_{5,75,v_{dg}}$ [-]	$\hat{\sigma}$ [-]	α_W [-]	β_W [-]
	Mean	0.146		0.93	-	-	-	-
Eiffel bridge	Charact. Normal	0.048	-0.707	-	1.90	0.37	-	-
	Charact. Weibull	0.043		-	-	-	1.34	1.48
	Mean	1.827		0.94	-	-	-	-
S235	Charact. Normal	0.740	-0.772	-	2.07	0.25	-	-
	Charact. Weibull	0.630		-	-	-	1.77	1.30
	Mean	0.287		0.97	-	-	-	-
S355	Charact. Normal	0.207	-0.542	-	1.93	0.20	-	-
	Charact. Weibull	0.199		-	-	-	2.32	1.23
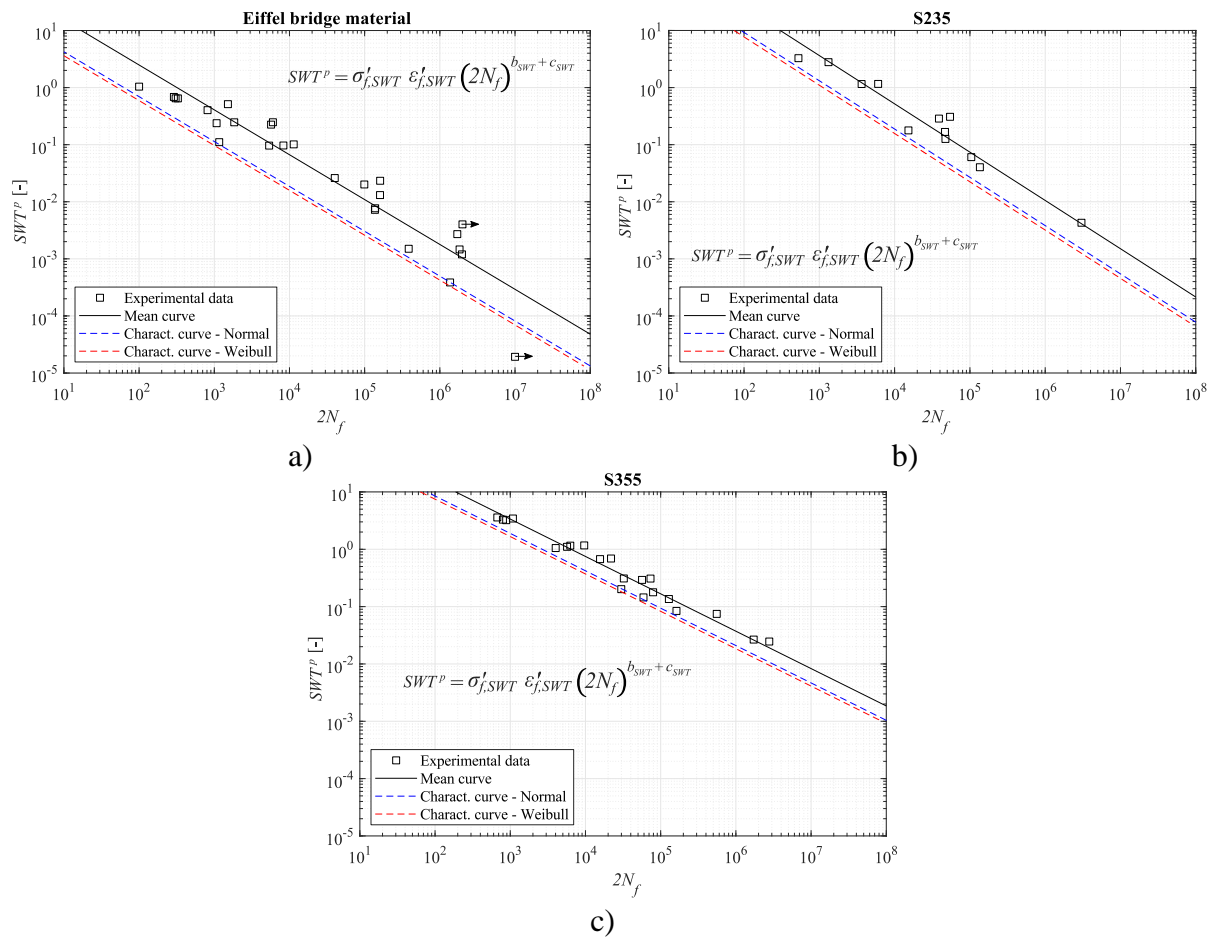
Figure 3.31. Statistical analysis of **plastic SWT-life data**: a) Eiffel bridge material; b) S235; c) S355.

2.c) Total SWT-life

Total SWT-life curve for Eiffel bridge material was computed using mean and characteristic values, as presented in Figure 3.32a). The transition point between elastic and plastic regimes is at $2N_f = 484$ considering the mean curve. It is evident that most of tests were performed under the main influence of elastic properties. If characteristic curves are considered, the transition point is at $2N_f = 110$ and $2N_f = 95$ for normal and Weibull distribution functions, respectively. Both statistical methods can be implemented, however using normal distribution function leads to results with a closer relation with experimental evidence.

Figure 3.32b) presents total strain-life curve obtained for S235 for both mean and characteristic values. For this material, the transition between elastic and plastic regimes occurs for $2N_f = 8\,642$ in the mean curve (considerably higher when compared to the value found for Eiffel bridge material) and for characteristic curves $2N_f = 2\,775$ and $2N_f = 2\,268$ for normal

and Weibull distribution functions, respectively. Both normal and Weibull characteristic curves can be used as a reliable design prediction, however normal distribution function leads to higher strain-life performance, especially in plastic strain domain.

Total strain-life curve for S355 was computed using mean and characteristic values, as presented in Figure 3.32c). Normal and Weibull distribution functions were implemented, and both can be considered as reliable design approaches, however the characteristic curve based in normal distribution function is recommended since it represents a higher SWT-life performance. The transition between elastic and plastic strain domain occurs at $2N_f = 11\ 566$ which means that both domains were relevant for this curve. This transition occurs at $2N_f = 9\ 723$ and $2N_f = 10\ 783$ for characteristic curves obtained with normal and Weibull distribution functions, respectively.
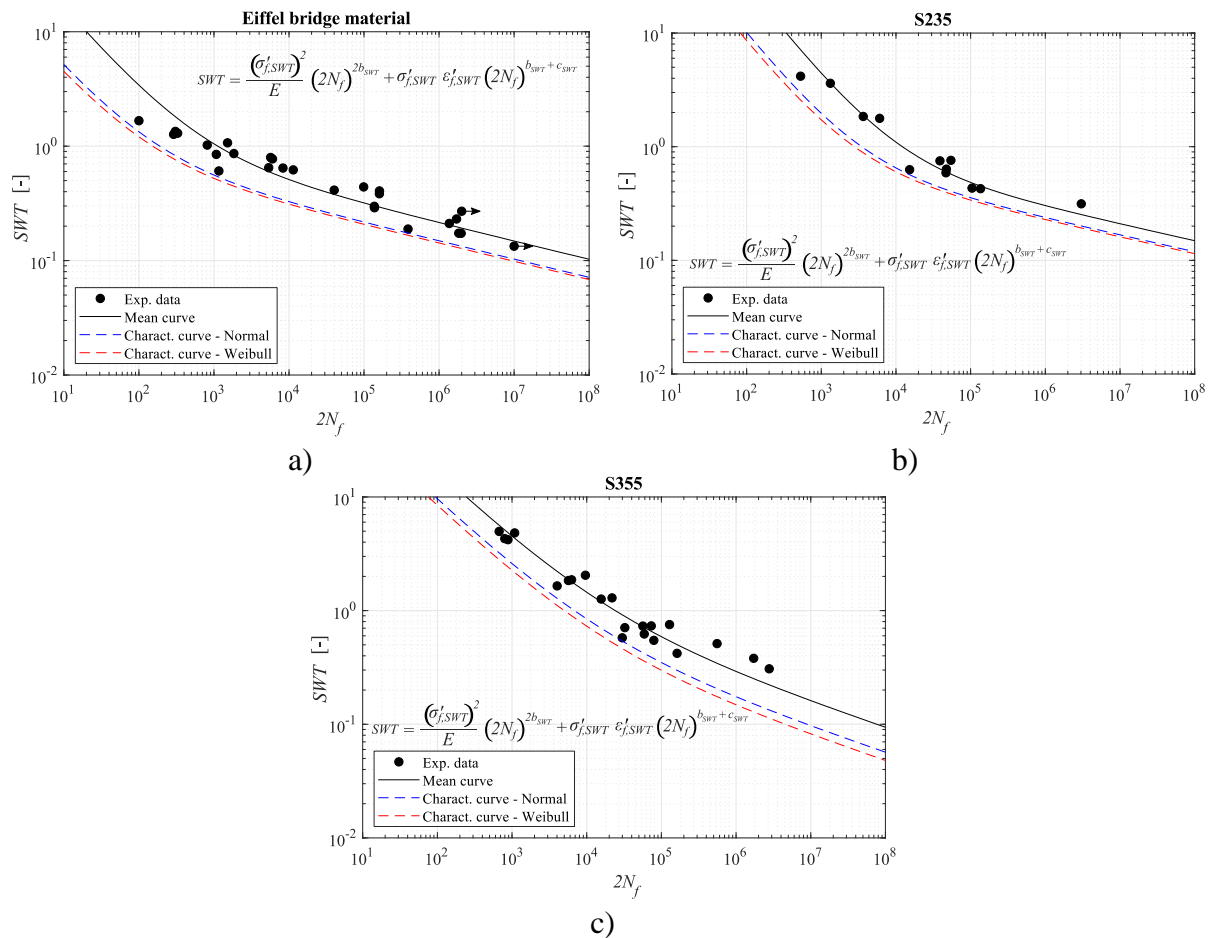
Figure 3.32. Mean and characteristic values for SWT-life curves: a) Eiffel bridge material; b) S235; c) S355.

2.d) Comparison

The characteristic curve obtained for each material is now compared in Figure 3.33. It is verified that SWT-life performance of Eiffel bridge material is considerably inferior when compared to modern steels within all the SWT range values. SWT-life behaviour of S355 is generally better when compared to S235, especially in plastic domain. For number of reversals superior to 10^5, S355 presents lower SWT-life performance when compared to S235, however it should be noted that for S235 the number of tests within these values of SWT is considerably low.

$$SWT = \frac{\left(\sigma'_{f,SWT}\right)^2}{E} \left(2N_f\right)^{2b_{SWT}} + \sigma'_{f,SWT}\ \varepsilon'_{f,SWT} \left(2N_f\right)^{b_{SWT}+c_{SWT}}$$
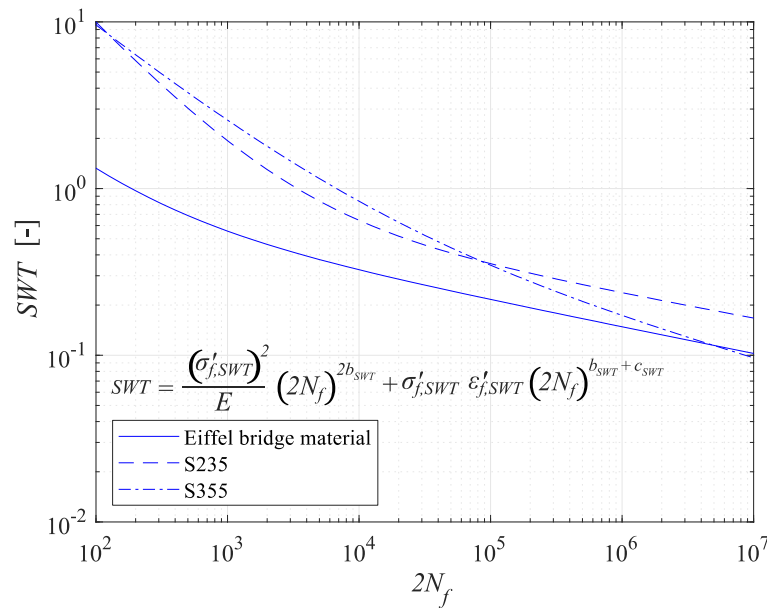
Figure 3.33. Comparison between characteristic SWT-life curves defined for Eiffel bridge material, S235 and S355.

3) Strain energy damage parameter

The implementation of Huffman [38] damage model expressed using the strain function presented in Eq. (2.17) is now analysed for the two non-alloy structural steels under study. The prediction of strain-life performance using Huffman model was made with dislocation density values obtained from XRD described in Section 3.2.2.2. The average, minimum and maximum value of dislocation density obtained from XRD were used to compute the fatigue strength and fatigue ductility parameters of strain-life relation using Equations (2.18), (2.19), (2.20) and (2.21) and results are presented in Table 3.20. The comparison between Huffman model prediction curves and experimental results is shown in Figure 3.34 and Figure 3.35 for S235 and S355, respectively. The relation between Huffman model predictions and LCF

experimental results was assessed by computing the mean squared error (MSE) considering the predicted and experimental value of number of reversals for each strain amplitude used in experimental campaign.

Within the dislocation density values obtained from XRD, the maximum value led to a lower mean squared error and better correlation with experimental results. Furthermore, the value of dislocation density that minimizes the mean squared error was found as 4.20E15 m^{-2} for S235 and 6.42E15 m^{-2} for S355. In both cases, the optimized value of dislocation density is very similar to the maximum value found by XRD which means that it can be used for reliable strain-life predictions.

Table 3.20. Huffman model parameters for S235 and S355 for different dislocation density values obtained with XRD.

Material	Dislocation density		$\sigma'_{f,Huffman}$	$b_{Huffman}$	$\varepsilon'_{f,Huffman}$	$c_{Huffman}$	MSE
	Approach	[m^{-2}]	[MPa]	[-]	[-]	[-]	[-]
S235	Average	2.74E15	562.5		1.619		0.217
	Min	1.32E15	513.1	-0.063	0.493	-0.812	1.070
	Max	4.36E15	596.4		3.448		0.094
	Optimized	4.20E15	593.6		3.243		0.089
S355	Average	3.32E15	749.5		0.585		0.606
	Min	1.04E15	604.8	-0.095	0.116	-0.716	2.798
	Max	6.36E15	852.2		1.544		0.127
	Optimized	6.42E15	853.8		1.566		0.124
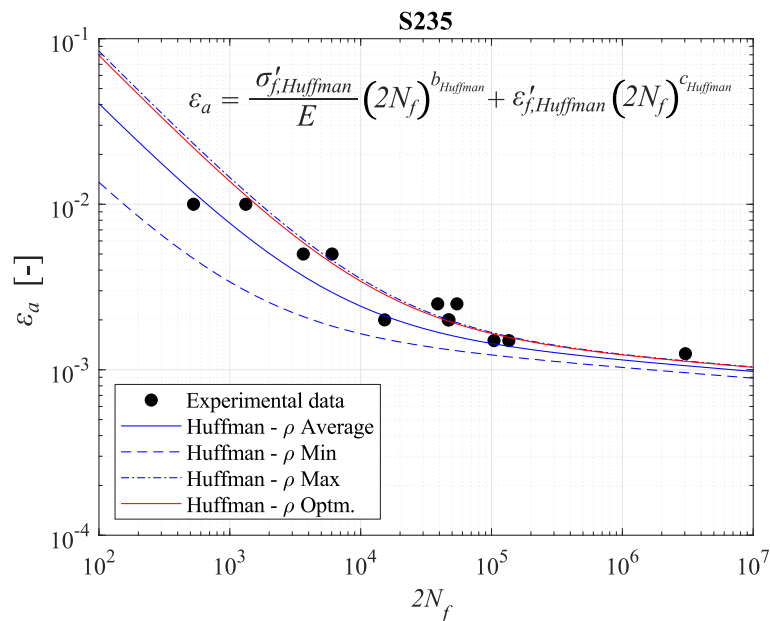
Figure 3.34. Huffman model prediction for S235 based on dislocation density values obtained from XRD.

$$\varepsilon_a = \frac{\sigma'_{f,Huffman}}{E}\left(2N_f\right)^{b_{Huffman}} + \varepsilon'_{f,Huffman}\left(2N_f\right)^{c_{Huffman}}$$
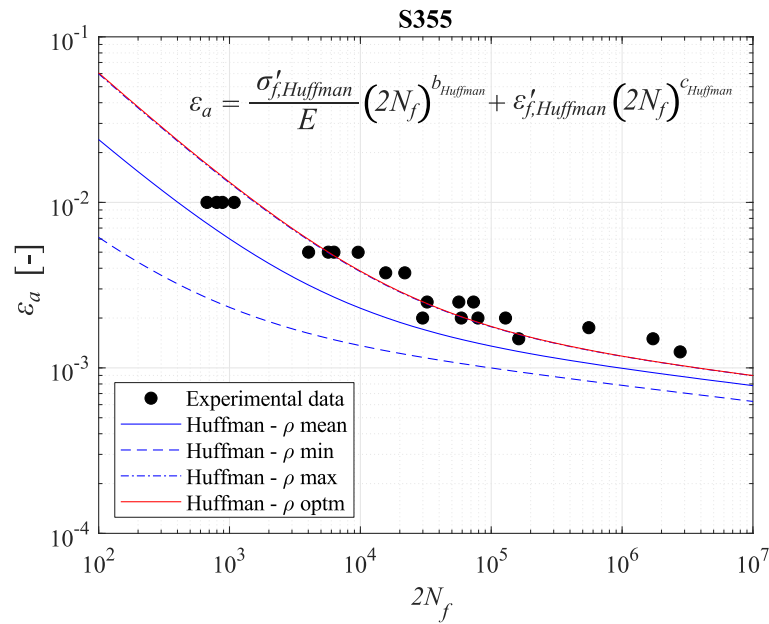
Figure 3.35. Huffman model prediction for S355 based on dislocation density values obtained from XRD.

3.3.4 Crack growth behaviour

3.3.4.1 Introduction

Paris and Erdogan [45] established the power function described in Eq. (3.17) to relate crack growth rate, da/dN, and stress intensity factor range, ΔK, where C and m are material parameters.

$$\frac{da}{dN} = C(\Delta K)^m \tag{3.17}$$

This law is used to describe the called Paris region in which experimental data follow a linear relation when using a logarithmic scale. In this chapter, the fatigue crack growth behaviour of Eiffel bridge material, S235 and S355 is investigated. A set of experimental data was collected for all these materials from literature and new experimental FCG tests were conducted for S235 and S355 aiming to propose reliable material laws based on experimental evidence.

Experimental data is compared with fatigue crack growth design curves for steels in non-aggressive environments proposed in BS 7910 [94]. This recommendation is valid for

steels (ferritic, austenitic or duplex ferritic austenitic) with yield or 0.2% proof strengths ≤ 700 MPa operating in air or other non-aggressive environments at temperatures up to 100ºC.

The design curve proposed in this standard is divided in two stages as presented in Figure 3.36, whose parameters are described in Table 3.21. While Stage B can be directly related with Paris region, Stage A establish the region in which fatigue crack growth is influenced by threshold value. The effect of stress ratio, R_σ, is considered by proposing an FCG design curve for stress ratio lower than 0.5 and another for stress ratio higher than 0.5. It should be also stated that these design curves were defined by shifting the mean curve within a distance of two times the standard deviation ($2\hat{\sigma}$).
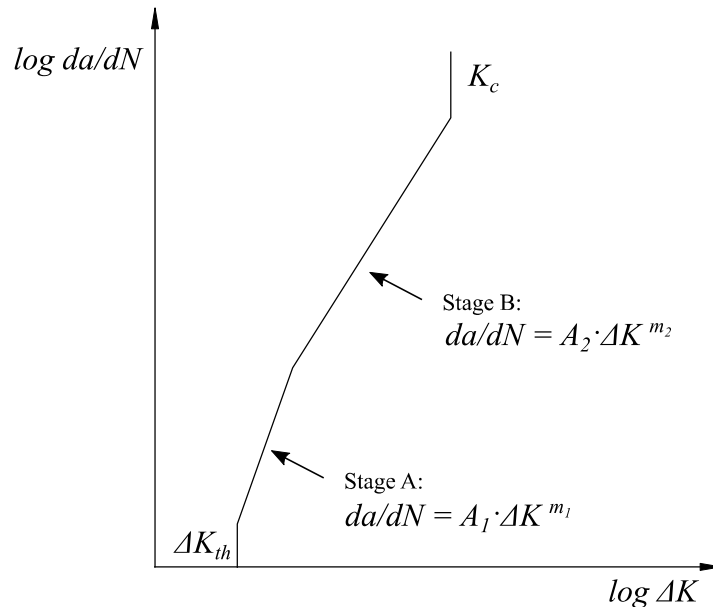
Figure 3.36. Fatigue crack growth design law proposed in BS 7910 [94].

Table 3.21. Design FCG curves for steel in air proposed in BS 7910 [94].

R_σ	Stage A		Stage B		Transition point ΔK [MPa.m$^{0.5}$]	Threshold ΔK_{th} [MPa.m$^{0.5}$]
	$C*$	m	$C*$	m		
<0.5	7.59E-14	8.16	1.41E-8	2.88	9.96	1.99
≥0.5	9.38E-10	5.10	2.70E-8	2.88	4.55	$5.38 - 6.77R_\sigma$

*da/dN [mm/cycle] and ΔK [MPa.m$^{0.5}$]

3.3.4.2 Eiffel bridge material

Fatigue crack propagation tests on Eiffel bridge material were performed by Jesus *et al.* [104] using CT specimens in accordance with the procedure described on ASTM E647 [44] under

load control conditions. The geometry of specimens was defined by W_{CT} (width) = 50 mm and B_{CT} (thickness) = 12 mm. Three specimens were tested under stress ratio $R_\sigma = 0.1$ and two specimens were tested under stress ratio $R_\sigma = 0.5$. Frequency was set to 20 Hz. CT specimens were extracted from the web and from the angle presented in Figure 3.37.

Figure 3.37. Structural elements extracted from the Eiffel bridge [13].

Mean FCG curve obtained with linear regression analysis of experimental data can be observed in Figure 3.38 and Figure 3.39 for $R_\sigma = 0.1$ and $R_\sigma = 0.5$, respectively. Material constants are presented in Table 3.22. The coefficient of determination, R^2, for mean curves was found as 0.86 and 0.96, which means that the quality of this statistical analysis is high.

Even if puddled iron materials are out of the scope of the standard BS 7910 [94], a comparison is established in order to evaluate how distinct is the FCG behaviour of puddled iron from structural steels. It is verified that the slope (m = 5.06 for $R_\sigma = 0.1$ and m = 5.53 for $R_\sigma = 0.5$) obtained with experimental data differs significantly from the slope proposed in the standard (m = 2.88). There is also a significant amount of data that is above the standard FCG design curve when stress intensity factor range is higher than 20 MPa.m$^{0.5}$ in both stress ratios which means that a crack can growth faster than the value predicted in the standard. In this sense, the prediction presented in this standard is unsafe for this material and new design curves should be presented.

Two characteristic FCG curves for each stress ratio were defined. One based on the approach proposed in BS 7910 [94] (sifting the mean curve by $2\hat{\sigma}$) and the other based on shifting the mean curve by $3\hat{\sigma}$. As it is observed in Figure 3.38 and Figure 3.39, for both for $R_\sigma = 0.1$ and for $R_\sigma = 0.5$, the characteristic curve defined based on the approach of the standard leads to unsafe predictions since there are experimental values above it. In the other hand, shifting the mean curve by $3\hat{\sigma}$ leads to reliable and safe predictions.
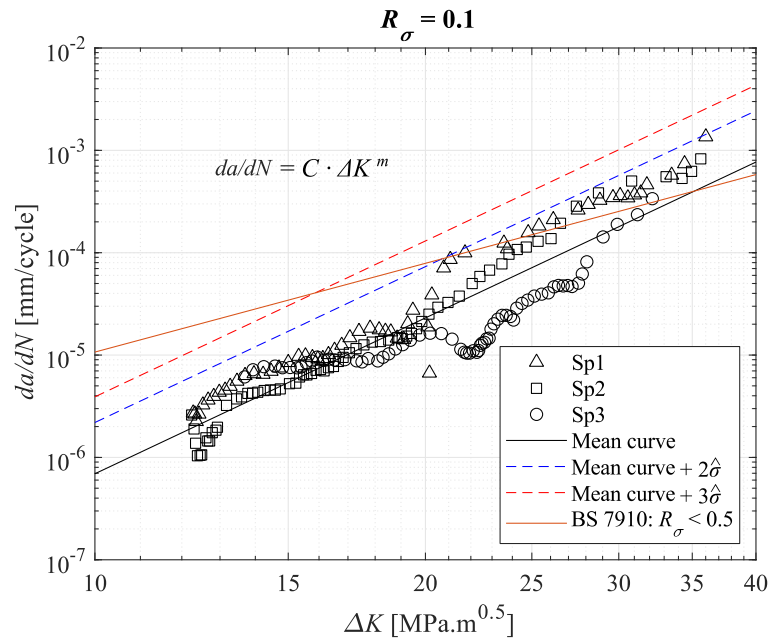
Figure 3.38. Statistical determination of FCG behaviour of **Eiffel bridge material**: $R_\sigma = 0.1$.
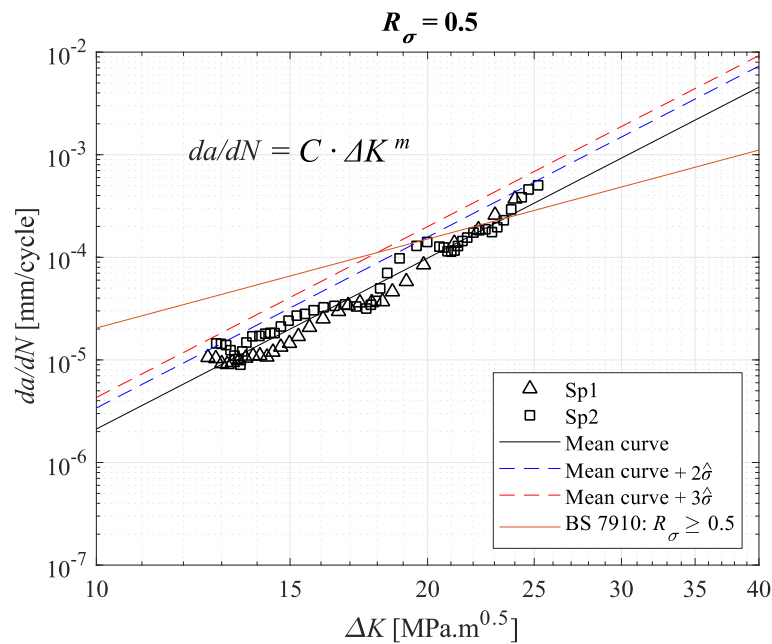
Figure 3.39. Statistical determination of FCG behaviour of **Eiffel bridge material**: $R_\sigma = 0.5$.

The influence of stress ratio is analysed in Figure 3.40 by comparing mean and characteristic curves obtained for stress ratio 0.1 and stress ratio 0.5. It is found that FCG of Eiffel bridge material is affected by the mean stress value, especially within higher values of the stress intensity factor range. The velocity of crack propagation is reduced for positive stress ratios closer to zero. However, due to the high level of scatter of results, especially for $R_\sigma = 0.1$,

additional FCG should be performed to further validate the mean stress effect on Eiffel bridge material.

Table 3.22. FCG parameters obtained for Eiffel bridge material using statistical analysis.

Stress ratio	Statistical	C^*	m	R^2	$\hat{\sigma}$
	Mean curve	6.05E-12		0.86	-
0.1	Mean curve + $2\hat{\sigma}$	1.92E-11	5.06	-	0.25
	Mean curve + $3\hat{\sigma}$	3.41E-11		-	0.25
	Mean curve	6.20E-12		0.96	-
0.5	Mean curve + $2\hat{\sigma}$	9.93E-12	5.53	-	0.10
	Mean curve + $3\hat{\sigma}$	1.26E-11		-	0.10

*da/dN [mm/cycle] and ΔK [MPa.m$^{0.5}$]
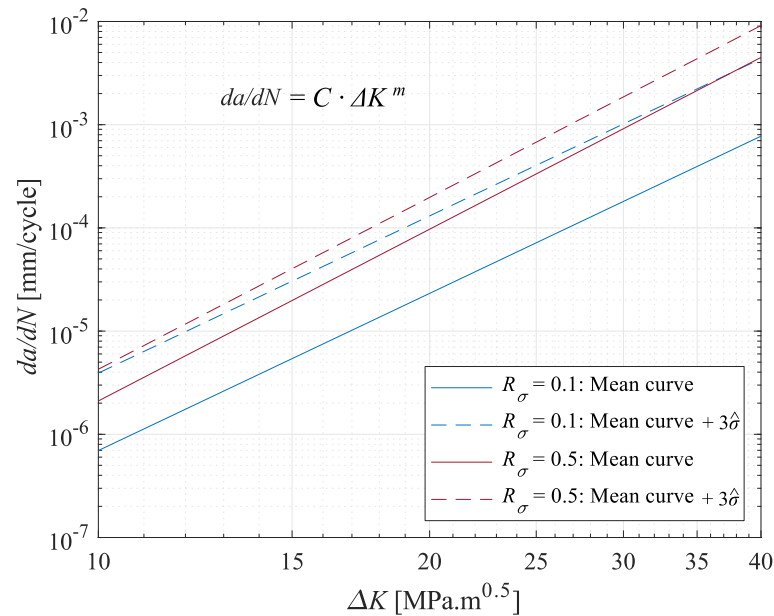
Figure 3.40. Stress ratio effect analysis for Eiffel bridge material.

3.3.4.3 S235

A set of fatigue crack growth tests were conducted at room temperature on CT specimens made from S235 – see Figure 3.41a) – using a 10 kN capacity Instron EletroPuls E10000 machine – see Figure 3.41b). The standard procedure described in ASTM E 647 [44] based on constant amplitude of loading was followed. The geometry of these specimens is shown in Figure 3.42. The thickness of the specimen, B_{CT}, was considered as 4 mm and the width, W_{CT}, equal to 36 mm. Stress ratio effect was studied by testing two different values: 0.05 and 0.5. Test frequency was set to 10 Hz.

The notch was prepared using electrical discharge machining (EDM) and the tip radius was defined as $\rho^* = 0.25$ mm. The pre-crack procedure was performed before the fatigue crack growth test using a stress intensity factor with maximum value of 15 MPa.m$^{0.5}$. Crack length (a) was measured every 0.1 mm of crack propagation using a travelling microscope (45x) with an accuracy of 10 μm. Crack growth rates were determined by incremental polynomial method using five consecutive points of a-N curves.

a)   b)
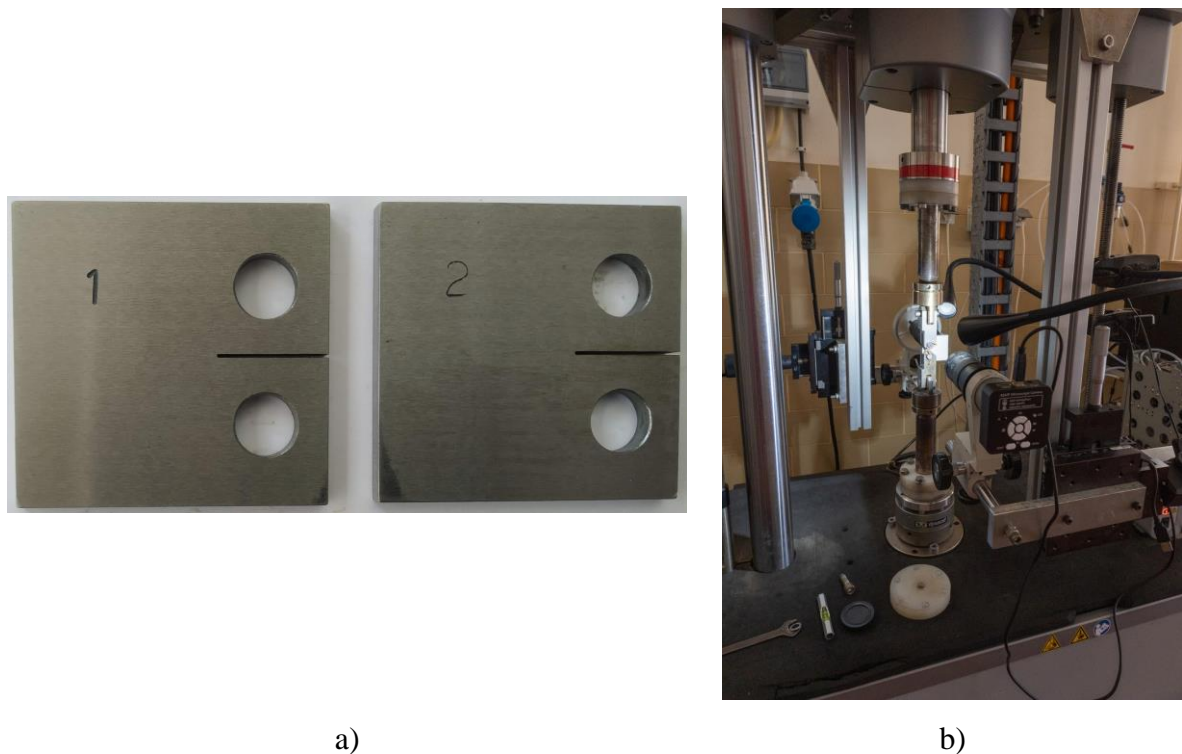
Figure 3.41. Experimental FCG tests on S235: a) CT specimens; b) execution of test.

Applied stress intensity factor ranges were computed using Eq. (3.18) in which ΔF is the applied force range and α is the ratio a/W_{CT}.

$$\Delta K_{app} = \frac{\Delta F}{B_{CT}\sqrt{W_{CT}}} \frac{(2+\alpha)}{(1-\alpha)^{3/2}} (0.886 + 4.64\alpha - 13.32\alpha^2 + 14.72\alpha^3 - 5.6\alpha^4) \quad (3.18)$$

The crack propagation rate obtained for R_σ equal to 0.05 and 0.25 is presented in Figure 3.43. A mean curve was defined considering the experimental data for each stress ratio to determine FCG material constants. It is evident that crack propagation rate of this material is affected by stress ratio since the FCG test with higher stress ratio led to faster crack growth rates.
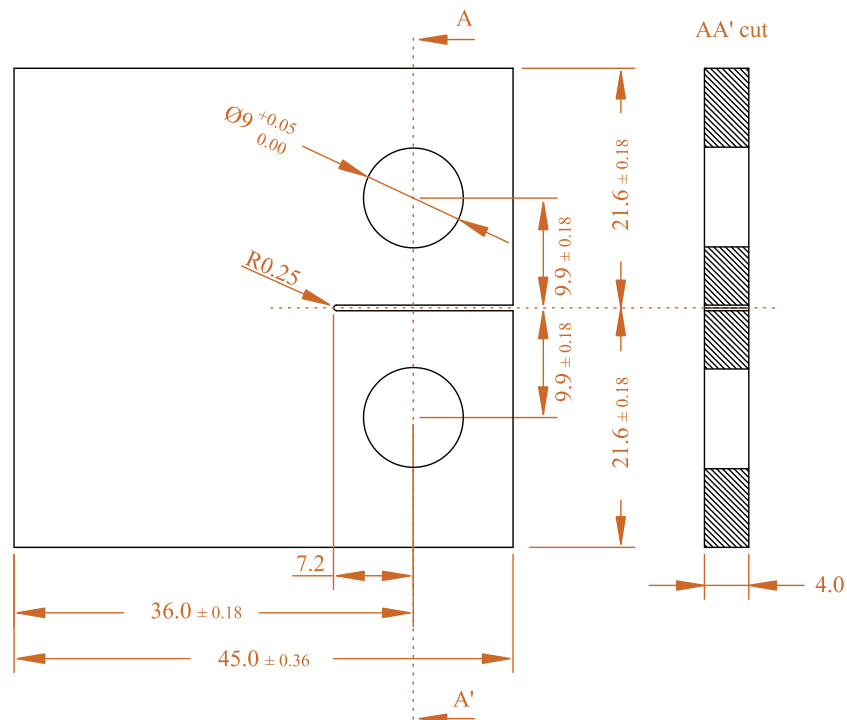
Figure 3.42. Geometric parameters of S235 CT specimens to characterize FCG (dimensions in mm).
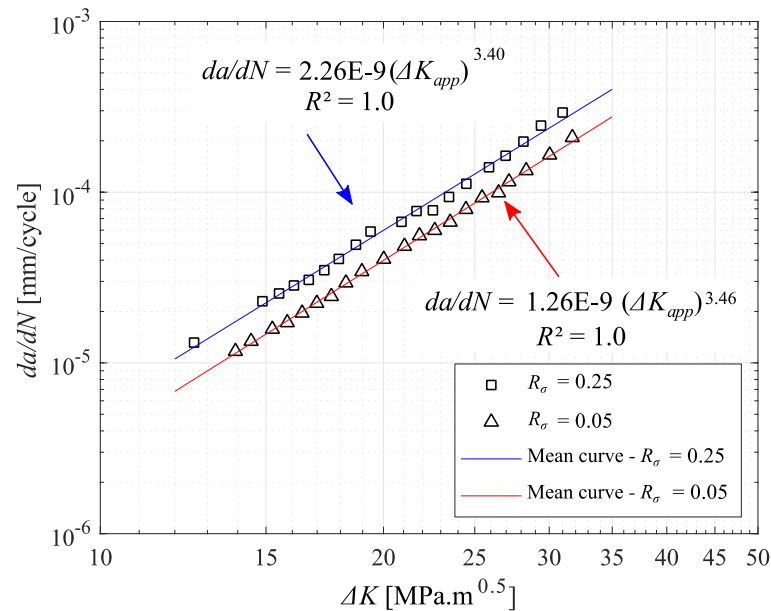
Figure 3.43. Fatigue crack propagation rate obtained with S235 CT specimens.

Fatigue crack propagation tests on S235 were also performed by Carvalho [108] (identified as C1) using CT specimens in accordance with the procedure of ASTM E647 [44] under load control conditions. The geometry of specimens was defined by W_{CT} (width) = 50 mm and

B_{CT} (thickness) = 4 mm. Two specimens were tested under stress ratio $R_\sigma = 0.01$ and two specimens were tested under stress ratio $R_\sigma = 0.5$. Frequency was set to 20 Hz. Experimental results obtained by Carvalho [108] are compared with findings described above in order to establish a general FCG design curve for stress ratio inferior to 0.5 and for stress ratio higher or equal to 0.5.

Mean curves for FCG data of $R_\sigma < 0.5$ and $R_\sigma \geq 0.5$ were obtained by means of a linear regression analysis and results can be observed in Figure 3.44 and Figure 3.45, respectively. Material constants are presented in Table 3.23 as well as the coefficient of determination, R^2, for mean curve which was found as 0.98 and 0.99 for $R_\sigma < 0.5$ and $R_\sigma \geq 0.5$, respectively. These values so close to one are a guarantee that this linear regression has a high quality and that the material scatter is reduced. It is also verified that the slope ($m = 3.83$ and $m = 3.70$) obtained with experimental data for both stress ratios differ from the slope proposed in the standard ($m = 2.88$). In the case of the design FCG curve proposed in BS 7910 [94], it is verified that it stands as an unsafe design approach for $R_\sigma < 0.5$ especially for stress intensity factor range superior to 25 MPam$^{0.5}$ while for $R_\sigma \geq 0.5$ it can be considered as a conservative method. New characteristic FCG curves for S235 were defined for each stress ratio. It was verified that shifting the mean curve by $2\hat{\sigma}$ does not lead to safe predictions. It is proposed to define characteristic FCG curves based on shifting the mean curve by $3\hat{\sigma}$.
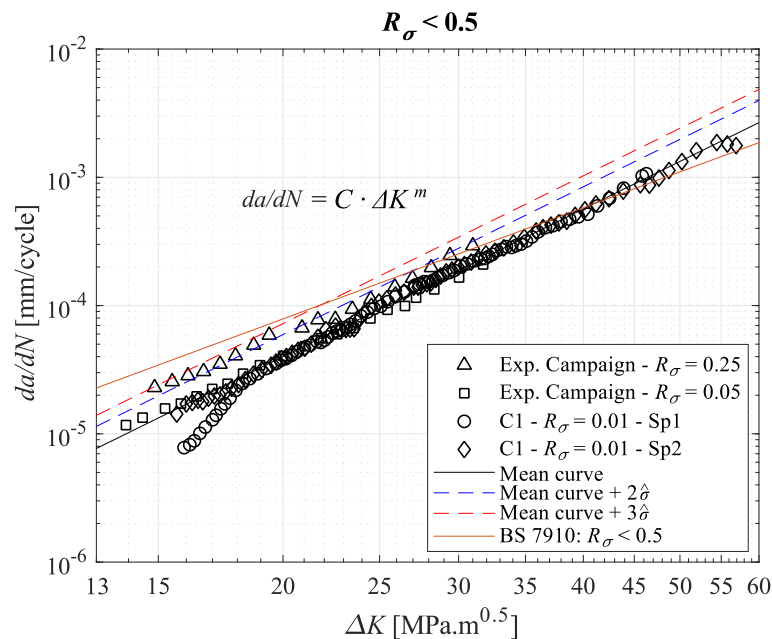
Figure 3.44. Statistical determination of FCG behaviour for **S235**: $R_\sigma < 0.5$.
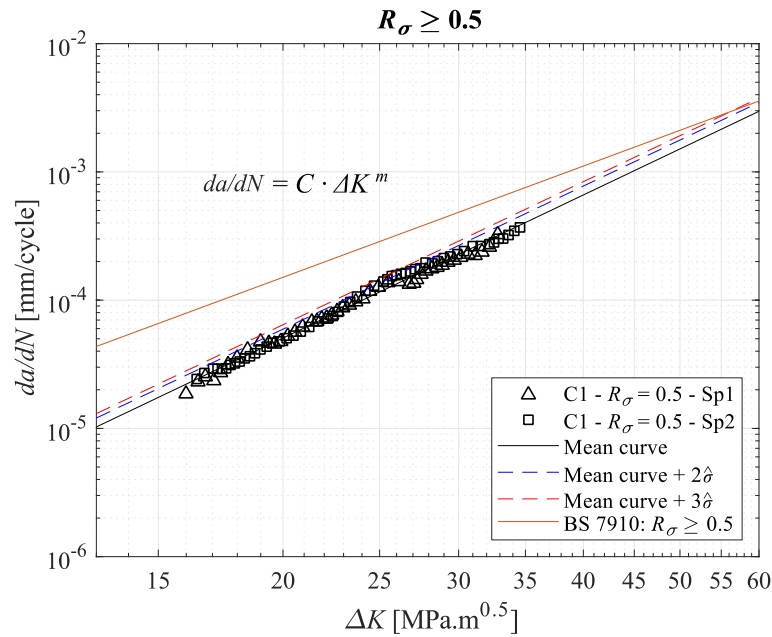
Figure 3.45. Statistical determination of FCG behaviour of **S235**: $R_\sigma \geq 0.5$.

Table 3.23. FCG constants obtained for S235 material using statistical analysis.

Stress ratio	Statistical	C^*	m	R^2	$\hat{\sigma}$
	Mean curve	4.22E-10		0.98	-
<0.5	Mean curve + $2\hat{\sigma}$	6.27E-10	3.83	-	0.09
	Mean curve + $3\hat{\sigma}$	7.65E-10		-	0.09
	Mean curve	7.67E-10		0.99	-
≥0.5	Mean curve + $2\hat{\sigma}$	8.99E-10	3.70	-	0.03
	Mean curve + $3\hat{\sigma}$	9.73E-10		-	0.03

*da/dN [mm/cycle] and ΔK [MPa.m$^{0.5}$]

3.3.4.4   S355

A set of fatigue crack growth tests were conducted at room temperature on CT specimens made from S355 using an MTS 180 machine rated to 100 kN. The geometry of specimens was established using the values presented in Figure 3.46. The standard procedure described in ASTM E 647 [44] based on constant amplitude of loading was followed for stress ratio equal to 0.5 while the K-decreasing procedure was used for stress ratio equal to 0.1. In this way, the influence of the mean stress effect was assessed. Test frequency was set to 12 Hz. The notch was prepared using electrical discharge machining (EDM) and the tip radius was defined as $\rho^* = 0.25$ mm. Pre-crack procedure was performed before the fatigue crack growth test using a stress intensity factor with maximum value of 15 MPa.m$^{0.5}$. Figure 3.47 presents a specimen during FCG test.
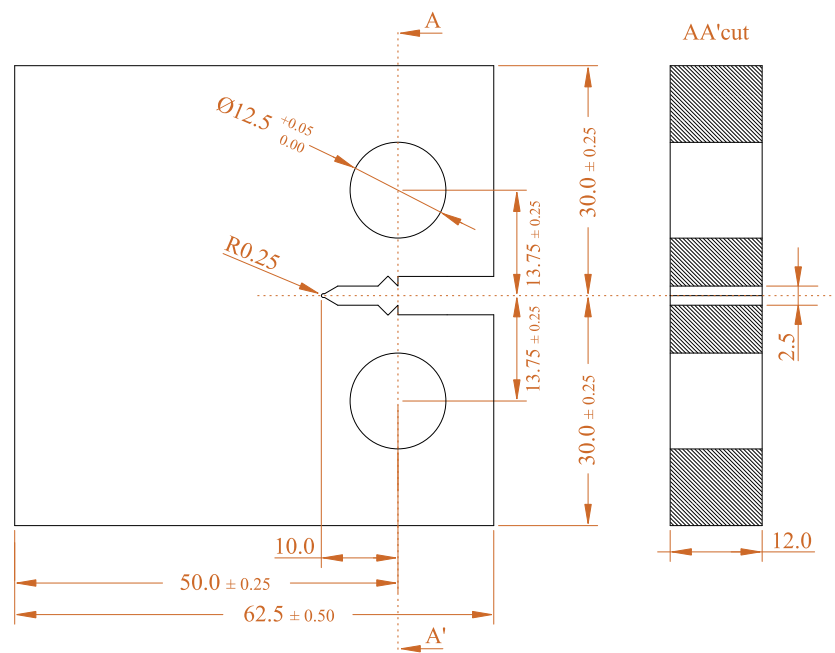
Figure 3.46. Geometric parameters of S355 CT specimens to characterize FCG behaviour (dimensions in mm).

a)   b)
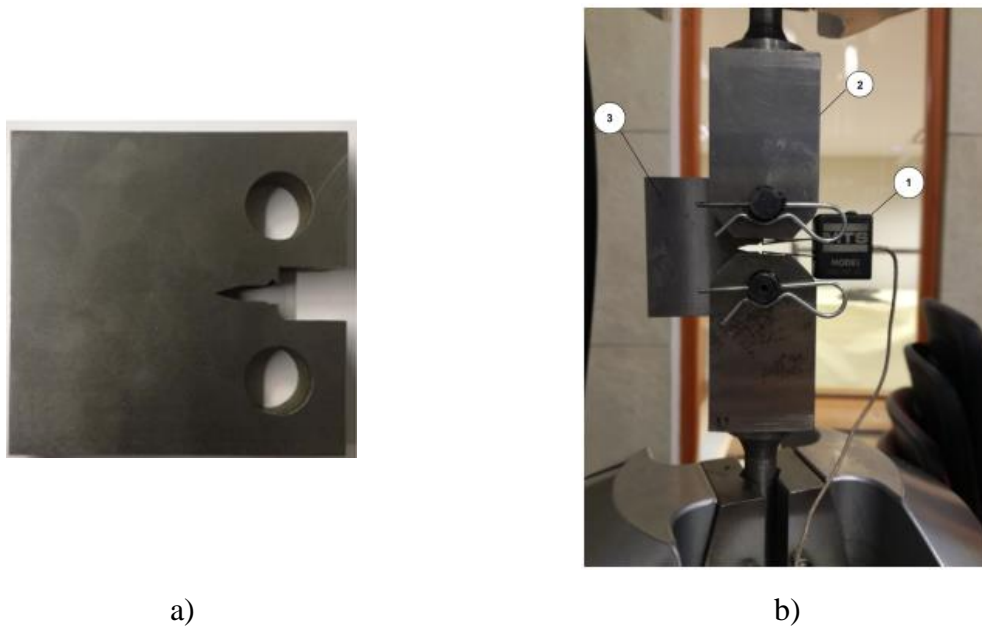
Figure 3.47. a) CT specimen made from S355. b) Apparatus of FCG test: 1-MTS clip gage (extensometer); 2-MTS clevis grip for fracture mechanics; 3-specimen.

These tests were conducted using the MTS controlling software and the FlexTest console as shown in Figure 3.48. The monitorization of crack length, a, was done using the front-face compliance method described in Eq. (3.19) in which C_0, C_1, C_2, C_3, C_4 and C_5 are coefficients

defined in ASTM E 647 [44] depending on the position of the extensometer. The values adopted in this campaign are presented in Table 3.24.

$$a = (C_0 + C_1 u_x + C_2 u_x^2 + C_3 u_x^3 + C_4 u_x^4 + C_5 u_x^5)W_{CT} \qquad (3.19)$$

Table 3.24. Coefficients used in compliance method.

C_0	C_1	C_2	C_3	C_4	C_5
1.0002	-4.062	11.242	-106.04	464.33	-650.68

The variable, u_x, presented in Eq. (3.19) is computed using Eq. (3.20) in which v_c is the crack opening displacement (COD), F is the applied force and E is the Young's modulus. The applied stress intensity factor range was computed with Eq. (3.18).

$$u_x = \frac{1}{\sqrt{\dfrac{B_{CT}E v_c}{F}} + 1} \qquad (3.20)$$

Crack growth rates were determined using the incremental polynomial method. The relation between crack propagation rate and applied stress intensity factor for the two tests of S355 material are presented in Figure 3.49. The regression line computed for both tests show a coefficient of determination very close to one meaning that they are a good representation of the obtained data. The mean stress effect is evident in the results in the sense that not only the slope changes when the stress ratio is changed but also the C constant varies significantly. It is clear that for higher stress ratio, fatigue crack growth rate increases.

Crack propagation tests on S355 were also performed by Carvalho *et al*. [108] and Jesus *et al*. [109] (identified as C1 and J2, respectively) and the details of these works are presented in Table 3.25. Different values of stress ratio were used, and, in this sense, the analysis of the data is done by separating the data with stress ratio lower than 0.5 from those that were performed with 0.5 or higher stress ratio as recommended in BS 7910 [94].

All FCG experimental data for S355 was analysis to obtain a representative mean for $R_\sigma < 0.5$ and $R_\sigma \geq 0.5$. Linear regression analysis results are presented in Figure 3.50 and Figure 3.51 and

material constants are shown in Table 3.26. The coefficient of determination for mean curve was found as $R^2 = 0.99$ and $R^2 = 0.98$, respectively for stress ratio inferior to 0.5 and for stress ratio superior or equal to 0.5. These values guarantee that the quality of this statistical analysis is high. It is verified that the slope obtained for $R_\sigma \geq 0.5$ ($m = 2.96$) is similar to the slope proposed in the standard ($m = 2.88$), however for $R_\sigma < 0.5$ ($m = 3.49$) it is significantly different.
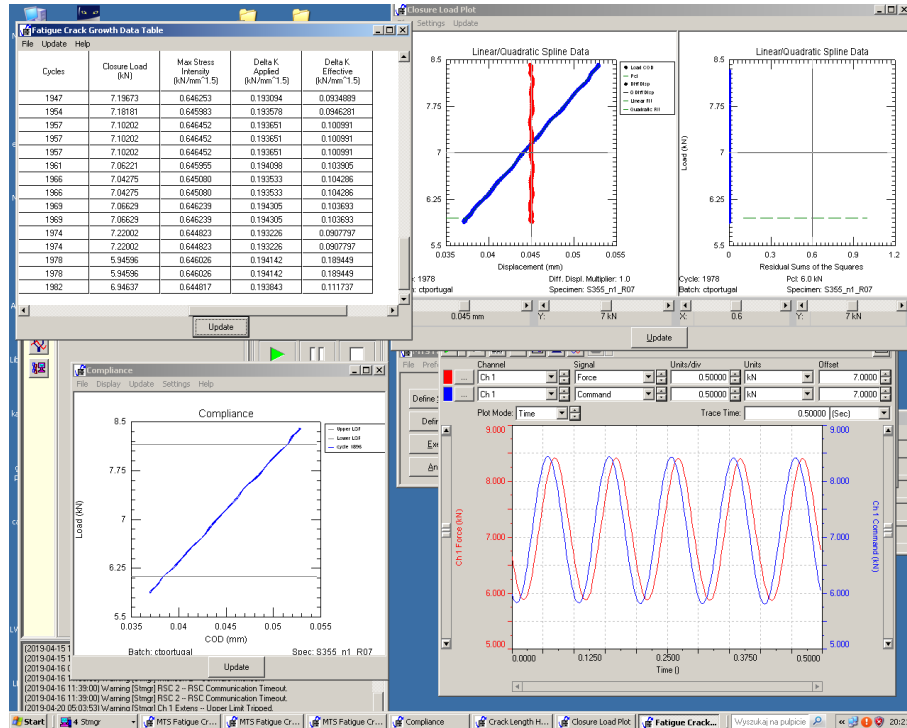
Figure 3.48. Computer display during FCG test.
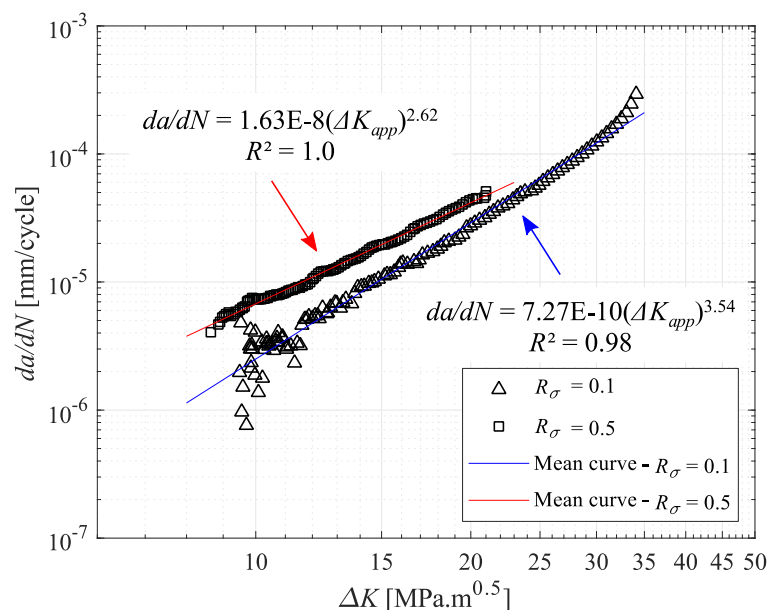
Figure 3.49. Fatigue crack growth rate for S355 specimens.

Table 3.25. Data collection of FCG tests on S355 specimens.

Authors	R_σ	Nº of Sp.	W_{CT} [mm]	B_{CT} [mm]
Carvalho *et al.* [108] – C1	0.01	4	50	4 and 8
	0.50	4		
Jesus *et al.* [109] – J2	0.01	4	50	8
	0.50	2		
	0.75	1		

Regarding the FCG curves proposed in BS 7910 [94], it is verified that they stand as a conservative design approach for both stress ratios, especially for $R_\sigma \geq 0.5$. In this sense, defining characteristic curves by shifting the mean curve by $3\hat{\sigma}$ stand as a reliable design approach for both $R_\sigma < 0.5$ and $R_\sigma \geq 0.5$ scenarios.
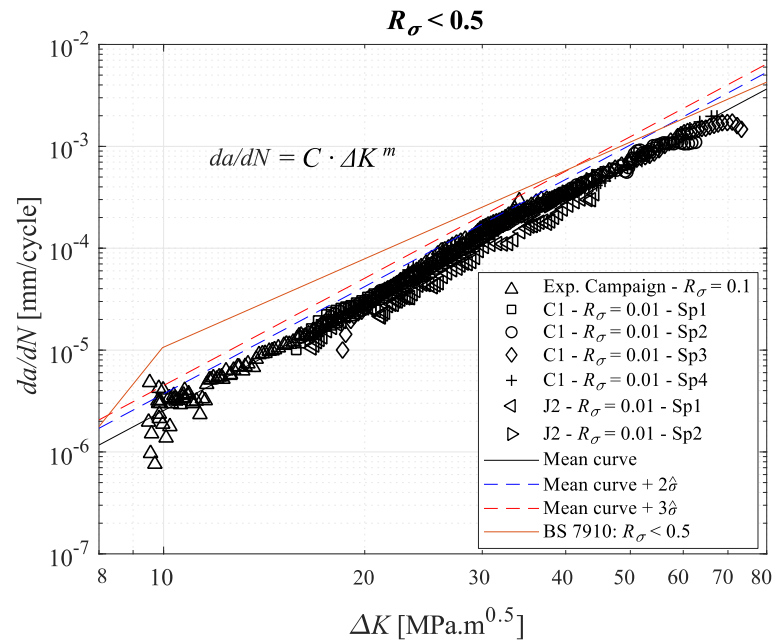
Figure 3.50. Statistical determination of **S355** FCG behaviour: $R_\sigma < 0.5$.

Table 3.26. FCG constants obtained for S355 material using statistical analysis.

Stress ratio	Statistical	C^*	m	R^2	$\hat{\sigma}$
<0.5	Mean curve	8.17E-10		0.99	-
	Mean curve + $2\hat{\sigma}$	1.19E-09	3.49	-	0.08
	Mean curve + $3\hat{\sigma}$	1.44E-09		-	0.08
≥0.5	Mean curve	7.22E-09		0.98	-
	Mean curve + $2\hat{\sigma}$	1.00E-08	2.96	-	0.07
	Mean curve + $3\hat{\sigma}$	1.19E-08		-	0.07

*da/dN [mm/cycle] and ΔK [MPa.m$^{0.5}$]
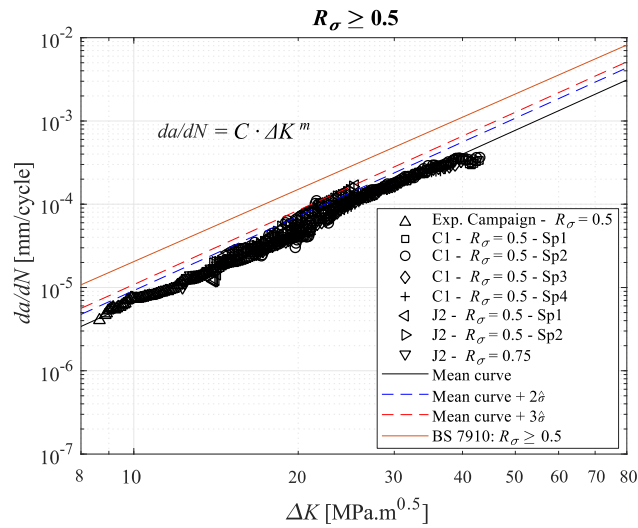
Figure 3.51. Statistical determination of **S355** FCG behaviour: $R_\sigma \geq 0.5$.

3.3.4.5   Comparison

A comparison between these three materials was established considering characteristic fatigue crack growth curves (Mean curve + $3\hat{\sigma}$) with stress ratio lower than 0.5 and bigger than 0.5 as presented in Figure 3.52 and Figure 3.53, respectively. It is observed that the velocity of crack propagation in Eiffel bridge material is higher when compared to the other materials in all values of stress ratio. It is evident that the heterogeneity of its microstructure, its chemical composition and its higher grain size contribute to increase the velocity of the crack in puddled iron when compared to modern steels. In the case of fatigue crack growth rate from S235 and S355, a consistent improvement in the fracture performance is obtained for S355 when tests are conducted with stress ratio lower than 0.5. However, for higher values of stress ratio, similar performance is found.
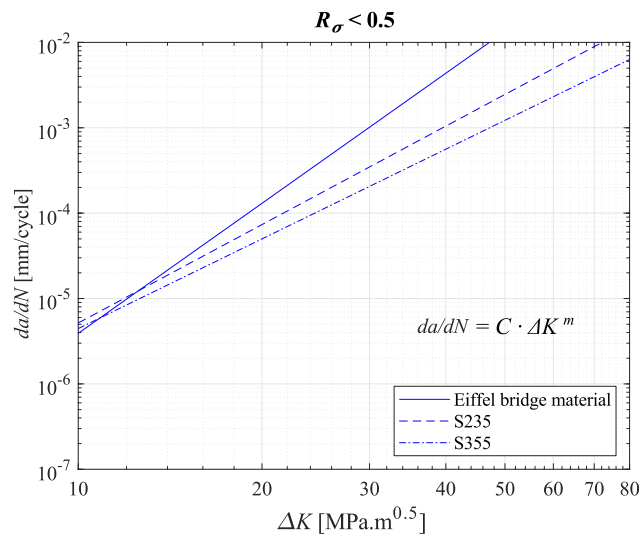
Figure 3.52. Comparison of fatigue crack growth for different materials - $R_\sigma < 0.5$.

$$R_\sigma \geq 0.5$$
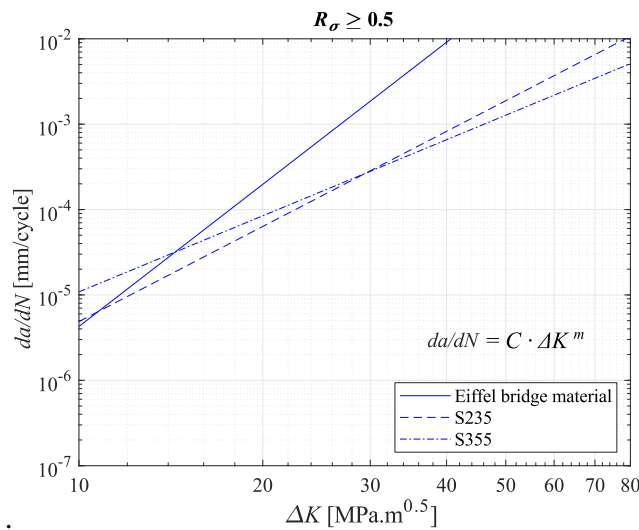
Figure 3.53. Comparison of fatigue crack growth for different materials - $R_\sigma \geq 0.5$.

3.4   Conclusions

Three distinct metallic materials were selected to conduct a metallographic and mechanical assessment: puddled iron extracted from Eiffel bridge structural components, S235 and S355. This selection allowed to: a) establish a clear distinction between metallic materials used in bridges built at the end of the 19th century and modern steels; b) identify microstructural differences between steel materials with distinct strength level, and; c) establish a relation between metallographic properties and mechanical performance (monotonic, cyclic, fatigue and fracture behaviour).

Significant differences were found between puddled iron and modern steels at microstructural level. The first is characterized by a significant heterogeneity and abundant presence of non-metallic inclusions. While puddled iron showed elongated grains oriented through the lamination direction, modern steels are homogeneous with perlite-ferrite microstructure and no visible orientation of grains. The size of the grains is significantly smaller in modern steels compared to puddled iron which has a key role to improve mechanical performance, especially in what concerns fatigue crack growth. Furthermore, a reduction of grain size is also visible within modern steels with higher strength, since S355 presented smaller results.

Modern steels were also characterized in terms of its nanostructure, namely their crystallite size and dislocation density. XRD was used to estimate these properties. The mean value of the

crystallite size for S235 and S355 was similar, around 20 nm. However, the scatter of results is higher for S355. In what concerns dislocation density, the average value found for both materials was around 3E-3 nm^{-2} which is within the typical values for highly deformed metals.

Comparing chemical composition, the most significant aspect is the relevant presence of phosphorus in puddled iron which influences its mechanical performance, negatively. On the other hand, manganese found in modern steels is essential to guarantee good weldability and improved mechanical properties. The lower carbon content in modern steels is associated with higher ductility which was proved in Vickers hardness tests. It was found that puddled iron from Eiffel bridge is harder than modern steels. S355 presented a higher level of hardness compared to S235 which means that the improvement on strength is associated with lower ductility.

Monotonic tensile tests were performed for these three materials showing that elastic behaviour is similar but plastic region is very distinct. The percentage of elongation after fracture of puddled iron is nearly four times smaller when compared to modern steels which can be associated with differences in chemical composition and microstructure.

Considering experimental LCF results for each material, mean and characteristic cyclic stress-strain curves were defined. It was found that normal distribution function led to a more reliable approach, generally. Cyclic stress-strain performance of puddled iron is similar to modern steels in predominately elastic region, but for high level of strain (from 0.5 to 1%) comparison is not possible due to lack of data from puddled iron. In fact, the brittleness of this material leads to very low fatigue endurance for such levels of strain. Within modern steels, an improved cyclic curve was found for S355, especially for higher values of strain. Recommendations from DNV-RP-C208 [93] for S235 cyclic behaviour are very distinct from experimental evidences, while for S355, recommendations are acceptable comparing to experimental data, however characteristic curves proposed in this thesis represent a better approach.

Fatigue life behaviour was assessed by means of three distinct damage models. Characteristic fatigue life curves were proposed for each material and normal distribution showed to be the best approach. Recommendations from DNV-RP-C208 [93] for strain-life damage parameter of S235 and S355 showed to be a very conservative approach, especially for S235. Eiffel bridge

material presented lower performance when compared to modern steels, while an improvement is clear for S355 when compared with S235.

Dislocation density values determined with XRD for each modern steel were used to assess the fatigue behaviour based on Huffman model. A good correlation with experimental fatigue data was found with the maximum value of dislocation density assessed by XRD. Optimized values of dislocation density were found as: $4.20E15$ m^{-2} for S235 and $6.42E15$ m^{-2} for S355

Finally, in what concerns fatigue crack growth, it was proposed to define characteristic FCG curves by implementing a shift in the mean curve of 3 times the standard deviation. It showed good correlation with experimental data. Design recommendations proposed in BS 7910 represented an unsafe prediction for S235, while for S355 it can be considered as a conservative prediction. In BS 7910 there is no distinction for design FCG curves based on material type, however the comparison of FCG behaviour between these materials showed that S355 has improved (slower) FCG behaviour than S235 for stress ratio lower than 0.5. Furthermore, FCG results showed that all these materials are influenced by the mean stress effect since distinct results were obtained when stress ratio is changed.

4   FCG PREDICTION CONSIDERING PLASTICITY INDUCED CRACK CLOSURE

4.1   Introduction

Considering a crack under a fatigue tensile load in which minimum stress is zero, it could be expected that it gets closed only at minimum load. However, Elber [47] discovered that the crack gets closed before stress become zero. For a sheet specimen with a central crack as shown in Figure 4.1, a plastic zone is created during cyclic loading when stress goes from S_{min} to S_{max} whose size is proportional to $(K_{max}/\sigma_{yield})^2$ and elongated in loading direction [23]. Consequently, a cyclic plastic zone is created during unloading with size significantly smaller than the monotonic plastic zone. Since crack tip plasticity occurs in every cycle, crack is growing through plastic zones of previous cycles. This phenomenon has been designated as *plasticity induced crack closure* [23].
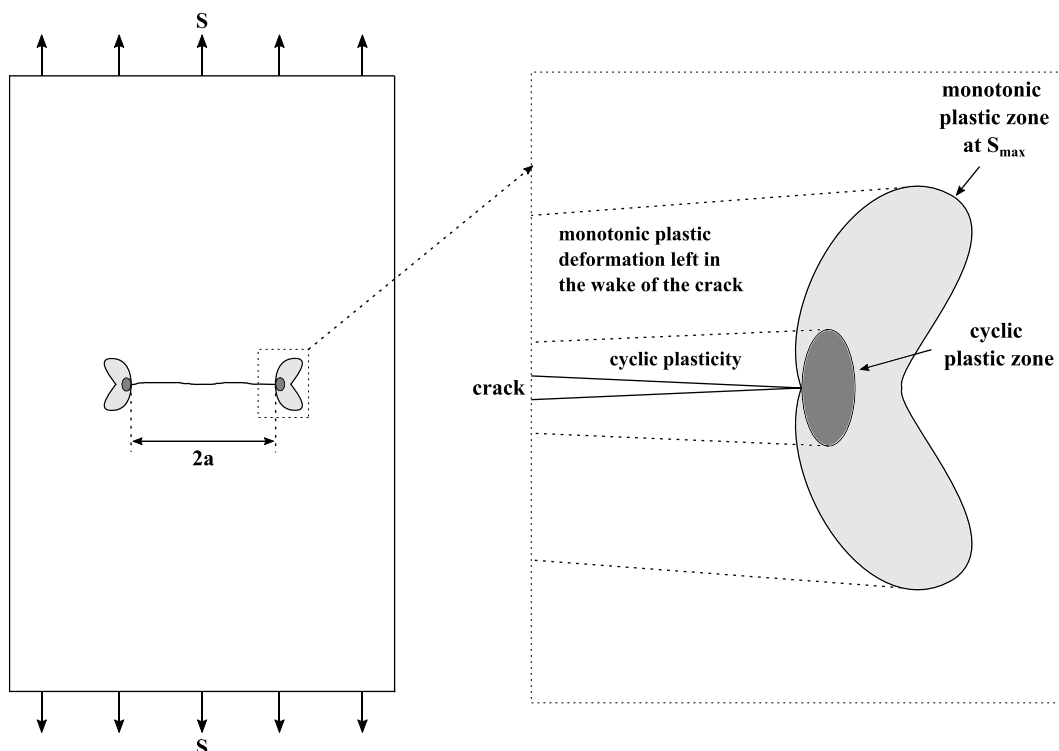
Figure 4.1. Plastic zones during fatigue crack growth. Adapted from Schijve [23].

Considering this phenomenon, Elber [47] proposed that crack growth should be correlated with the load cycle that corresponds to the period when the crack is open, which can be designated

as an effective load cycle, instead of the total load cycle. Consequently, the value of the stress intensity factor range should follow the same approach and fatigue crack growth rate is correlated with its effective value as presented in Eq. (4.1).

$$\frac{da}{dN} = C_{eff}\left(\Delta K_{eff}\right)^{m_{eff}}$$

(4.1)

Mean stress effects are included in this approach since reversed crack tip plasticity relies on S_{min}, thus the plastic wake field of the crack depends on the mean stress level (stress ratio). Elber also introduced the parameter U, which corresponds to the ratio between the effective and the applied values of the stress intensity factor range as presented in Eq. (4.2).

$$U = \frac{\Delta K_{eff}}{\Delta K_{app}}$$

(4.2)

One possible approach to predict fatigue crack growth considering the effect of plasticity induced crack closure is to create a model based on the elastoplastic crack tip stress-strain history. The Unigrow model [62] is an example of this approach in which the effect of residual (compressive) stresses induced by reversed plastic deformation is accounted in the analysis.

In this chapter, the effect of plasticity induced crack closure on fatigue crack propagation of S355 and S235 is analysed. These materials are commonly used in civil engineering structures that are subjected to fatigue loading conditions, therefore it is essential to properly acknowledge the behaviour of a fatigue crack in such materials aiming to establish reliable predictions on the fatigue life of structural metallic details in which these materials are used. Experimental, analytical and numerical procedures are implemented to propose a generic fatigue crack growth model based on local stress-strain analysis.

4.2   Local approaches for fatigue crack growth modelling

In 1985, Glinka [60] introduced the use of strain-based fatigue models to analyse FCG process. He developed the concept of discretization using elementary material blocks whose failure is used to derive fatigue crack growth. Later on 1999, Peeker and Niemi [61] proposed a model

for FCG prediction based on the superposition of the near threshold and stable fatigue crack growth regimes using cyclic elastoplastic stress-strain and strain-life constants.

More recently, Noroozi and Glinka [62–64] developed the UniGrow model based on the elastoplastic crack tip stress-stain history analysis in which the influence of the compressive stress field formed ahead of the crack tip during FCG is included. This model was develop using the Smith-Watson-Topper as fatigue damage parameter. In 2007, Hurley and Evans [66] presented a new methodology based on the assumption that the number of cycles to propagate a crack through the cyclic plastic zone is the same as the one to initiate a crack in a specimen under plain strain conditions, while in 2017, Ferreira *et al.* [111] proposed the use of strip-yield mechanics to model fatigue crack growth.

New developments on fatigue crack propagation models that consider the effect of residual stresses has been proposed by Correia *et al.* [112], Hafezi *et al.* [113] and Jesus and Correia [114] by computing the elastoplastic stress fields ahead of the crack tip by means of finite element analysis. It is also important to refer that the implementation of probabilistic analysis to FCG models based on local approaches has been performed by Correia *et al.* [115] and Bogdanov *et al.* [116]. These FCG models have also been used in procedures to compute *S-N* curves of structural details, as was the case in Correia *et al.* [117,118] for notched plates.

General applications of UniGrow model are related with FCG for long cracks (> 0.5-1.0 mm), however Bang *et al.* [119] proposed a modification on the model for short cracks based on experimental results on aluminium and titanium alloys. Two improvement modelling methods were presented: stress intensity correction and data fitting. Results from both methods were better for high stress levels and stress intensity correction method lead to more accurate predictions. Later on 2019, Bang *et al.* [120] further improved the proposed modifications on the UniGrow model in order to consider both short and long crack growth behaviour. More recently, Bang *et al.* [121] developed a unified modelling framework that integrates both short and long crack propagation in the formulation of the crack driving force of the UniGrow model.

Stress ratio effects on FCG have also been studied by Daniel Kujawski [122–124]. An analytical method to estimate the elastoplastic stress-strain field ahead of the crack tip was proposed and

results were compared with experimental and numerical data [122]. Moreover, in 2021 a damaging stress intensity function was proposed (analogous to SWT parameter) to analyse stress ratio effects in metallic materials under constant amplitude loading mainly in threshold and lower Paris region of FCG [123]. Later on 2022, the new crack driving force proposed by Daniel Kujawski [124] was extended to a wide variety of different alloys and for both positive and negative stress ratios.

4.3   Fatigue crack growth model

4.3.1   General description

Considering the importance of the UniGrow model within the scientific community and its recent improvements, it was chosen as the basis for the approach to assess the fatigue crack growth behaviour of the selected materials. In the following paragraphs, the proposed modelling approach is described.

Fatigue crack growth process is mainly controlled by the stress-strain field ahead of the crack tip. However, it is not easy to compute elastoplastic stresses and strains at the crack tip since they are strongly dependent on the applied method. To overcome this problem, the most common approach to fatigue crack growth is based on fracture mechanics concept which uses global parameters such as nominal stress, crack length and geometry, combined into one general parameter, usually, the stress intensity factor (SIF). However, the effect of residual stresses induced by reversed plastic deformations is neglected in this approach.

There are several scientific investigations in literature aiming to model the crack based on the mechanics of continuum. Irwin [39] and Hutchinson [125] computed stresses and strains near the crack tip using a sharp crack (tip radius $\rho^* = 0$) which leads to unrealistically high values. More recently, several authors ([60,126]) implemented the approach of modelling the crack as a notch with a small but finite tip radius $\rho^* > 0$. Notch analytical theories are applied and stress-strain field ahead of the crack tip become more realistic. Noroozi *et al.* [62] suggested that there is a minimum value of the notch tip radius, ρ^*, that can be considered as a material property and results in the maximum stress concentration which can be generated in the material. Noroozi *et al.* [62] also emphasizes that the plastic yielding around the crack tip

formed during one load reversal generates plastic deformations which resists to be deformed during subsequent reversals of cyclic loading. The effect of plastic deformations ahead of the crack tip can be determined by solving the notched body boundary problem using elastoplastic material properties resulting in the residual stress field, σ_r. Even if nominal stress ratio is positive, a compressive (residual) stress field is generated ahead of the crack tip when the load is at the minimum level as described in Figure 4.2. This residual compressive stress field increases as the stress ratio is closer to zero.
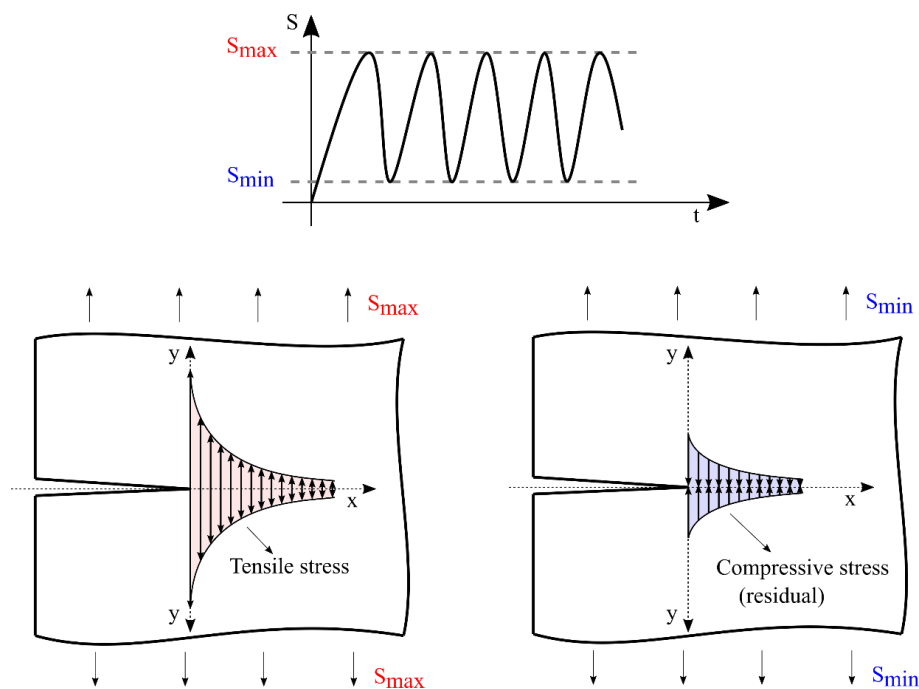
Figure 4.2. Schematic representation of remote applied stress and resulting local crack tip stress fields.

Within the Unigrow model, Glinka [60] proposes to model the crack with a finite tip radius, ρ^*, allowing the calculation of crack tip stress and strain distributions with notch theories assuming that the crack region just behind the tip remains open – see Figure 4.3. Noroozi *et al*. [62] also suggested that notch tip radius, ρ^*, can be considered an elementary block size of the material which can be used to discretize the medium of the material in order to determine the relevant stresses and strains ahead of the crack tip to derive fatigue crack growth rate. In this sense, the main parameter of UniGrow model, ρ^*, is used not only for the determination of elastoplastic stress-strain field but also as a crack growth increment used to determine fatigue crack growth rate. The assessment of this parameter has been made by the referred authors considering only

the adjustment of the predicted fatigue crack growth rate with experimental values without the validation of the stress-strain field.

In this chapter, the implemented fatigue crack growth model is based on the main assumptions of the Unigrow model presented by Noroozi *et al*. [62], however, the improvement proposed in this research is to establish a distinction between the value of the crack tip radius, ρ^*, used to generate the stress-strain field ahead of the crack tip during fatigue loading and the value of the parameter used to derive fatigue crack growth rate which is now designated as *process block size* and is identified as δ_p. While the crack tip radius, ρ^*, is found by correlation with experimental and numerical results of residual stress intensity factor, fatigue crack growth rate is derived using the process block size, δ_p, whose value was found by correlation with fatigue crack growth rate experimental data. Furthermore, a generic expression is proposed to determine the size of the process block.

The FCG model used in the scientific investigation is based on the following assumptions:
- The crack is analysed as a notch with a tip radius ρ^* to obtain the elastoplastic stress-strain field ahead of the crack tip;
- Ramberg-Osgood cyclic stress-strain formulation is used to express the material behaviour;
- The relevant stresses and strains used to determine fatigue crack growth rate are measured within a distance ahead of the crack tip which is designated as process block size which is identified as δ_p – see Figure 4.3. This parameter is a function of the effective stress intensity factor range, ΔK_{eff}, and the cyclic yield strength of the material, σ_0' according to Eq. (4.3);

$$\delta_p = \frac{1}{15\pi}\left(\frac{\Delta K_{eff}}{\sigma_0'}\right)^2 \tag{4.3}$$

- Fatigue crack growth is considered as successive crack re-initiations over the distance δ_p;

- The number of cycles N_{block} to reach failure within the process block size ahead of the crack tip can be determined using the Smith-Watson-Topper (SWT) fatigue damage parameter:

$$SWT_{block} = \sigma_{max,block}^{eff} \varepsilon_{a,block}^{eff} \tag{4.4}$$

$$= \frac{(\sigma'_{f,SWT})^2}{E}(2N_{block})^{2b_{SWT}} + \sigma'_{f,SWT}\varepsilon'_{f,SWT}(2N_{block})^{b_{SWT}+c_{SWT}}$$

where $\sigma_{max,block}^{eff}$ corresponds to the maximum effective stresses over the block size and $\varepsilon_{a,block}^{eff}$ is the effective strain amplitude over the process block size;

- Fatigue crack growth rate is determined as the average fatigue crack growth rate over the process block size, δ_p, according to Eq. (4.5).

$$\frac{da}{dN} = \frac{\delta_p}{N_{block}} \tag{4.5}$$
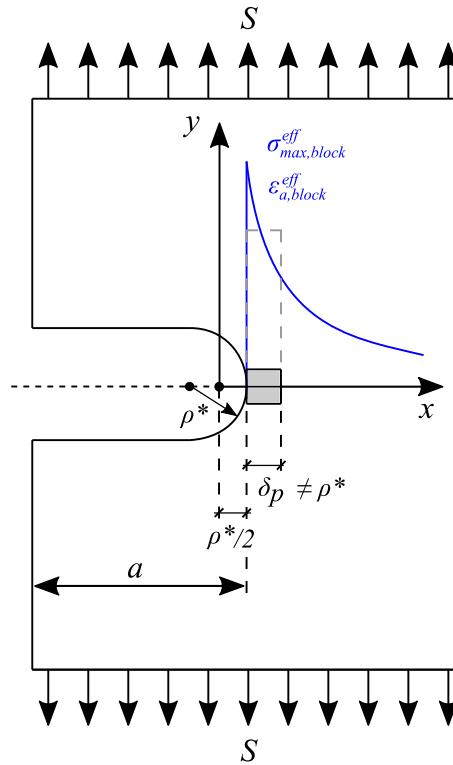
Figure 4.3. Schematic representation of conceptual crack tip modelling and stress-strain distribution induced by a tensile load.

A schematic representation of the proposed fatigue crack growth model for $R_\sigma > 0$ is shown in Figure 4.4. Elastoplastic stress-strain field formed ahead of the crack tip during fatigue loading is determined based on the crack tip radius and material cyclic parameters determined in Chapter 3 allowing to compute residual (compressive) stress field. Weight function method is then used to compute residual stress intensity factor which is compared with the value found by means of the experimental procedures.
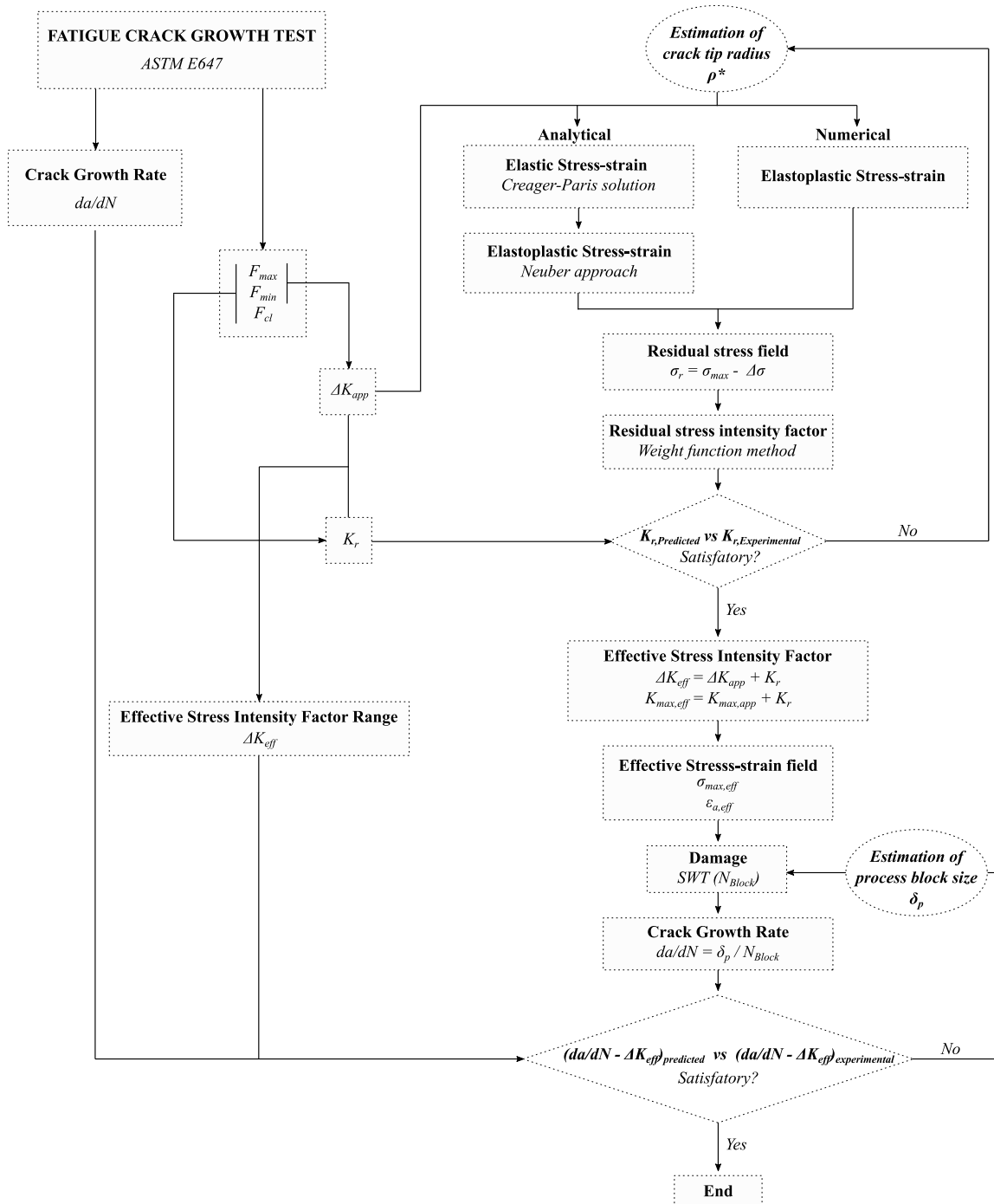
Figure 4.4. Schematic diagram of fatigue crack propagation model.

Then, the effective value of the stress intensity factor range is determined which allow to compute the effective stress-strain field formed ahead of the crack tip during fatigue loading. After, the process block size is defined, and the fatigue damage can be assessed. Finally, the crack growth rate is determined considering the value of the process block size and the number of cycles to reach failure. It was found that the value of the process block size that lead to good correlation with experimental evidence can be determined by means of Eq. (4.3).

4.3.2   Stress-strain computation

The Neuber rule [127] is used to compute elastoplastic stresses and strains ahead of the crack tip in which linear elastic values are used as input data. In the following subsections, the demonstration is made for the case of tensile loading ($R_\sigma > 0$).

4.3.2.1   Elastic analysis

Linear elastic stress field is computed using the concept of linear elastic fracture mechanics (LEFM) by assuming a notch with tip radius ρ^* and crack length a. The Creager-Paris solution [128] was used to compute stress and strain field ahead of the crack tip at the maximum load which resulted in Eq. (4.6) and Eq. (4.7), respectively.

$$\begin{cases} \sigma_{max,x}^e = \dfrac{K_{max}}{\sqrt{2\pi x}}\left(1 - \dfrac{\rho^*}{2x}\right) \\ \sigma_{max,y}^e = \dfrac{K_{max}}{\sqrt{2\pi x}}\left(1 + \dfrac{\rho^*}{2x}\right) \end{cases} \qquad (4.6)$$

$$\begin{cases} \varepsilon_{max,x}^e = \dfrac{1}{E}\left(\sigma_{max,x}^e - \nu \cdot \sigma_{max,y}^e\right) \\ \varepsilon_{max,y}^e = \dfrac{1}{E}\left(\sigma_{max,y}^e - \nu \cdot \sigma_{max,x}^e\right) \end{cases} \qquad (4.7)$$

With these equations, the elastic stress-strain field ahead of the crack tip is fully characterized for maximum applied load. Variables $\sigma_{max,x}^e$ and $\sigma_{max,y}^e$ are the elastic normal stresses (directions according to Figure 4.3), ν is the Poisson coefficient, K_{max} is the applied stress intensity factor at maximum load and E is the Young's modulus. Then, elastic stress-strain

amplitude field ahead of the crack tip is obtained considering the maximum value and the stress ratio, R_σ, as presented in Eq. (4.8) and Eq. (4.9), respectively for stress and strain.

$$\begin{cases} \sigma_{a,x}^e = \dfrac{\sigma_{max,x}^e \cdot (1 - R_\sigma)}{2} \\ \sigma_{a,y}^e = \dfrac{\sigma_{max,y}^e \cdot (1 - R_\sigma)}{2} \end{cases} \tag{4.8}$$

$$\begin{cases} \varepsilon_{a,x}^e = \dfrac{1}{E}\left(\sigma_{a,x}^e - \nu \cdot \sigma_{a,y}^e\right) \\ \varepsilon_{a,y}^e = \dfrac{1}{E}\left(\sigma_{a,y}^e - \nu \cdot \sigma_{a,x}^e\right) \end{cases} \tag{4.9}$$

4.3.2.2 Elastoplastic analysis

Elastoplastic stress-strain analysis is used to determine the actual stress-strain field ahead of the crack tip. This is accomplished using the Neuber rule which uses the equivalence of strain energy density at the notch tip between the hypothetical linear-elastic notch tip stress-strain input data and the actual elastic-plastic response. This approach was originally derived for a uniaxial stress state, but recently Moftakhar *et al.* [129] extended it for multi-axial proportional and non-proportional loading conditions. The near tip stress-strain field is tri-axial, but the third principal stress is a function of the other two. Additionally, the components of the elastic stress tensor change proportionally during loading which means that Hencky equations of the theory of plasticity can be used. In this sense, the whole notch-tip stress-strain problem can be reduced to the solution of a set of five nonlinear algebraic equations including Hencky stress-strain relationships, Ramberg-Osgood equation and multi-axial Neuber rule:

A) Generalized Neuber rule

$$\sigma_y^e \varepsilon_y^e + \sigma_x^e \varepsilon_x^e = \sigma_y^{e-p} \varepsilon_y^{e-p} + \sigma_x^{e-p} \varepsilon_x^{e-p} \tag{4.10}$$

B) Constitutive stress-strain relationships

$$\varepsilon_z^{e-p} = -\frac{\nu}{E}\left(\sigma_y^{e-p} + \sigma_x^{e-p}\right) - \frac{f\left(\sigma_{eq}^{e-p}\right)}{2\sigma_{eq}^{e-p}}\left(\sigma_y^{e-p} + \sigma_x^{e-p}\right) \tag{4.11}$$

$$\varepsilon_y^{e-p} = \frac{1}{E}\left(\sigma_y^{e-p} - v\sigma_x^{e-p}\right) + \frac{f\left(\sigma_{eq}^{e-p}\right)}{2\sigma_{eq}^{e-p}}\left(\sigma_y^{e-p} - 0.5\sigma_x^{e-p}\right) \tag{4.12}$$

$$\varepsilon_x^{e-p} = \frac{1}{E}\left(\sigma_x^{e-p} - v\sigma_y^{e-p}\right) + \frac{f\left(\sigma_{eq}^{e-p}\right)}{2\sigma_{eq}^{e-p}}\left(\sigma_x^{e-p} - 0.5\sigma_y^{e-p}\right) \tag{4.13}$$

where

$$\sigma_{eq}^{e-p} = \sqrt{\left(\sigma_y^{e-p}\right)^2 - \sigma_y^{e-p}\sigma_x^{e-p} + \left(\sigma_x^{e-p}\right)^2} \tag{4.14}$$

$$f\left(\sigma_{eq}^{e-p}\right) = \left(\frac{\sigma_{eq}^{e-p}}{K'}\right)^{\frac{1}{n'}} \tag{4.15}$$

C) The fractional contribution of the total strain energy density

$$\frac{\sigma_y^e \varepsilon_y^e}{\sigma_y^e \varepsilon_y^e + \sigma_x^e \varepsilon_x^e} = \frac{\sigma_y^{e-p} \varepsilon_y^{e-p}}{\sigma_y^{e-p} \varepsilon_y^{e-p} + \sigma_x^{e-p} \varepsilon_x^{e-p}} \tag{4.16}$$

In these set of equations σ_x^e, σ_y^e and ε_x^e, ε_y^e and ε_z^e are the elastic normal stresses and strains, respectively, and σ_x^{e-p}, σ_y^{e-p} and ε_x^{e-p}, ε_y^{e-p} and ε_z^{e-p} are the elastoplastic normal stresses and strains, respectively (directions according to Figure 4.3). Additionally, v corresponds to the Poisson coefficient, E is the Young's modulus, K' is the cyclic strain hardening coefficient and n' is the cyclic strain hardening exponent.

4.4   Residual stress intensity factor

The computation of residual stress field ahead of the crack tip was conducted for S235 and S355 FCG results presented in Section 3.3.4.3 and 3.3.4.4, respectively. Considering S355 material, residual stress intensity factor was computed using experimental, analytical, and numerical approaches while for S235, only analytical methods were implemented.

4.4.1   Experimental approach

During experimental FCG tests on S355 specimens described in Chapter 3.3.4.4, a set of cycles were selected to register at least two hysteresis loops to compute F-v_c relation. The effective

stress intensity factor range, ΔK_{eff}, was determined using the Elber concept [47] by computing, at crack closure point, the force, F_{cl}, which consists of splitting the recorded F-v_c curve into linear and nonlinear segments. This approach is illustrated in Figure 4.5. It is assumed that within the linear component of the results, the crack is open and in the non-linear part the crack is "closed".
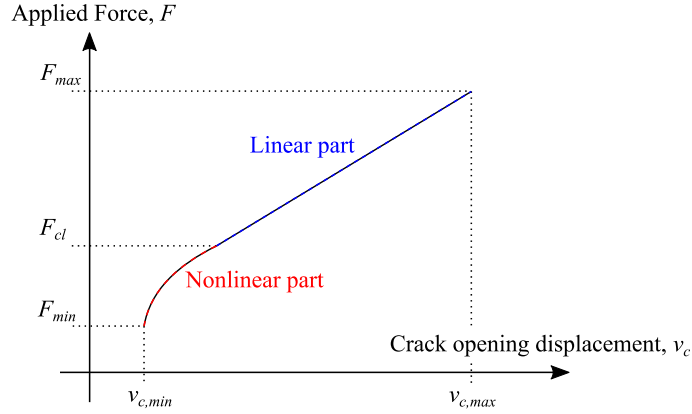
Figure 4.5. Determination of crack closure force in a load cycle.

The linear and nonlinear components of the curve are described using Eq. (4.17) and Eq. (4.18), respectively.

$$v_L = A_0 + A_1 F \tag{4.17}$$

$$v_Q = B_0 + B_1 F + B_2 F^2 \tag{4.18}$$

Coefficients A_0 and A_1 are determined by linear regression method, while B_0, B_1 and B_2 were obtained with the following conditions:

$$v_L = v_Q \tag{4.19}$$

$$\frac{d(v_Q)}{dF} = \frac{d(v_L)}{dF}, for\ F = F_{cl} \tag{4.20}$$

In this case, B_0, B_1 and B_2 should be optimal from the mathematical point of view which can be found by minimizing the value of the residual sum of squares (RSS).

$$\xi = \frac{1}{(v_{c,max} - v_{c,min})^2} \sum_{j=1}^{n} \left(\begin{array}{l} (v_Q - v_j)^2, for\ F_j < F_{cl} \\ (v_Q - v_j)^2, for\ F_j \geq F_{cl} \end{array} \right) \tag{4.21}$$

Parameters $v_{c,max}$ and $v_{c,min}$ are the extreme values of crack opening displacement (COD) measured by extensometer for every selected cycle. This approach can be easily used in automated experiments, however data can be influenced by large degree of noise or wrong tuning. The effective stress intensity factor range can then be calculated using U parameter as:

$$\Delta K_{eff} = U \cdot \Delta K_{app} = \frac{F_{max} - F_{cl}}{F_{max} - F_{min}} \Delta K_{app} = \Delta K_{app} + K_r \qquad (4.22)$$

Where U is the crack closure level, $F_{max\,(min)}$ represents the maximum (and minimum) force in each cycle of loading and F_{cl} is the crack closure force obtained from hysteresis loop analysis. The values of U parameter obtained from FCG tests on S355 specimens are presented in Figure 4.6. Experimental evidence shows that U parameter is nearly constant throughout each FCG test, and it is evident that higher stress ratio leads to higher values of U parameter which means lower influence of residual stresses. Since minimum applied load is at a higher level when stress ratio is increased, the residual (compressive) stress field generated ahead of the crack tip has lower magnitude, and by consequence, U parameter is closer to one. Since the Elber parameter is constant for each test, the relation between the applied stress intensity factor range and the residual stress intensity factor is linear as shown in Figure 4.7. Residual stress intensity factor increases as the applied stress intensity factor range is increased. Residual values are smaller for the specimen with higher stress ratio.
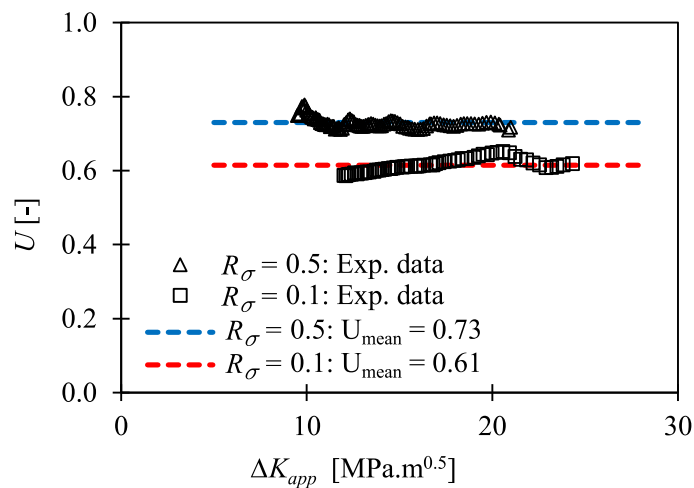
Figure 4.6. Elber parameter obtained from FCG tests on S355 specimens.
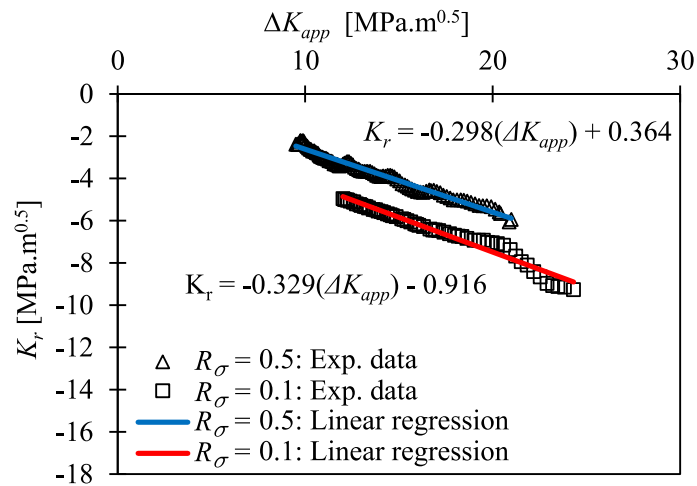
Figure 4.7. Residual stress intensity factor obtained in FCG tests for S355.

Considering experimental results for residual stress intensity factor and Eq. (4.22), the effective values of stress intensity factor range were computed for both $R_\sigma = 0.1$ and $R_\sigma = 0.5$ experimental tests and results are presented in Figure 4.8. It is observed that the influence of the stress ratio is correctly considered since experimental data can be correlated with a unique FCG curve with high level of correlation ($R^2 = 0.98$).

Figure 4.8. Fatigue crack growth rate for S355 using effective stress intensity factor range computed by experimental approach.

4.4.2   Analytical approach

The set of equations presented in Section 4.3.2 enable the computation of stress-strain field ahead of the crack tip induced by a load reversal which can be represented by the fluctuations

of the stress intensity factor, ΔK_{app} as shown in Figure 4.9a). The analysis and computation of residual stress field, $\sigma_r(x)$, formed ahead of the crack tip by a load reversal is then executed. Figure 4.9b) represents a schematic distribution of stresses ahead of the crack tip corresponding to maximum and minimum applied load level for positive (but close to zero) value of stress ratio. In this situation, a compressive residual stress field is generated at minimum load level whose effects need to be included in the analysis.

a)   b)
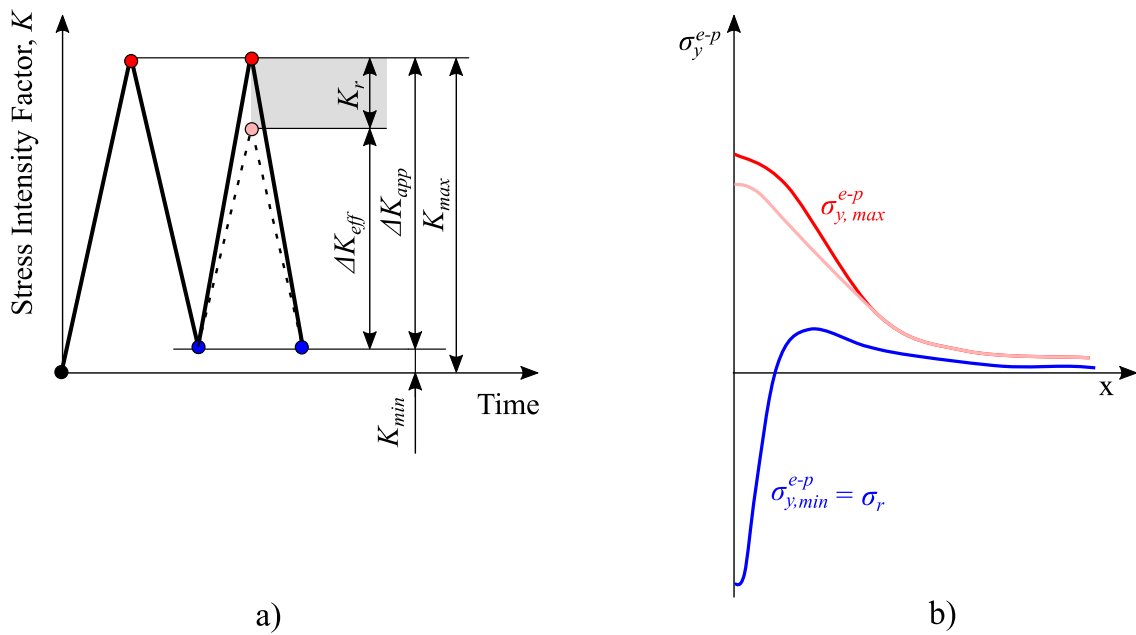
Figure 4.9. a) Schematic representation of stress intensity factor history; b) elastic-plastic stress field induced by cyclic loading ahead of the crack tip.

The computation of residual stress field ahead of the crack tip enables the determination of residual stress intensity factor using the weight function method [62] expressed in Eq. (4.23).

$$K_r = \int_0^a \sigma_r(x)\, m(x,a)\ dx \qquad (4.23)$$

The physical crack tip location at '$x = a$' was chosen as the upper limit of the integration and the universal weight function expression for CT specimens – Eq. (4.24) – was used.

$$m(x,a) = \frac{2}{\sqrt{2\pi(a-x)}}\left[1 + M_{w,1}\left(1 - \frac{x}{a}\right)^{1/2} + M_{w,2}\left(1 - \frac{x}{a}\right)^{1} + M_{w,3}\left(1 - \frac{x}{a}\right)^{3/2}\right] \quad (4.24)$$

The geometry dependent factors $M_{w,1}$, $M_{w,2}$ and $M_{w,3}$ for a CT specimen are given in Glinka [62]. The effective values of stress intensity factor are obtained considering the applied values of stress intensity factor and the residual stress intensity factor. As it is presented in Figure 4.9a), the influence of residual stress intensity factor is considered by changing (decreasing) the maximum value of the stress intensity factor while the minimum value remains equal to the applied value. The effective value of the stress intensity factor range, ΔK_{eff}, and the effective value of the maximum stress intensity factor, K_{max}^{eff}, are computed using Eq. (4.25) and Eq. (4.26), respectively. Since residual stress intensity factor is obtained from compressive stresses, its value is negative.

$$\Delta K_{eff} = \Delta K_{app} + K_r \tag{4.25}$$

$$K_{max}^{eff} = K_{max} + K_r \tag{4.26}$$

The main parameter which influences residual stresses is the crack tip radius, ρ^*. The criterion chosen to define the correct value of the crack tip radius was by minimizing the mean squared error (MSE) when analytical values of residual stress intensity factors are compared to experimental results. Eq. (4.27) presents how MSE is computed in which $K_{r,j}$ is the experimental value, $\widehat{K}_{r,j}$ is the estimation analytical value of the residual stress intensity factor and n is the sample size.

$$MSE = \frac{1}{n} \sum_{j=1}^{n} \left(K_{r,j} - \widehat{K}_{r,j} \right)^2 \tag{4.27}$$

Table 4.1 presents analytical results of residual stress intensity factor for S355. The first attempt to compute residual stress intensity factors was made with $\rho^* = $ 1E-5 m which is similar to the value proposed in Correia *et al.* [115] ($\rho^* = 5.5E^{-5}m$), however, it was found that it leads to low values of residual stresses and high value of MSE (greater than 2) meaning that it is not close to experimental evidence. In fact, the value of the crack tip proposed in Correia *et al.* [115] was based only on numerical and analytical approaches. Decreasing the value of the crack tip radius led to higher stresses at the crack tip and by consequence higher residual stresses. In this sense, the application of $\rho^* = $ 1E-6 m and $\rho^* = $ 1E-7 m was tested. Results have shown that the

smaller the crack tip radius, the closer the obtained value of residual stress intensity factor is to experimental results. For the smallest value of crack tip radius, $\rho^* = 1E\text{-}7$ m, U parameter is nearly the same as obtained in Figure 4.6 and the value of MSE is very close to zero (0.07).

Table 4.1. Analytical results of residual stress intensity factor for **S355** and comparison with experimental values.

R_σ [-]	ΔK_{app} [MPa.m$^{0.5}$]	$\rho^* = 1E\text{-}5$ m			$\rho^* = 1E\text{-}6$ m			$\rho^* = 1E\text{-}7$ m		
		U [-]	K_r [MPa.m$^{0.5}$]	MSE	U [-]	K_r [MPa.m$^{0.5}$]	MSE	U [-]	K_r [MPa.m$^{0.5}$]	MSE
0.5	9.50	0.87	-1.25	2.13	0.79	-2.03	0.37	0.75	-2.35	0.07
	13.45	0.84	-2.20		0.77	-3.06		0.75	-3.41	
	20.99	0.80	-4.10		0.76	-5.04		0.74	-5.43	
0.1	12.01	0.75	-8.95	2.47	0.66	-7.89	0.23	0.62	-7.45	0.07
	15.95	0.72	-11.42		0.64	-10.28		0.62	-9.82	
	24.31	0.68	-16.58		0.63	-15.34		0.61	-14.83	

The comparison between experimental and analytical values of residual stress intensity factor obtained using a crack tip radius of $\rho^* = 1E\text{-}7$ m is shown in Figure 4.10. This value was used in the next steps of fatigue crack growth model implementation.
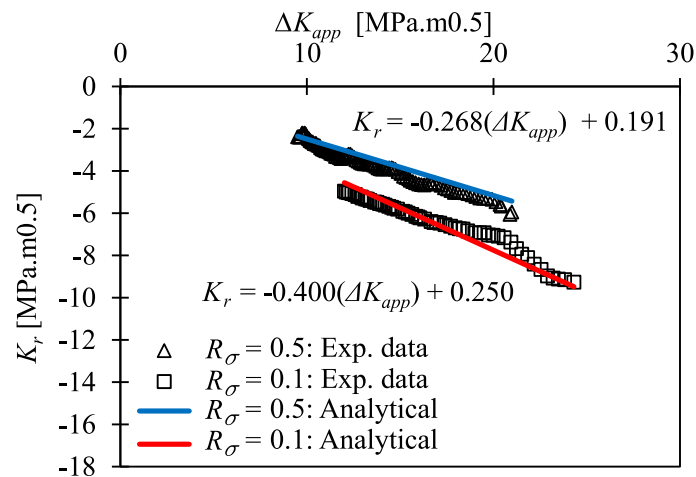
Figure 4.10. Analytical computation of residual stress intensity factor for S355.

The computation of residual stress intensity factor for FCG tests on S235 specimens by means of analytical approach was implemented considering the same three values of crack tip radius as used in S355. Since there were no experimental computation of residual stress intensity factor, the analysis of results is made by computing its variation (difference) by decreasing the crack tip radius. If $\rho^* = 1E\text{-}6$ m is used, the value of the residual stress intensity factor increases

between 10 to 20% when compared to the values obtained with $\rho^* = $ 1E-5 m. If $\rho^* = $ 1E-7 m is used, the value of the residual stress intensity factor increases between 4 and 6% when compared to the values obtained with $\rho^* = $ 1E-6 m. This means that for $\rho^* = $ 1E-7 m, the value of residual stress intensity factor is already stabilized, and no significant changes will be obtained by decreasing more the value of the crack tip radius. Furthermore, the computation time when using, for example, $\rho^* = $ 1E-8 m, increases significantly. Results are shown in Table 4.2. Considering the analytical results obtained with $\rho^* = $ 1E-7 m, a graphical representation is shown in Figure 4.11. It is possible to observe that residual stresses for $R_\sigma = $ 0.05 are higher when compared to results obtained for $R_\sigma = $ 0.25, as was expected.

Table 4.2. Analytical results of residual stress intensity factor for **S235**.

R_σ [-]	ΔK_{app} [Mpa.m$^{0.5}$]	$\rho^* = $ 1E-5 m		$\rho^* = $ 1E-6 m			$\rho^* = $ 1E-7 m		
		U [-]	K_r [MPa.m$^{0.5}$]	U [-]	K_r [MPa.m$^{0.5}$]	Diff. [%]	U [-]	K_r [MPa.m$^{0.5}$]	Diff. [%]
0.05	16.39	0.67	-5.40	0.61	-6.43	16.0	0.58	-6.81	5.5
	21.05	0.65	-7.35	0.60	-8.41	12.6	0.58	-8.80	4.4
	27.19	0.63	-9.93	0.59	-11.02	9.9	0.58	-11.43	3.6
0.25	14.87	0.71	-4.28	0.65	-5.25	18.5	0.62	-5.61	6.3
	18.69	0.69	-5.73	0.64	-6.73	14.8	0.62	-7.10	5.2
	24.49	0.68	-7.94	0.63	-8.97	11.5	0.62	-9.35	4.1
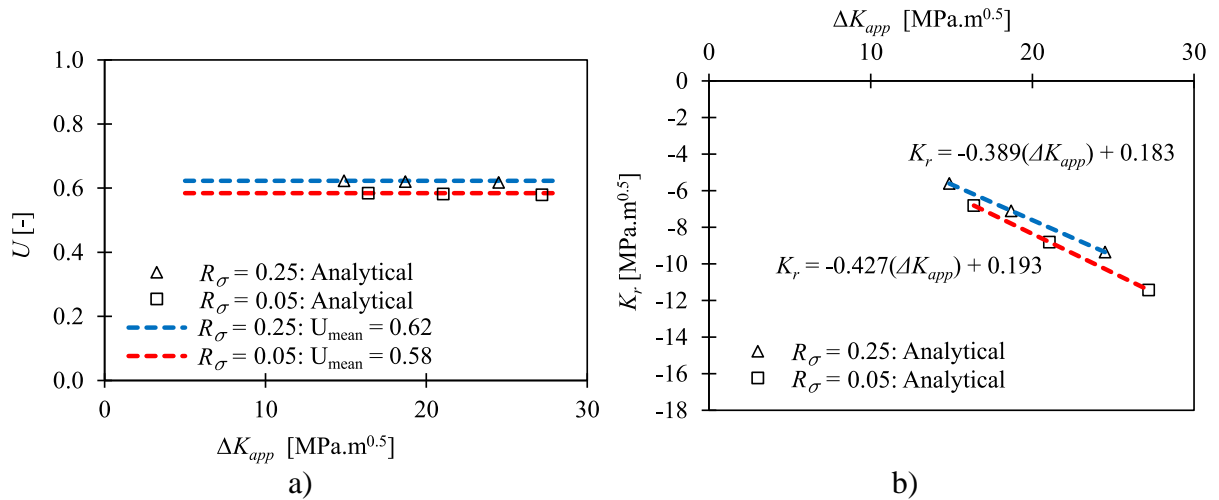
Figure 4.11. Analytical results for FCG tests on S235: a) U parameter; b) Residual stress intensity factor.

Since S235 has a lower value of the yield stress when compared to S355, it is expected that higher level of plasticity is formed for S235 leading to higher residual stresses. Moreover, the thickness of S235 specimens (4 mm) is smaller than the thickness of S355 specimens (12 mm)

which means that it is closer to plain stress conditions and, therefore, the plastic radius should be higher. Considering these aspects, the comparison of U parameter obtained for S235 and S355 – see Figure 4.12a) – shows that U parameter is smaller for S235 which is coherent with previous statements. The relation between the applied stress intensity factor range and the residual stress intensity factor for S235 is presented in Figure 4.11b).
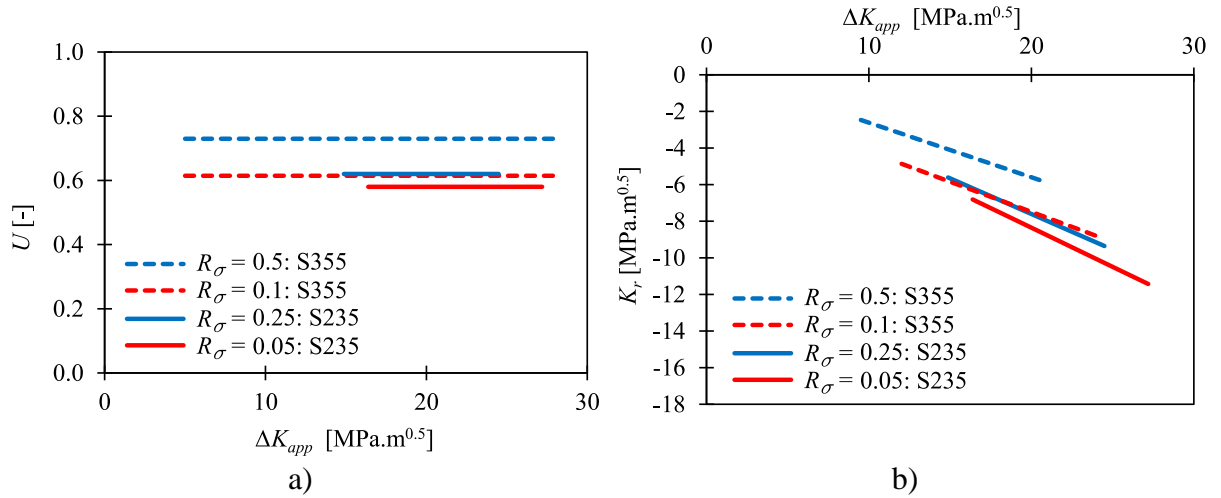
Figure 4.12. Comparison between S355 and S235: a) U parameter; b) Residual stress intensity factor.

Considering these analytical results for residual stress intensity factor and Eq. (4.22), the effective values of stress intensity factor range were computed for both $R_\sigma = 0.05$ and $R_\sigma = 0.25$ and results are presented in Figure 4.13. Crack growth rates used in this figure were extracted from experimental results presented on Section 3.3.4.3.

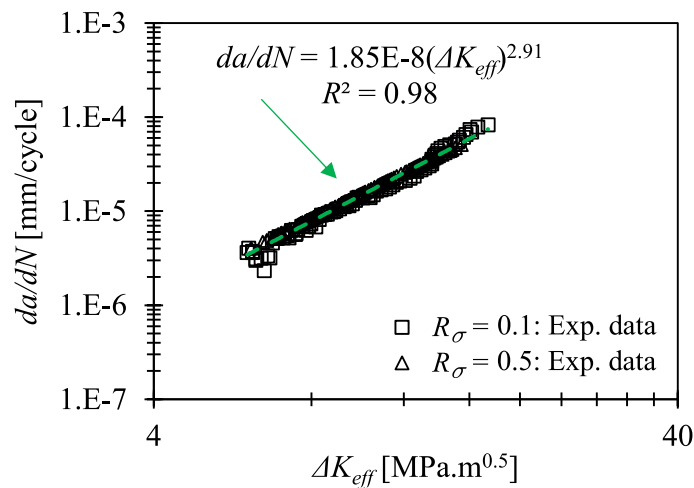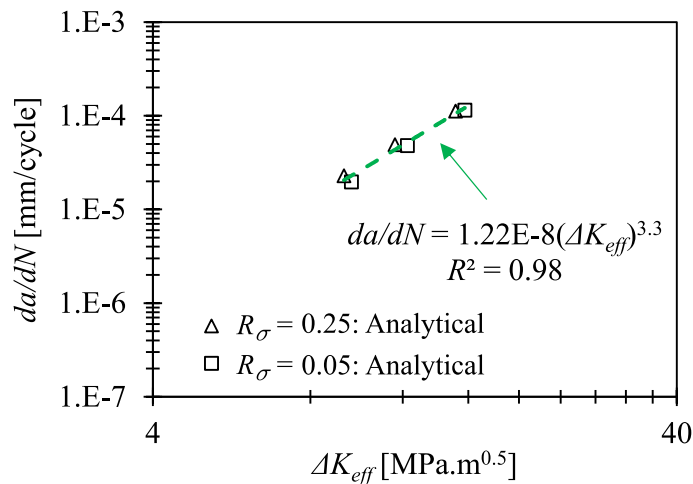
Figure 4.13. Fatigue crack growth rate for S235 using effective stress intensity factor range computed by analytical approach.

Then, the obtained values for effective stress intensity factor ranges can be compared for both materials. As it is shown in Figure 4.14, S355 has slower fatigue crack growth rates when compared with results from S235 considering the effect of the residual stresses (effective stress intensity factor ranges). This is coherent with results obtained using the applied values of the stress intensity factor range presented on Section 3.3.4.5.
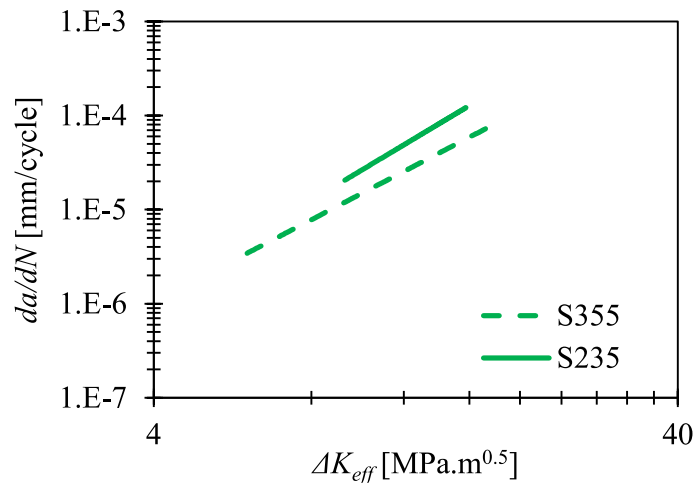
Figure 4.14. Comparison between S355 and S235 FCG based on effective stress intensity factor ranges.

4.4.3   Numerical approach

To complement this study,

Three analyses were performed for each value of R_σ varying the value of the crack length, a. The material model implemented in this numerical analysis follows the values obtained for the cyclic elastoplastic behaviour of S355 presented in Section 3.3.3.2. Boundary conditions of the numerical model are $U_y = UR_x = UR_z = 0$ in the symmetry line and $U_x = 0$ in the hole of the loading pin. Finite element mesh is presented in Figure 4.16 and it is composed of CPS3 two-dimensional elements (3-node linear plane stress triangle). The geometric discontinuity in the crack tip requires a refined mesh to get accurate values of stresses and strains, therefore the envelope of this zone has a mesh size smaller than the mesh size in the model and the minimum size in this zone is 4.6E-5 mm.
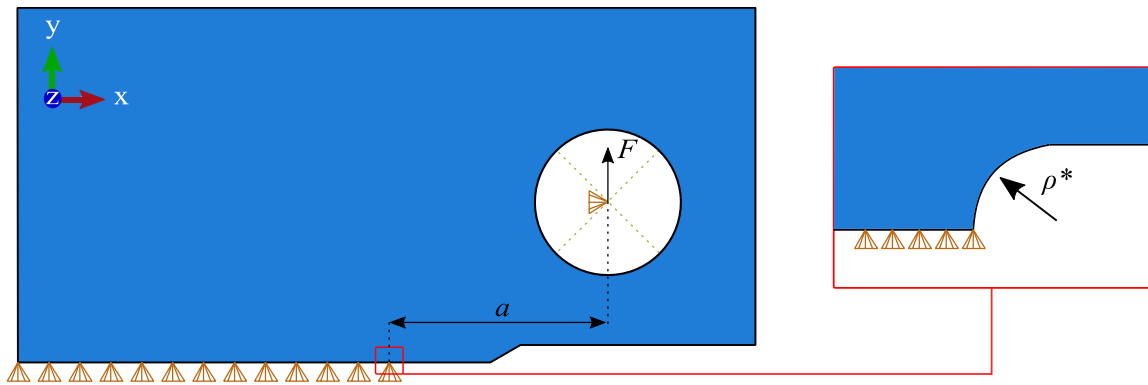
Figure 4.15. Boundary conditions and load definitions of the numerical model to compute residual stresses ahead of the crack tip during FCG.
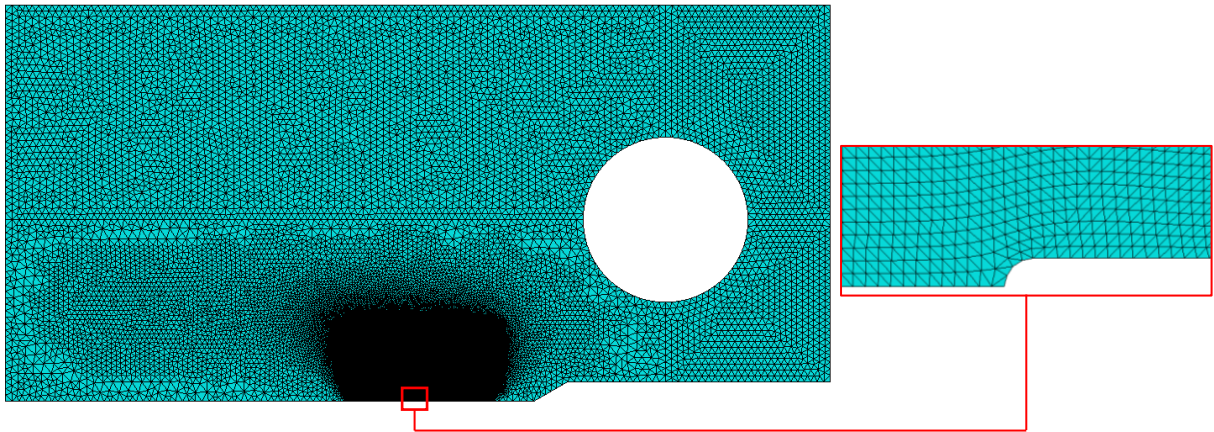
Figure 4.16. Finite element mesh of the numerical model.

These numerical analyses enable to get the stress field ahead of the crack tip aiming to compute compressive (residual) stresses and then residual stress intensity factor. From Figure 4.17 to Figure 4.22 it is possible to observe the stress field at maximum applied load and at half of the applied load range for three models with stress ratio equal to 0.1 and for three models with stress ratio equal to 0.5 varying the crack length. Residual stresses generated from each load reversal were computed considering the stress field ahead of the crack tip at maximum applied load minus two times the stress field ahead of the crack tip at half of the applied load range as presented in the Eq. (4.28). The value of the applied load was taken from experimental data.

$$\sigma_r = \sigma_{y,max}^{e-p} - 2 \cdot \sigma_{y,a}^{e-p} \qquad\qquad (4.28)$$
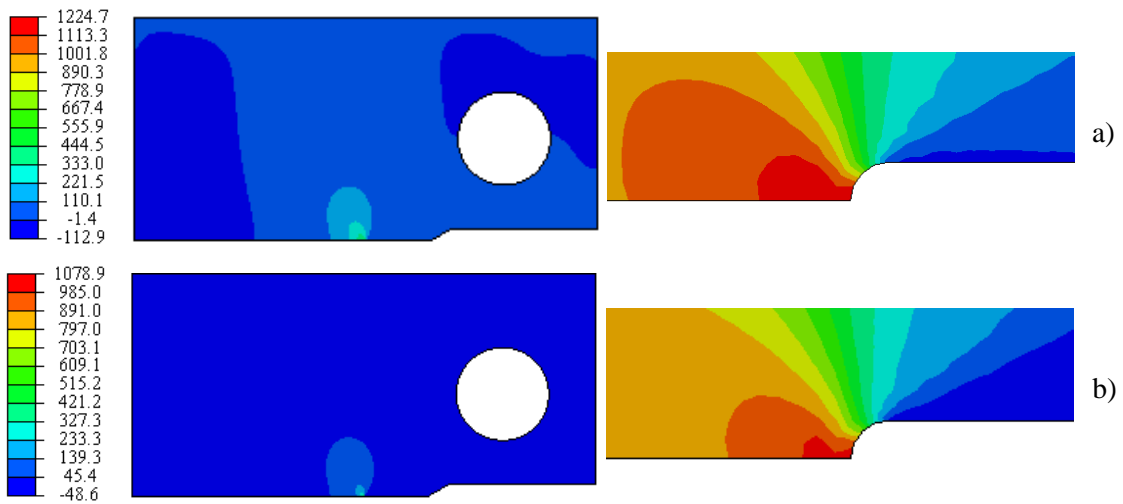
Figure 4.17. Elastoplastic stress field (in MPa) σ_y^{e-p} for crack length $a = 18.67mm$ and $R_\sigma = 0.1$:
a) at maximum load $F = F_{max}$; b) at half of range load value $F = \Delta F/2$.
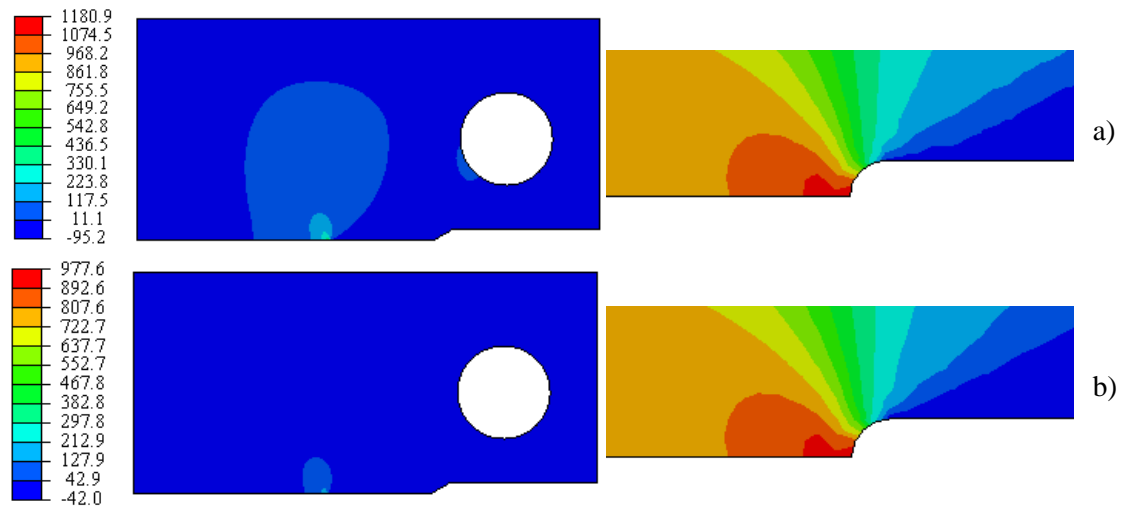
Figure 4.18. Elastoplastic stress field (in MPa) for crack length $a = 23.92mm$ and $R_\sigma = 0.1$:
a) at maximum load $F = F_{max}$; b) at half of range load value $F = \Delta F/2$.
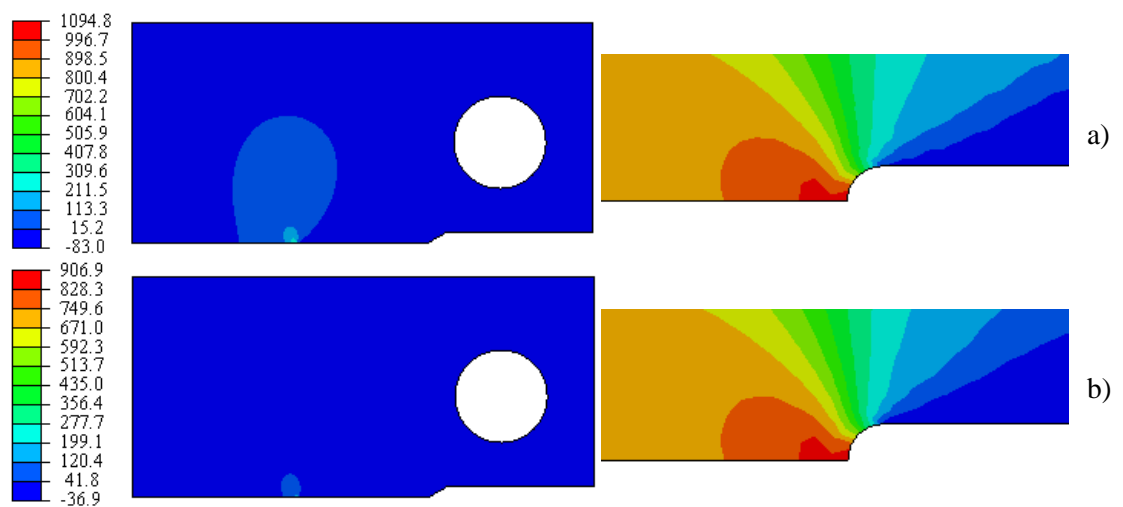
Figure 4.19. Elastoplastic stress field (in MPa) for crack length $a = 27.64mm$ and $R_\sigma = 0.1$:
a) at maximum load $F = F_{max}$; b) at half of range load value $F = \Delta F/2$.
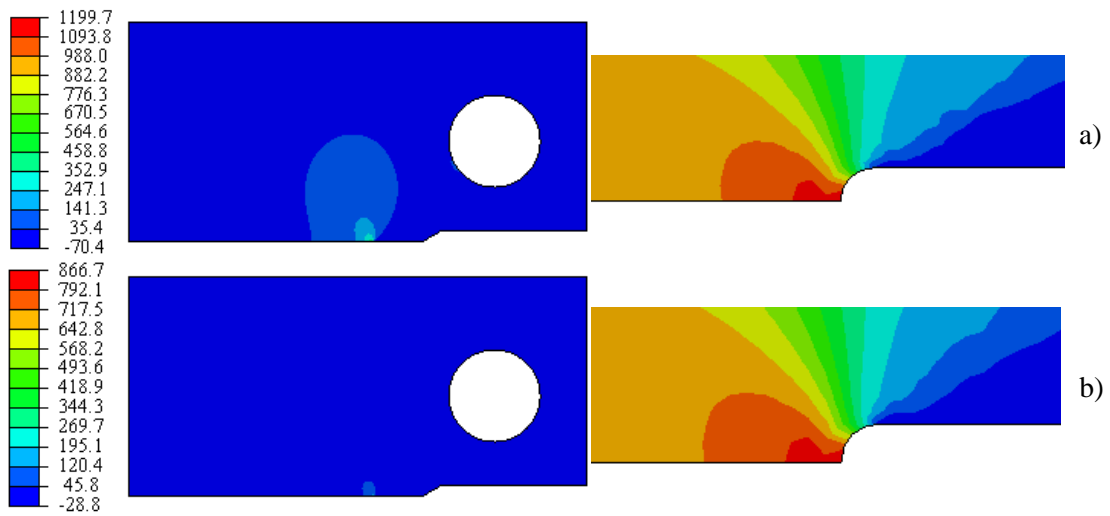
Figure 4.20. Elastoplastic stress field (in MPa) for crack length $a = 16.53mm$ and $R_\sigma = 0.5$: a) at maximum load $F = F_{max}$; b) at half of range load value $F = \Delta F/2$.
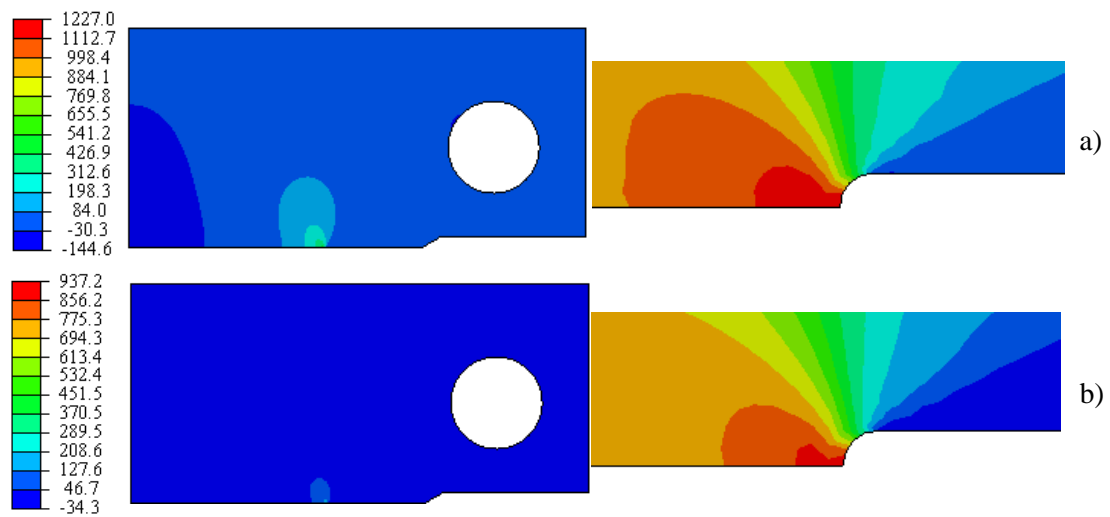
Figure 4.21. Elastoplastic stress field (in MPa) for crack length $a = 23.12mm$ and $R_\sigma = 0.5$: a) at maximum load $F = F_{max}$; b) at half of range load value $F = \Delta F/2$.
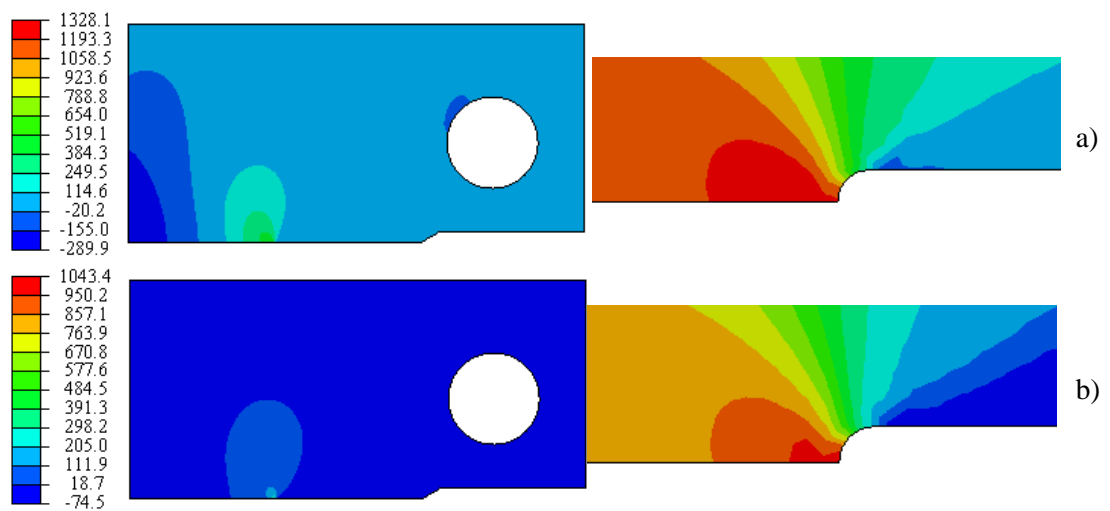
Figure 4.22. Elastoplastic stress field (in MPa) for crack length $a = 29.98mm$ and $R_\sigma = 0.5$: a) at maximum load $F = F_{max}$; b) at half of range load value $F = \Delta F/2$.

The comparison between Unigrow analytical procedure and numerical approach to compute residual stress field ahead of the crack tip is presented in Figure 4.23. The internal (residual) stresses induced by the reversed cyclic plasticity is shown for three different values of crack length for each stress ratio. It is possible to observe a very good correlation between analytical and numerical results.
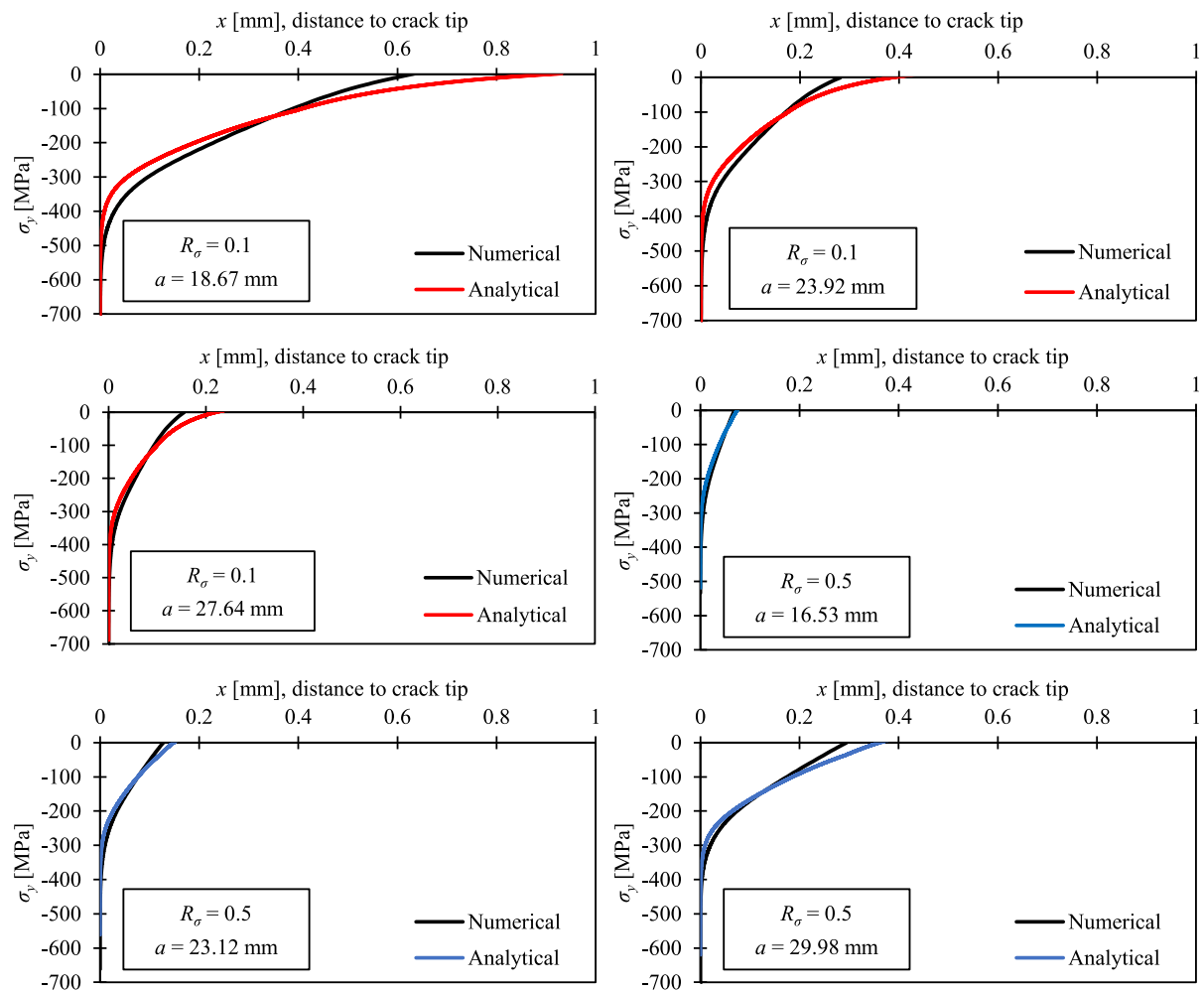
Figure 4.23. Residual compressive stresses ahead of the crack tip induced by reversed cyclic plasticity on S355 CT specimen: comparison between numerical and analytical approaches.

The compressive residual stresses ahead of the crack tip were then used to compute the residual stress intensity factor, K_r, using the integration method presented in Eq. (4.23). Table 4.3 presents the results for the three values of crack length selected for each value of stress ratio comparing the results for experimental, analytical, and numerical approaches. It is possible to

observe a very good correlation between both analytical and numerical approaches to experimental results.

Table 4.3. Residual stress intensity factor for FCG on S355 CT specimens obtained by experimental, analytical and numerical procedures.

$R_\sigma = 0.1$								
a [mm]	18.67			23.92			27.64		
K_r [MPa.m$^{0.5}$]	Exp.	Ana.	Num.	Exp.	Ana.	Num.	Exp.	Ana.	Num.
	-9.3	-9.5	-10.4	-6.2	-6.1	-6.8	-4.9	-4.6	-4.9
$R_\sigma = 0.5$								
a [mm]	16.53			23.12			29.98		
K_r [MPa.m$^{0.5}$]	Exp.	Ana.	Num.	Exp.	Ana.	Num.	Exp.	Ana.	Num.
	-2.4	-2.4	-2.7	-3.7	-3.4	-3.8	-5.9	-5.4	-5.7

The relation between residual stress intensity factor and the applied stress intensity factor range considering numerical, analytical and experimental approach is presented in Figure 4.24. Higher values of applied stress intensity factor range conducted to higher values of residual stress intensity factor. Residual stress intensity factor is smaller for higher values of stress ratio. It is also possible to observe the good correlation between analytical and numerical approaches with experimental results for all values of applied stress intensity factor range. The error found for numerical computation of residual stress intensity factor was measured using MSE parameter resulting in 0.59 for $R_\sigma = 0.1$ and 0.28 for $R_\sigma = 0.5$, which allow the statement that numerical results are very close to experimental evidence.
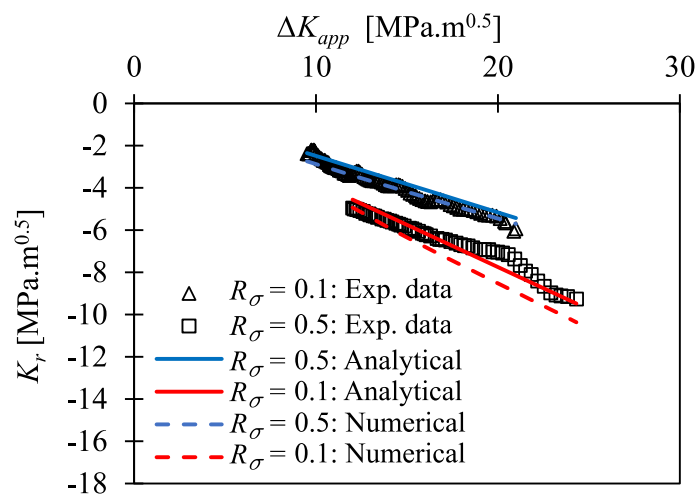
Figure 4.24. Relation between residual stress intensity and applied stress intensity factor range for S355: comparison between experimental, analytical and numerical approaches.

4.5   Fatigue crack growth rates

Using the values for effective stress intensity factor range obtained for three crack length values for both $R_\sigma = 0.1$ and $R_\sigma = 0.5$, fatigue crack growth rates of S355 were computed by means of the model described in Section 4.3. The original UniGrow model assumes that the process block size used to collapse FCG data is the same as the crack tip radius. This approach neglects the effect of the increasing plastic zone ahead of the crack tip during FCG test with constant stress ratio as represented in Figure 4.25. To consider this effect, the process block size, δ_p, used in this investigation to collapse FCG data is based on a similar relation used to obtain the crack tip plasticity radius. As it is described in Eq. (4.3), the proposed expression relies on the effective stress intensity factor, ΔK_{eff}, and on the cyclic yield strength of the material, σ_0'.
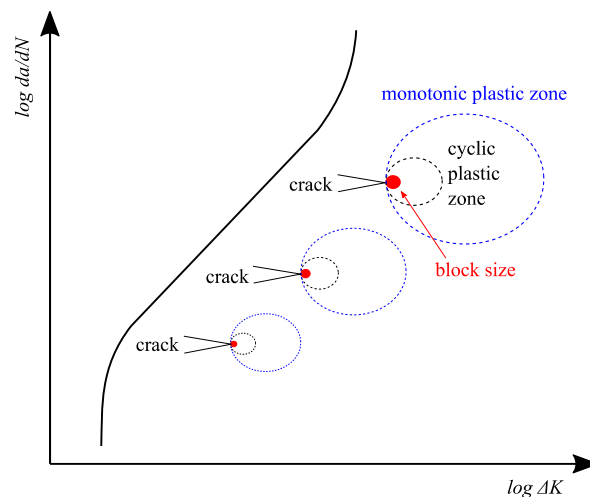
Figure 4.25. Schematic illustration of monotonic, cyclic plastic zone and block size during FCG test.

Fatigue crack growth data and effective stress intensity factor range obtained experimentally are compared with predicted values in Figure 4.26. Mean predicted values compare very well with experimental evidence which means that Eq. (4.3) stands as a reliable approach to determine the size of the process block to derive fatigue crack growth rate. For each value of effective stress intensity factor range, there is a correspondent block size – see Table 4.4 – which is used to compute fatigue crack growth rate using Eq. (4.5). The number of cycles is dependent on the damage parameter (SWT-life) which is obtained based on the effective values of strain amplitude and maximum stress found ahead of the crack tip within the size of the process block.

Mean FCG curve for S355 was based on mean values of cyclic elastoplastic curve and mean values of SWT damage parameter computed in Section 3.3.3 while characteristic FCG curve was defined with characteristic values of SWT damage parameter of S355 also presented in Section 3.3.3. With this approach, a reliable design FCG curve for S355 is obtained as it is possible to observe in Figure 4.26.

Table 4.4. Predicted values of fatigue crack propagation rate based on effective stress intensity factor range – **S355**.

ΔK_{eff} [MPa.m$^{0.5}$]	Process block size δ_p [m]	Mean values			Characteristic values		
		SWT_{block} [-]	$2N_{block}$ [-]	da/dN [mm/cycle]	SWT_{block} [-]	$2N_{block}$ [-]	da/dN [mm/cycle]
7.3	1.3E-5	4.73	3731	7.1E-6	4.71	1266	2.1E-5
9.9	2.3E-5	5.05	3297	1.5E-5	5.01	1133	4.3E-5
15.2	5.5E-5	5.45	2842	4.1E-5	5.39	991	1.2E-4
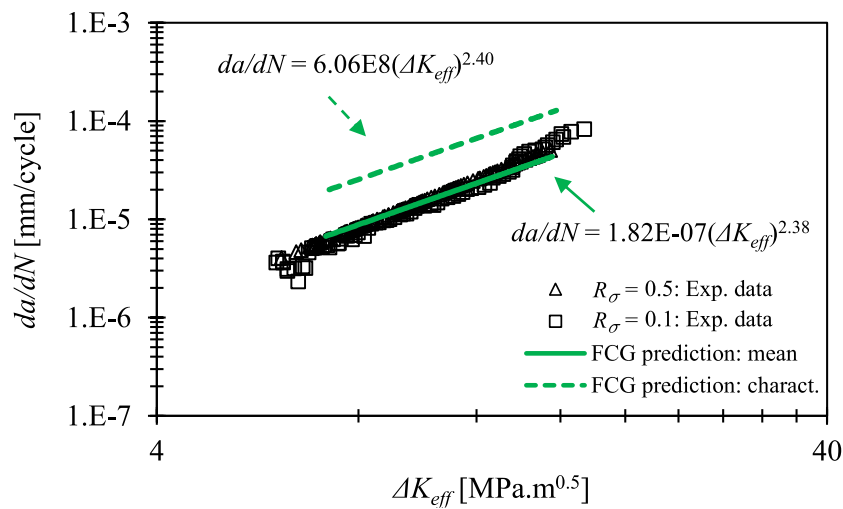
Figure 4.26. Comparison between predicted and experimental values of effective fatigue crack growth rates for **S355**.

It should be stated that, if process block size, δ_p, is assumed as the same as the value of crack tip radius, $\rho^* = 1.0\text{E-7}$ m, SWT_{block} increases significantly leading to very low number of cycles to collapse the material ahead of the crack tip and high fatigue crack growth rates that cannot be correlated with experimental results. The proposed FCG model was also applied for S235 to obtain prediction values of fatigue crack propagation rate. In Table 4.5, the values of process bock size computed with Eq. (4.3) are presented for three different values of effective stress

intensity factor range. The average value of effective strain amplitude and effective maximum stress within the block size distance ahead of the crack tip were computed based on material formulations. SWT damage parameter was then obtained to determine the number of cycles to achieve fatigue failure. Finally, fatigue crack propagation rate was found. This procedure was implemented using mean and characteristic values of material parameters determined in Section 3.3.3.

Table 4.5. Predicted values of fatigue crack propagation rate based on effective stress intensity factor range – **S235**.

ΔK_{eff} [MPa.m$^{0.5}$]	Process block size δ_p [m]	Mean values			Characteristic values		
		SWT_{block} [-]	$2N_{block}$ [-]	da/dN [mm/cycle]	SWT_{block} [-]	$2N_{block}$ [-]	da/dN [mm/cycle]
9.4	2.0E-5	4.60	2726	1.6E-5	4.61	784	5.5E-5
11.9	3.3E-5	4.84	2515	2.7E-5	4.85	724	9.3E-5
15.4	5.5E-5	5.10	2324	4.7E-5	5.10	670	1.6E-4

Figure 4.27 shows the relation between fatigue crack growth rate and effective stress intensity factor for S235 considering experimental data and analytical model predictions. It is observed that experimental evidences are within mean and characteristic prediction values. Characteristic material parameters used in the FCG model led to reliable design prediction of fatigue crack growth for S235.
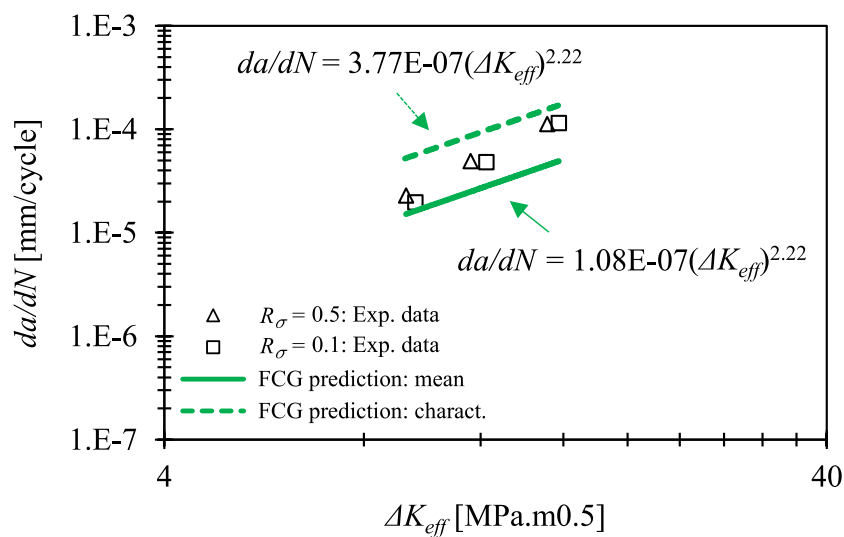
Figure 4.27. Comparison between predicted and experimental values of effective fatigue crack growth rates for **S235**.

4.6   Conclusions

A unified two-stage fatigue methodology based on Unigrow model was implemented to assess the fatigue crack growth behaviour of S355 and S235 considering plasticity induced crack closure effect. This model relies on elastoplastic stress-strain field formed ahead of the crack tip during fatigue loading. Crack closure effect induced by plasticity is assessed with residual stress intensity factor.

In this chapter, experimental FCG results on S355, and S235 CT specimens were analysed. Residual stress intensity factor was evaluated by means of experimental, analytical, and numerical approaches. During fatigue crack growth tests of S355, applied load and crack opening displacement were recorded for several cycles to evaluate crack opening force and U parameter. Lower values of applied stress ratio originate lower values of U parameter which means that mean stress effect increases. This relation between effective and total load ranges is kept constant through all experimental test procedure. Residual stress intensity factor increases (absolute value) when the applied stress intensity factor range increases showing that these parameters are linearly dependent. Fatigue crack growth rates were then correlated with effective stress intensity factor ranges showing that crack closure effects were successfully considered since experimental results from tests with different stress ratios converged in a unique FCG curve.

In the case of analytical approach to compute residual stress intensity factor, UniGrow model formulations were used considering different values of crack tip radius, ρ^*. Analytical and experimental results for S355 were compared using mean squared error approach. It was found that smaller values of crack tip radius led to better results. It is proposed to consider $\rho^* = 1\text{E-}7\text{m}$ for both S235 and S355. Fatigue crack growth rates of S235 and S355 based on effective stress intensity factor ranges computed by means of this analytical approach were compared and it was possible to observe that S355 has a better performance indicating that higher tensile mechanical properties originate lower fatigue crack growth rates.

In what concerns numerical approach, used only for S355, it was intended to show that stress-strain field ahead of the crack tip can also be assessed by means of numerical procedures.

Residual stresses and residual stress intensity factor obtained numerically are similar to experimental results.

Finally, the prediction of fatigue crack growth rates considering crack closure effect was done with the proposed FCG model. The main difference from original UniGrow model stands on the assumption that process block size depends on material properties (cyclic yield strength) and effective stress intensity factor range. In this sense, a new formulation was proposed to determine this parameter which is similar to plasticity radius formulations. Mean and characteristic values of material properties determined in previous chapter were used to assess SWT damage within the process block size ahead of the crack tip for several stages of FCG tests. Mean FCG predictions based on this approach presented very good correlation with experimental data and characteristic FCG predictions can be considered as a reliable and safe design approach.

5   FATIGUE MODELLING OF BOLT HOLE DETAIL BASED ON GLOBAL AND LOCAL APPROACHES

5.1   Introduction

Fatigue behaviour of bolted or riveted connections is dependent on the stress level that their components are subjected. Fatigue cracks emerging from the connecting plate are more frequent because geometric discontinuities lead to high stress concentrations. A peak of stresses is found at the edges of the bolt hole. This high level of stresses can originate a crack which will propagate perpendicular to the load direction.

This chapter intends to be a valuable contribute to analyse the fatigue mechanisms in bolt hole details by conducting experimental fatigue tests on representative specimens and to address different approaches to model fatigue life. A schematic representation about the contents of this chapter is presented in Figure 5.1.

Fatigue tests on steel plates with a hole aim to evaluate fatigue crack initiation and propagation phases as well as the fatigue life in which the crack becomes visible (in a real bolted connection). Experimental fatigue results are compared with similar research campaigns found in literature to assess the impact of three important parameters on the fatigue life: application of corrosion protection methods, methodology used to execute the hole in the plate and selection of metallic material.

Different prediction methodologies are addressed to establish reliable methods to assess the fatigue life of this detail. Generally, global prediction methods address fatigue life based on applied nominal stress range values, as it is the case in the design procedure prescribed in EN 1993-1-9 [15]. In this chapter, the reliability of this method is discussed by establish a comparison with experimental fatigue results. Alternatively, local approaches are related with specific fatigue mechanisms allowing for a more detailed analysis. These approaches allow to distinguish initiation and propagation phases and establish reliable predictions for each part. In this sense, the number of fatigue cycles to initiate a crack is addressed by implementing damage models based on local stresses and strains. Three damage models are implemented in this research to analyse the reliability of each method by comparing the results with fatigue life

obtained from experimental tests. Recommendations on DNV-RP-C208 [93] are also implemented to verify its reliability. In what concerns fatigue crack propagation phase, numerical and experimental procedures are used to predict the fatigue life. Furthermore, mean and characteristic values of fatigue material parameters determined in Chapter 3 are used for both initiation and propagation phases to define not only the expected fatigue life of this detail, but also to define a reliable design approach.
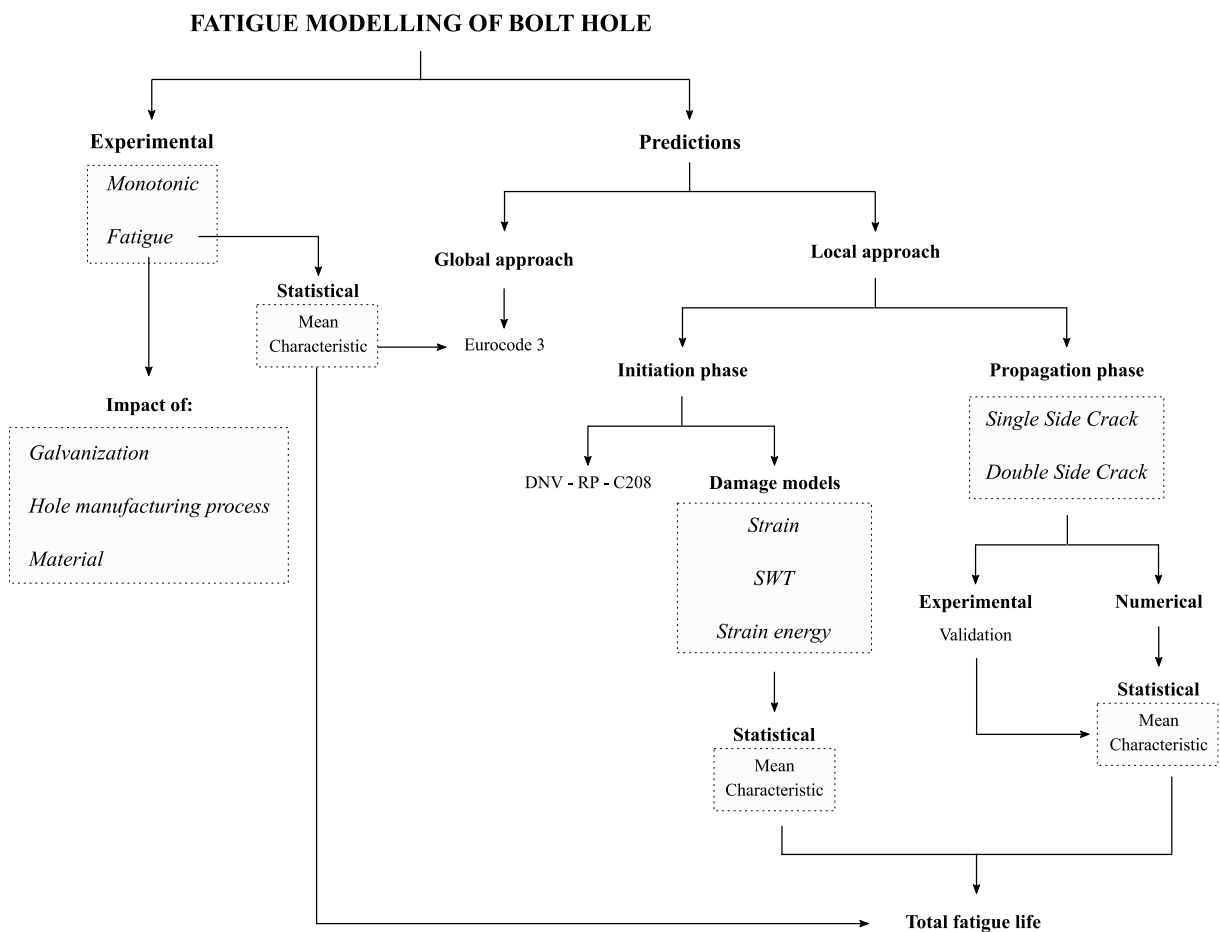
Figure 5.1. Schematic representation for Chapter 5.

5.2   Detail description and monotonic tests

The geometry of the bolt hole used in this investigation is presented in Figure 5.2. It has 18 mm of diameter which means that this detail aims to be representative of a plate component from a bolted shear connection with M16 bolts. According to standard requirements, washers would have 30 mm of outer diameter which means that if a crack emerges from the hole, it will become visible only when its length is greater than 6 mm (starting from the edge of the hole). The

"visible" plate width would be 15 mm in each side of the plate. EN 1993-1-8 [80] indicates a minimum distance from the centre of the hole to the edge of the plate, $e_{2,min} = 1.2 * d_0$. Since $e_{2,plate} = 30\ mm > 1.2 * d_0 = 21\ mm$, geometric requirements are satisfied.
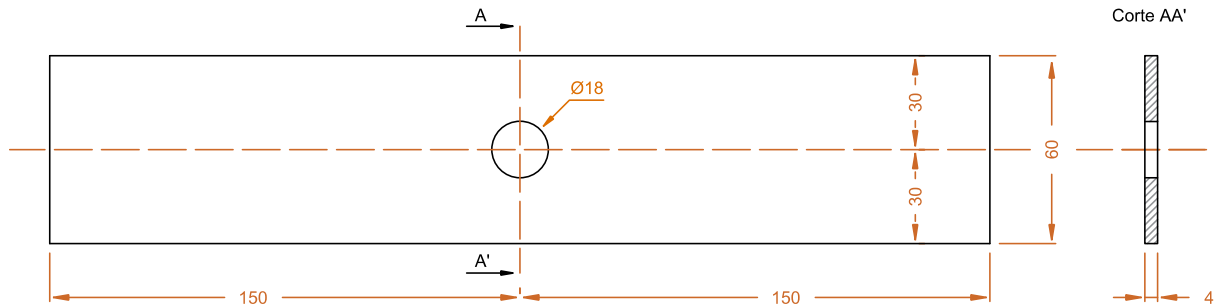
Figure 5.2. Geometry of S235 bolt hole used in experimental campaign (dimensions in mm).

Specimens were machined from a plate according to EN 10025-2 [105]. The hole in the plate was drilled in four stages. The first step was to drill a pilot hole to initiate the drilling process and facilitate the subsequent step of drilling with a drill closer to the final size. Boring ensures that the required diameter is achieved with accuracy and the final process is reaming which guarantees a good quality of surface finishing.

Two static tests were performed in a hydraulic machine Instron 8801 rated to 100 kN – see Figure 5.3 – to obtain the monotonic behaviour of this detail. Specimens were loaded in tension until failure at a loading rate of 1 mm/min. These monotonic tests were essential to define the parameters for fatigue experimental campaign.

Figure 5.3. Experimental test on S235 bolt hole conducted in a hydraulic machine.

The applied load and total displacement were recorded during each test aiming to define the relation between nominal stress computed with net cross-section, σ_{net}, and displacement. Results are presented in Figure 5.4. There is a strong similarity between specimen 1 (Sp. 1) and specimen 2 (Sp. 2) meaning that heterogeneity in material properties and geometric differences between specimens are not significant. The average value of yield and ultimate net cross-section stresses obtained from experimental results are 316.4 MPa and 427.1 MPa, respectively, which are very similar to the yield and ultimate strength obtained from coupon tests of S235 presented in Section 3.3.2 (R_{eH} = 323.3 MPa and R_m = 429.4 MPa).
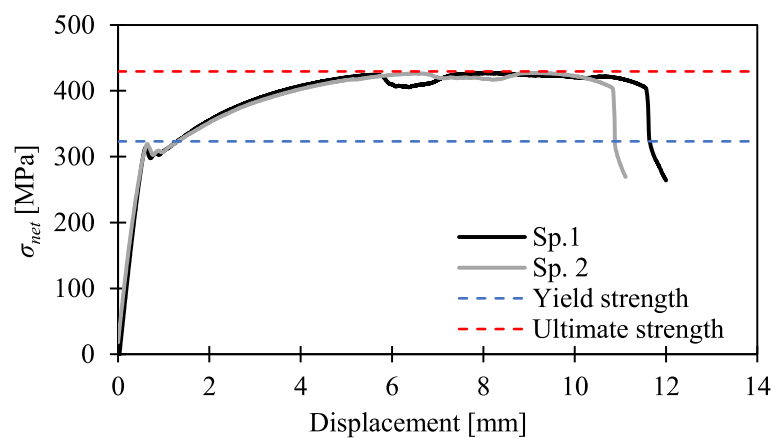
Figure 5.4. Experimental results of static tests on S235 bolt hole.

5.3   Fatigue tests

A set of fatigue tests were performed in the same hydraulic machine used for static tests. These tests were conducted under tensile load control with a stress ratio equal to 0.1. Fatigue tests was distributed in five stress levels, and, for each stress level, three tests were performed, except for $\Delta\sigma_5$ in which only one test was conducted (the lower stress level). The applied load for each test was defined considering static results. The maximum applied load in fatigue tests is lower to the average yield stress obtained experimentally aiming to have predominantly elastic behaviour. Test frequency was defined as 10 Hz, except for $\Delta\sigma_1$ (highest stress level) in which 7.5 Hz was used. These values were defined considering a compromise between the capacity of the machine, the test time and possible heating effects. The number of cycles, N_f, corresponds to the number of cycles at complete failure of specimen. Experimental parameters

and fatigue results are described in Table 5.1. Mean stress effects were considered by computing the normalized stress range, $\Delta\sigma_{net,norm}$, as it is described in Section 2.3.2.

Table 5.1. Experimental results from fatigue tests on S235 bolt hole.

Specimen	Stress level	$\Delta\sigma_{net}$ [MPa]	$\Delta\sigma_{net,norm.}$ [MPa]	A_{net} [mm^2]	σ_{net} [MPa]		f [Hz]	N_f
					Max	Min		
1		250.0	261.1	168.1	277.8	27.8	7.5	66 477
2	$\Delta\sigma_1$	250.0	261.1	168.0	277.8	27.8	7.5	60 751
3		250.0	261.1	167.9	277.8	27.8	7.5	78 408
4		225.0	235.0	167.8	250.0	25.0	10	151 510
5	$\Delta\sigma_2$	225.0	235.0	168.2	250.0	25.0	10	173 280
6		225.0	235.0	168.1	250.0	25.0	10	124 497
7		200.0	208.9	168.2	222.2	22.2	10	276 345
8	$\Delta\sigma_3$	200.0	208.9	167.9	222.2	22.2	10	164 680
9		200.0	208.9	168.0	222.2	22.2	10	191 054
10		175.0	182.8	168.2	194.4	19.4	10	533 947
11	$\Delta\sigma_4$	175.0	182.8	168.0	194.4	19.4	10	1 374 248
12		175.0	182.8	167.9	194.4	19.4	10	748 312
13	$\Delta\sigma_5$	150.0	156.7	168.1	166.7	16.7	10	2 433 191*

*Run-out

Displacement range, Δd, was recorded and representative results are shown in Figure 5.5. There are no significant differences between fatigue tests for the same applied stress range in what concerns the displacement range. Higher displacement values are obtained for higher values of applied stress ranges. It is also observed that displacement range is nearly constant throughout the fatigue test which means that specimens are under linear elastic regime during a major part of the test. The influence of the crack growing process and consequent loose of stiffness is visible only at the final stage of the test.

For the two lower stress levels, $\Delta\sigma_3$ and $\Delta\sigma_4$, the number of cycles for crack propagation phase were estimated based on the deformation values presented in Figure 5.5. Results are shown in Table 5.2. In this analysis, it is assumed that the beginning of the crack occurs when the deformation range value starts to increase up to final rupture. It is known that this assumption will lead to an underestimation of N_p, however it will be important to use as comparison for local fatigue approaches detailed further ahead on this thesis.

Table 5.2. Estimated number of cycles for crack propagation based on deformation values.

Stress level	Specimen	Estimated N_p	
		Value	Mean
$\Delta\sigma_3$	7	16 345	
	8	22 180	19 860
	9	21 054	
$\Delta\sigma_4$	10	13 947	
	11	34 248	28 836
	12	38 312	
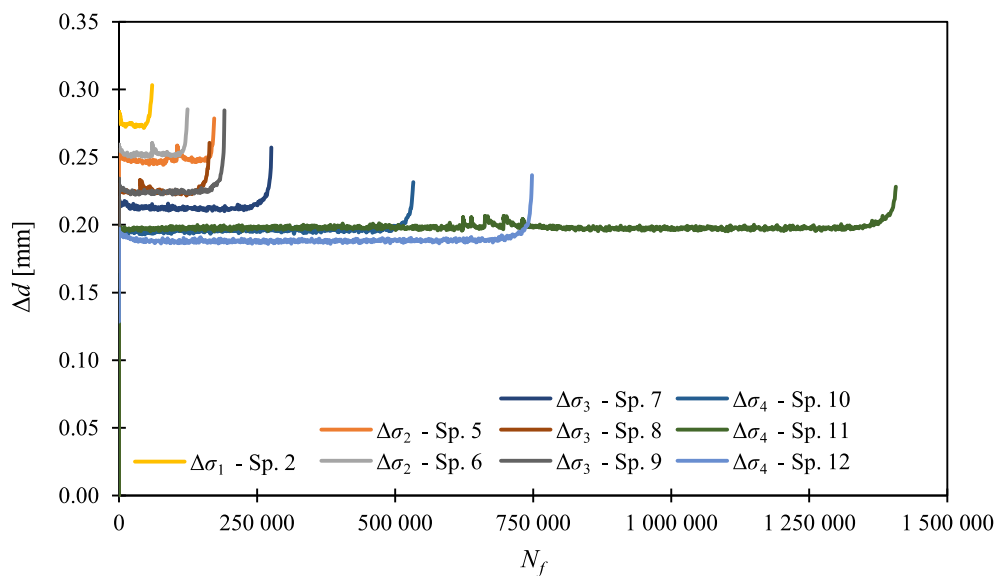
Figure 5.5. Deformation range during fatigue tests on S235 bolt hole.

After each test, fracture surface was analysed. All cracks initiated at the edge of the hole and propagated perpendicularly to the load direction. It was visible that fatigue crack did not start at the same time in both sides of the hole which could be caused by small geometric differences, defects produced in the hole manufacturing process or small load misalignment. From fracture surfaces, it can be observed that typically fatigue crack propagation can be divided in three stages: initiation in the edge of the hole, propagation through the thickness and then through the width of the plate until failure.

Fracture surfaces are shown from Table 5.3 to Table 5.6 for different stress range levels. Crack propagation area can be identified in the fracture surface by its higher smoothness when compared to the region of final static rupture which presents an irregular form. The size of the crack when static rupture happens, a_f, was estimated by analysing fracture surface of each specimen – see Table 5.3 to Table 5.6. This instant of the test (identified in each figure by a red

arrow) is marked by a transition line that has a curved shape, generally. Considering this rounded smoother area, it is expected that crack has initiated in the surface of the plate in which this region is larger. The values of final crack length, a_f, (measured from the edge of the hole until the curved line) are smaller for the highest stress range and they increase when stress range is decreased. For higher stress levels, the final crack length is between 1 to 2 mm while for lower stress level the final crack length is between 5 to 10 mm.

Table 5.3. Analysis of fracture surface for specimens tested under $\Delta\sigma_1$.
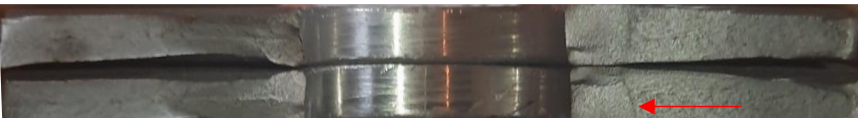
Sp.	Images	a_f [mm]	
		Left	Right
1		1.0	2.0
2		0.5	2.0
3		0.0	2.5

Table 5.4. Analysis of fracture surface for specimens tested under $\Delta\sigma_2$.
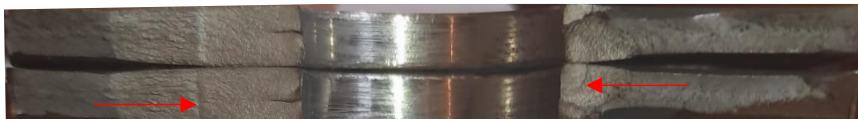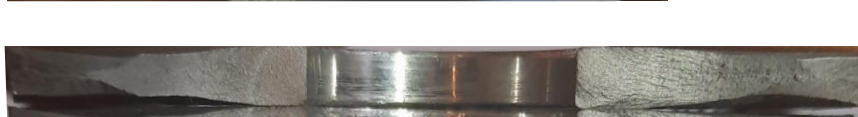
Sp.	Images	a_f [mm]	
		Left	Right
4		5.0	2.5
5		3.5	3.5
6		2.0	3.5

Table 5.5. Analysis of fracture surface for specimens tested under $\Delta\sigma_3$.
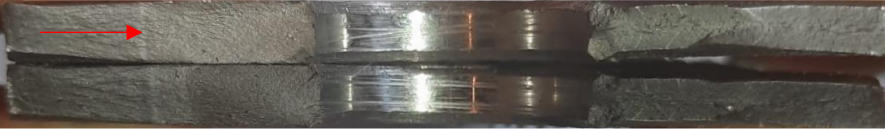
Sp.	Images	a_f [mm]	
		Left	Right
7		11.0	0.0
8		8.5	0.0
9		9.0	0.0

Table 5.6. Analysis of fracture surface for specimens tested under $\Delta\sigma_4$.

Sp.	Images	a_f [mm]	
		Left	Right
10		7.5	5.5
11		10.5	0.0
12		9.5	4.0

With the results presented in the previous tables, it is possible to understand that if this plate is part of a bolted connection, the fatigue crack would be visible before final rupture ($a > 6$mm) only for $\Delta\sigma_3$ and $\Delta\sigma_4$. Furthermore, when the crack becomes visible, the remaining fatigue life is very small when compared to the total number of cycles. The average value of the final crack

length for each stress level is presented in Table 5.7.

Table 5.7. Summary of final crack length for fatigue tests.

Stress level	a_f [mm]		
	Left side	Right side	Mean
$\Delta\sigma_1$	0.50	2.17	1.33
$\Delta\sigma_2$	3.50	3.17	3.33
$\Delta\sigma_3$	9.50	0.00	4.75
$\Delta\sigma_4$	9.17	3.17	6.17

5.4 Global approach

5.4.1 Analysis of experimental data

The fatigue behaviour of this detail can be predicted using the global approach presented in EN 1993-1-9 [15]. The S-N curve recommended in this standard is defined in Table 8.1 dedicated to plain members and mechanically fastened joints. Constructional detail label with number 11 whose description is "structural element with holes subjected to bending and axial forces" was selected. It corresponds to a S-N curve with $m = 3.0$ and detail category 90.

The analysis of the experimental fatigue results was done with a linear regression analysis (run-out value was excluded) to define a mean S-N curve. It resulted in a curve with $m = 6.6$ and $R^2 = 0.89$ which means that the quality of the regression line is good – see Figure 5.6. However, it is noted that the value of the slope is very distinct from the value indicated in the standard. The S-N curve proposed in the standard leads to unsafe results for stress range values above 240 MPa, since fatigue life of specimens tested for $\Delta\sigma_1$ stand below the S-N curve from EN 1993-1-9 [15]. In fact, this design approach seems to be suitable for intermediate stress levels $\Delta\sigma_2$ and $\Delta\sigma_3$ but not for $\Delta\sigma_1$ neither for $\Delta\sigma_4$ and $\Delta\sigma_5$ in which fatigue predictions represent a very conservative approach.

The maximum nominal net stress for $\Delta\sigma_1$ (277.8 MPa) represents 86% of the yield strength obtained in static test. Plasticity level formed around the hole could have affected the fatigue performance of these tests leading to distinct behaviour when compared to intermediate stress levels. Furthermore, in the case of $\Delta\sigma_4$, the maximum nominal net stress (194.4 MPa) represents

60% of the yield strength. Fatigue limit could had affected these tests leading to distinct fatigue performance comparing to intermediate stress levels. These evidences indicate that linear global fatigue models might not be the best suitable approach to establish a full range reliable prediction for the fatigue life of this detail.
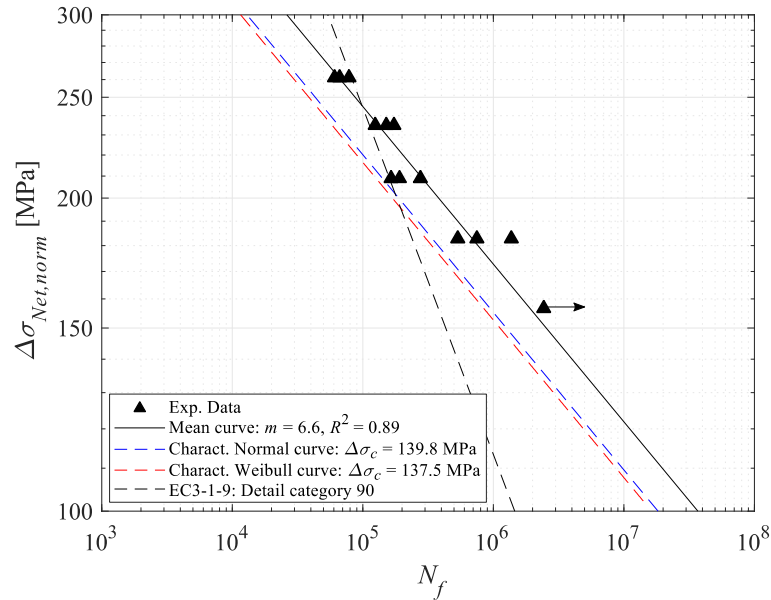
Figure 5.6. Statistical analysis of fatigue experimental results and comparison with EN 1993-1-9 [15] design recommendation (logarithmic scale).

In terms of characteristic *S-N* curve, normal and Weibull distributions were implemented. For the first case, the detail category was found as 139.8 MPa which is superior to the value defined in EN 1993-1-9 [15] but direct comparison cannot be made because the slope is distinct. The one-sided tolerance limit was found as $k_{5,75,v_{dg}} = 2.07$ and the standard deviation as $\hat{\sigma} = 0.15$.

For characteristic *S-N* curve using Weibull distribution, results of the four estimation methods used to determine α_W and β_W parameters are presented in Figure 5.7. The optimal estimation method was found by goodness-of-fit tests and results showed that Maximum Likelihood Method (MLM) has the best correlation with BMR data. In this sense, the values of α_W and β_W parameters used in Weibull distribution function are the values found with MLM which are 3.05 and 1.17, respectively – see Table 5.8. The characteristic curve using Weibull distribution was then defined and the detail category was found as 137.5 MPa. It can be stated that characteristic *S-N* curve using normal distribution function should be used to predict the fatigue

behaviour of this structural detail since it leads to higher fatigue life than the prediction using Weibull distribution function and has a good correlation with experimental results.

Table 5.8. Parameters of Weibull distribution and goodness-of-fit statistics for experimental fatigue data on bolt hole.

Method		LLSM	WLLSM	MLM	MM
α_w		3.34	2.82	3.05	3.31
β_w		1.17	1.15	1.17	1.17
Goodness-of-fit	KS	0.126	0.124	0.129	0.126
	AD	0.543	0.556	0.537	0.538
	χ^2	0.107	0.250	0.152	0.111
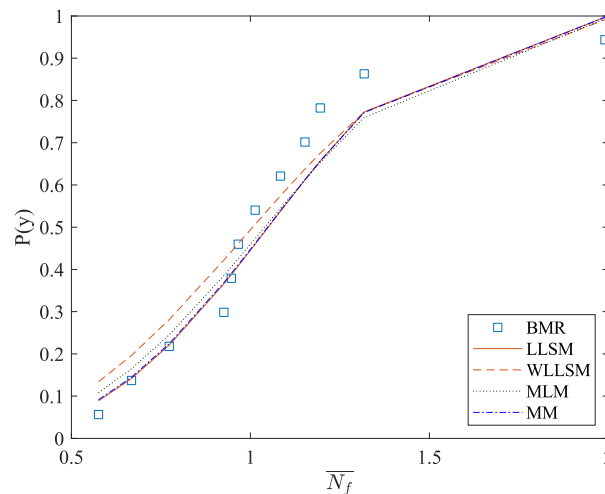
Figure 5.7. Comparison of cumulative Weibull distribution function for experimental fatigue data on bolt hole.

5.4.2   Effect of galvanization, hole manufacturing process and material

The structural detail under analysis has been studied by several authors. It was the case of Valtinat and Huhn [130] in which a similar detail (steel S235 JR plate with a drilled central hole) was also tested under fatigue loading. The main difference is that all specimens were hot dip galvanized. In this sense, a comparison is established between non-galvanized and galvanized specimens to analyse its influence in fatigue life. In Figure 5.8, fatigue experimental results are compared with data from Valtinat and Huhn [130]. Even if the number of tests is low, it is observed that above 180 MPa the fatigue life can be considered similar between galvanized and non-galvanized specimens. However, for stress levels below 180 MPa the fatigue life of galvanized specimens is lower. The statistical analysis implemented in galvanized

specimens led to a *S-N* curve with lower slope ($m = 4.1$) and lower detail category ($\Delta\sigma_c = 107.3$ MPa). In fact, several authors demonstrated that galvanization affects negatively the fatigue performance mainly due to an embrittlement of the detail. There is an acceleration of the fatigue damage due to rapid formation of cracks in the coating [131–133]. As it is possible to observe from these results, the impact of galvanization on the fatigue life is mainly visible in high cycle fatigue region.

It is also possible to observe that there is one result from galvanized specimens ($\Delta\sigma_{net,norm}$ 249.6 MPa and N_f = 82 205) that is below the EN 1993-1-9 [15] design curve. In fact, it was tested with a maximum stress level that represents 86% of the yield stress. This level of stress can explain the reduced fatigue life by the influence of the plasticity formed in the region of the hole.
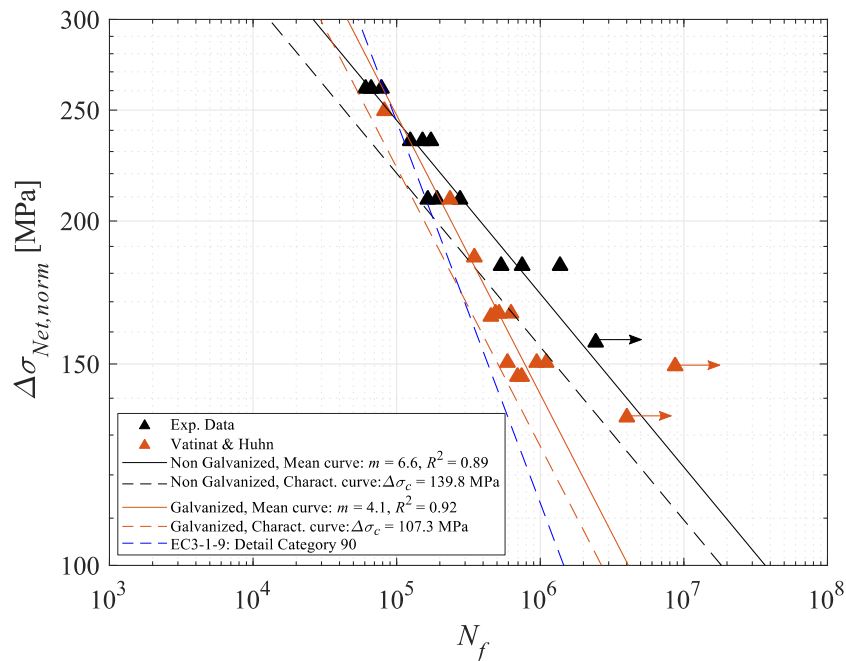
Figure 5.8. Comparison between the fatigue life of galvanized and non-galvanized bolt holes.

There are several mechanical procedures that can be implemented to manufacture the bolt hole. The European standard EN 1090-2 [78] allows both drilling and punching processes. However, fatigue performance is influenced by the mechanical process that is selected as shown in Figure 5.9. It establishes a comparison with fatigue results obtained by Valtinat and Huhn [130] for galvanized S235 JR plate with a punched central hole. It is visible that punching procedure

leads to lower fatigue results for all stress levels. In fact, punching procedure is characterized by introducing macro-defects in the hole that influence negatively fatigue endurance of details [134]. The statistical analysis of fatigue data from galvanized punched hole details led to a *S-N* curve with lower slope ($m = 3.8$) and lower detail category ($\Delta\sigma_c = 86.9$ MPa). Furthermore, the design curve proposed in EN 1993-1-9 [15] is not adequate for this type of structural detail since there is a significant number of test results with lower fatigue life.
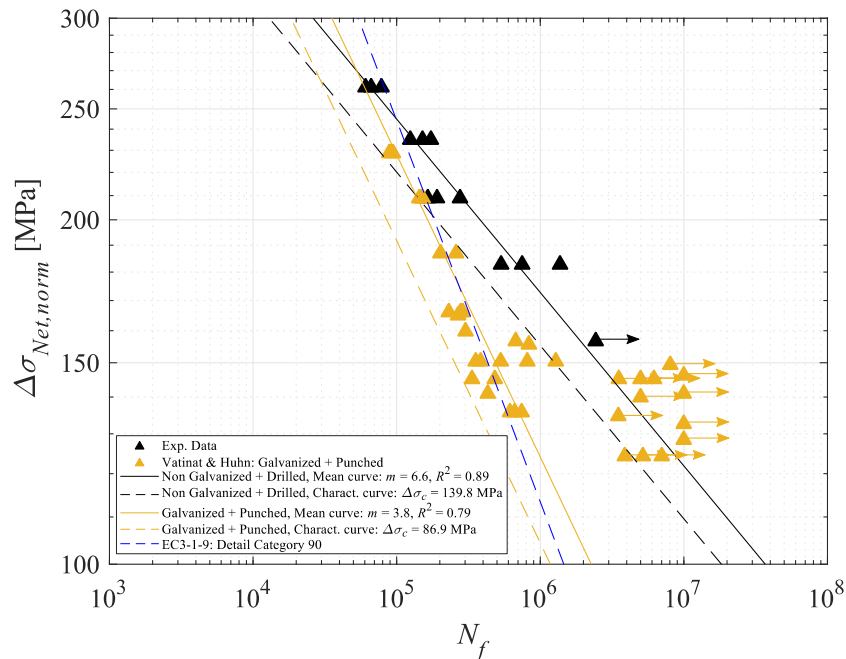
Figure 5.9. Comparison between the fatigue life of galvanized + punched bolt hole and non-galvanized + drilled bolt hole.

Another important impact on fatigue performance of a detail is related to its material properties. It is expected that the microstructure and chemical composition play a role on the fatigue behaviour. In this sense, experimental data acquired for S235 was compared with fatigue test results made by Berto *et al.* [135] on a similar detail (plate with a hole drilled in the centre) but composed of S355 – see Figure 5.10. Experimental results from S355 bolt hole details presented higher fatigue life compared to S235 bolt hole details for tests conducted under a normalized net stress above 200 MPa. Below this stress level, fatigue life can be considered similar for these two materials. The fatigue result tested by Berto *et al.* [136] under $\Delta\sigma_{net,norm} = 340$ MPa is the only specimen that led to fatigue life inferior to the prediction using detail category 90 from EN 1993-1-9 [15]. The level of stress for this specimen is 81% considering the maximum

applied stress and the static yield strength. This result enhances the fact that when a specimen is tested under a fatigue maximum load higher than 80% of the static yield force of the detail, fatigue life predictions from EN 1993-1-9 [15] are unsafe.
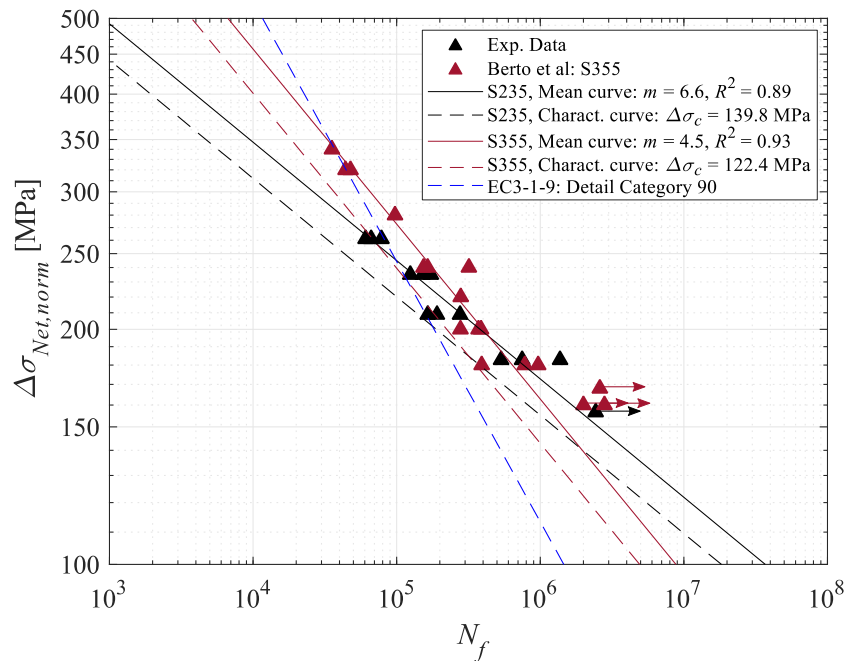
Figure 5.10. Comparison between the fatigue life of S235 and S355 bolt hole details.

5.5   Local approach

The local approach implemented to assess the fatigue life of this bolt hole detail is based on fatigue local models for crack initiation and propagation phases. The number of cycles to initiate a crack is estimated with strain (Coffin-Manson-Basquin model), stress-strain (SWT model) and strain energy (Huffman model) damage parameters while the number of cycles for propagation phase is estimated by means of numerical and experimental analysis based on stress intensity factor.

5.5.1   Initiation phase

5.5.1.1   Stress-strain analysis

The application of strain, SWT and Huffman damage models rely on local stresses and local strains formed during fatigue loading. In this sense, the stress-strain field was evaluated by

means of numerical calculations. Figure 5.11 presents the boundary and loading conditions of numerical model. It takes the advantage of the symmetrical plane in X direction. Within the symmetrical plane, the displacement in X direction is restrained. In one side of the plate, displacement in both X and Y directions is restrained while in the opposite side of the plate, no boundary condition is present, but load is applied.
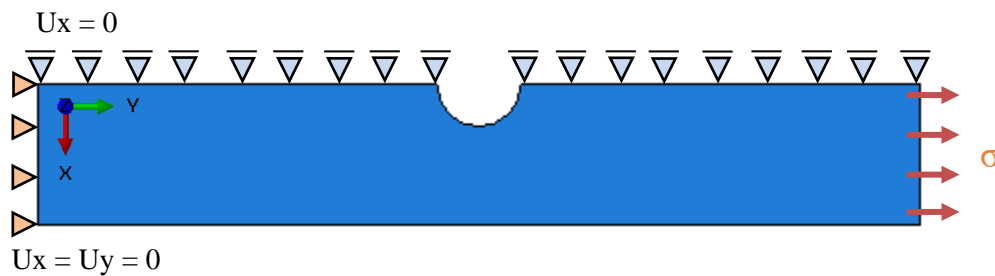
Figure 5.11. Numerical model used to compute the local stress-strain field for the bolt hole detail.

The first analysis was conducted aiming to study the influence of the mesh. Material properties were defined considering mean stabilized elastoplastic cyclic curve computed for S235 in Section 3.3.3.2. In this sense, six different numerical models were created with varying mesh sizes as presented in Figure 5.12. The finite element type used in these models is the shell 4-node bilinear plane stress quadrilateral element designated as CPS4R. It has reduced integration and hourglass control.

One complete load cycle was implemented in each model to determine stress and strain values in the region of the hole at maximum and minimum stress levels. The load cycle applied in this mesh study corresponds to a net stress range equal to 200 MPa ($R_\sigma = 0.1$). Results are presented in Table 5.9. Strain amplitude and SWT computed for each analysis become stable in the numerical model with Mesh 5 (0.001 mm minimum size). In this sense, Mesh 5 was selected to be used in this study. The relevant stress and strain fields obtained with Mesh 5 for $\Delta\sigma_{net} = 200$ MPa are presented in Figure 5.13.

This analysis was implemented for the five stress levels used in experimental tests considering not only mean values of stabilized cyclic stress-strain curve of S235, but also characteristic lower and upper boundary values determined by normal distribution function – see Section

3.3.3.2. Local maximum strain and stress values at maximum and minimum nominal net stress levels are presented in Table 5.10 and Table 5.11, respectively.
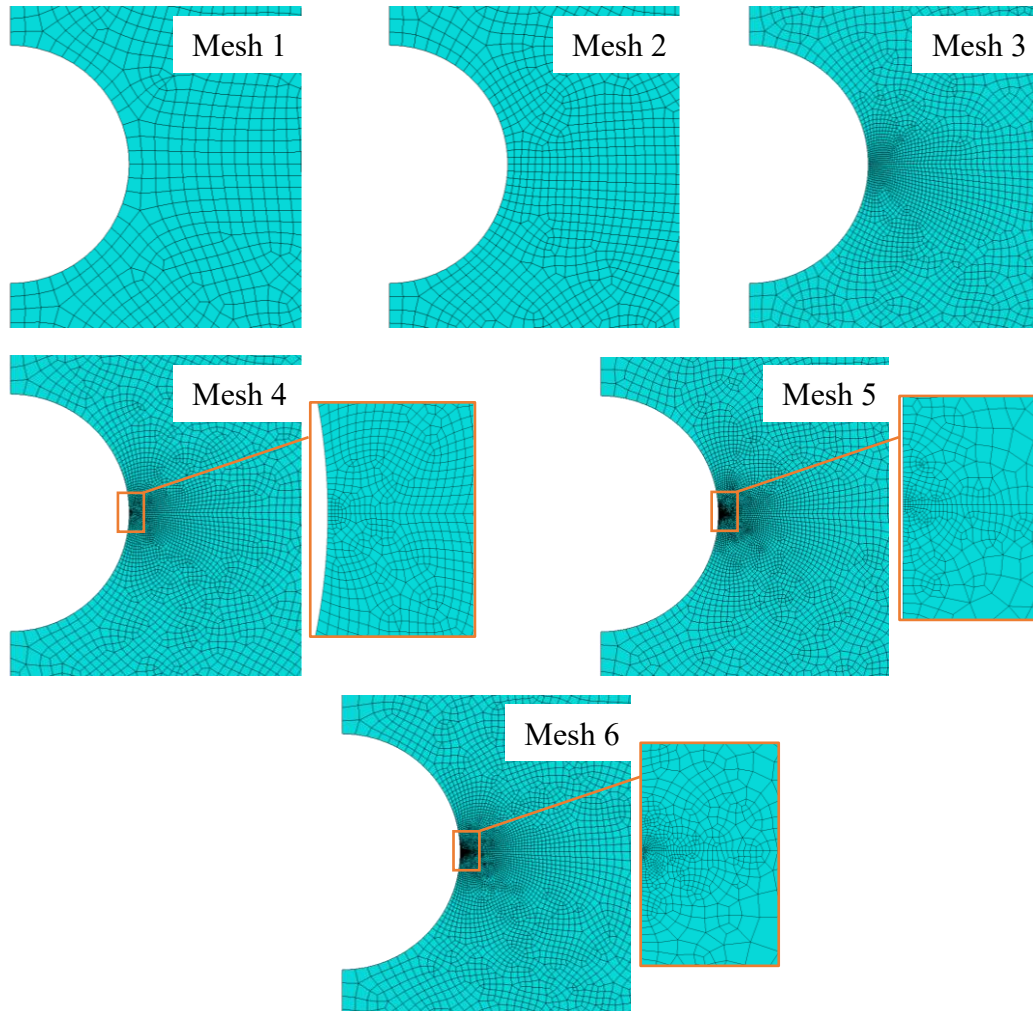
Figure 5.12. Different mesh patterns created for mesh sensitivity analysis.

Table 5.9. Mesh sensitivity evaluation for local fatigue analysis ($\Delta\sigma_{net}$ = 200 MPa).

Mesh No.	Minimum mesh size [mm]	$\varepsilon_{y,max}$ [-]		$\varepsilon_{y,a}$ [-]	Diff. [%]	$\sigma_{y,max}$ [MPa]	SWT [-]	Diff. [%]
		$\sigma_{net,max}$	$\sigma_{net,min}$					
1	1	0.003079	0.001124	0.000977	-	331.166	0.32371	-
2	0.5	0.003296	0.001209	0.001044	6.36	332.274	0.34684	6.67
3	0.1	0.003455	0.001266	0.001094	4.63	332.819	0.36427	4.78
4	0.05	0.003512	0.001281	0.001115	1.89	332.845	0.37124	1.88
5	0.001	0.003527	0.001276	0.001126	0.92	332.859	0.37467	0.91
6	0.0005	0.003532	0.001280	0.001126	0.01	332.868	0.37474	0.02
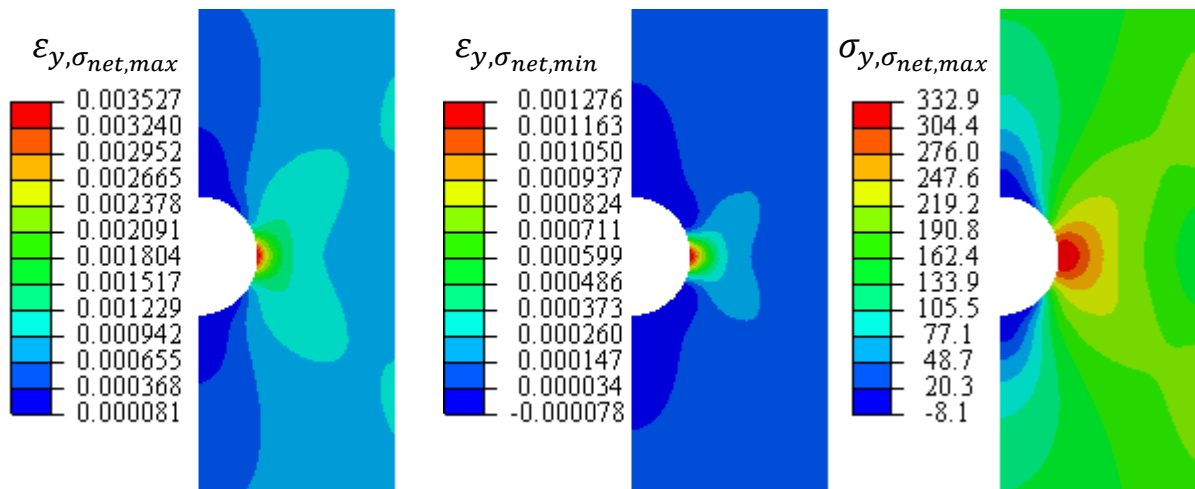
Figure 5.13. Relevant stresses and strains around the hole for $\Delta\sigma_{net}$ = 200 MPa using Mesh 5.

Table 5.10. Local **maximum strain**, $\varepsilon_{y,max}$, obtained with S235 mean and characteristic material cyclic elastoplastic curve and DNV-RP-C208 recommendations.

$\Delta\sigma_{net}$ [MPa]	$\varepsilon_{y,max}$							
	$\sigma_{net,max}$				$\sigma_{net,min}$			
	Experimental curves			DNV-RP-C208	Experimental curves			DNV-RP-C208
	Mean	Characteristic			Mean	Characteristic		
		Lower	Upper			Lower	Upper	
250	6.5E-3	1.3E-2	4.8E-3	9.5E-2	3.6E-3	1.0E-2	2.0E-3	9.2E-2
225	4.6E-3	7.3E-3	3.9E-3	3.8E-2	2.1E-3	4.8E-3	1.3E-3	3.5E-2
200	3.5E-3	4.7E-3	3.2E-3	1.6E-2	1.3E-3	2.4E-3	9.0E-4	1.3E-2
175	2.8E-3	3.2E-3	2.6E-3	7.4E-3	8.1E-4	1.3E-3	5.8E-4	5.5E-3
150	2.2E-3	2.4E-3	2.1E-3	4.1E-3	4.9E-4	7.4E-4	3.6E-4	2.4E-3

Table 5.11. Local **maximum stress**, $\sigma_{y,max}$, obtained with S235 mean and characteristic material cyclic elastoplastic curve and DNV-RP-C208 recommendations.

$\Delta\sigma_{net}$ [MPa]	$\sigma_{y,max}$							
	$\sigma_{net,max}$				$\sigma_{net,min}$			
	Mean	Characteristic		DNV-RP-C208	Mean	Characteristic		DNV-RP-C208
		Lower	Upper			Lower	Upper	
250	366.9	338.4	396.1	331.3	-230.3	-263.4	-197.7	-265.2
225	348.5	318.0	381.2	300.9	-186.5	-221.8	-151.6	-237.5
200	332.9	299.0	366.0	272.6	-140.5	-178.2	-106.8	-206.3
175	318.0	282.2	348.7	248.4	-95.7	-132.8	-65.0	-169.4
150	300.6	267.5	326.1	226.8	-54.0	-87.1	-28.5	-129.3

This local stress-strain assessment allowed to determine local fatigue damage parameters relevant for the selected fatigue local models: local strain amplitude, ε_a, local mean stress,

σ_{mean}, and SWT, $\varepsilon_a\sigma_{max}$. Results are presented in Table 5.12. Strain amplitude is not influenced by the statistical analysis of cyclic stress-strain material data, however mean and maximum stresses depend on the selected curve. In this sense, characteristic values of fatigue damage parameters used for fatigue life predictions were defined using the results from the upper boundary of the cyclic curve in order to implement the worst-case scenario. Higher fatigue damages are obtained using this approach.

Table 5.12. Fatigue damage parameters obtained with mean, characteristic and DNV-RP-C208 material cyclic elastoplastic curve for S235.

$\Delta\sigma_{net}$ [MPa]	ε_a [-]				σ_{mean} [MPa]			$SWT = \varepsilon_a\,\sigma_{max}$		
	Mean	Characteristic		DNV-RP-C208	Mean	Characteristic		Mean	Characteristic	
		Lower	Upper			Lower	Upper		Lower	Upper
250	1.4E-3	1.4E-3	1.4E-3	1.4E-3	68.3	37.5	99.2	0.52	0.48	0.56
225	1.3E-3	1.3E-3	1.3E-3	1.3E-3	81.0	48.1	114.8	0.44	0.40	0.48
200	1.1E-3	1.1E-3	1.1E-3	1.1E-3	96.2	60.4	129.6	0.37	0.34	0.41
175	9.8E-4	9.8E-4	9.8E-4	9.8E-4	111.1	74.7	141.8	0.31	0.28	0.34
150	8.4E-4	8.4E-4	8.4E-4	8.4E-4	123.3	90.2	148.8	0.25	0.23	0.28

5.5.1.2 Fatigue life prediction

The prediction of number of cycles for initiation phase was done considering both mean and characteristic parameters of strain-life and SWT-life damage models. Predictions based on Huffman model were based on the optimized dislocation density ρ = 4.20E+15 m^{-2} which represent a mean fatigue life prediction. Furthermore, the number of cycles for crack initiation phase were also computed based on DNV-RP-C208 recommendations. Results are presented in Table 5.13.

Table 5.13. Fatigue life prediction for initiation phase, N_i, of bolt hole detail using local damage parameters.

$\Delta\sigma_{net}$ [MPa]	N_i					
	Mean			Characteristic		DNV-RP-C208
	Strain	SWT	Huffman	Strain	SWT	
250	7.5E+04	3.8E+4	6.8E+04	1.1E+04	7.9E+3	1.4E+04
225	1.3E+05	7.1E+4	1.1E+05	1.6E+04	1.3E+4	1.9E+04
200	2.5E+05	1.5E+5	2.3E+05	2.6E+04	2.4E+4	2.7E+04
175	6.2E+05	3.9E+5	6.3E+05	5.1E+04	5.8E+4	3.9E+04
150	2.2E+06	1.4E+6	3.2E+06	1.4E+05	2.0E+5	6.2E+04

Fatigue life predictions for initiation phase are compared with experimental fatigue data in Figure 5.14. Mean fatigue life predictions are very close to experimental fatigue data, especially for strain and Huffman models. In the case of SWT, fatigue life predictions showed lower values. In what concerns characteristic S-N curves based on strain and SWT damage models, it is visible that they represent a conservative approach as well as the predictions based on DNV-RP-C208 [93]. The validation of these fatigue life predictions should be implemented not only with the number of cycles for crack initiation phase, but also with crack propagation since experimental fatigue data is represented with total fatigue life.
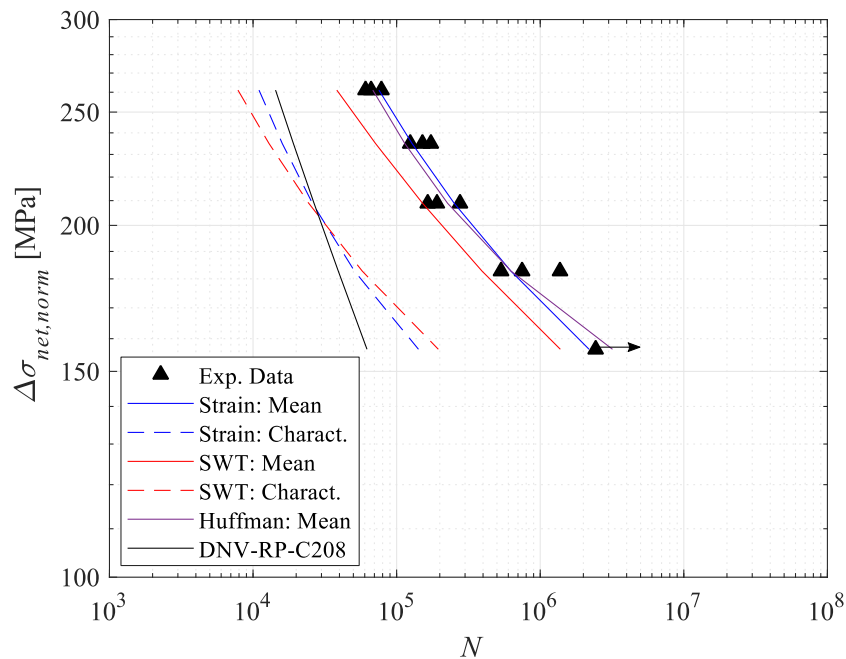
Figure 5.14. Comparison between predicted fatigue life for initiation phase and experimental fatigue data.

5.5.2   Propagation phase

5.5.2.1   Numerical analysis

The computation of number of cycles for fatigue crack propagation phase for this detail was determined using a numerical procedure based on stress intensity factor. It was performed using the domain integral method [137] which is based on the computation of J-integral that relates the energy release and the crack growth. For linear elastic material behaviour and Mode-I fatigue crack growth, it can be related with stress intensity factor using the relation presented

in Eq. (5.1) where $\bar{E}$ is equal to the elastic modulus, E, for plane stress conditions or equal to $E/(1 - v^2)$ for plane strain conditions.

$$J = \frac{K^2}{\bar{E}} \tag{5.1}$$

For 2D problems in a quasi-static analysis, J-integral can be computed as presented in Eq. (5.2) where Γ is a contour that surrounds the crack tip and connects top and bottom crack surface – see Figure 5.15a), the limit $\Gamma \to 0$ is an indication that the contour decreases onto the crack tip, q is a vector that indicates the direction of the crack growth and n_J is the normal vector to Γ [137].

$$J = \lim_{\Gamma \to 0} \int_{\Gamma} n_J \cdot H \cdot q \ d\Gamma \tag{5.2}$$

Variable H is computed as presented in Eq. (5.3) where W is the elastic strain energy and σ is the stress tensor.

$$H = W - \sigma \frac{\partial u}{\partial x} \tag{5.3}$$

In the case of elastic material properties, no body forces and traction on the crack surfaces, J-integral is path independent which means that contour can be specified anywhere enclosing the crack tip [137]. Alternatively, a 2D closed contour integral can be defined – see Figure 5.15b) – by rewriting Eq. (5.2) as presented in Eq. (5.4) where $\bar{q}$ is a weighting function within the closed region $C_J + C_J^+ + \Gamma + C_J^-$ assuming the value q on Γ and 0 on C_J. The variable m_J is an outward normal vector which assumes the value $-n_J$ on Γ.

$$J = -\oint_{C_J+C_J^++\Gamma+C_J^-} m_J \cdot H \cdot \bar{q} \ d\Gamma \tag{5.4}$$

This closed contour integral can be converted into a domain integral using the divergence theorem as shown in Eq. (5.5) where A_J is the domain enclosed by the contour $C_J + C_J^+ + \Gamma + C_J^-$ which includes the crack-tip region as $\Gamma \to 0$ [137].

$$J = -\int_{A_J} \left(\frac{\partial}{\partial x}\right) \cdot (H \cdot \bar{q}) \ dA_J \tag{5.5}$$

If equilibrium is satisfied, the final form of the 2D integral can be written as presented in Eq. (5.6) where the gradient of the strain energy for a homogeneous material has constant material parameters. The letter f_J represents the body force per unit volume. This equation disregards thermal influence.

$$J = \int_{A_J} \left[H{:}\frac{\partial \bar{q}}{\partial x} + f_J \cdot \frac{\partial u}{\partial x} \cdot \bar{q} \right] dA_J \tag{5.6}$$
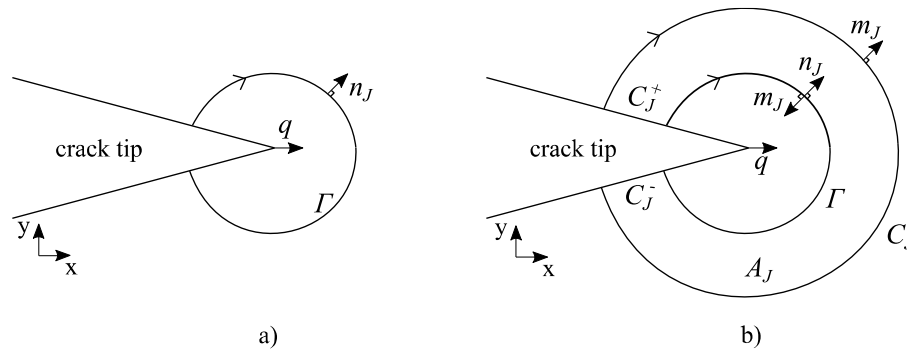
Figure 5.15. Contour integral definition: a) open contour; b) closed contour.

In Abaqus, these integrals are defined considering the rings of elements that surround the crack tip. The first contour includes all finite elements directly connected to crack-tip and each subsequent contour consists of adding the next ring of elements that share nodes with the elements in the previous contour. This approach is able to provide accurate results even with rather coarse meshes [138].

A numerical model was created in Abaqus to compute stress intensity factor considering two possible crack paths: single side crack and double side crack – see Figure 5.16a) and b), respectively. It shows load and boundary conditions defined in this model which are similar to the model used in crack initiation studies but in this case a crack was implemented. The q vector which indicates the crack growth direction was defined as well as a more refined mesh region in which a swept meshing is used around the crack tip.
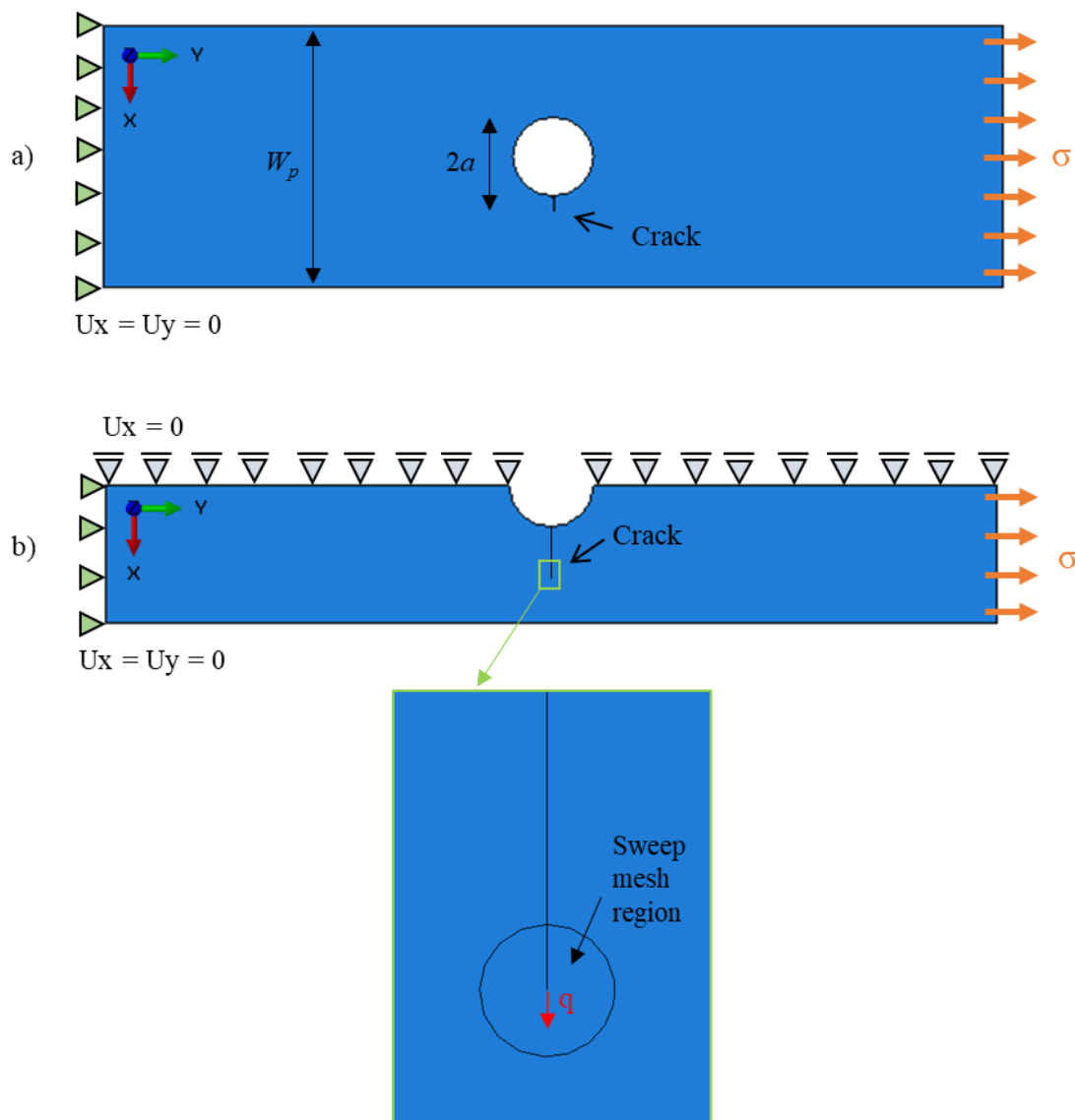
Figure 5.16. Numerical model used to compute stress intensity factors: a) single side crack; b) double side crack.

This numerical model is composed of 8-node plane stress element (CPS8) and in the swept region the size of the elements varies between 0.001 and 0.02 mm leading to 10 rings of elements around the crack tip. Mesh is illustrated in Figure 5.17. Material properties used in these numerical studies are based on linear elastic properties: $E = 210$ GPa and $v = 0.3$. Stress intensity factor was computed by several values of crack length and considering an applied remote stress of 100 MPa. Results are presented in Table 5.14 for five contours. It is evident from the average difference computed for each contour considering the value of the previous contour, that the value of stress intensity factor is stable at the fifth contour (average difference

inferior to 0.05%). In this sense, it was selected for the following calculations. An example of the elastic stress field in the region of the crack is presented in Figure 5.18.
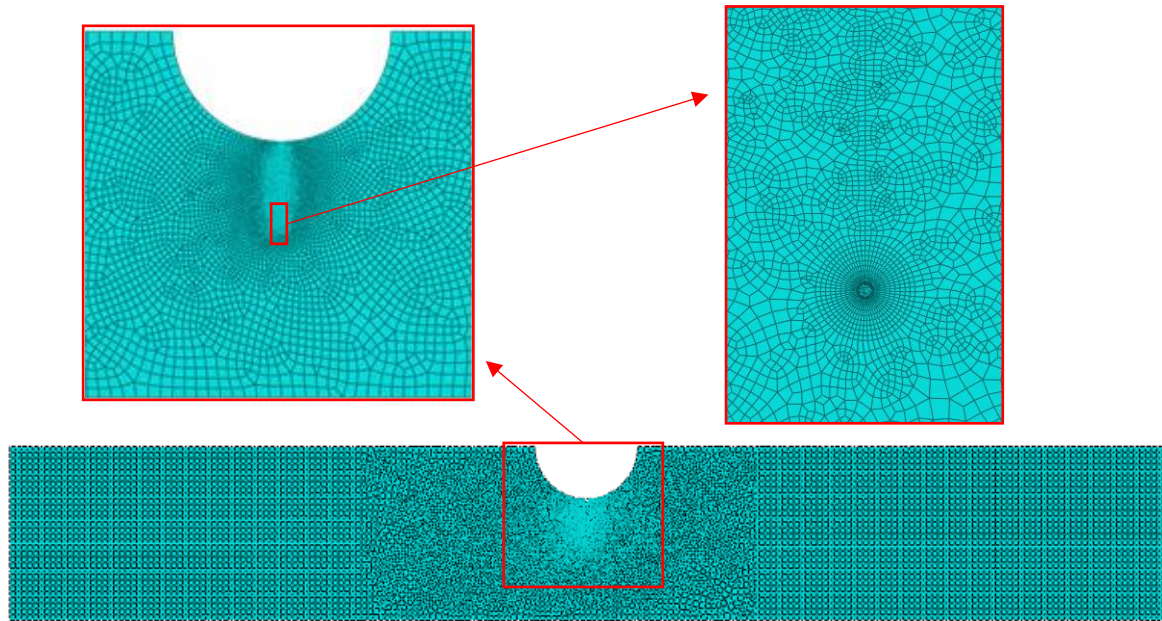
Figure 5.17. Identification of mesh in numerical model used to compute stress intensity factor.

Table 5.14. Stress intensity factor for single and double side crack computed by means of numerical approach (σ = 100 MPa).

K [MPa.m$^{0.5}$]											
Single Side Crack						**Double Side Crack**					
$2a/W_p$	**Contour**					$2a/W_p$	**Contour**				
	1	**2**	**3**	**4**	**5**		**1**	**2**	**3**	**4**	**5**
0.300	2.0	2.1	2.1	2.1	2.1	0.300	1.9	2.1	2.1	2.1	2.1
0.301	4.5	4.7	4.7	4.7	4.7	0.302	4.6	4.7	4.8	4.8	4.8
0.308	12.8	13.3	13.3	13.4	13.4	0.317	12.9	13.4	13.5	13.5	13.5
0.317	16.4	17.0	17.1	17.1	17.1	0.333	16.7	17.3	17.4	17.4	17.4
0.325	18.5	19.2	19.3	19.3	19.3	0.350	17.9	19.4	19.5	19.5	19.5
0.350	21.4	22.2	22.3	22.3	22.3	0.400	21.5	23.3	23.5	23.5	23.5
0.400	23.9	24.8	24.9	24.9	24.9	0.500	26.1	28.3	28.5	28.5	28.5
0.467	27.2	28.3	28.4	28.4	28.4	0.633	35.1	36.4	36.5	36.6	36.6
0.517	31.2	32.4	32.5	32.5	32.5	0.733	43.1	44.8	44.9	45.0	45.0
0.567	37.9	39.4	39.5	39.6	39.6	0.833	57.4	59.5	59.7	59.8	59.8
0.600	47.3	49.1	49.3	49.4	49.4	0.900	70.9	76.8	77.3	77.4	77.5
0.617	56.2	58.4	58.6	58.7	58.7	0.933	87.0	94.1	94.8	94.9	95.0
Av. Diff. [%]		3.68	0.38	0.09	0.03	Av. Diff. [%]		5.61	0.52	0.11	0.03

The values of stress intensity factor obtained numerically should now be normalized considering the applied stress (net stress in this case) – see Figure 5.19. The normalized value

of stress intensity factor is described as Y_K and its evolution in relation to the crack length is adjusted to a trendline expressed by a 8-grade polynomial presented in Eq. (5.7) and (5.8), for single and double side crack, respectively, where $\alpha = 2a/W_p$.
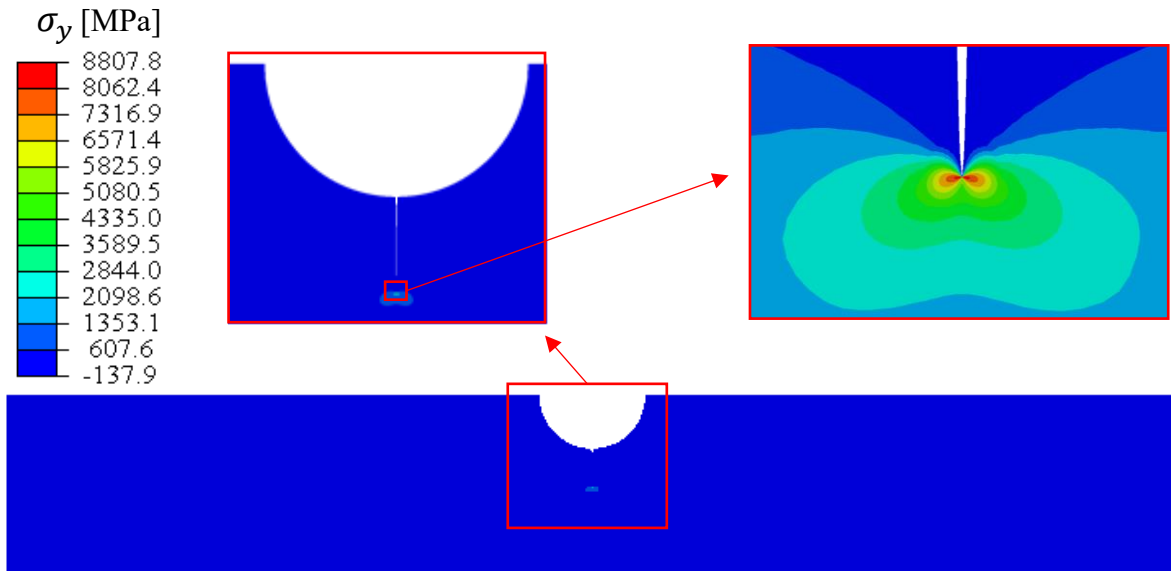
Figure 5.18. Stress field in double side crack model obtained for $2a/W_p = 0.5$ and $\sigma = 100$ MPa.
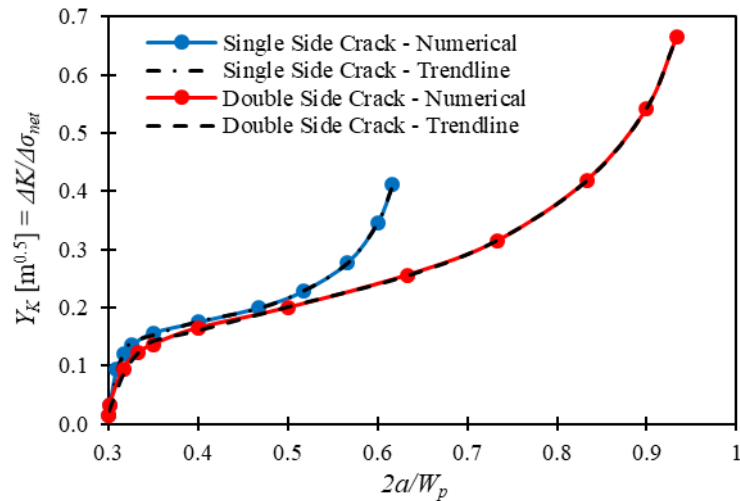
Figure 5.19. Stress intensity factor evolution in relation with crack length for single and double side crack.

The number of fatigue cycles for crack propagation phase can be obtained by integration of Paris law as presented in Eq. (5.9). The value of the material constants, C and m, used in this

study to determine mean S-N curve was 1.26E-9 and 3.46, respectively, which are the values found experimentally for stress ratio equal to 0.05 – see Section 3.3.4.3.

In the case of characteristic S-N curve, material constants used to integrate Paris law correspond to the values found using Mean + $3\hat{\sigma}$ approach on experimental data for stress ratio inferior to 0.5 – see Table 3.23. Material constants C and m for this characteristic curve were defined as 7.65E-10 and 3.83, respectively.

$$
\begin{aligned}
Y_{K,Single\ Side} = &-6.51 \times 10^{-9}\alpha^8 + 5.61 \times 10^{-7}\alpha^7 - 1.99 \times 10^{-5}\alpha^6 \\
&+ 3.78 \times 10^{-4}\alpha^5 - 4.13 \times 10^{-3}\ \alpha^4 + 2.63 \times 10^{-2}\alpha^3 \\
&- 9.32 \times 10^{-2}\alpha^2 + 1.73 \times 10^{-1}\alpha + 2.01 \times 10^{-2}
\end{aligned}
\tag{5.7}
$$

$$
\begin{aligned}
Y_{K,Double\ Side} = &-4.10 \times 10^{-9}\alpha^8 + 3.96 \times 10^{-7}\alpha^7 - 1.54 \times 10^{-5}\alpha^6 \\
&+ 3.16 \times 10^{-4}\alpha^5 - 3.67 \times 10^{-3}\alpha^4 + 2.45 \times 10^{-2}\alpha^3 \\
&- 8.93 \times 10^{-2}\alpha^2 + 1.71 \times 10^{-1}\alpha + 2.04 \times 10^{-2}
\end{aligned}
\tag{5.8}
$$

This integration of Paris law was computed considering an initial crack length of 0.5 mm (within the typical values found in literature [52]) and crack increments of 0.01 mm. It is assumed that the crack intensity factor is constant within the length of the crack increment. The final increment is reached when the stress intensity factor reaches the value 50.6 MPa.m$^{0.5}$ which corresponds to the maximum value reached in experimental FCG tests of S235.

$$
N_p = \int_{a_i}^{a_f} \frac{1}{C \cdot \Delta K^m}\ da
\tag{5.9}
$$

The values obtained numerically are compared with experimental results in Figure 5.20. It shows that fatigue life propagation prediction is below the total fatigue life obtained by experimental tests which was expected since experimental data is related to total fatigue life. It is observed that single side crack leads to higher fatigue life. A reduction of nearly 30% is observed when the crack propagates in both sides of the detail.
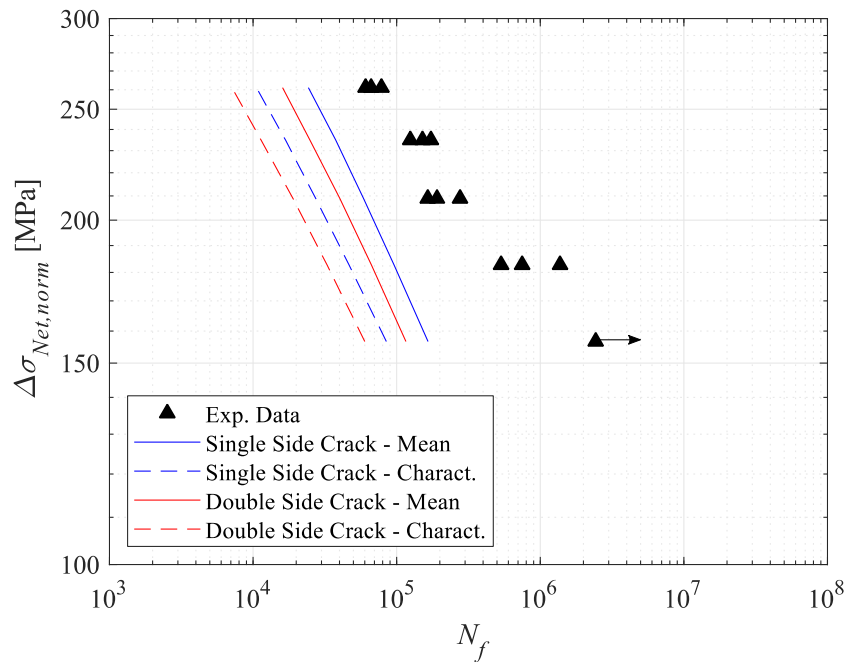
Figure 5.20. Comparison between fatigue crack propagation prediction life and fatigue experimental data of bolt hole detail.

5.5.2.2 Experimental analysis

Fatigue crack propagation phase in this bolt hole detail was analysed by means of specific fatigue crack growth tests. Specimens used in this investigation were prepared with a notch on the hole which intends to localize the beginning of the crack. The radius of the notch is 0.25 mm aiming to generate a high level of stress concentration in its tip leading to very low number of cycles to initiate a crack. With this approach, only the fatigue crack propagation phase is obtained. The length of the notch was defined as 0.5 mm. Two scenarios were studied: single side crack and double side crack as presented in Figure 5.21. Specimens were extracted from the same plate base material (S235 JR) and with the same crack growth orientation. A total of four tests were conducted on a Fatigue Test Hydraulic Machine MTS 810 rated to 100 kN under a sinusoidal tensile load with the same fatigue loading parameters used in stress level $\Delta\sigma_4$ for fatigue tests – see Table 5.1. This means that $\Delta\sigma_{net}$ = 175 MPa, $\sigma_{net,max}$ = 194.4 MPa, $\sigma_{net,min}$ = 19.4 MPa and R_σ = 0.1. Frequency was set to 5 Hz.

One surface of the specimen was polished to monitor the crack length throughout the test using a traveling microscope – see Figure 5.22. For one specimen of each typology (single side and

double side crack), the opposite surface was painted with white colour with a pattern of black dots (speckle pattern) to implement the Digital Image Correlation (DIC) method and monitor the crack length and displacements in the relevant zone – see Figure 5.22. Specifications of DIC are presented in Table 5.15 while the domain of the analysis and the speckle pattern are described in Figure 5.23. Fatigue load was applied for periods of 5 000 cycles after which crack length measurements and DIC analysis were conducted.
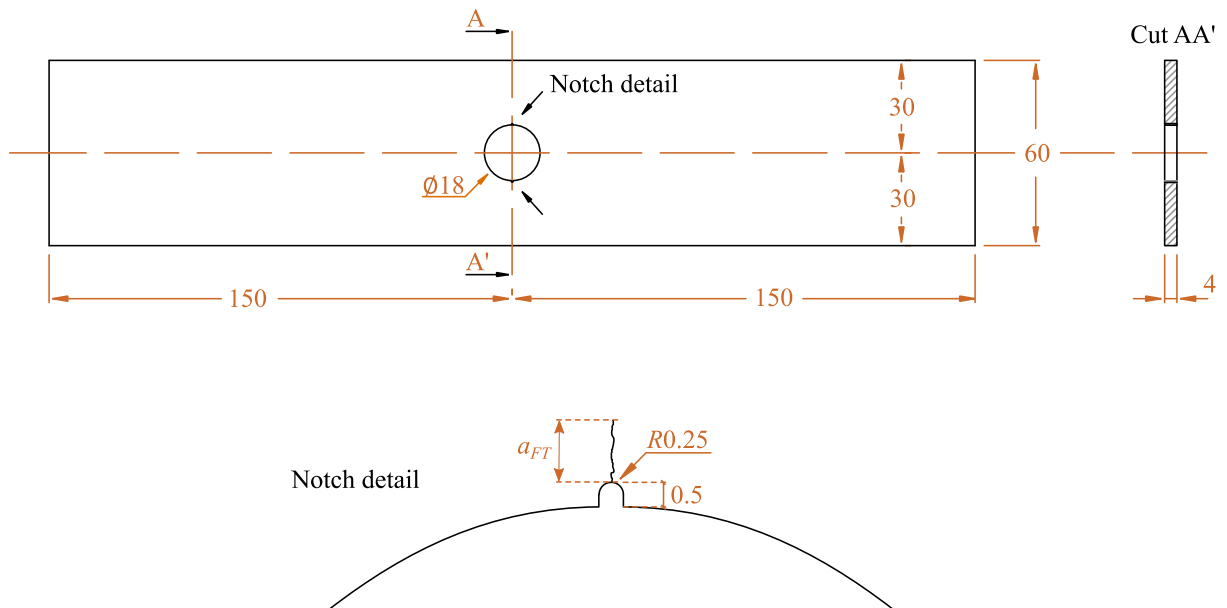
Figure 5.21. Schematic representation of specimens used for FCG study on bolt hole detail (dimensions in mm).
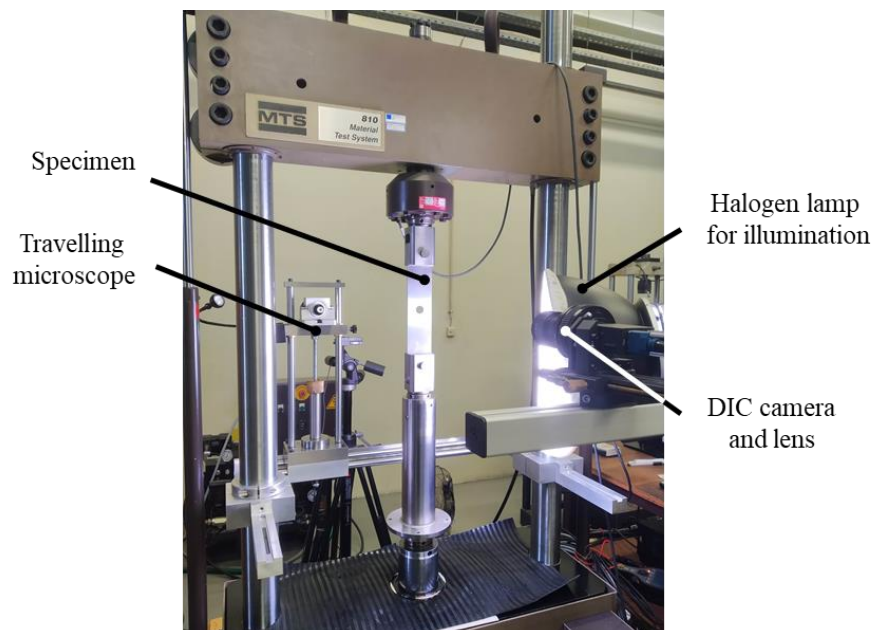
Figure 5.22. Image of experimental campaign of FCG tests on notched bolt hole specimens.

Table 5.15. 2D DIC specifications

Camera specifications	2048 x 2048 [px^2] - Gazelle camera
Camera lens	C-Mount Rodagon 80 [mm] – modular focus
Software	VIC-2D 7$^{©}$ - Correlated Solutions
Illumination	A 250 [W] – halogen lamp
Subset size	17 [px]
Step size	6 [px]
Problem domain	57 x 33 [mm^2] or 1860 x 1092 [px^2]
Speckle pattern size	0.21 – 0.28 [mm] or 7 – 9 [px]
Painting method	Airbrush
Calibration ratio	0.031
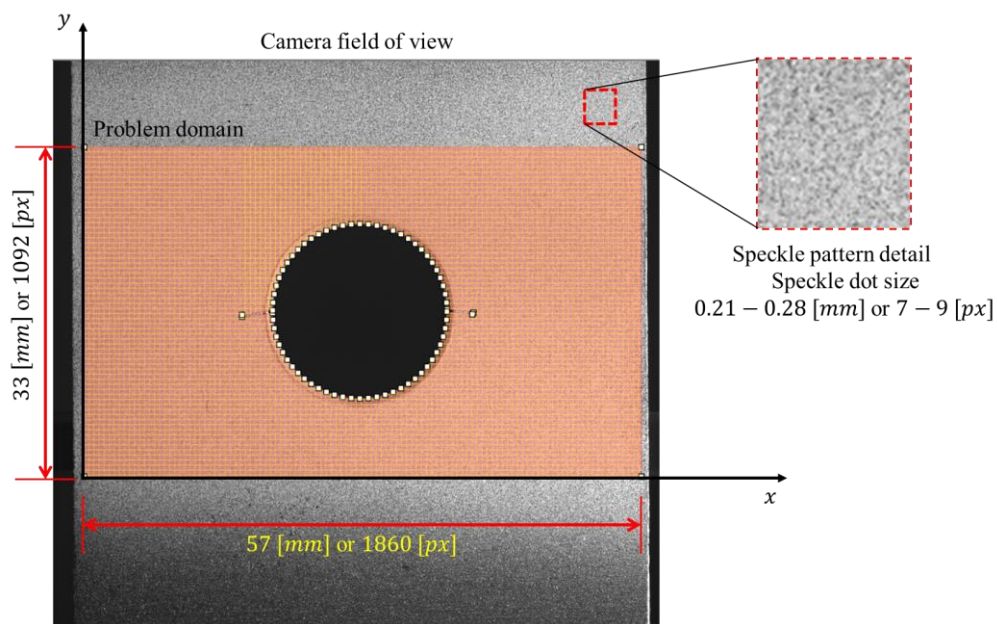
Figure 5.23. DIC method: speckle pattern detail and problem domain.

A summary of crack length values measured at several stages of fatigue life is presented in Table 5.16. This measurement of crack length, a_{FT}, was made from the tip of the notch as illustrated in Figure 5.21. For double side crack specimens, crack was monitored on both sides of the hole (right and left side). The average number of cycles at failure for double side crack specimens was 50 890 cycles while for single side crack specimens it was 78 441 cycles which represents an increase of 54% when the crack is growing in only one side of the hole. Considering that a crack emerging in a bolted connection with a hole of 16 mm would be visible when $a_{FT} > 5.5$ mm, it is observed that for double side crack specimens this crack length is achieved almost at the end of the test which means that the remaining fatigue life is very small.

In the case of single side crack specimens, crack would be visible when the remaining fatigue file is around 28%.

Table 5.16. Experimental results from FCG tests on bolt hole specimens.

Double side crack						Single side crack			
Sp. 1			Sp. 2			Sp. 1		Sp. 2	
N	a_{FT} [mm]		N	a_{FT} [mm]		N	a_{FT}	N	a_{FT}
Cycles	Right	Left	Cycles	Right	Left	Cycles	[mm]	Cycles	[mm]
10 000	0.07	0.00	10 000	0.09	0.22	10 894	0.20	10 000	0.20
15 000	0.35	0.40	15 000	0.51	0.54	15 000	0.39	15 000	0.48
20 000	0.70	0.75	20 000	1.01	1.04	20 000	0.74	20 000	0.79
24 000	1.00	1.18	23 642	1.48	1.67	25 000	1.18	25 000	1.00
30 000	1.50	1.85	27 392	1.99	1.98	30 000	1.60	30 000	1.15
35 000	2.28	2.55	30 000	2.50	2.40	35 000	2.28	35 000	1.52
40 000	3.12	3.47	35 000	3.78	3.46	40 000	2.89	40 000	2.12
45 000	4.55	4.30	40 000	5.42	4.94	45 000	3.58	45 000	2.52
50 000	6.05	6.32	45 000	8.16	7.39	50 000	4.56	50 000	3.39
54 848	-	-	46 931	-	-	55 000	5.64	55 000	4.19
						60 000	6.94	60 000	4.95
						65 000	8.50	65 000	5.80
						70 000	10.71	70 000	6.73
						74 570	-	75 000	9.80
						-	-	82 313	-

The relation between the crack length (using the parameter $\alpha = 2a/W_p$) and the number of cycles for both single and double side crack specimens is presented in Figure 5.24. The evolution of the crack is more stable when there is only one crack leading to higher fatigue resistance.
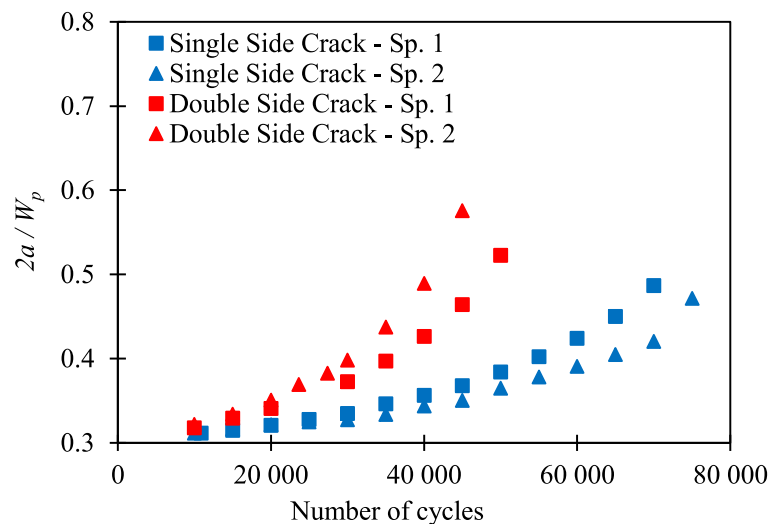
Figure 5.24. Evolution of crack length for single and double side notch specimens during FCG tests.

The number of cycles obtained with these FCG tests can be compared with numerical predictions. It is observed from the comparison presented in Table 5.17 that numerical predictions are coherent with experimental evidence since the obtained values are between mean and characteristic values in both single and double side crack.

Table 5.17. Comparison between experimental and numerical predicted number of cycles for fatigue crack propagation phase at $\Delta\sigma_4$.

Crack type	Experimental		Numerical	
	Specimen	N_p	Mean	Charact.
Single Side	1	74 570		
	2	82 313	95 952	46 586
	Mean	78 441		
Double Side	1	54 848		
	2	46 931	66 687	32 744
	Mean	50 890		

Experimental FCG results can also be compared with the number of cycles at propagation phase extracted from deformation range computed for global fatigue tests presented in Table 5.2, whose mean value for $\Delta\sigma_4$ was found as 28 836. It is evident that this approach leads to an underestimation of the number of cycles at propagation phase.

During these FCG tests on bolt hole specimens, DIC system was implemented to analyse displacement field at different stages of fatigue crack length. Figure 5.25 shows the vertical displacement field for single and double crack specimens for a crack length close to the end of the test and applying the maximum force of the loading cycle.

In both pictures, the crack path can be identified by a grey line emerging from the hole notch. Crack growth occurs through a perpendicular direction to the applied load in both single and double side crack specimens. It is visible that vertical displacement field is symmetrical to the line that defines the crack path when the crack develops in both sides of the hole, while for single side crack, the symmetrical line can be considered as crossing the detail in the centre of hole through a line that makes 45º with horizontal direction.
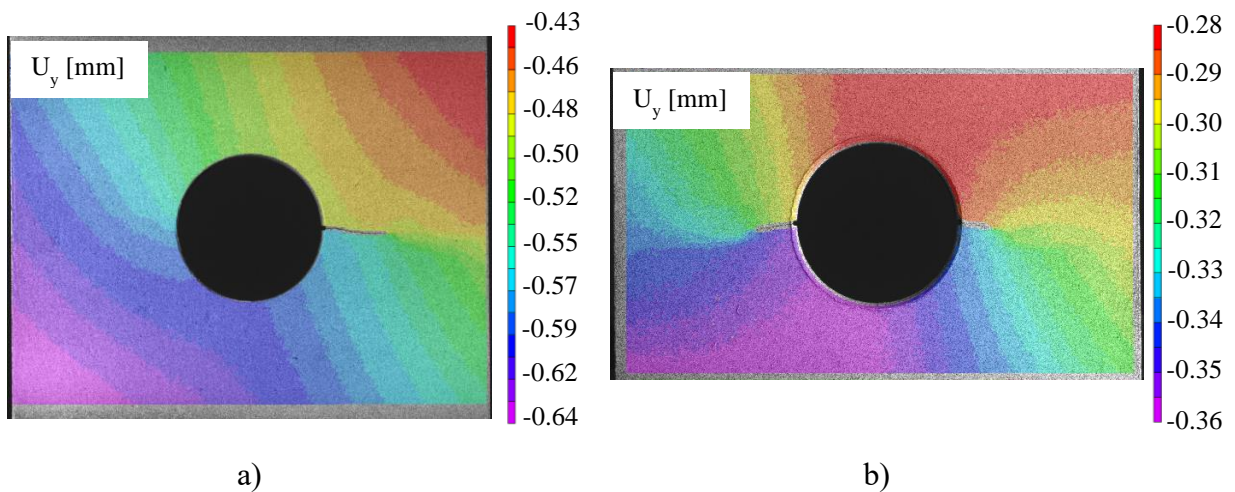
Figure 5.25. Vertical displacement: a) single side crack specimen at 50 000 cycles, $a_{FT} = 4.56$ mm and F_{max}; b) double side crack specimen at 40 000 cycles, $a_{FT,Right} = 5.42$ mm, $a_{FT,Left} = 4.94$ mm and F_{max}.

5.5.3 Total fatigue life

Total fatigue life predictions are obtained by adding the number of cycles at initiation phase computed for each fatigue local model and the number of cycles at propagation phase computed by numerical analysis. Comparison between experimental results and predicted number of cycles is shown in Figure 5.26 considering strain, SWT and Huffman damage parameters. Both single and double side crack approaches of fatigue crack growth are presented showing that its influence is not significant in final S-N curve, however double side crack approach should be used because it represents the worst-case scenario.

Considering the number of cycles for fatigue crack propagation phase obtained for double side crack approach, total mean and characteristic S-N curves obtained with strain, SWT and Huffman damage models are compared in Figure 5.27. It is possible to observe that mean S-N curves obtained with strain and Huffman damage models lead to fatigue life predictions similar to experimental data, while mean S-N curve obtained with SWT damage model led to lower number of cycles when compared to experimental data. The evaluation of each fatigue life prediction model was made computing the mean squared error (MSE) considering predicted mean S-N curves and experimental data (run-out excluded). It was found that the local approach that leads to better correlation with experimental data was using Huffman damage model since

MSE was found as 0.018 while for strain model and SWT it resulted in 0.022 and 0.038, respectively.
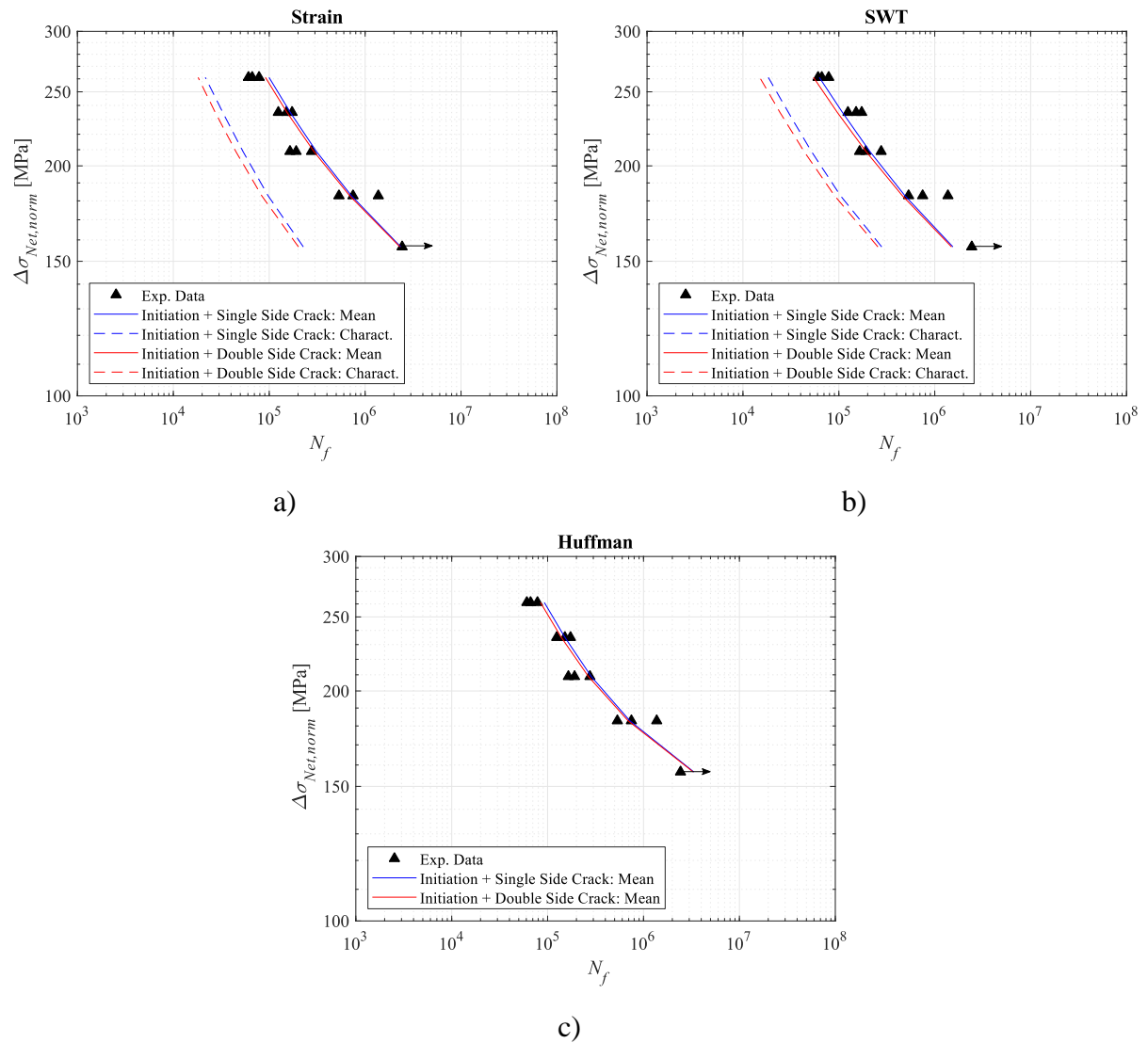
Figure 5.26. Comparison between total fatigue life predictions an experimental data: a) Strain-life model; b) SWT model; c) Huffman model (logarithmic scale).

In what concerns characteristic *S-N* curves computed with strain and SWT damage models, it is observed that the distance between mean and characteristic *S-N* curves is higher than the scatter observed in experimental results which means that they represent a very conservative approach. It is expected that with a higher sample of LCF tests, characteristic values would become closer to experimental evidence. However, the proposed characteristic *S-N* curves

represent a better approach to predict the fatigue life of this detail comparing to DNV-RP-C208 [93] whose values lead to underestimated fatigue results, especially in high cycle fatigue region.

Finally, comparing fatigue life predictions based on local approaches and fatigue life predictions based on the global approach using the *S-N* curve proposed in EN 1993-1-9 [15], it is observed that local fatigue modelling guarantees a much better correlation with experimental fatigue data.
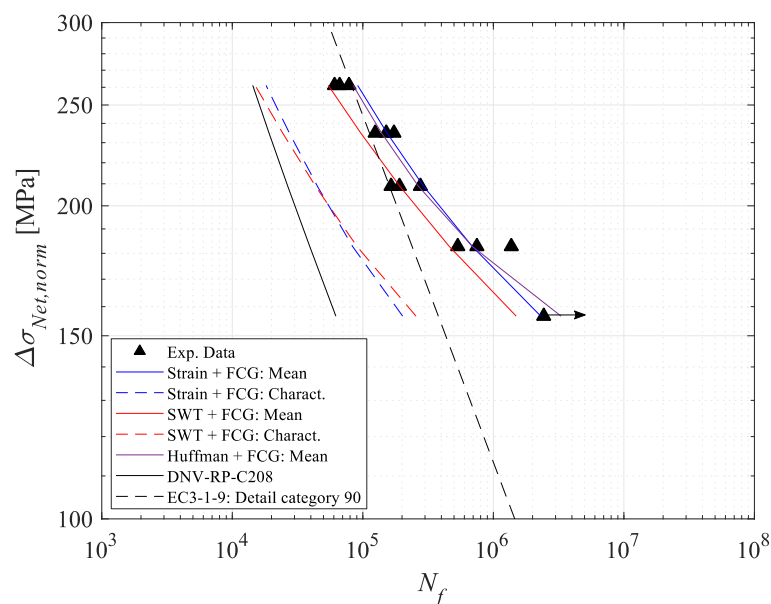
Figure 5.27. Comparison between global and local fatigue life predictions with experimental results.

5.6   Conclusions

Experimental fatigue tests were conducted to characterize the fatigue behaviour of a bolt hole detail. The deformation range was recorded during these tests and results allowed to understand that it is constant during the main part of the fatigue life. The moment in which displacement range starts to increase can be assumed as the beginning of the crack, however, as it was compared with FCG tests, it leads to an underestimation of the fatigue crack propagation life. Fracture surfaces were analysed and the size of the crack at the moment of failure was measured. It decreases for higher stress range values. Even if for lower stress range values, the crack size at failure corresponds to visible/inspectionable area, the remaining number of cycles is very small.

It was found that using a global linear model with slope equal to 3 is not adequate to predict the fatigue life of this detail because it led to unsafe results for high stress range values and very conservative results for low stress range values. Furthermore, it was possible to determine that, when the maximum nominal net stress exceeded 80% of the material yield strength, design recommendations in EN 1993-1-9 [15] represent unsafe predictions.

The effect of hot-dip galvanization was assessed, and the reduction of fatigue life was evident, especially in high cycle fatigue region. It can be explained by an embrittlement of the detail after galvanization and to rapid formation of cracks in the coating during fatigue testing. The influence of the method used to execute the bolt hole was also analysed by comparison with fatigue results from bolt holes executed by punching. It was found that it affects the fatigue endurance, and that drilling method conducts to a significant improvement of fatigue life. Finally, the assessment related to material type opposing S235 and S355 details allowed to understand that fatigue life is influenced by the material, mainly in low cycle fatigue region.

Fatigue life predictions for initiation phase were implemented using strain, SWT and Huffman damage models. Stress-strain field formed near the bolt hole during fatigue loading was assessed by means of numerical computation using the mean curve of S235 stabilized cyclic behaviour and the characteristic curve of S235 stabilized cyclic behaviour (upper boundary) defined by the normal distribution which corresponds to the worst-case scenario (higher fatigue damage parameter).

The number of cycles at propagation phase was determined by integration of Paris equation with stress intensity factor range computed by means of numerical approach. The possibility of having a crack in only one side of the hole or in both sides was analysed showing that the second situation leads to 30% reduction on the fatigue life. Experimental FCG tests were conducted for the lower stress range value to validate the number of cycles determined numerically. Experimental results were found within the range between mean and characteristic number of cycles showing that numerical procedures were accurate.

Comparison between total number of cycles (initiation plus propagation) determined with local approaches and experimental fatigue results showed very good correlation. Mean stress effect influences fatigue life of this detail, and these damage models were efficient to consider it.

Within the three selected fatigue local approaches, the Huffman damage model led to better correlation with experimental results as indicated by mean squared error computation. Furthermore, characteristic S-N curves based on local approaches stand as a conservative approach although with better correlation with experimental results when compared to EN 1993-1-9 [15] global predictions or DNV-RP-C208 recommendations.

6   ASSESSMENT OF RESIN BASED MATERIAL FOR SHEAR CONNECTORS

6.1   Introduction

The mechanical behaviour of injection bolts under static loading is similar to fitted bolts but the stiffness of the connection using injection bolts is directly dependent on the mechanical properties of the resin [139]. Any resin can be implemented as far as conditions in EN 1090-2 [78] are fulfilled which are related to its viscosity (ability to fill the cavity), thixotropic behaviour (it should remain in the cavity after injection) and its pot life (minimum 15 minutes). However, the design bearing strength of an injection bolt is directly dependent on the bearing strength of the resin (Eq. 3.4 of EN 1993-1-8 [80]) which is determined with an extended creep test procedure (Annex G of EN 1090-2 [78]). It corresponds to the maximum applied bearing stress considering 0.3 mm as the limit for the displacement during the design life of the structure. In this sense, materials with high stiffness and small creep deformations should be preferable for static design.

RenGel® SW 404 + HY 2404/5159 has been intensively studied and it is the only two component resin that has been approved by the Dutch Ministry of Infrastructures and Water Management [140] to use in injection bolts. Experimental tests proved that this material allows to fulfil the requirements related to the cumulative connection slip at the end of the service life (not more than 0.3 mm) when normalized holes are used [141].

Injection bolts have also been studied for application in hybrid structures (steel-FRP) for innovative light-weight bridges [142–144], in crane girders [79], towers for wind turbines and stadium roofs [141]. Fatigue tests on preloaded injected bolted connections were conducted by several authors showing that there is a contribute to reduce the scatter on the results and to improve the fatigue life [9,18,145,146].

However, using resin injections in bolted connections with oversized holes requires additional attention since the load-bearing resin volume is larger and deformations will increase. Such oversized holes are crucial when using resin-injected bolted shear connectors in demountable steel-concrete composite floor systems. Nijgh *et al.* [147,148] conducted scientific

investigations on the demountability and reusability of a tapered steel-concrete composite beam whose dimensions replicate typical dimensions of a multi-story car park building. Demountable resin-injected shear connectors were proposed – see schematic representation in Figure 6.1 – using M20 bolts and 32 mm for the diameter of holes in the beam flange. To account for tolerances in the construction process, the hole clearance is 4 times larger than normalized hole dimensions. In accordance with these dimensions, a set of creep tests was conducted by Nijgh [147] using double-lap shear connections with M20 bolts in oversized holes with 32 mm of diameter. Results for a normal bearing stress of 175 MPa are presented in Figure 6.2a) and it is possible to observe that by extrapolating results to 50 years, the maximum deformation criterion prescribed in EN 1090-2 [78] (0.30 mm) is not verified for conventional resin while for steel-reinforced resin this requirement is verified. This reinforced solution has been studied at Delft University of Technology [149]. Steel shots are used as the reinforcement of the epoxy resin as they are made of stiffer material – see Figure 6.2b). It is expected to achieve higher compressive strength and an improvement of the creep behaviour leading to a global enhanced performance under monotonic (quasi-static) and probably cyclic loading conditions (remains to be investigated) [150]. Additionally, the costs of the injected material are certainly less expensive, because the shots are a by-product after blasting and occupy about 60% of the injected volume.
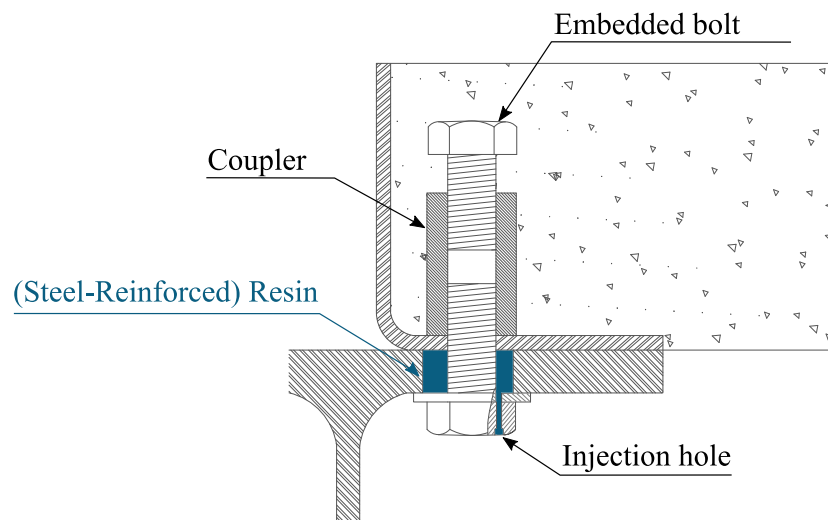
Figure 6.1. Resin-injected bolted shear connector for demountable and reusable composite floor systems. Adapted from [148].

The design of injected bolted connections is typically governed by its long-term behaviour, therefore the characterization of compressive creep properties of injection materials is crucial.

Preliminary tests were made by Nijgh [150] to study the long-term behaviour of injected bolted connections using the steel-reinforced resin. Time-dependent deformation was obtained by uniaxial compressive tests on unconfined specimens and the benefit of steel-reinforced resin was evident. However, the complete characterization of creep behaviour of injectants should be conducted using confined specimens.
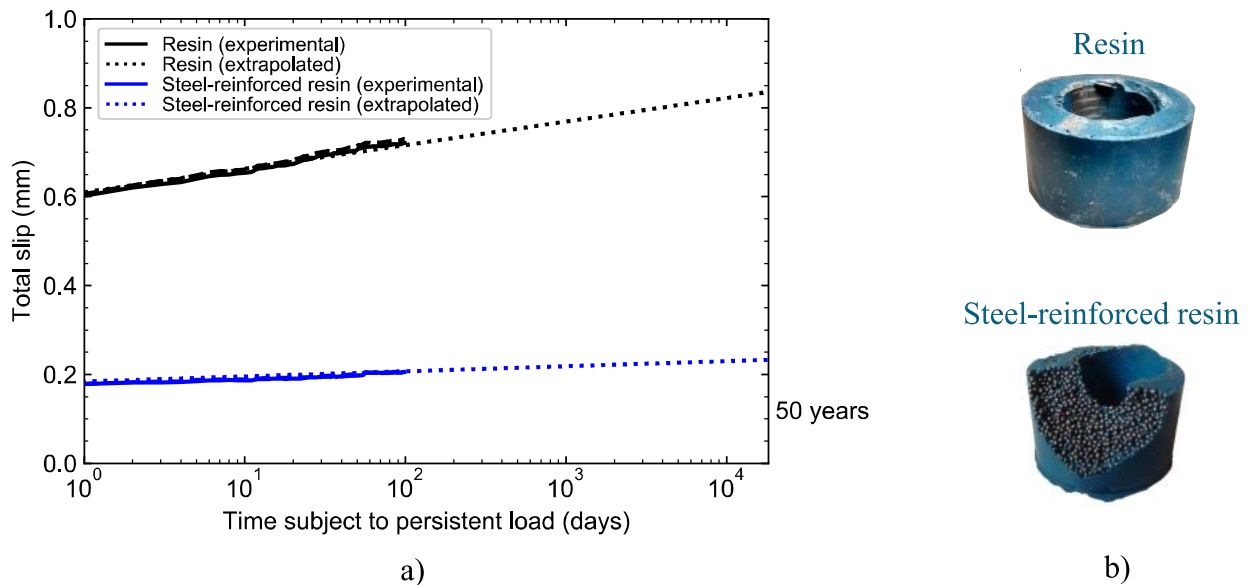
Figure 6.2. a) Slip vs. time diagram for a double-lap shear connection with an M20 bolt and a (steel-reinforced) resin-injected oversized hole with 32 mm in the centre plate subject to a nominal bearing stress of 175 MPa [16]; b) Injection materials.

Nijgh *et al.* [151] and Xin *et al.* [152] assessed the material response of epoxy resin RenGel® SW 404/ HY2404 and the respective steel-reinforced solution under compressive static loading for both confined and unconfined conditions. However, the thickness of the steel cylinder used to confine resin specimens in those experimental tests was small leading to yielding of the confinement piece which influenced the characterization of the material.

In this chapter, compressive material tests on RenGel® SW404/HY5159 (same base material as used by Nijgh *et al.* [151] and Xin *et al.* [152] but different hardener) under unconfined/confined conditions are presented. Young's modulus, yield strength and hardening behaviour are obtained from unconfined tests while the stiffness, the residual plastic strain and the viscoelastic strain under confined conditions were assessed using an experimental layout in which specimens are confined with a steel cylinder (its thickness was defined to avoid yielding).

Bare resin and steel-reinforced resin specimens are compared. Finite element simulations of the confined resin and steel-reinforced resin tests were conducted to validate the proposed parameters for the linear Drucker-Prager plastic model. This research intends to be a valuable contribution to numerical assessments and practical design of bolted shear connectors using steel-reinforced resin as injection material.

6.2   Material model under confined conditions

A constitutive model which includes pressure-dependent behaviour is needed to consider the influence of the hydrostatic pressure on the material behaviour as is described in Figure 6.3. It ranges from a brittle performance to strain hardening behaviour and material softening does not take place when the hydrostatic pressure is sufficiently high.

The linear Drucker-Prager yield surface [153] represented in the meridional plane ($p - t_D$ plane) is defined by a straight line as presented in Figure 6.4. The equation that defines the yield criterion in the meridional plane is:

$$t_D = d_{DP} + p \tan \beta_f \tag{6.1}$$

where t_D is the deviatoric stress, p is the hydrostatic pressure, β_f is the material angle of friction and d_{DP} is the cohesion of the material defined by (if hardening is defined in compression):

$$d_{DP} = \left(1 - \frac{1}{3}\tan \beta_f\right) f_{y,c} \tag{6.2}$$

where $f_{y,c}$ is the uniaxial compressive yield stress. The deviatoric stress is defined in the Eq. (6.3).

$$t_D = \frac{q_{eq}}{2}\left[1 + \frac{1}{K_{tc}} - \left(1 - \frac{1}{K_{tc}}\right)\left(\frac{a_{inv}}{q_{eq}}\right)^3\right] \tag{6.3}$$

where q_{eq} is the von Mises equivalent stress and a_{inv} is the third invariant of deviatoric stress. Fitting the best straight line through the triaxial compression results provides β_f and d_{DP} for

the linear Drucker-Prager model. The triaxial compression and tension lines must intercept the p-axis at the same point, and the ratio of values of q_{eq} for triaxial tension and compression at the same value of p then gives K_{tc}.
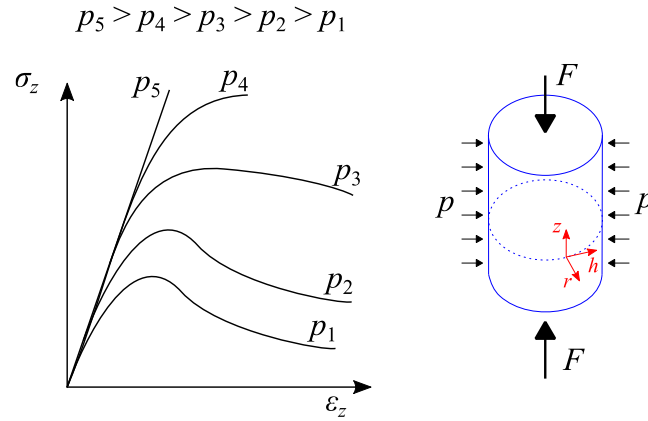
Figure 6.3. Schematic material behaviour for different levels of hydrostatic pressure.

The flow potential of the linear Drucker-Prager model is defined as presented in the following equation:

$$G_f = t_D - p \tan \psi \tag{6.4}$$

where ψ is the dilation angle in the p-t_D plane. The plastic strain increment $d\varepsilon^{pl}$ is assumed to follow the potential flow rule:

$$d\varepsilon^{pl} = \frac{d\bar{\varepsilon}^{pl}}{c_{MC}} \frac{\partial G_f}{\partial \sigma} \tag{6.5}$$

where c_{MC} is defined as presented in the following equation (if hardening is defined in uniaxial compression) and $d\bar{\varepsilon}^{pl}$ is the equivalent plastic strain increment.

$$c_{MC} = \left(1 - \frac{1}{3} \tan \psi\right) \tag{6.6}$$
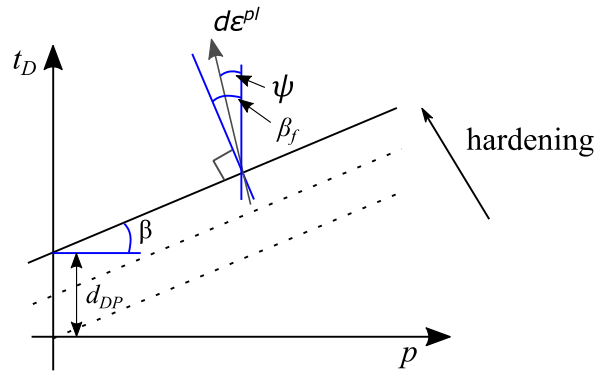
Figure 6.4. Linear Drucker-Prager model: yield surface and flow direction in the p(hydrostatic pressure) - t(deviatoric stress) meridional plane [154].

If the experimental data is not directly available to obtain the triaxial parameters, the simple way to proceed is to match the Mohr-Coulomb parameters to the Drucker-Prager model. The Mohr-Coulomb failure model is based on plotting Mohr's circle for states of stress at failure in the plane of the maximum and minimum principal stresses σ_1 and σ_3. This procedure is described in the Abaqus manual [154]. The failure criterion defined by Mohr-Coulomb is given as:

$$\frac{\sigma_1 - \sigma_3}{2} = \left[\frac{\sigma_1 + \sigma_3}{2}\right] \sin \varphi + c_{MC} \cos \varphi \qquad (6.7)$$

which can also be expressed as

$$\sigma_1 \frac{(1 - \sin \varphi)}{2 c_{MC} \cos \varphi} - \sigma_3 \frac{(1 + \sin \varphi)}{2 c_{MC} \cos \varphi} = 1 \qquad (6.8)$$

where φ and c_{MC} represent the angle of internal friction and cohesion, respectively. If the uniaxial tensile and compressive yield stresses are known, the Mohr-Coulomb parameters can be determined as:

$$f_{y,t} = \frac{2 c_{MC} \cos \varphi}{1 + \sin \varphi} \qquad (6.9)$$

$$f_{y,c} = \frac{2 c_{MC} \cos \varphi}{1 - \sin \varphi} \qquad (6.10)$$

In the case of associated flow (dilatation angle equal to internal friction angle), the parameters of the Drucker-Prager model d_{DP} and β_f can be expressed with the Mohr-Coulomb parameters as:

$$\tan \beta_f = \frac{\sqrt{3} \sin \varphi}{\sqrt{1 + \frac{1}{3} \sin^2 \varphi}} \qquad (6.11)$$

$$\frac{d_{DP}}{c_{MC}} = \frac{\sqrt{3} \cos \varphi}{\sqrt{1 + \frac{1}{3} \sin^2 \varphi}} \qquad (6.12)$$

The parameter K_{tc} is determined by

$$K_{tc} = \frac{3 - \sin \varphi}{3 + \sin \varphi} \geq 0.778 \qquad (6.13)$$

In this study, the Drucker-Prager parameters were determined by calibrating the numerical results with experimental data.

6.3   Experimental program

6.3.1   Unconfined tests

6.3.1.1   Specimens and materials

A set of specimens was prepared to assess the compressive behaviour at room temperature [150]. The specimens consisted of resin RenGel® SW 404 + HY 5159. It is a two-component epoxy resin with mixing ratio 100:8. Bare resin specimens were used and steel-reinforced resin specimens composed of resin and spherical steel shots produced by J444 standard [155] with 0.8 mm nominal diameter (size class S330) in a loose random packing corresponding to a nominal particle volume fraction of 60%. Three specimens were tested for each material and the geometry of the specimens was Ø26 x 50 mm – see Figure 6.5. Load was applied under displacement control at a speed of 0.01 mm/s.
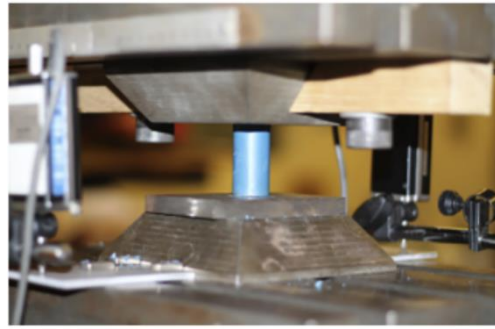
Figure 6.5. Experimental set-up for unconfined compression tests [152].

6.3.1.2 Experimental results

The engineering stress-strain curves for resin and steel-reinforced resin specimens are illustrated in Figure 6.6. For resin specimens, the stress-strain curve has four phases: i) linear stress-strain performance; ii) yielding; iii) hardening phase; iv) fracture. The stress-strain curve for steel-reinforced specimens has only two main phases: i) linear stress-strain performance; ii) fracture.
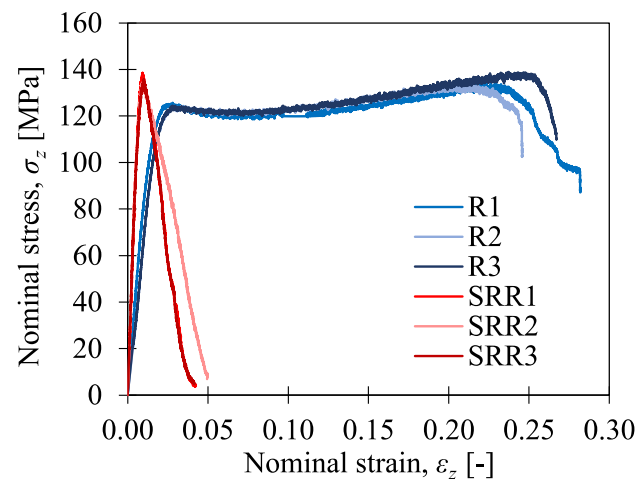
Figure 6.6 Nominal stress-strain performance for unconfined resin and steel-reinforced resin specimens.

A set of material parameters obtained from these tests is presented in Table 6.1. Steel-reinforced resin specimens showed significantly higher Young's moduli (increase of 181%) compared to resin specimens. A significant change in the material behaviour is observed in terms of ductility, since the fracture strain is considerably reduced for steel-reinforced resin. The failure of these brittle specimens was initiated by separation of the resin and the steel particles. For the resin

specimens, ductile behaviour was observed, and failure was initiated with longitudinal and diagonal cracks until sudden explosive spalling along these cracks. The stress value until which the material shows elastic behaviour has a small increase for steel-reinforced resin of 9.1% when compared to resin specimens.

The Poisson's ratio was found as 0.315 and 0.220 for resin and steel-reinforced resin, respectively. The density of each specimen was determined, and the average values were found as 5.26 g/cm^3 for steel-reinforced resin and 1.86 g/cm^3 for resin.

Table 6.1. Results for resin and steel-reinforced resin in unconfined tests (nominal values).

Material	Specimen	Young's Modulus E_Z [GPa]	Yield Strength $f_{y,c}$ [MPa]	Fracture Initiation Strain $\varepsilon_{z_0}^f$ [-]	Fracture Ultimate Strain $\varepsilon_{z_u}^f$ [-]
Resin	R1	8.6	125.7	0.229	0.282
	R2	7.5	124.3	0.201	0.246
	R3	7.4	124.4	0.237	0.267
	Average	7.8	124.8	0.222	0.265
	St. dev.	0.6	0.8	0.019	0.018
Steel-reinforced resin	SRR1	23.3	138.6	0.009	0.042
	SRR2	21.8	134.5	0.009	0.049
	SRR3	20.6	135.8	0.010	0.041
	Average	21.9	136.2	0.010	0.044
	St. dev.	1.3	2.1	0.001	0.004

6.3.2   Confined tests

6.3.2.1   Experimental setup

Experimental tests were conducted to characterize the material performance of resin under compressive-compressive quasi-static cyclic loading in confined conditions. The test setup – presented in Figure 6.7 – includes a cylindrical resin specimen with ∅16mm × 36mm or a steel-reinforced resin specimen with ∅16mm × 32mm nominal dimensions. This geometry represents a height nearly 2 times the diameter which is recommended to decrease the influence of friction effects (higher height will lead to higher friction). Smaller specimens will have large variations in internal stresses [156].

The specimens were placed inside a confining steel cylinder whose interior surface was coated with a dicronite layer [157]. Under the specimen was a bearing steel component with Ø15.8mm and above the specimen there was a loading pin with the same diameter. The gap of 0.1 mm between the pin (and bearing) and the confinement was enough to accommodate the lateral expansion of these components without contact with the confinement.

Resin and steel-reinforced resin used in these experimental tests were the same as used in unconfined tests. Metallic components were produced from structural bolts (steel grade 8.8 for confinement and steel grade 12.9 for loading pin and bearing). A hinge was placed under the bearing to ensure vertical force flow through the specimen. Linear variable differential transformers were placed to record the displacement between the top of the loading pin and the bottom of the bearing.

Two loading sets were used. In the ascending loading set (A-Set), the specimens were loaded up to 150 kN in 10 steps of 15 kN as represented in Figure 6.8a). After unloading in each step, a force of 1-2 kN was maintained for at least 3 minutes to distinguish the viscoelastic from the plastic strain. In the descending loading set (D-Set), specimens were loaded in 10 consecutive steps in a descending order as presented in Figure 6.8b). This loading protocol was defined aiming to evaluate the variation of the material mechanical properties when specimens are subjected to varying load magnitudes.
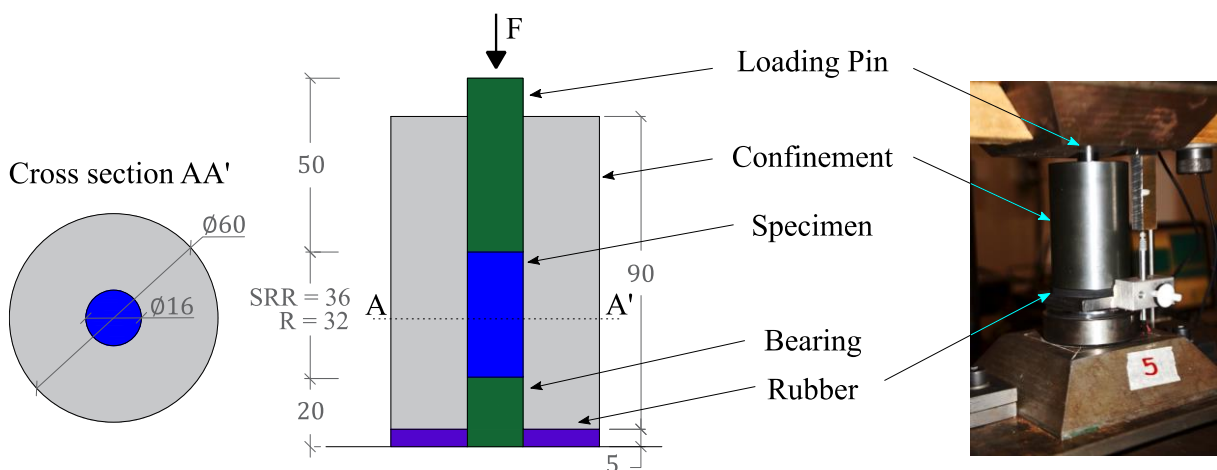
Figure 6.7. Experimental setup for confined tests (dimensions in mm).
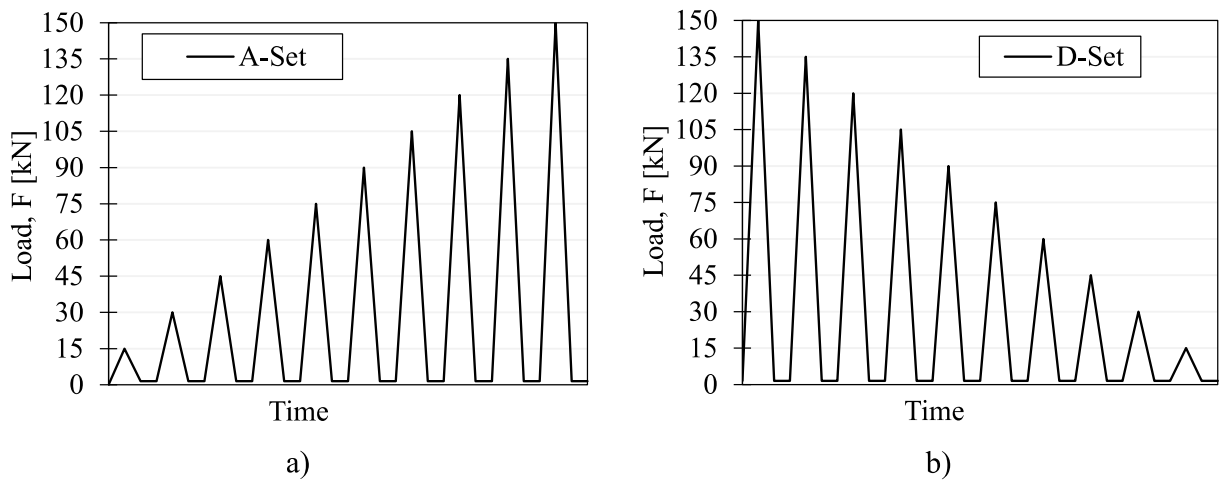
Figure 6.8. Schematic quasi-static loading sets: a) Ascending set; b) Descending set.

6.3.2.2   Ascending set (A-set)

Three resin specimens were tested under A-set. Nominal stress-strain behaviour is presented in Figure 6.9a). The first cycle (maximum stress 75 MPa) presents a linear-elastic behaviour while in the second cycle (maximum stress 150 MPa) there is a non-linear performance (stiffness changes). This non-linear behaviour was found in all four tests, and it indicates that there was a small difference between the diameter of the specimen and the inner diameter of the confinement piece (inner gap). The specimen reached its yield strength and lateral expansion occur until full confined conditions are reached. In the following cycles (with higher load levels) this phenomenon does not occur, and the loading phase is nearly linear.

Each cycle i was analysed separately to compute the stiffness of the loading phase and residual strain. Figure 6.9b) represents the analysis conducted for cycle 10 (the last cycle) of specimen A-Set-R1. The regression line of the loading phase is used to compute the stiffness of the material under confined conditions $E_{conf,i}$. Further, residual strain $\varepsilon_{z,r,i}$ given by the sum of the residual plastic strain $\varepsilon_{z,r,pl,i}$ and the residual viscoelastic strain $\varepsilon_{z,r,visc,i}$ is evaluated per cycle.

Three specimens were produced with steel-reinforced resin and tested under A-Set. Figure 6.10 presents the stress-strain behaviour during 10 cycles of loading. The inner gap is also visible for these results since there is a stress plateau in all three tests around 120-135 MPa. From 3rd to 10th cycle, the loading and unloading phases have a constant performance.

a)   b)
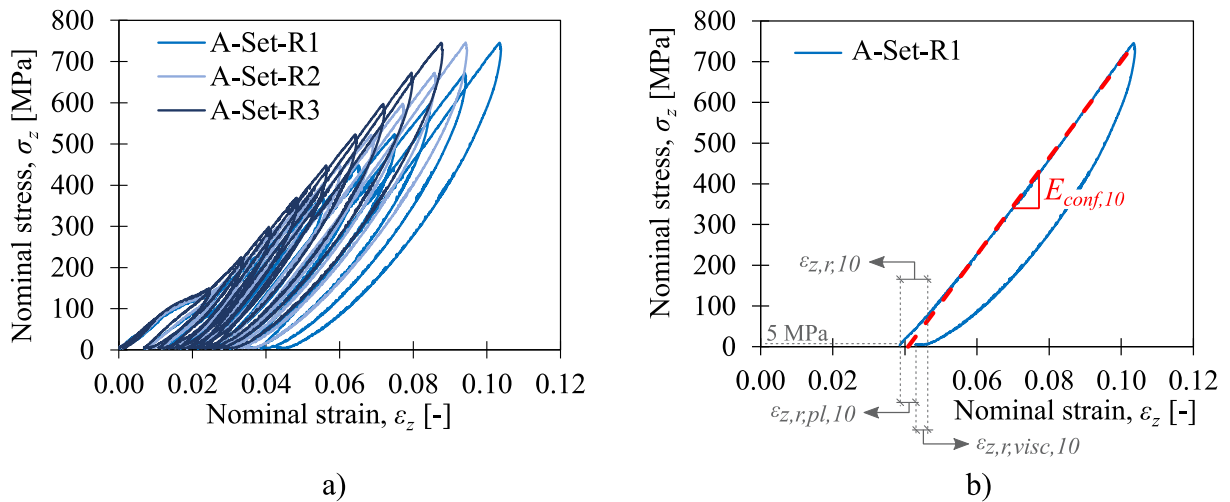
Figure 6.9. Resin specimens under A-Set: a) complete stress-strain performance; b) analysis of cycle 10 for specimen A-Set-R1.
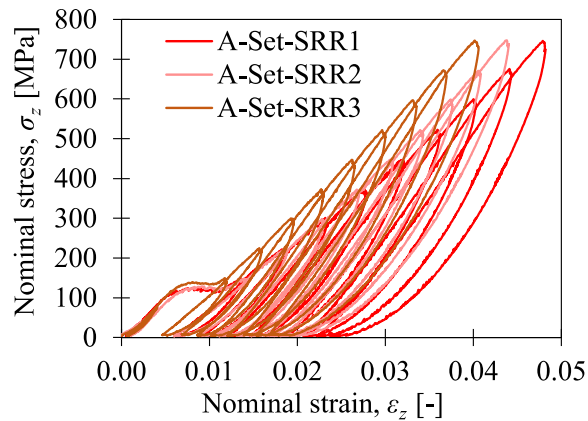
Figure 6.10. Steel-reinforced resin specimens under A-Set.

The evolution of stiffness for all sets of tests are presented in Figure 6.11. For both resin and steel-reinforced resin, the firsts cycles have a similar value to the stiffness obtained in the unconfined test. This shows that specimens are not in fully confined conditions in first and second cycles. Only after specimens have expanded laterally and overcome the small gap between specimen and confinement, the behaviour is governed by the confined conditions and the stiffness increases. After these first settling cycles, there is an increase of stiffness in both materials, but while for resin specimens, it stabilizes around 12 GPa after cycle 5, for steel-reinforced resin it increases until the last cycle. This difference can be related to the composite nature of the steel-reinforced solution and to the densification of the material caused by the rearrangement of the steel spheres and filling the voids.

Residual strain $\varepsilon_{z,r,i}$ was computed for every cycle and results are presented in Figure 6.12. Plastic $\varepsilon_{z,r,pl,i}$ and viscoelastic $\varepsilon_{z,r,visc,i}$ components were computed as represented in Figure 6.9b). After first cycle with almost no residual strain (load level under the yield stress of the material), the second cycle has the highest value due to plastification of specimen and lateral expansion until the gap between specimen and confinement piece is filled completely. From second cycle on, specimens are in fully confined conditions and residual strain decreases. Resin specimens exhibited higher residual strains than steel-reinforced specimens. The presence of steel shots in steel-reinforced specimens reduces the quantity of resin (the main source of viscosity effects) and consequently residual strain is lower. From cycle 7 beyond, the average value of viscoelastic strain represents 45% of the total residual strain for both resin and steel-reinforced specimens.
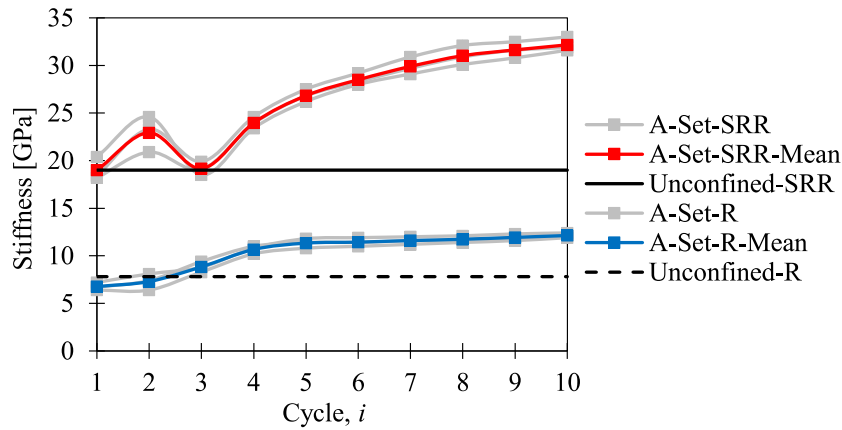
Figure 6.11. Development of the stiffness for steel and steel-reinforced resin specimens: A-Set.
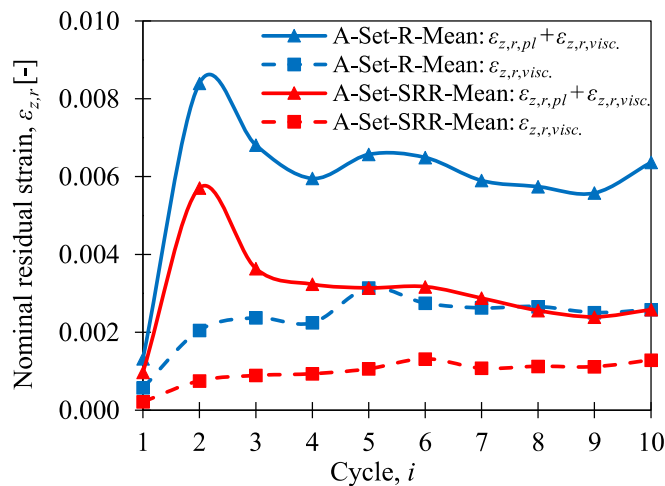
Figure 6.12. Residual strain for resin and steel-reinforced resin specimens: A-Set.

6.3.2.3 Descending set (D-set)

Four tests with resin specimens were performed under D-Set. Nominal stress-strain was computed, and results are presented in Figure 6.13. In the first loading step, a non-linear behaviour is obtained, while in subsequent steps the behaviour is mainly linear due to the fully confined conditions. The stiffness computed with the results obtained before the stress plateau is 7.3 GPa which is like the value obtained for unconfined solution (7.8 GPa).
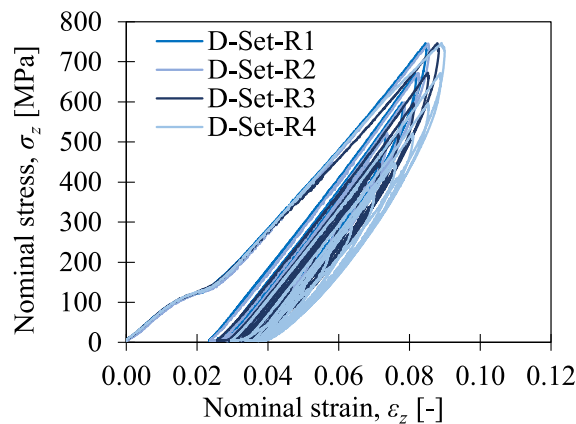
Figure 6.13. Resin specimens under D-Set.

For steel-reinforced material, two specimens were tested in D-Set. Results can be observed in Figure 6.14. In the first cycle (highest load magnitude) there is a significant residual deformation compared to the following cycles due to the same reasons that were given for resin specimens (test settling and transition from unconfined to confined state). The average stiffness computed before the stress plateau, which occurs at nominal stress around 130 MPa (yield stress), is 18 GPa and like unconfined result (19 GPa). After yielding and lateral expansion of specimen in stress plateau, a nearly linear performance is observed until maximum stress is reached. This linearity is maintained in the following cycles.

The stiffness value of each cycle is presented in Figure 6.15. The stiffness of first cycle (computed for results after stress plateau) is closer to the value for unconfined conditions. Even if confined conditions are achieved, in this first cycle the specimen is in a settling process in which voids are compressed. The difference between first and second cycle is more significant for steel-reinforced material which can be attributed to its composite nature and densification of the steel shots matrix. For resin specimen, from the second cycle beyond, the value of stiffness stabilizes around 11.5 GPa and in the final step, in which the load magnitude is below

the yield stress of the material, the stiffness has a small decrease of 1 GPa which can be explained by not fully confined conditions. For steel-reinforced resin specimens, after first cycle, material gets denser, and the value of stiffness increases significantly; then it is nearly constant until cycle 8. In the last two cycles in which the applied load level is smaller, specimens return to not fully confined conditions and stiffness decreases to a value near the unconfined solution.
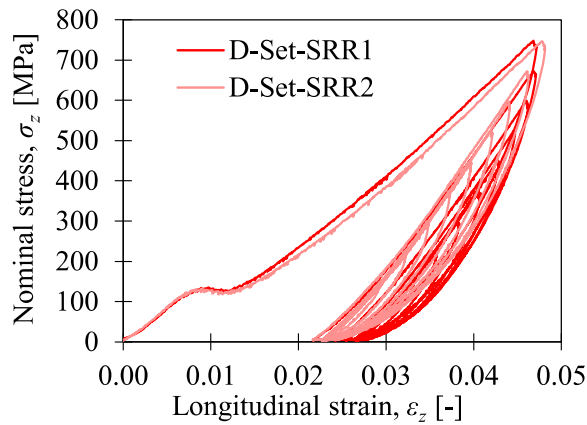
Figure 6.14. Steel-reinforced resin specimens under D-Set.

The analysis of residual strain is presented in Figure 6.16 showing that resin specimens present higher total residual strain values in all cycles compared to steel-reinforced resin specimen. The first cycle (with higher load) has a higher residual strain comparing to the following cycles which is caused by the settling process and transition between unconfined to confined state. From cycle 5 on, the percentage of viscoelastic strain is always superior to 90% of the total residual strain.
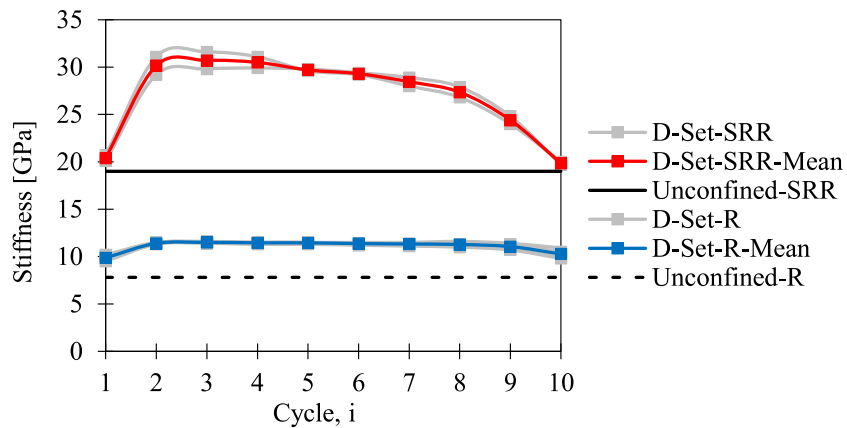
Figure 6.15. Stiffness evolution for steel and steel-reinforced resin specimens: D-Set.
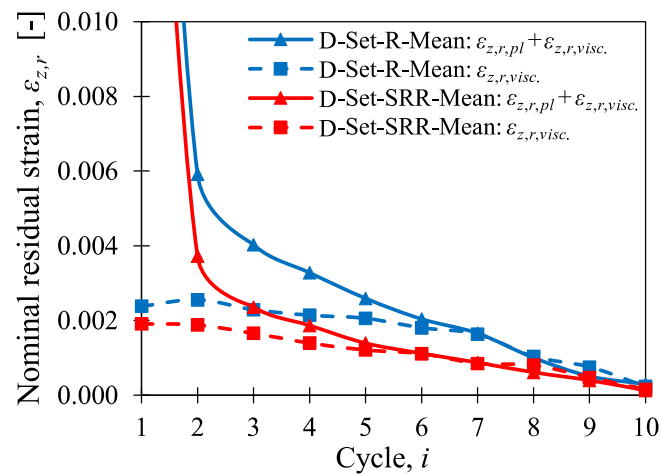
Figure 6.16. Residual strain for resin and steel-reinforced resin specimens: D-Set.

6.3.2.4   Summary of results

These experimental tests allow to define the material properties of resin and steel-reinforced resin specimens under unconfined and confined conditions:

- From the unconfined tests it was found that using a steel matrix together with an epoxy resin influenced the stiffness and ductility. Then Young's modulus increased by 181% and fracture strain for steel-reinforced solution is 17% of the value found for bare resin specimens. The yield stress was not significantly changed which means that it is mainly influenced by resin material properties.

- The experimental setup defined for confined tests was efficient to test specimens under confined conditions after first cycles.

- Both materials present a linear behaviour on loading phase under confined conditions. Stiffness in confined conditions is 148% and 157% higher than in unconfined conditions for resin and steel-reinforced resin material, respectively – see Table 6.2.

- Under confined conditions, after 10 cycles the stiffness of steel-reinforced specimens is around 2.6 times higher than the stiffness of resin specimens;

- After initial settling, the stiffness for resin specimens does not vary when the specimen is in confined conditions; however, for steel-reinforced specimens the stiffness increases due to the densification of the material;

- When using steel shots and fewer resin (steel-reinforced solution), residual plastic strain and viscoelastic strain are decreased which is caused by different Young's moduli and hardening behaviours; This reduction on material strain will contribute to reduce the slip at the connection level.

- Scatter on results is higher for steel-reinforced resin due to material heterogeneities.

Table 6.2. Stiffness of resin and unconfined resin materials.

Resin			Steel-reinforced resin		
Confined		Unconfined	Confined		Unconfined
A-Set	11.7 GPa	7.8 GPa	A-Set	30.0 GPa	21.9 GPa
D-Set	11.4 GPa		D-Set	29.5 GPa	

6.4   Numerical simulation

6.4.1   Model setup

A 3D finite element model of the experimental setup was developed using ABAQUS 2020 – see Figure 6.17 – using C3D8R finite elements [154]. The maximum element size was 1 mm. The load was applied on top of loading pin in ZZ direction and all translation degrees of freedom on the bottom surface of the bearing piece were fixed. Contact between the components was defined with the surface-to-surface contact methodology based on tangential and normal behaviour. The friction coefficient between specimens and the surrounding elements (confinement, loading pin and bearing) was set as 0.075 and 0.350 for resin and steel-reinforced resin specimens, respectively. When steel-reinforced resin specimens are used, the value of the friction coefficient is increased due to the presence of the steel shots. Since specimens are in unconfined state at the beginning of the test due to small differences in diameter of the specimen and the inner circle of the confinement piece, it was decided to model a gap between the specimen and the confinement piece of 0.1 mm.
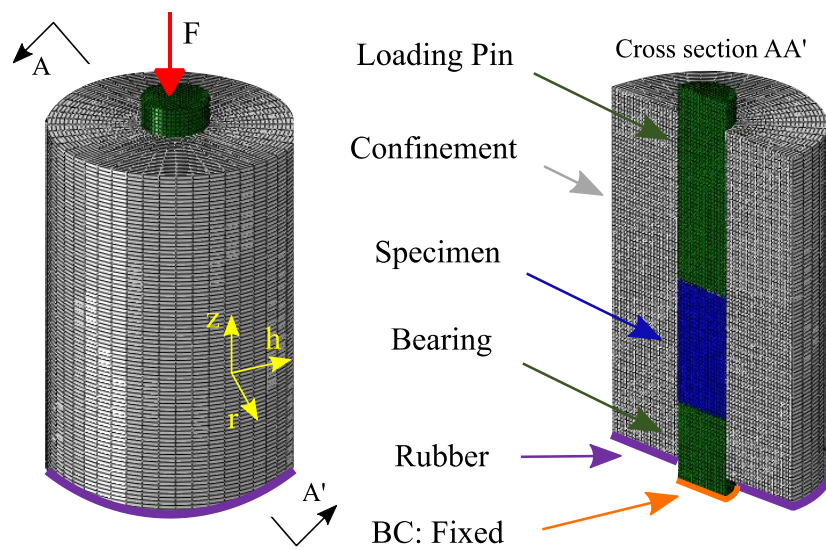
Figure 6.17. Finite element model of confined material test.

6.4.2   Material parameters

All metallic components (loading pin, bearing and confinement piece) were modelled using a linear model with 210 GPa of Young's modulus and 0.3 for Poisson's coefficient. The material model used for the specimens was based on elastic parameters, hardening performance (see Table 6.3) and Drucker-Prager yield criterion.

Table 6.3. Hardening law for resin and steel-reinforced resin.

Resin		Steel-reinforced resin	
True stress σ_z [MPa]	True plastic strain $\varepsilon_{z,pl}$ [-]	True stress σ_z [MPa]	True plastic strain $\varepsilon_{z,pl}$ [-]
125.0	0.0000	135.0	0.0000
120.0	0.0115	136.2	0.0039
115.0	0.0395	130.0	0.0074
110.0	0.0895	100.0	0.0154
106.0	0.1895	20.0	0.0354

The implementation of the Drucker-Prager model depends mainly on the internal friction angle φ. It influences the shape of the stress-strain curve during the loading phase and the residual plastic strain. The parameters of the linear Drucker-Prager model for resin and steel-reinforced resin were defined by calibration with the experimental results. Their values are presented in Table 6.4.

Table 6.4. Parameters to define Drucker-Prager model.

	φ [º]	c_{MC} [MPa]	β_j [º]	K_{tc} [-]	ψ [º]
Resin	25.0	39.8	35.42	0.778	35.42
Steel-reinforced resin	65.0	21.7	54.28	0.778	54.28

6.4.3   Numerical results

The numerical computation for resin and steel-reinforced resin specimens under the ascending and descending loading sets were conducted. Longitudinal (ZZ-direction) deformation, von Mises stresses and radial deformation at maximum applied load of cycle 10 are presented in Figure 6.18a), b) and c), respectively.
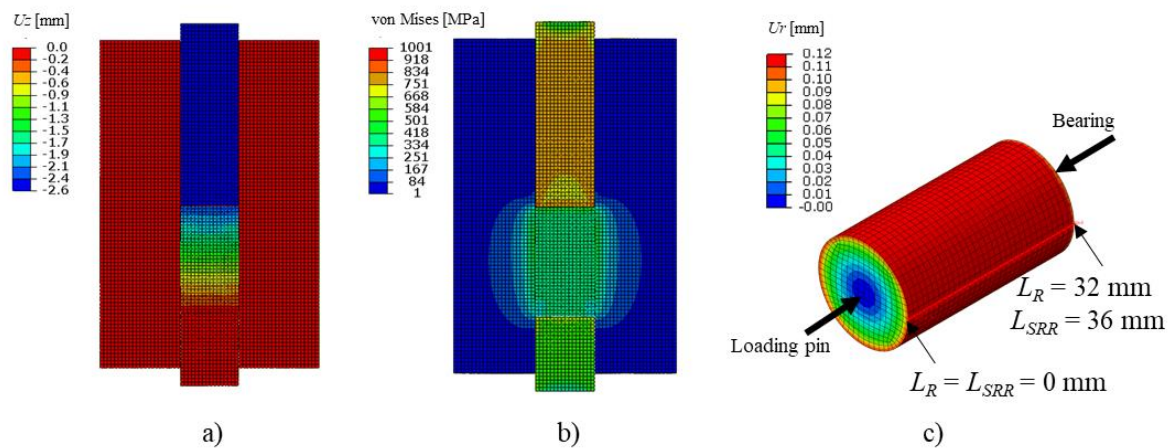
Figure 6.18. Numerical results for **resin** specimen (**A-Set**) at maximum applied load of cycle 10: a) longitudinal deformation; b) von Mises stresses; c) radial deformation.

The correlation between numerical and experimental results of the longitudinal nominal stresses and strains for cycle 2 of A-Set is presented in Figure 6.19. This is the cycle where the stress plateau occurs. In these figures, all data is translated to zero strain coordinates considering the linear regression defined to compute the stiffness of the loading phase. The numerical model can efficiently predict the stress plateau observed in cycle 2. In Figure 6.20, the same comparison is established but in this case for cycle 10. It shows that the behaviour is linear during the loading phase and the numerical results correlate well with the experimental evidences.
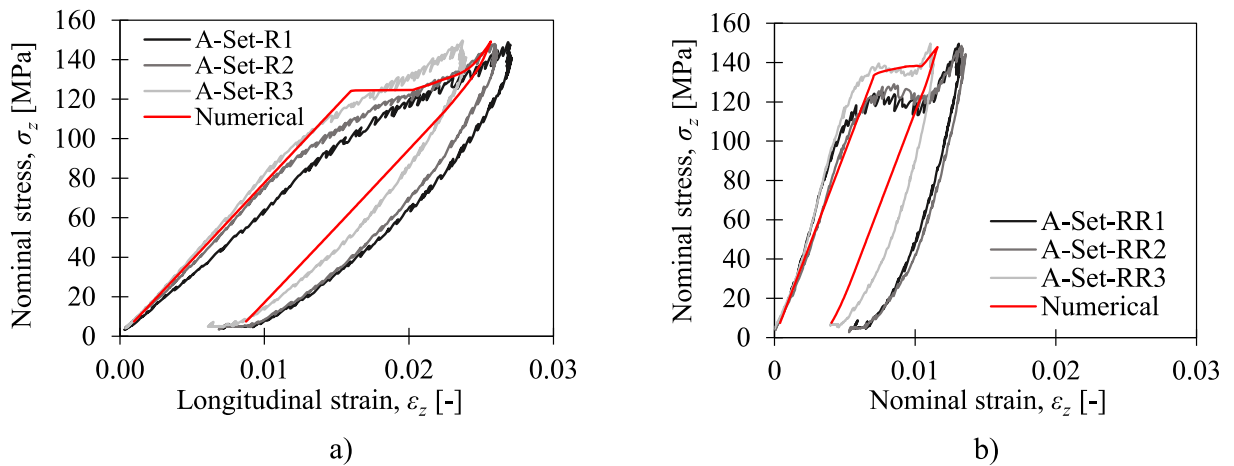
Figure 6.19. Numerical and experimental stress-strain for **cycle 2** of **A-set**: a) resin; b) steel-reinforced resin.
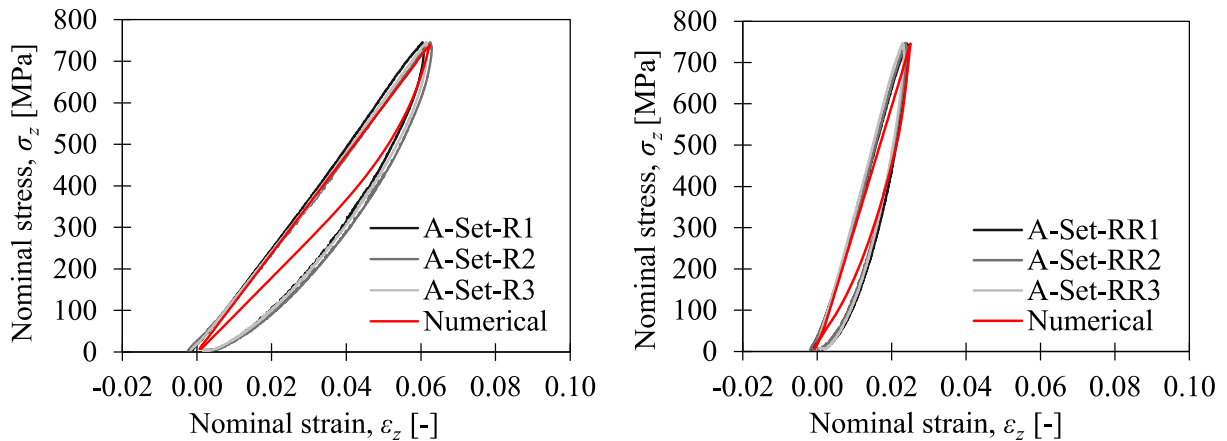
Figure 6.20. Numerical and experimental stress-strain for **cycle 10** of **A-set**: a) resin; b) steel-reinforced resin.

Radial deformation at maximum applied load of each cycle of the A-Set was computed over the length of the specimen – see Figure 6.18c). For both resin and steel-reinforced resin specimens, results are presented in Figure 6.21. In the first cycle, radial deformation is higher in the middle of the specimen for both materials but the maximum value for steel-reinforced resin represents 29% of the value found for resin specimens. Both specimens are in unconfined conditions during the first cycle. In the second cycle, resin specimen is almost completely in confined conditions since the radial deformation is 0.1 mm for nearly all its length, however for steel-reinforced resin, only a small region in the middle of the specimen reached confined state. This difference is related to its higher stiffness. For the first and second cycles, radial deformation has a symmetrical shape over the length of the specimen, but in the following

cycles the values are higher at the upper part of the specimen, near the loading pin. This effect is attributed to the friction forces which are developed when the specimen is in contact with the confinement piece. Radial deformation in the last cycles is higher for resin specimens which is attributed to its lower stiffness and higher Poisson coefficient.
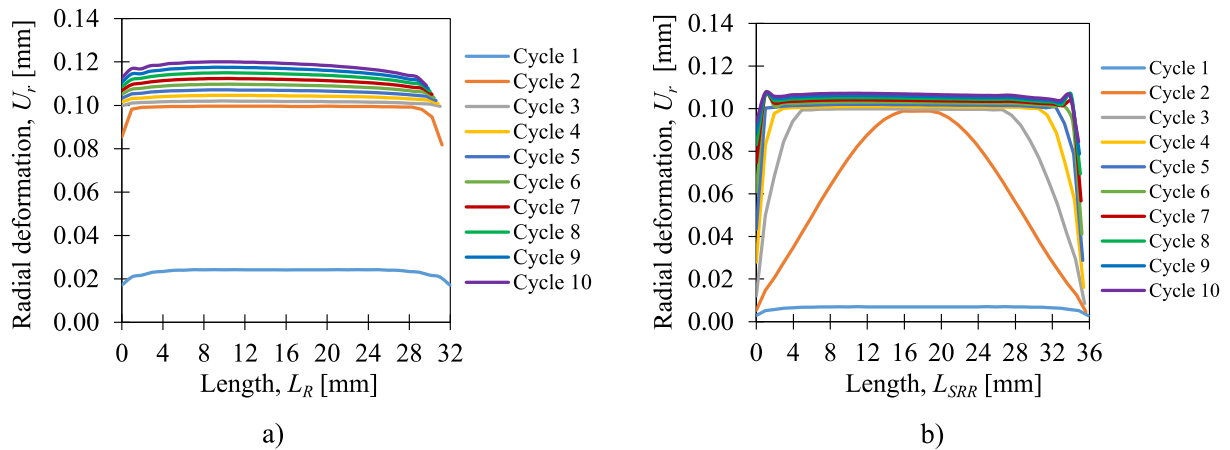
Figure 6.21. Radial deformation at maximum load of each cycle for **A-Set**: a) resin; b) steel-reinforced resin.

Radial deformation for resin and steel-reinforced resin specimens under D-Set are presented in Figure 6.22. This loading case in which the first cycle has the highest load, specimens are in fully confined conditions during the entire test and a non-symmetrical distribution of radial deformation is evident from the first cycle and beyond. Since the central part of the specimen gets in contact with the confined piece in a first stage, friction forces start to be developed in that region originating higher radial deformation in the upper part of the specimen. Resin specimens present higher radial deformations as in the previous loading set due to its material properties. Steel-reinforced resin specimens show peaks of radial deformation near to the edges which is related to higher friction forces developed in that region.

Longitudinal true stresses over the length of the specimen at maximum load of each cycle for the A-Set are presented in Figure 6.23. The first cycles present a nearly constant value since specimens are in unconfined conditions. In the following cycles, longitudinal stresses have a non-uniform distribution over the length, since specimens get in contact with the confinement piece and friction forces are developed. It is evident that higher stresses are developed in the upper part of the specimen in which the load is applied, and friction forces are more relevant.

The difference between top and bottom longitudinal stresses is more significant for steel-reinforced specimens mainly due to higher friction forces that are developed.
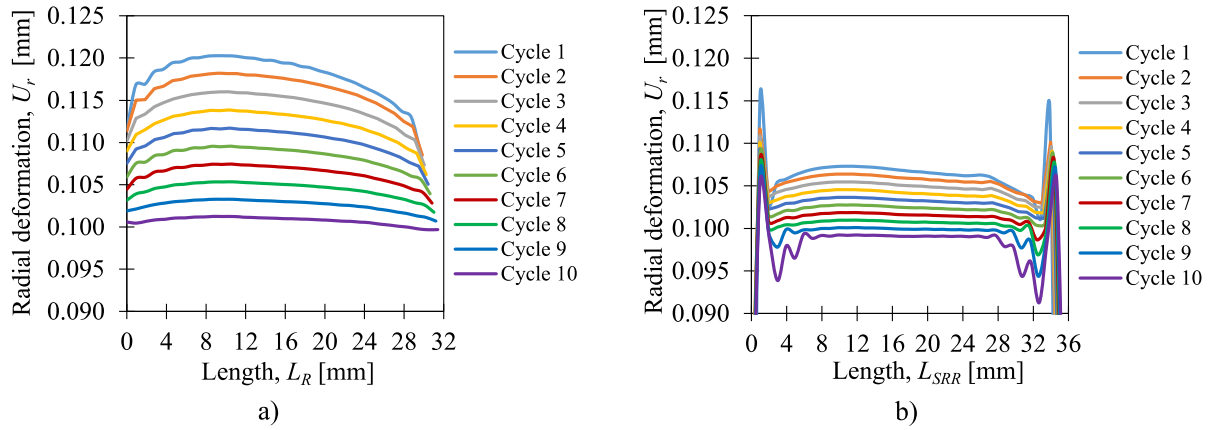
Figure 6.22. Radial deformation at maximum load of each cycle for **D-Set**: a) resin; b) steel-reinforced resin.
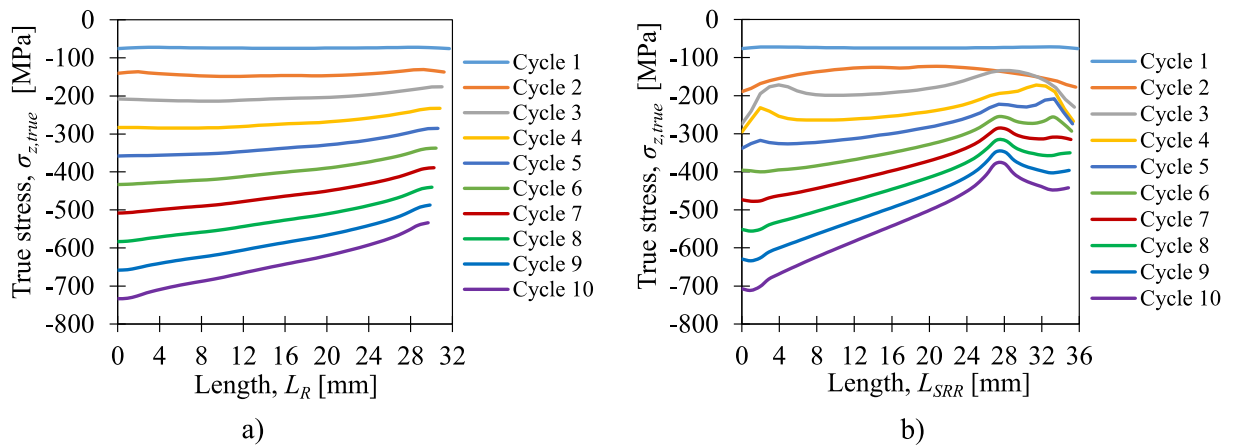
Figure 6.23. Longitudinal stresses at maximum load of each cycle for **A-Set**: a) resin; b) steel-reinforced resin.

Longitudinal true stresses under the D-Set are presented in Figure 6.24. They show a reversed, yet very similar performance to longitudinal stresses computed for A-Set. Friction forces are higher in the upper part of the specimen leading to higher stresses in that region. A non-uniform distribution of the stresses is evident from the first load cycle.

Finally, the value of the stiffness obtained by numerical analysis is compared with experimental results. In Figure 6.25a), it is possible to observe a good agreement for resin specimens in A-set and D-Set. In the case of steel-reinforced resin, a comparison is established in Figure 6.25b).
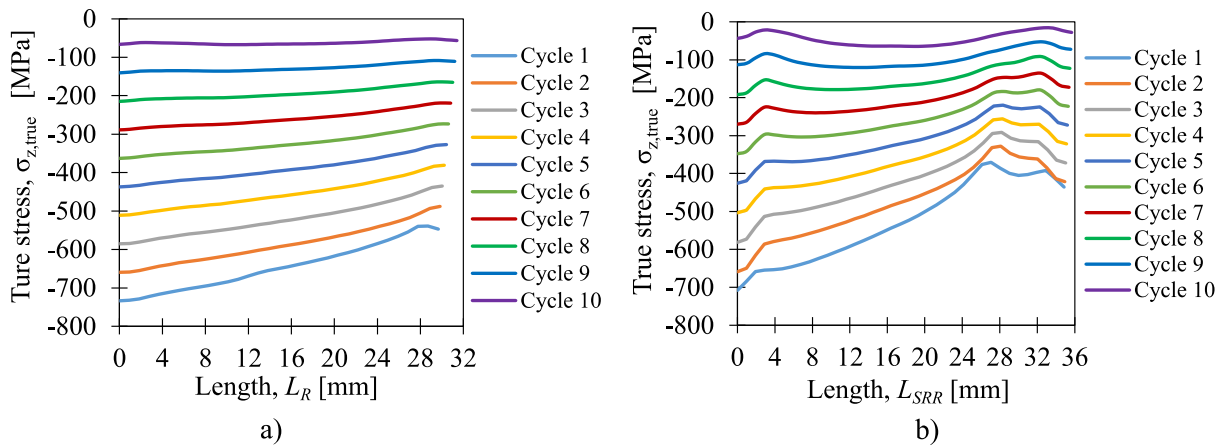
Figure 6.24. Longitudinal stresses at maximum load of each cycle for **D-Set**: a) resin; b) steel-reinforced resin.
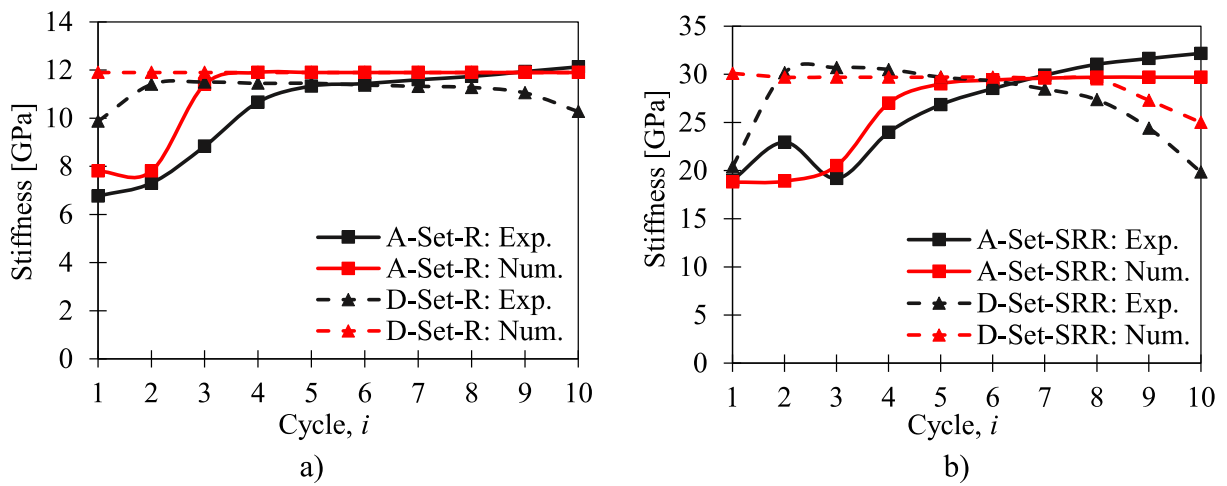
Figure 6.25. Numerical and experimental stiffness: a) resin specimens; b) steel-reinforced resin specimens.

In A-Set, from cycle 1 to cycle 3, numerical results are coherent with experimental results by presenting a stiffness similar to the stiffness found for the unconfined solution. Reaching cycle 5, the stiffness stabilizes around 30 GPa which is very well correlated with experimental results. For D-Set, excluding cycle 1 which is affected by specimen settling, there is a good agreement between numerical and experimental results.

Numerical model is able to predict the loss of stiffness in the last two cycles due to partially confined conditions. This effect is more evident for steel-reinforced specimens because residual strains are considerably lower when compared to resin specimens.

6.5   Conclusions

The mechanical performance of a two-component epoxy resin, designated as RenGel® SW 404 + HY 5159, was assessed with unconfined and confined compressive tests of bare resin and steel-reinforced resin specimens.

Unconfined experimental results allowed to define uniaxial material properties, such as the Young's modulus, Poisson coefficient and hardening/softening behaviour [150]. Steel-reinforced resin led to 1.8 times higher stiffness and a significant reduction of strain at failure.

When confined, steel-reinforced specimens provide a constant increase in stiffness after the specimen's settlement due to the densification of material, while resin specimens showed a constant value. In the last cycle, steel-reinforced resin specimens have 2.6 times higher stiffness comparing to bare resin specimens. Furthermore, steel-reinforced solution presented lower strains – both viscoelastic and residual plastic strains – which would lead to a reduction of slip at the connection level.

The behaviour of the two materials under confined conditions was efficiently described using linear Drucker-Prager plastic model implemented in a finite element simulation. The friction angle, the ratio of the yield stress in triaxial tension to the yield stress in triaxial compression and the dilation angle were obtained based on experimental and numerical homogenization. The effect of the lateral confinement was successfully considered by combining Drucker-Prager parameters and the unconfined experimental results.

A summary of the material properties evaluated based on experimental and numerical work is presented in Table 6.5. The higher stiffness of steel-reinforced resin compared to bare resin material is fundamental to achieve slip-resistant connections. The definition of material models under confined conditions developed in this chapter can be used to perform efficient numerical modelling of bolted shear connectors.

Table 6.5. Material properties of resin-based solutions (mean values).

Property		Resin		Steel-reinforced resin	
Components		RenGel® SW 404 + Ren© HY 5159		[RenGel® SW 404 + Ren© HY 5159] + Steel shots	
Density [g/cm^3]		1.86		5.26	
Poisson's ratio [-]		0.315		0.220	
Stiffness [GPa]	Unconfined	7.8		21.9	
	Confined	11.6		29.8	
Drucker-Prager model	φ [°]	25		65	
	c_{MC} [MPa]	39.8		21.7	
	β_j [°]	35.42		54.28	
	K_{tc} [-]	0.778		0.778	
	ψ [°]	35.42		54.28	
Hardening law		True stress [MPa]	True plastic strain [-]	True stress [MPa]	True plastic strain [-]
		125.0	0.0000	135.0	0.0000
		120.0	0.0115	136.2	0.0039
		115.0	0.0395	130.0	0.0074
		110.0	0.0895	100.0	0.0154
		106.0	0.1895	20.0	0.0354

7 PRELOADED INJECTION BOLTS – FATIGUE PERFORMANCE IN A BRIDGE STRENGTHENING SCENARIO

7.1 Introduction

Since the end of the 19th century, the number of metallic bridges constructed all over the world has been increasing. A significant number of these structures have long service lives and, therefore, they are prone to present high levels of structural degradation. For the majority, traffic intensity has increased significantly and their material properties have been degraded [1]. Scientific investigations have been showing that the most common evidences of structural damages in metallic bridges with long service lives are the presence of corroded elements and fatigue cracks [3–5,13].

There are several possibilities for repairing and strengthening operations on metallic riveted bridges, such as: implementation of fibre reinforced polymer (FRP) plates (bonded/unbonded and pre-stress/non-pre-stressed) or addition of supplementary steel plates. FRP plates can be effective by restoring the capacity of a damaged steel section or even strengthen it for higher loads than originally designed. Recent studies have shown that fatigue strengthening of steel members with FRP composites is promising, namely by delaying initial cracking, reducing the crack growth rate, extend the fatigue life and decrease the stiffness decay with residual deflection [158–161]. Strengthening using additional steel plates can be conducted using rivets, welding, high strength friction grip bolts or injection bolts, however the use of injection bolts has been considered as a better solution concerning their mechanical performance and protection against corrosion [18,19]. Injection bolts can be used to connect new steel plates but also to replace faulty rivets.

Several authors [162–168] have investigated the fatigue strength behaviour of riveted, bolted and welded connections, as well as the characterization of their fatigue fracture mechanism. Hosseini *et al.* [162] presented an experimental characterization study of bolted shear connectors and local failure of concrete under static and fatigue loading conditions. Liu *et al.* [166] suggested a simplified fatigue approach based on the continuum damage mechanics for metallic bolted connections under uni- and multi-axial loading conditions.

Leonetti *et al*. [164] proposed the fatigue life prediction of riveted shear connections based on a reliability modelling combined with local approaches.

Injection bolts can be produced from standard bolts adapting them for the injection process [78]. As is shown in Figure 7.1, the gap between the plates and the bolt shank is filled with an adhesive. After the curing process, it is intended to obtain a slip resistant connection. Most of the studies focused on the static or quasi-static performance of injection bolts [20,21,169] showing that this methodology has good results.
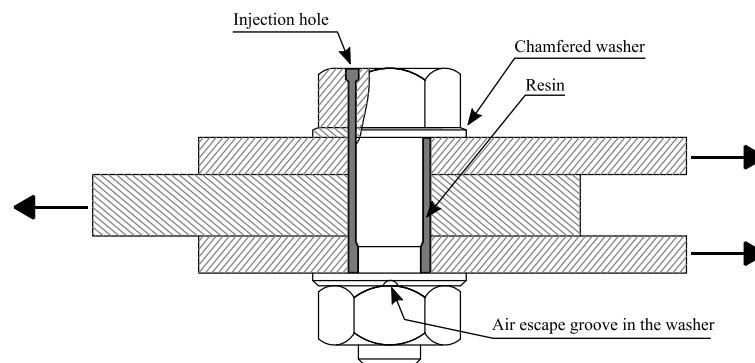
Figure 7.1. Injection bolt configuration.

Recent investigations have been made to evaluate the potential of different materials to be used in the injection. Rodrigues *et al*. [170] made an experimental characterization of two structural adhesives aiming to obtain their performance under static and fatigue loading conditions. Mechanical results showed that the epoxy-based resin Sikadur®-52 is suitable to be used in injection bolts. Koper [171] studied the application of epoxy-based resins on injection bolts under static loading, concluding that the viscosity is the first parameter to be accounted for in order to achieve a successful injection. Kolstein *et al*. [172] also found that grout materials, such as Sikadur®-30, are not adequate for injection bolts. In Nijgh [149], an innovative solution was created by filling the space with steel shots prior to injection with resin. This reinforced resin was created to increase connection stiffness and improve its creep performance. Additionally, experimental, numerical, and analytical assessments of compressive behaviour under confined and unconfined conditions for different adhesives to be used in injection bolts were studied by different authors [151,152]. It was found that steel-reinforced resin has higher

compressive strength values and shows to be a promising solution for injection bolts, however, this solution is only feasible for oversized bolt holes.

The application of preload on bolted connections influences the fatigue behaviour, mainly because the load transfer mechanism is by friction of plates when preload forces are implemented, and by shear of bolts and bearing of plates when there is no preload. For bolted connections designed as bearing-type, fatigue crack initiates at the edge of the hole and grows in the region of the net cross-section [69]. In the case of preloaded bolted connections, stress concentration occurs in the geometric discontinuity between outer and inner plates and between washers and outer plates. This type of fatigue failure is governed by the fretting mechanism and is obtained at the gross cross-section of plates [70,71]. The influence of preload magnitude on the fatigue life of bolted connections was assessed by Jiménez-Peña *et al*. [71] by means of experimental and numerical investigations. Results showed that higher fatigue performance can be obtained with higher preload forces. In fact, the beneficial effect of preload has been proven by several authors [72–75].

For single shear connections, there is one fundamental aspect related to the eccentricity in the neutral line. The main differences between connections with and without eccentricities are additional tensile load (which causes bending on the plates) and asymmetric loading conditions in the fastener leading to an inhomogeneous bearing pressure along the hole [23].

In what concerns fatigue design recommendations, the following *S-N* curves are proposed in EN 1993-1-9 [15]: detail category 112 should be used for double-covered symmetrical joints with preloaded high strength bolts or preloaded injection bolts; detail category 90 should be used for double-covered joints with fitted bolts or non-preloaded injection bolts, and one-sided connections with preloaded high strength bolts or preloaded injection bolts. Additionally, in 1994, the *European Recommendations for Bolted Connections with Injection Bolts* [19] was published with practical guidelines for static and fatigue design. However, the fatigue strength characterization of bolted connections with injected bolts combining puddled iron plates and current structural steels plates is not yet studied. The structural reinforcement of existing metallic bridges is frequently done considering the replacement of old metallic elements by structural elements of current steel [173]. Wang *et al*. [174] presented a fatigue performance

study on centenary metallic bridges using reinforcement techniques based on the application of new steel plates through bonding or bolting. In this sense, the fatigue strength characterization and the identification of failure mechanisms of structural connections combining existing metallic plates and current steel plates deserves special attention, especially the definition of reliable *S-N* curves.

Preload bolted connection with injection bolts has been considered as good solution to replace faulty rivets [20]. Generally, fatigue damages in riveted connections are found in the hole of the plates because load is transfer mainly through the rivet shank. Replacing this faulty rivet by preloaded bolt guarantees that pre-existing damages are not extended by transferring stress concentration to gross cross-section. In addition, by combining preload and injection bolt it is aimed that the stiffness of the solution does not rely only in friction surface quality of plates but also in the contribute of the resin. This is especially relevant when connecting new structural element to existing ones.

In this chapter, an experimental campaign is addressed in which fatigue tests have been conducted on preloaded bolted connections with injected and standard bolts aiming to understand the influence of the adhesive and to define reliable *S-N* design curves. Specimens were built combining current and old material plates in order to be as close as possible to a bridge strengthening scenario.

Since this study is focused on structural details to be implemented on bridges, the application of preload on bolts is essential to guarantee a satisfactory fatigue strength level. The fatigue performance of preloaded bolted connections is much better than the fatigue performance of fitted bolts (or rivets) [52,77]. However, load transfer in friction-type connections occurs mainly through the contact surfaces of plates and the fatigue crack develops at the gross cross-section due to fretting, generally. In this case, the effect of the adhesive around the bolt shank (injection bolt) is relevant if the load overcomes the slip resistance of the joint. This behaviour occurs in multiple situations: when it is not possible to guarantee a good level of friction coefficient between the contact surfaces, when preload losses are significant or in the case of overloads.

Additionally, results are compared with the design *S-N* curves included in EN 1993-1-9 [15] and proposed by Taras and Grainer [32]. The comparison between structural components composed by old metallic materials and current standards has been done by several authors, as for example DiBattista *et al*. [175].

7.2   Experimental campaign details

Experimental fatigue tests were performed to assess the fatigue strength of bolted connections with preloaded injection bolts in a context of structural rehabilitation of an old metallic bridge by establishing a comparison with bolted connections with preloaded standard bolts (without injection resin). A total of 46 specimens have been tested under fatigue loading varying the type of connection (single and double shear), type of bolt (injected and standard) and stress range (high, medium and low cycle fatigue regimes). Geometry of specimens is presented in Figure 7.2 and details of this experimental program are presented in Table 7.1.
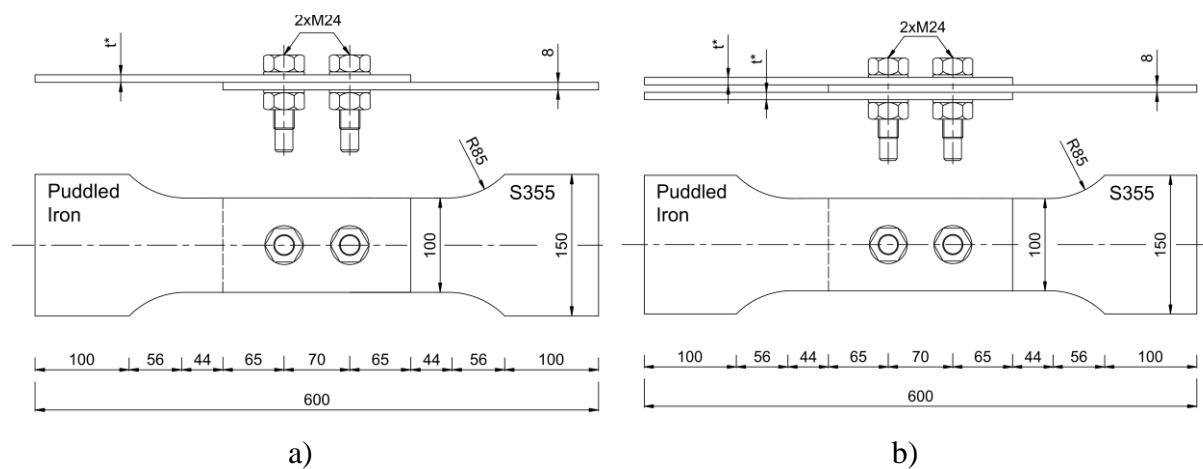
Figure 7.2 Geometry of specimens (*thickness varies between 6 and 8mm): a) single shear; b) double shear. (dimensions in mm)

This study aims to reproduce as close as possible the real situation of bridge strengthening techniques, therefore specimens are composed of steel plates manufactured with low alloy structural steel (S355) and plates extracted from the web of the main girders of a centenary Portuguese bridge named Eiffel bridge. The thickness of the plates extracted from structural elements of this bridge varied between 6 and 8 mm. An advanced level of installed corrosion was found. The Eiffel bridge was inaugurated in 1886 and was built in puddled iron, which is

a material with many heterogeneities, responsible for significant scatter in its material properties [77]. This bridge is the oldest Portuguese bridge in service.

Table 7.1. Fatigue experimental tests on bolted connections.

Type of connection	Type of bolt	Stress Range	N. of Specimens
Single shear	Standard	Low cycle – $\Delta\sigma_1$	3
		Medium cycle – $\Delta\sigma_2$	3
		Medium cycle – $\Delta\sigma_3$	3
		High cycle – $\Delta\sigma_4$	3
	Injected	Low cycle – $\Delta\sigma_1$	2
		Medium cycle – $\Delta\sigma_2$	3
		Medium cycle – $\Delta\sigma_3$	3
		High cycle – $\Delta\sigma_4$	4
Double shear	Standard	Low cycle – $\Delta\sigma_1$	3
		Medium cycle – $\Delta\sigma_2$	3
		Medium cycle – $\Delta\sigma_3$	3
		High cycle – $\Delta\sigma_4$	3
	Injected	Low cycle – $\Delta\sigma_1$	3
		Medium cycle – $\Delta\sigma_2$	3
		Medium cycle – $\Delta\sigma_3$	3
		High cycle – $\Delta\sigma_4$	1

Single shear connections are composed of one S355 steel plate and one puddled iron plate, while double shear connections are composed of two puddled iron plates positioned in the same side and one S355 steel plate in the opposite side. Higher stresses are obtained in puddled iron plate in the case of single shear connections (the thickness of the puddled iron plate is inferior to the thickness of the S355 steel plate) while in double shear connections higher stresses are obtained in the S355 steel plate.

The assembly is composed of two M24 bolts of high strength class 10.9 tightened using the torque method. Considering the procedure described in EN 1090-2 [78], the specified bolt preload is obtained by $F_{p,C} = 0.7 f_{ub} A_s$, where f_{ub} is the ultimate tensile strength of the bolt and A_s is the tensile stress area. Furthermore, the relation between the torque, M_b, and the specified preload force, $F_{p,C}$, is given by $M_b = k_b d F_{p,C}$, where k_b is the correlation coefficient and d is the bolt diameter. Table 7.2 summarizes the obtained values.

Holes in metallic plates have standard dimensions (d + 2 mm = 26 mm). They were executed through the following steps: drills were used first for spotting and then for complete drilling;

after that, helical boring was implemented to enlarge the holes to its required size; and finally, surfaces of the hole were finished with a boring head. This execution of holing reduces the presence of geometrical defects which could influence negatively the fatigue life.

Table 7.2. Calculation of bolt torque.

A_s [mm^2]	f_{ub} [MPa]	$F_{p,C}$ [kN]	k_b [-]	d [mm]	M_b [kN.m]
353	1000	247	0.123	24	729

The adhesive used for injection bolts was the epoxy-based resin Sikadur®-52. It is a low viscosity injection resin with good adhesion to steel. In fact, the viscosity level is a key aspect to guarantee that the small clearance (gap with 1 mm width, approximately) is filled with the adhesive, completely. The viscosity level of Sikadur®-52 [176] is compared with Araldite® [177] and Sikadur®-30 [178] in Table 7.3. It is observed that Sikadur®-52 [176] has lower viscosity properties than Araldite®. Although no information is presented in Sikadur®-30 [178] related to its viscosity properties, it should have higher viscosity than Sikadur®-52 [176] since it is a grout material.

Table 7.3. Viscosity properties of different structural resins.

Adhesive		Temperature [ºC]	Viscosity [mPa.s]
Sikadur®-52		20	430
Araldite®	RenGel SW 404	25	min 55000
	HY 2404	25	min 3500
Sikadur®-30*		-	-

*Grout material

Sikadur®-52 is used to fill voids in structures, such as bridges, and it not only forms an effective barrier against water infiltration and corrosion damage, but it also structurally bonds the assembled elements. It is characterized by its high strength properties, as shown in Table 7.4. Modulus of elasticity in compression is 1.25 GPa and in tension is 1.80 GPa. Specimens with resin-injected bolts were subjected to a cure time of at least 7 days, which resulted into near maximum strength properties.

Sikadur®-52 [176] is a two-part epoxy resin as shows Figure 7.3(a), which should be mixed in defined quantities leading to a homogeneous injection liquid – see Figure 7.3(b) and (c). Syringes were used for the measurement of the necessary quantities of each component to obtain the final

homogeneous adhesive, as well as for its injection in the specimen. The potlife of Sikadur®-52 is 25 minutes (for 1 kg of mixture A+B) at 20ºC, approximately. Thus, this resin meets the requirement prescribed in EN 1090-2 [78] of at least 15 minutes for the potlife.

Table 7.4. Monotonic mechanical properties of Sikadur®-52 [176].

Cure time	Compressive Strength (+23ºC)	Shear Strength (+23ºC)	Tensile Strength (+23ºC)
7 days	Aprox. 55 MPa	Aprox. 63 MPa	Aprox. 37 MPa

The adaptation of bolts and washers were performed taking into account the information in the annex K of EN 1090-2 [78]. A hole in the head of the bolt was drilled with the geometry indicated in Figure 7.4a). Washers are chamfered in the interior side to facilitate the resin injection process and the washers to use under the nut were prepared with an air scape groove – see Figure 7.4d).

a)   b)   c)
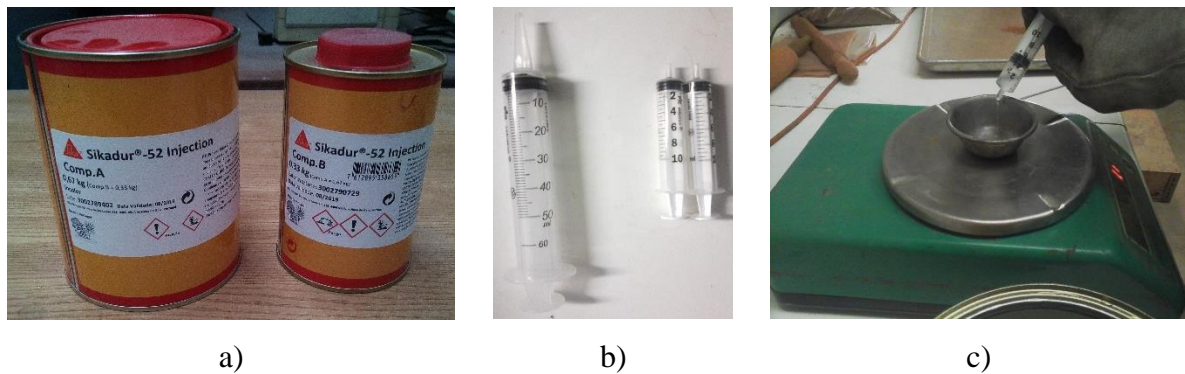
Figure 7.3. Preparation of resin Sikadur®-52 [176].

a)   b)   c)   d)

Figure 7.4. a) geometry of injection hole; b) bolt with injection hole; c) chamfered washer to use under the bolt's head; d) chamfered washer to use under the nut with the air scape groove.

Comparison between experimental fatigue results and design S-N curves must be performed considering a normalized stress range value, $\Delta\sigma_{norm}$, which considers mean stress effects introduced by different values of stress ratio R_σ. In this sense, experimental results presented

in this chapter were normalized by computing the normalized stress range, $\Delta\sigma_{norm}$, as is shown in Section 2.3.2.

7.3   Experimental tests – Single shear specimens

7.3.1   Preliminary static design

The components considered for the design of single shear specimens are **bolts in shear**, **plastic resistance of the gross cross-section**, **ultimate resistance of the net cross-section** and **tension resistance of the net cross-section**. The calculation of these components was performed with the standards EN 1993-1-1 [179] and EN 1993-1-8 [80] considering partial safety factors γ_{M0} and γ_{M2} equal to 1. Table 7.5 summarizes the analytical design of single shear specimens according to standards. It is concluded that the failure mode is at the net cross-section of puddled iron plate for an external load of 156.5 kN and the plastic limit is also at the net cross-section for an external load of 147.3 kN. The ultimate tensile strength of bolts, f_{ub}, was defined with the nominal value presented in EN 1993-1-8 [80], while the yield and ultimate strength of plates were defined considering experimental results presented in Section 3.3.2.

Table 7.5. Design of single shear specimens according to Eurocode 3.

Component	Equation	Variables		Resistance [kN]
Bolts in shear (Table 3.4, EN 1993-1-8)	$F_{v,Rd} = 2\dfrac{\alpha_v\,A_b\,f_{ub}}{\gamma_{M2}}$	α_v A_b [mm^2] f_{ub} [MPa]	0.5 353.0 1000.0	353.0
Plastic resistance of the gross cross-section (6.6, EN 1993-1-1)	$F_{pl,Rd} = \dfrac{A_{gross}\,f_y}{\gamma_{M0}}$	A_{gross} [mm^2] f_y [MPa]	650.0 306.3	199.1
Ultimate resistance of the net cross-section (6.6, EN 1993-1-1)	$F_{u,Rd} = \dfrac{0.9\,A_{net}\,f_u}{\gamma_{M2}}$	A_{net} [mm^2] f_u [MPa]	481.0 361.5	156.5
Tension resistance of the net cross-section (6.8, EN 1993-1-1)	$F_{net,Rd} = \dfrac{A_{net}\,f_y}{\gamma_{M0}}$	A_{net} [mm^2] f_y [MPa]	481.0 306.3	**147.3**

7.3.2   Monotonic test

A single shear specimen with the geometry presented in Figure 7.2a) was tested under monotonic loading conditions. The main goal of this experimental test was to assess the slip resistance and the static resistance to define the details of fatigue experimental tests. Normal

bolts were used (without resin) and all the conditions related to preload force and surface treatment are the same as used in fatigue tests. This test was conducted under displacement control (0.01 mm/s). The force-displacement curve of this monotonic test is plotted in Figure 7.5. The slip resistance of this connection was obtained as F_s = 64 kN. The slip factor can be obtained with equation (7.1) where n_p is the number of slip planes (in this case is 1) and $F_{p,C,}$ is the bolt preload force (247 kN). The obtained value was μ_e = 0.13. The ultimate resistance was obtained as F_u = 180.8 kN. The static capacity is limited by the tension resistance at net section of the puddled iron plate as shown in Figure 7.6.

$$\mu_e = \frac{F_s}{n_p \ 2 \ F_{p,C}} \tag{7.1}$$

Considering the obtained values, fatigue experimental tests were defined considering that the maximum stress level should be superior to the slip resistance of the connection (σ_{gross} > 64 000 N / 650 mm^2 = 98 MPa) in order to obtain load transfer by bearing of the resin and inferior to the plastic tension resistance of the net cross-section (σ_{gross} < 147 300 N / 650 mm^2 = 226.6 MPa).
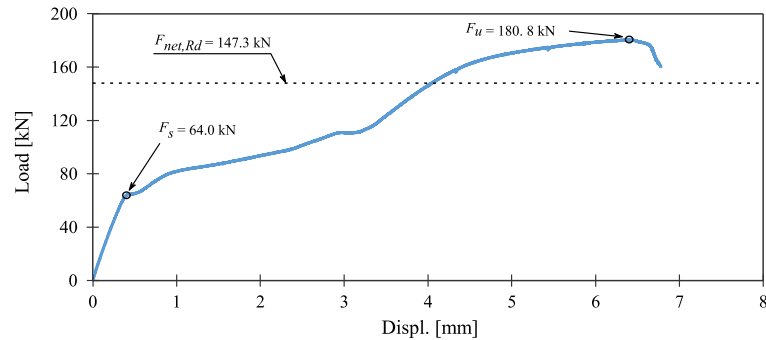
Figure 7.5. Monotonic test of single shear bolted connection.

Figure 7.6. Metallic plates from single shear specimen assembly after monotonic test.

7.3.3 Fatigue tests

Specimens were tested on a WALTERBAI Multipurpose Servo Hydraulic Universal Testing Machine rated to 600 kN. All fatigue tests were carried out under load control with a stress R-ratio equal to 0.1. The test frequency was set to 5 Hz for all tests except for one high-cycle fatigue test where load frequency was defined as 10 Hz to reduce the time of the test. It should be noted that when adhesives are used, test frequency should be small. ASTM D7791 [180] indicates a test frequency between 1-25 Hz and recommends the lowest value as much as possible. When no fatigue failure is obtained at 5 million cycles, the test is stopped, and it is considered as a run-out. This value corresponds to the constant amplitude fatigue limit defined in EN 1993-1-9 [15].

A single shear specimen during fatigue test is presented in Figure 7.7 and experimental results of fatigue tests on single shear specimens are presented in Table 7.6. Fatigue life obtained for test with frequency of 10 Hz was similar to fatigue life obtained for comparable test with frequency of 5 Hz which means that this variation in the frequency did not influence the fatigue performance. Failure was obtained in puddled iron plate for all specimens, except for specimen No. 10 (rupture in S355 plate) due to adhesive partial injection. Non-valid data was found due to partial injection of the resin or early rupture.

Depending on the stress range level, specimen's rupture was observed in a zone closest to the net cross-section of the plate or closest to its gross cross-section – see Figure 7.8a) and b). For higher stress amplitudes, friction resistance between the plates was not enough to transfer all the load leading to shear of bolts and fatigue failure at net cross-section, while for lower stress amplitudes, load was mainly transferred by friction and fatigue failure occurred at gross-cross section. Consequently, fatigue failure was classified as at net cross-section, at gross cross-section or at net/gross cross-section whether failure cross-section area is closer to the net cross-section, to the gross cross-section or in the middle between both cross-section areas, respectively. After these fatigue tests were carried out, specimens were disassembled allowing to analyse if the injection process was successful. Figure 7.8c) shows that the resin filled the clearance between the bolt and plates. Only specimen No.10 presented partial injection of the resin. The failure surface obtained in puddled iron plates is presented in Figure 7.8d). The

heterogeneity of this material is evident. The brighter area of the failure surface corresponds to the crack growth region while the remaining darker region is associated with final static failure.

Figure 7.7. Fatigue test on single shear bolted connection.

Table 7.6. Fatigue experimental results from single shear bolted connections.

Stress level	Sp.	Resin	$\Delta\sigma_{gross}$ [MPa]	$\Delta\sigma_{gross,norm}$ [MPa]	$\sigma_{gross,max}$ [MPa]	f [Hz]	N_f [cycles]	Failure plate	Failure location
$\Delta\sigma_1$ (low cycle)	1		180	185	200	5	5 678	Invalid	
	2		166	177	184	5	164 054	Puddled iron	Gross
	3		166	170	184	5	40 220	Puddled iron	Net
	4	x	177	182	197	5	21 135	Puddled iron	Net
	5	x	172	177	191	5	132 357	Puddled iron	Net/Gross
$\Delta\sigma_2$ (medium cycle)	6		159	163	176	5	325 628	Puddled iron	Net
	7		153	157	170	5	57 990	Invalid	
	8		157	161	174	5	29 028	Invalid	
	9	x	156	161	174	5	175 045	Puddled iron	Gross
	10	x	137	141	152	5	277 647	Invalid	
	11	x	157	161	174	5	349 915	Puddled iron	Gross
$\Delta\sigma_3$ (medium cycle)	12		129	132	143	5	50 725	Invalid	
	13		131	134	145	5	675 759	Puddled iron	Gross
	14		133	137	148	5	92 855	Puddled iron	Net
	15	x	136	139	151	5	574 138	Puddled iron	Net
	16	x	133	136	147	5	531 952	Puddled iron	Net/Gross
	17	x	129	133	144	5	413 977	Puddled iron	Net
$\Delta\sigma_4$ (high cycle)	18		111	114	123	5	5 087 414	Run-out	
	19		121	124	134	5	601 553	Puddled iron	Net/Gross
	20		117	121	131	5	905 699	Puddled iron	Net/Gross
	21	x	115	118	128	5	703 018	Puddled iron	Gross
	22	x	116	119	129	5	1 289 745	Puddled iron	Gross
	23	x	119	122	132	5	1 667 047	Puddled iron	Gross
	24	x	111	114	123	10	5 115 822	Run-out	

a) Gross failure mode

c) Resin injection analysis

b) Net failure mode

d) Fatigue failure surface in puddled iron plate.
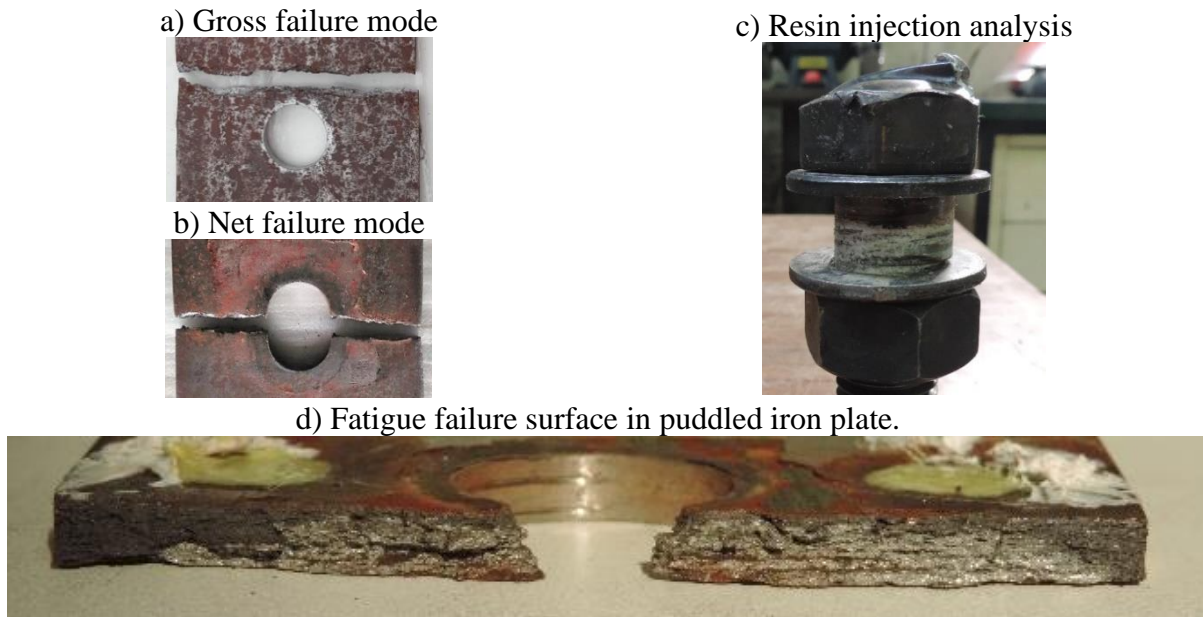
Figure 7.8. Analysis of single shear specimens after fatigue test.

The use of injection bolts should contribute to increase the stiffness of the connection and the slip displacement during fatigue tests should be lower when compared to standard bolted connections. Maximum deformation was recorded in every cycle during fatigue tests aiming to analyse the influence of the adhesive, therefore, in Figure 7.9 is shown the evolution of slip displacement for two fatigue tests (standard vs injected) for each stress level ($\Delta\sigma_1$ to $\Delta\sigma_4$). It is observed that using injected bolts contributed to decrease the slip of the connection. Considering only the tests presented in Figure 7.9, the reduction is nearly 60%, on average.
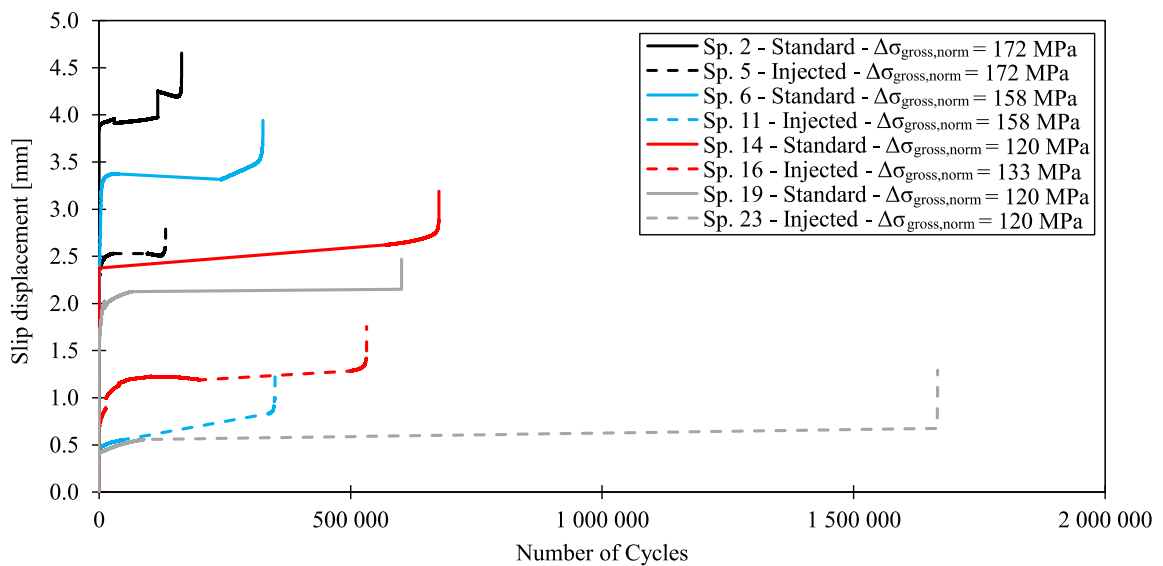
Figure 7.9. Slip displacement during fatigue tests – single shear specimens.

Experimental fatigue data is represented with an S-N diagram in Figure 7.10. Stress range values are computed using gross cross-section area of puddled iron plate, as is recommended in EN 1993-1-9 [15] for preloaded bolted connections. A linear regression analysis was implemented in the obtained fatigue data (run-out values were excluded) in order to define a mean S-N curve for injection bolts and a mean curve S-N for standard bolts. Mean S-N curve for standard bolted connections was found with an inverse slope of $m = 5.1$ and mean S-N curve for bolted connections with injection bolts with an inverse slope of $m = 6.9$. The level of scatter was assessed by the coefficient of determination (R^2). It is observed that implementing injection bolts contribute to reduce the level of scatter, since fatigue data for standard bolts has $R^2 = 0.5$ while fatigue data for injection bolts has $R^2 = 0.8$.
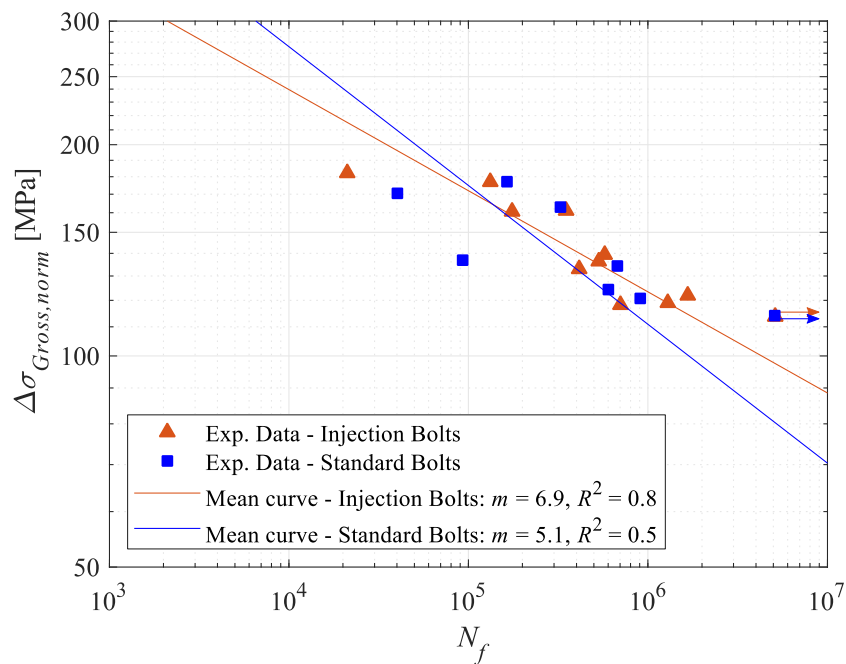
Figure 7.10. Mean S-N curves for single shear connections: comparison between injection and standard bolts (logarithmic scale).

In terms of characteristic S-N curves, normal and Weibull distributions were implemented. For the first case, the detail category was found as 92.4 MPa for injections bolts and 63.2 MPa for standard bolts – see Figure 7.12. Direct comparison cannot be made because the slope is distinct. The one-sided tolerance limit was found as $k_{5,75,v_{dg}} = 2.14$ for injection bolts and $k_{5,75,v_{dg}} = 2.25$ for standard bolts. Results for standard deviation were $\hat{\sigma} = 0.27$ for injection bolts and $\hat{\sigma} = 0.34$ for standard bolts.

For characteristic S-N curves using Weibull distribution, results of the four estimation methods used to determine α_W and β_W parameters are presented in Figure 7.11a) and b) for injection and standard bolts, respectively. The optimal estimation method was found by goodness-of-fit tests and results showed that Method of Moments (MM) lead to better correlation with BMR for injection bolts while for standard bolts it was the Linear Least Squared Method (LLSM). The characteristic curve using Weibull distribution was then defined and the detail category was found as 95.7 MPa for injection bolts and 64.9 MPa for standard bolts.

Table 7.7. Parameters of Weibull distribution and goodness-of-fit statistics for single shear bolted connections.

Fatigue data	Method		LLSM	WLLSM	MLM	MM
Injection	α_w		1.91	1.97	2.27	2.25
	β_w		1.32	1.31	1.29	1.29
	Goodness-of-fit	KS	0.093	0.092	0.075	0.078
		AD	0.177	0.162	0.157	0.154
		χ^2	0.036	0.036	0.055	0.053
Standard	α_w		1.22	1.27	1.83	1.90
	β_w		1.52	1.48	1.42	1.43
	Goodness-of-fit	KS	0.115	0.119	0.154	0.162
		AD	0.410	0.398	0.482	0.509
		χ^2	0.105	0.110	0.202	0.213
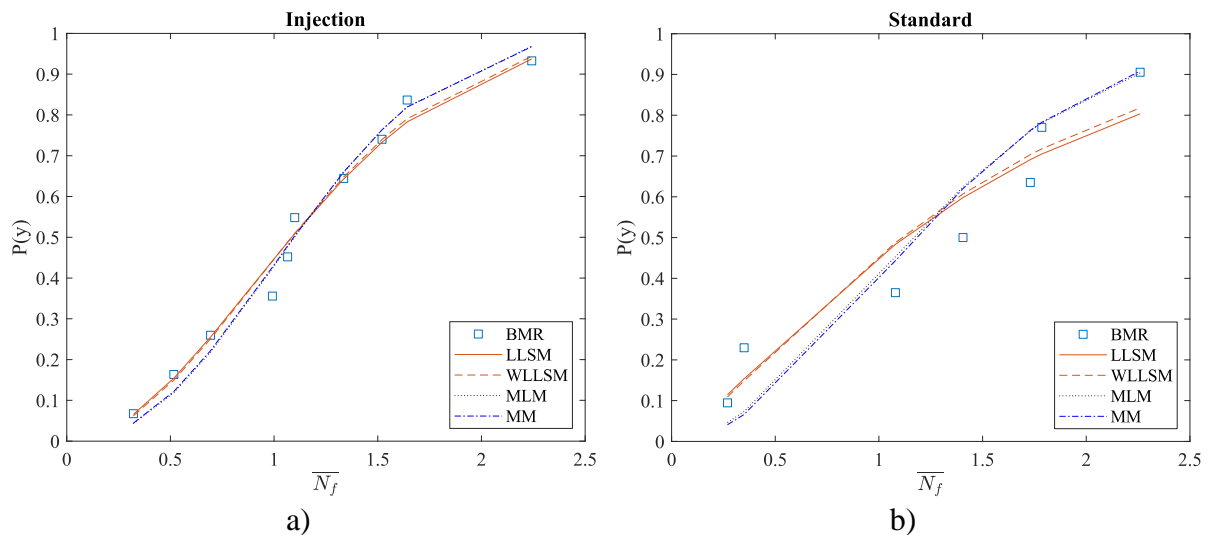
Figure 7.11. Comparison of cumulative Weibull distribution function for single shear bolted connections: a) Injection bolts; b) Standard bolts.
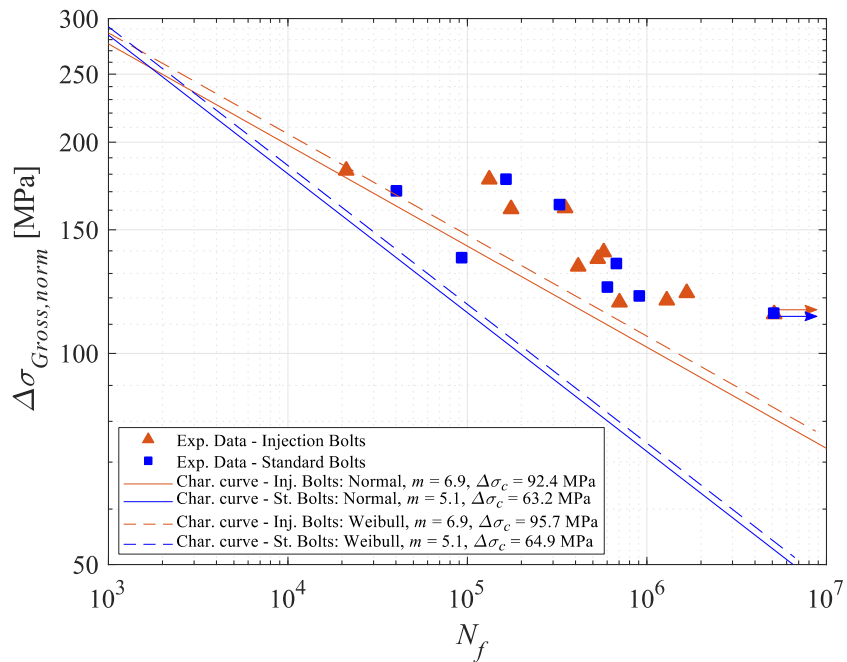
Figure 7.12. Characteristic S-N curves for single shear connections: comparison between injection and standard bolts (logarithmic scale).

Table 7.8 shows a comparison of fatigue life (computed on characteristic curves obtained with normal distribution function presented in Figure 7.12) for preloaded injection bolts and preloaded standard bolts on each stress range separately. It can be observed that the beneficial effect on the fatigue strength by using preloaded injection bolts is evident in all stress levels but with higher relevance for high-cycle fatigue regimes. The fundamental aspect is that the lower level of scatter verified for data from preloaded injection bolts led to higher fatigue strength in the characteristic curve for all fatigue regimes. In fact, on average, using preloaded injection bolts leads to 10% higher fatigue lives for the studied stress ranges (considering logarithmic scale values).

Table 7.8. Comparison of fatigue life from preloaded standard and injection bolts for each stress range using normal characteristic curves – **single shear specimens**.

Stress range [MPa]	Bolt type	Number of cycles N_f	Comparison Linear scale	Comparison Logarithmic scale
$\Delta\sigma_1 = 178$	Standard	10 652		
	Injection	21 078	+97.9%	+7.4%
$\Delta\sigma_2 = 162$	Standard	17 146		
	Injection	40 521	+136.3%	+8.8%
$\Delta\sigma_3 = 136$	Standard	41 510		
	Injection	136 426	+228.7%	+11.2%
$\Delta\sigma_4 = 119$	Standard	81 518		
	Injection	344 603	+322.7%	+12.8%

Fatigue experimental results were compared with design *S-N* curve proposed in EN 1993-1-9 [15] as shown in Figure 7.13. It is possible to see that the detail category recommended in this standard (detail category 90) does not represent a safe design criterion. In fact, this design curve is not able to represent the fatigue strength of metallic details whose endurance is based on old metallic materials such as puddled iron, as was already discussed by several authors [77,181]. Taras and Greiner [32] performed an analysis of a significant amount of fatigue tests using riveted connections from old bridges. They proposed a design *S-N* curve with an inverse slope $m = 5$ and a detail category of 71 for single shear riveted connections. This curve seems to be adequate to represent fatigue life of specimens composed of standard bolts.
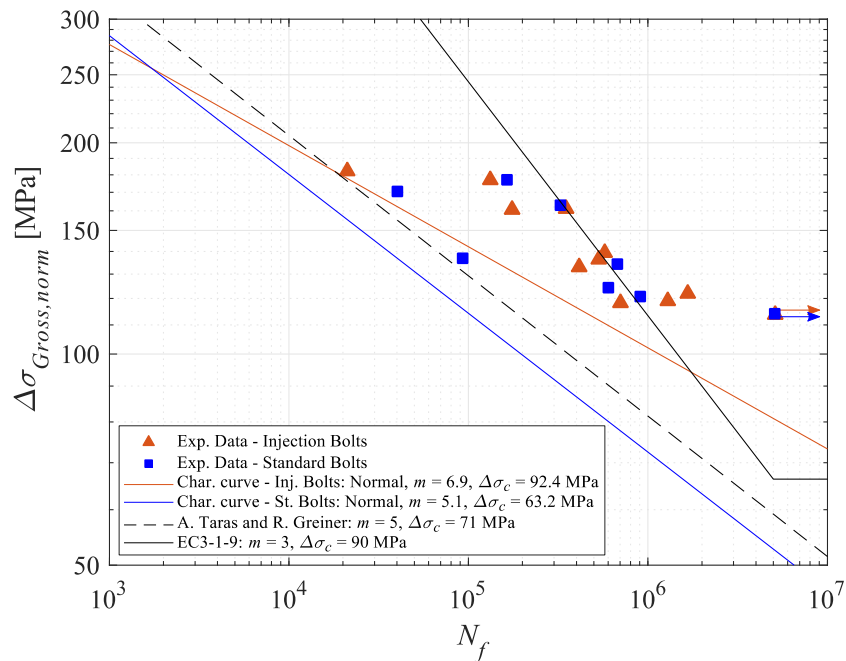
Figure 7.13. Experimental data for single shear specimens – comparison with design curves.

7.4   Experimental tests – Double shear specimens

7.4.1   Preliminary static design

The components considered for the design of double shear specimens are **bolts in shear**, **plastic resistance of the gross cross-section**, **ultimate resistance of the net cross-section** and **tension resistance of the net cross-section** which were computed with the standards EN 1993-1-1 [179] and EN 1993-1-8 [80]. Partial safety factors γ_{M0} and γ_{M2} were considered

equal to 1. Table 7.9 summarizes the analytical static design of double shear connections according to the referred standards. It is concluded that the failure mode is at the net cross section for an external load of 352.2 kN and the plastic limit is also at the net cross-section for an external load of 248.0 kN. The ultimate tensile strength of bolts, f_{ub}, was defined with the nominal value presented in EN 1993-1-8 [80], while the yield and ultimate strength of plates were defined considering experimental results presented in Section 3.3.2 for steel S355.

Table 7.9. Design of double shear specimens according to Eurocode 3.

Component	Equation	Variables		Resistance [kN]
Bolts in shear (Table 3.4, EN 1993-1-8)	$F_{v,Rd} = 4\dfrac{\alpha_v\,A_b\,f_{ub}}{\gamma_{M2}}$	α_v A_b [mm^2] f_{ub} [MPa]	0.5 353 1000	706.0
Plastic resistance of the gross cross-section (6.6, EN 1993-1-1)	$F_{pl,Rd} = \dfrac{A_{gross}\,f_y}{\gamma_{M0}}$	A_{gross} [mm^2] f_y [MPa]	800 419	335.2
Ultimate resistance of the net cross-section (6.6, EN 1993-1-1)	$F_{u,Rd} = \dfrac{0.9\,A_{net}\,f_u}{\gamma_{M2}}$	A_{net} [mm^2] f_u [MPa]	592 595	352.2
Tension resistance of the net cross-section (6.8, EN 1993-1-1)	$F_{net,Rd} = \dfrac{A_{net}\,f_y}{\gamma_{M0}}$	A_{net} [mm^2] f_y [MPa]	592 419	**248.0**

7.4.2   Monotonic test

A double shear specimen with the geometry presented in Figure 7.2b) was tested under monotonic loading conditions. The main goal of this experimental test was to assess slip and static resistances to define the details for fatigue experimental tests. Normal bolts were used (without resin) and all the conditions related to preload force and surface treatment are the same as used in fatigue tests. This test was conducted under displacement control (0.01 mm/s). The force-displacement curve of this monotonic test is plotted in Figure 7.14.

The slip resistance of this connection was obtained as $F_s = 104$ kN and slip factor was computed with equation (7.1) resulting in $\mu_e = 0.11$. The ultimate resistance was obtained as $F_u = 316.7$ kN. The static capacity is limited by the tension resistance at net section of the S355 steel plate as shown in Figure 7.15. Considering the obtained values, fatigue experimental tests were defined considering that the maximum stress level should be superior to the slip resistance of the connection ($\sigma_{gross} > 104\ 000$ N / 800 mm^2 = 130 MPa) in order to obtain load transfer

by bearing of the resin and inferior to the plastic tension resistance of the net cross-section ($\sigma_{gross} < 248\ 000$ N / 800 mm$^2 = 310$ MPa).
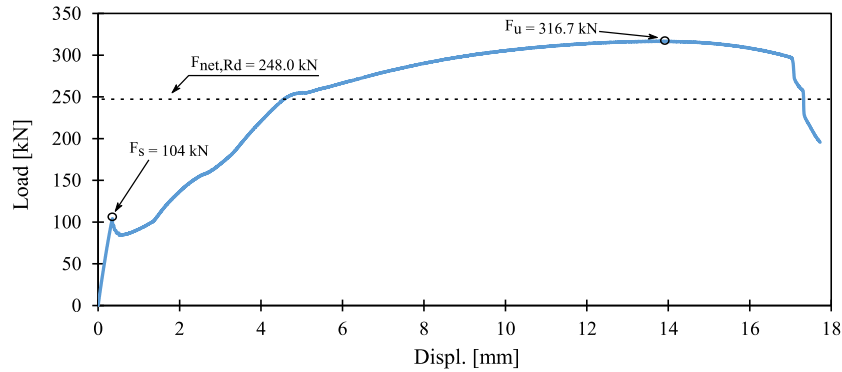
Figure 7.14. Monotonic test of double shear specimen.

Figure 7.15. Double shear assembly components after test.

7.4.3   Fatigue tests

Specimens were tested on a WALTERBAI Multipurpose Servohydraulic Universal Testing Machine rated to 600 kN. All fatigue tests were carried out under load control with a stress ratio equal to 0.1. The test frequency was set to 5 Hz for all tests except for high-cycle fatigue tests ($\Delta\sigma_4$) where test frequency was defined as 10 Hz. When no fatigue failure is obtained at 5 million cycles, the test is stopped, and it is considered as a run-out. In Figure 7.16 is presented a double shear specimen prepared for fatigue test.

Fatigue experimental data is presented in Table 7.10. Failure was obtained at S355 plate for most of the tested specimens since only four specimens failed at puddled iron plate. Four specimens did not fail at 5 million cycles.

Different types of failure were obtained as is presented in Table 7.11. The correspondence between the type of failure and the fatigue regime was studied. From Table 7.10, it is observed that for low-cycle fatigue regime, $\Delta\sigma_1$, fatigue failure at net cross-section is dominant, for medium low-cycle fatigue regime, $\Delta\sigma_2$, half of the specimens failed at net cross-section and the other half failed in a mixed mode type, for medium high-cycle fatigue regime, $\Delta\sigma_3$, fatigue failure through mixed mode type is dominant and for high-cycle fatigue regime, $\Delta\sigma_4$, failure at gross cross-section was obtained.
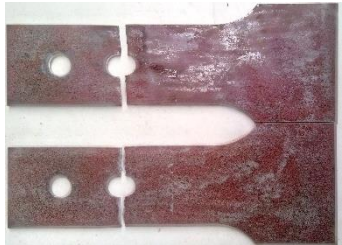
Figure 7.16. Double shear bolted connection.

Table 7.10. Fatigue experimental results from double shear bolted connections.

Stress level	Sp.	Resin	$\Delta\sigma_{gross}$ [MPa]	$\Delta\sigma_{gross,norm}$ [MPa]	$\sigma_{gross,max}$ [MPa]	f [Hz]	N_f [cycles]	Failure plate	Failure location
$\Delta\sigma_1$ (low cycle)	1		250	261	278	5	440 260	PI*	Net
	2		250	261	278	5	648 250	S355	Net/Gross
	3		250	261	278	5	91 024	S355	Net
	4	x	250	261	278	5	340 283	S355	Net
	5	x	250	261	278	5	510 796	S355	Net
	6	x	250	261	278	5	314 980	PI*	Net
$\Delta\sigma_2$ (medium cycle)	7		222	232	247	5	250 165	PI*	Net
	8		222	232	247	5	892 015	S355	Net/Gross
	9		222	232	247	5	1 596 924	PI*	Net
	10	x	222	232	247	5	1 118 960	S355	Net/Gross
	11	x	222	232	247	5	791 521	S355	Net
	12	x	222	232	247	5	856 283	S355	Net/Gross
$\Delta\sigma_3$ (medium cycle)	13		197	206	219	5	1 088 528	S355	Net/Gross
	14		198	207	220	5	1 606 433	S355	Net
	15		197	206	219	5	1 471 636	S355	Net/Gross
	16	x	198	206	220	5	5 000 000	Run-out	
	17	x	197	206	219	5	5 000 000	Run-out	
	18	x	197	206	219	5	1 128 094	S355	Net/Gross
$\Delta\sigma_4$ (high cycle)	19		175	183	194	10	5 000 000	Run-out	
	20		186	195	207	10	2 292 737	S355	Gross
	21		187	195	207	10	5 000 000	Run-out	
	22	x	187	195	207	4	4 234 000	S355	Gross

*PI = Puddled iron

Table 7.11. Fatigue failure analysis of double shear bolted connections

Failure location	Type of failure	Figure
S355 plate	Net cross-section failure	
	Net/Gross cross-section failure	
	Gross cross-section failure	
Puddled iron	Net cross-section failure	

In what concerns slip displacement of double shear specimens during fatigue tests, in Figure 7.17 is shown the evolution of slip for two fatigue tests (standard vs injected) for each stress level ($\Delta\sigma_1$ to $\Delta\sigma_4$). For the selected fatigue tests, slip displacement for standard specimens is above 3 mm while for injected specimens it is below 1.5 mm. The increase of stiffness (slip reduction) is around 80% on average which is much higher when compared to results from single shear specimens. It means that the beneficial effect of using injection bolts is superior for double shear configuration.
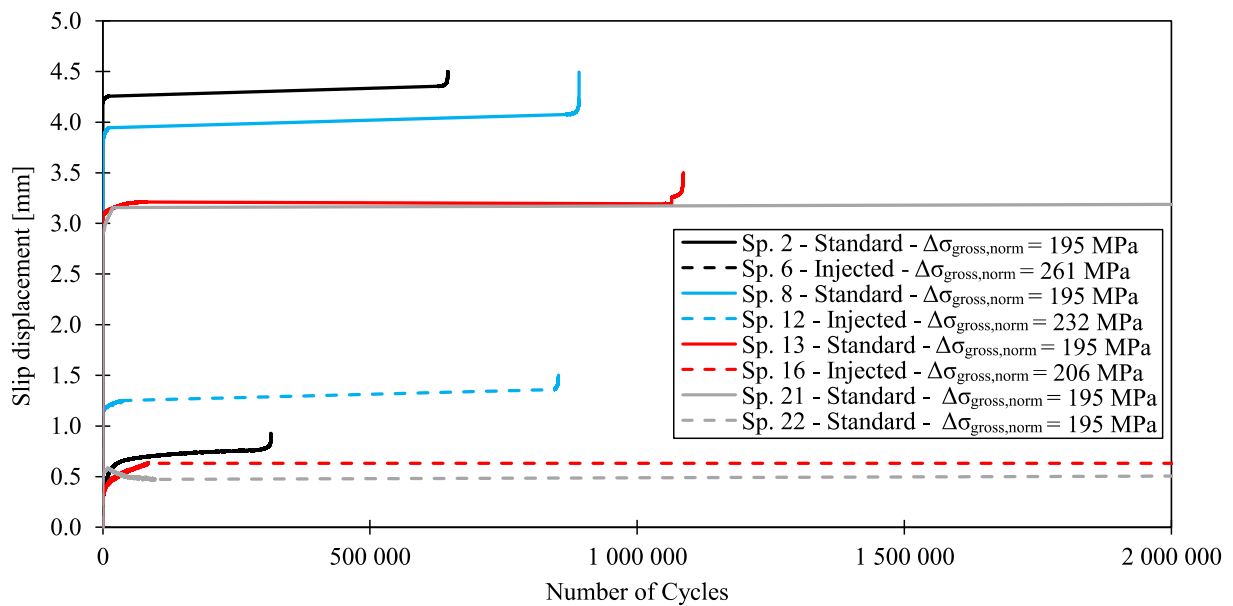
Figure 7.17. Slip displacement during fatigue tests – double shear specimens.

The statistical analysis was implemented for both experimental data as is presented in Figure 7.18. Following the recommendation on EN 1993-1-9 [15], the stress range was computed in the gross cross-section of the plate with higher stress level – S355 plate. Run-outs were not considered in this analysis. Mean curves for standard and injection bolts have a very similar slope, near to $m = 7$. An improved fatigue strength is achieved for bolted connections with injection bolts, since mean S-N curve for injection bolts is above the mean S-N curve for standard bolts for all fatigue regimes. This improvement is more significant for high cycle fatigue regime. Another relevant distinct between these two details is the reduction of the scatter level when injection bolts are implemented. While for standard bolts the coefficient of determination was found as $R^2 = 0.5$, for injection bolts this parameter increases to $R^2 = 0.9$.

In terms of characteristic S-N curve, normal and Weibull distributions were implemented. For the first case, the detail category was found as 184.5 MPa for injection bolts and 156.4 MPa for standard bolts – see Figure 7.20. The one-sided tolerance limit was found as $k_{5,75,v_{dg}} = 2.19$ for injection bolts and $k_{5,75,v_{dg}} = 2.10$ for standard bolts while standard deviation was found as $\hat{\sigma} = 0.13$ for injection bolts and $\hat{\sigma} = 0.29$ for standard bolts.

For characteristic S-N curves using Weibull distribution, results of the four estimation methods used to determine α_W and β_W parameters are presented in Figure 5.7a). The optimal estimation

method was found by goodness-of-fit tests and results showed that Linear Least Squared Method (LLSM) led to better correlation with BMR data for both injection and standard bolts. The characteristic curve using Weibull distribution was then defined and the detail category was found as 185.6 MPa for injection bolts and 156.8 MPa for standard bolts – see Figure 7.20.
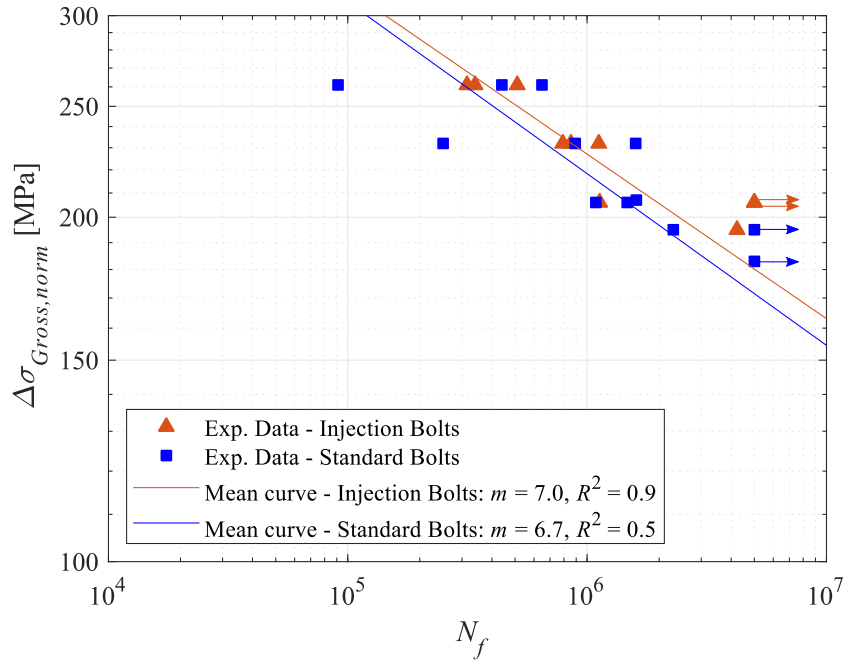
Figure 7.18. Experimental data for double shear specimens (injection vs. standard bolts): mean curves.

Table 7.12. Parameters of Weibull distribution and goodness-of-fit statistics for double shear bolted connections.

Fatigue data	Method		LLSM	WLLSM	MLM	MM
Injection	α_w		3.45	3.26	4.20	4.15
	β_w		1.16	1.15	1.15	1.15
	Goodness-of-fit	KS	0.116	0.101	0.138	0.136
		AD	0.289	0.302	0.352	0.345
		χ^2	0.079	0.087	0.114	0.109
Standard	α_w		1.62	1.58	1.89	1.87
	β_w		1.38	1.37	1.35	1.35
	Goodness-of-fit	KS	0.073	0.083	0.087	0.086
		AD	0.208	0.216	0.228	0.221
		χ^2	0.052	0.058	0.065	0.061

Very similar results were found for characteristic *S-N* curves for normal and Weibull distribution functions, thus both can be used as design reliable approach. A significative

improvement was found comparing injection to standard bolts. This fatigue life beneficial effect of using preloaded injection bolts is quantified for each stress range in Table 7.12 considering the values for normal characteristic *S-N* curve. The average fatigue life improvement is nearly constant for all stress range values: 8.6% (considering logarithmic scale).
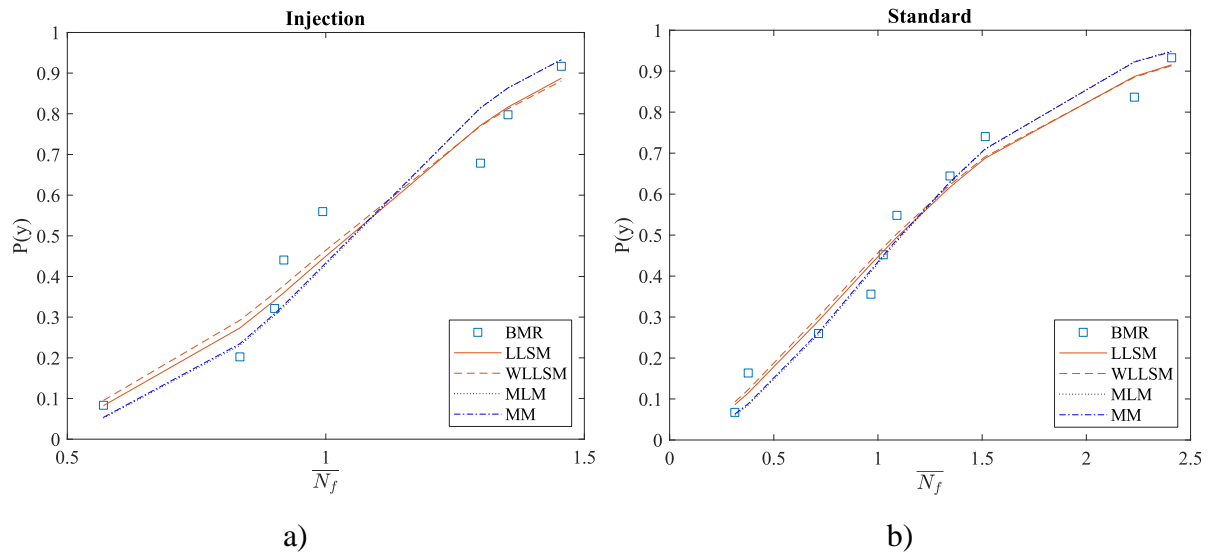
Figure 7.19. Comparison of cumulative Weibull distribution function for double shear bolted connections: a) Injection bolts; b) Standard bolts.

In Figure 7.20, fatigue experimental data from double shear bolted connections is compared with design recommendation on EN 1993-1-9 [15]. It is remarked that only one data point (from standard bolts) stand below the suggested curve which means that for this detail, EN 1993-1-9 [15] design curves present a better correlation with experimental evidence when compared to single shear specimens. However, it should be stated that the proposed slope ($m = 3$) is very distinct from the slope determined based on experimental tests leading to unsafe design predictions for low cycle fatigue regime and very conservative predictions for high cycle fatigue regime. Taras and Greiner [182] also proposed a design *S-N* curve for double shear connections (riveted bridge components) based on an inverse slope, $m = 5$, and fatigue strength of 90 MPa at 2 million cycles. From Figure 7.20, it is visible that this design approach is very conservative and is not adequate for this detail.
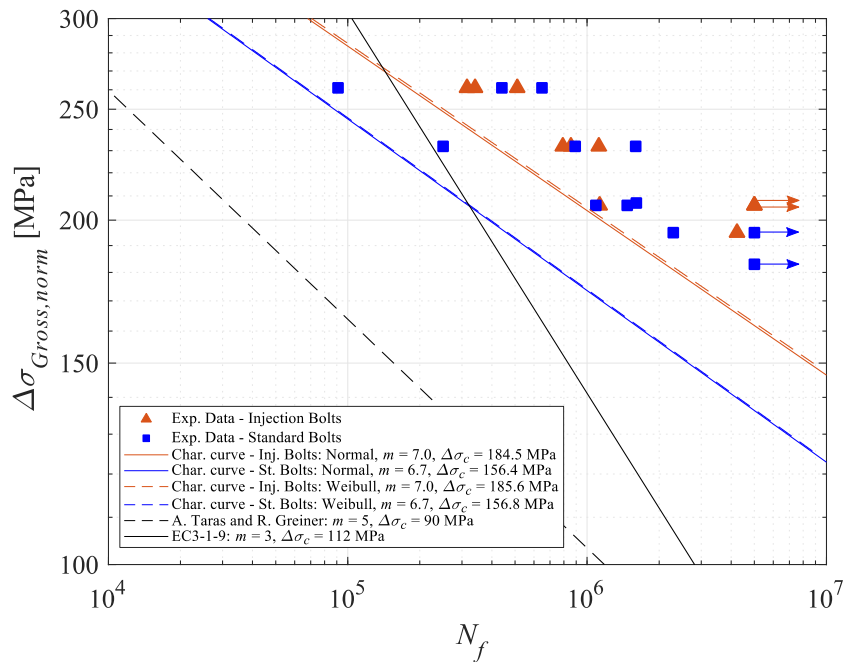
Figure 7.20. Experimental data for double shear specimens (injection vs. standard bolts): characteristic and design curves.

Table 7.13. Comparison of fatigue life from preloaded standard and injection bolts for each stress range using normal characteristic curves – **double shear specimens**.

Stress range [MPa]	Bolt type	Number of cycles N_f	Comparison	
			Linear scale	Logarithmic scale
$\Delta\sigma_1 = 261$	Standard	65 811		
	Injection	179 113	+172.2%	+9.0%
$\Delta\sigma_2 = 232$	Standard	144 354		
	Injection	406 544	+181.6%	+8.7%
$\Delta\sigma_3 = 206$	Standard	318 921		
	Injection	929 707	+191.5%	+8.4%
$\Delta\sigma_4 = 195$	Standard	459 855		
	Injection	1 362 077	+196.2%	+8.3%

7.5   Conclusions

Preloaded bolted connections were tested under fatigue loading conditions in order to assess the effect of using an adhesive in the gap between the bolt shank and the plate (injection bolts) in a scenario of old bridge strengthening.

Experimental results on fatigue tests have shown that using preloaded injection bolts instead of preloaded standard bolts on single shear connections contributes to increase the stiffness of the

joint by reducing the slip displacement in 60%, on average. However, for double shear specimens, this reduction on slip displacement increases to 80%. The resin around the bolt shank is more effective for double shear connections and the reduction of slip displacement is higher.

Fatigue experimental data from single and double shear connections was analysed using a statistical methodology and mean S-N curves were defined. Coefficient of determination allowed to quantify the level of scatter showing that injection bolts contribute to reduce the variability of results (0.5 for standard bolts to 0.8/0.9 for injection bolts), significantly. Lower values of scatter are of utmost importance to determine reliable design criteria. While for double shear connection, the slope of the S-N curve is similar between injection and standard bolts (approximately $m = 7$), in the case of single shear connections, the slope of standard bolts is higher. In fact, the load eccentricity on single shear connections plays an important role to mitigate the beneficial effect of the adhesive on the fatigue strength. This eccentricity is responsible to create stress concentration under the bolt head and, therefore, the phenomenon of fretting is significant. In this sense, the load that is transferred through the adhesive is lower than for double shear connections.

It was found that using normal distribution function for characteristic S-N curves, a better correlation with experimental data is achieved. The beneficial effect of using preloaded injection bolts was evident in both single and double shear connections and it was quantified in nearly 9% higher number of cycles at failure (considering logarithmic scale). This fatigue life improvement was evident for all fatigue regimes using double shear connections, however, for single shear connections, it was mainly for high cycle fatigue regime. This fact is associated with the eccentricity of single shear connection.

For single shear connections, EN 1993-1-9 [15] proposes a design curve that represents an unsafe design criterion since a significant quantity of data has lower fatigue life. Since the weakest component of this detail is in the plate composed of puddled iron, this design curve cannot be implemented. On the other hand, the proposal made by Taras and Greiner [182] for riveted connections of existing bridges can be used, especially for standard bolts. However, it does not consider the beneficial effect within high cycle regime when injection bolts are used.

Regarding double shear connections, S-N curve proposed in EN 1993-1-9 [15] has a better correlation with experimental evidences. Since fatigue life was limited by damage in the S355 plate, predictions are improved. However, the slope $m = 3$ is not adequate leading to unsafe design predictions for low cycle regime and conservative predictions for high cycle regime. For this detail, S-N curve proposed by Taras and Greiner [182] lead to very conservative results and it is not adequate.

A summary of the characteristic S-N curves derived from the experimental campaign described in this chapter is presented in Table 7.14. It considers not only the type of connection and type of bolt but also the material of the weakest component that limits fatigue life of the detail.

Table 7.14. Summary of characteristic S-N curves derived from the experimental campaign.

Type of connection	Type of bolt	Material of the weakest component	Charact. curve
Single shear	Preloaded standard bolt	Puddled iron	$m = 5.1$ $\Delta\sigma_C = 63.2$ MPa
	Preloaded injection bolt	Puddled iron	$m = 6.9$ $\Delta\sigma_C = 92.4$ MPa
Double shear	Preloaded standard bolt	S355	$m = 6.7$ $\Delta\sigma_C = 156.4$ MPa
	Preloaded injection bolt	S355	$m = 7.0$ $\Delta\sigma_C = 184.5$ MPa

8   CONCLUSIONS AND FUTURE WORK

8.1   Main conclusions

This thesis presented contributions towards the assessment of fatigue behaviour of resin-injected bolted shear connections considering a full comprehensive approach from material level to structural detail.

Since the most common location of fatigue damages on bolted shear connections is in the plates, the first part of the thesis is focussed on these components. Metallographic and mechanical material assessments allowed not only to establish a clear distinction between puddled iron and structural steels but also to define mean and characteristic parameters to describe cyclic, fatigue and crack growth behaviour of each material. Crack propagation mechanisms on structural steels were analysed to develop an analytical approach that consider the effect of crack closure residual stresses. This characterization at material level was essential to implement local fatigue approaches to assess the fatigue performance of bolt hole details. It was evident from the results presented on this thesis that local fatigue modelling is an efficient approach to establish reliable predictions on the fatigue life of structural details, especially using the Huffman damage model.

The mechanical performance of resin-injected bolted shear connections relies mainly on the injection material. In this sense, this thesis focussed also on defining material parameters to describe the quasi-static behaviour of two epoxy-resin solutions. This material behaviour characterization was performed considering specimens under fully confined conditions which enable for future numerical modelling of resin-injected bolted shear connectors.

Finally, the fatigue performance of preloaded bolted connections using injection bolts and standard bolts was compared by means of an experimental campaign. The beneficial effect of the adhesive around the bolt shank was evident especially for double shear configuration. It guarantees a reduced level of uncertainty on fatigue strength and a higher stiffness. If the applied load exceeds the slip resistance of the connection (overloads, bolt preload relaxation, etc.), the presence of the resin guarantees a fatigue strength superior to EN 1993-1-9 [15] predictions.

8.2   Summary of main findings

A summary of main results is now addressed in five topics.

I.   Metallic material assessment

Three materials that are commonly used in bridge structural components were selected: puddled iron from a Portuguese centenary bridge (still in service) and two non-alloy structural steels – S235 and S355. Concerning microstructural characterization:

- Puddled iron presented an abundant presence of non-metallic inclusions and a high level of heterogeneity. The lamination direction was easily identified considering the configuration and disposal of grains whose size is significantly bigger than structural steels;

- Microstructure of non-alloy structural steels showed a homogenous distribution composed by perlite-ferrite and no visible orientation of grains. The size of grains is lower for S355 than for S235.

The crystallite size was assessed for structural steels presenting similar values for S235 and S355, around 20 nm. This value was used to estimate the dislocation density resulting in 3E-3 nm^{-2} which is a typical value for highly deformed metals. In what concerns chemical composition, the presence of phosphorus and higher carbon content in puddled iron are key aspects for reduced ductility, while manganese and lower carbon content in structural steels guarantees good weldability and improved mechanical properties. Vickers hardness tests enable to quantify the ductility capacity of these materials showing that puddled iron is harder than modern steels. Furthermore, the ductility capacity of S355 is lower when compared to S235 which was also clear from monotonic tensile tests.

Cyclic stress-strain curves for each material were defined using mean and characteristic values of strain hardening parameters and the following conclusions can be stated:

- Normal distribution function led to characteristic cyclic stress-strain curves with better correlation with experimental results;

- Predominantly elastic region is similar for both puddled iron and structural steels;

- The brittleness of puddled iron does not allow to properly define predominantly plastic region and it can be considered negligible for strain amplitudes higher than 0.5%;

- Strain hardening coefficient for S355 is considerably higher (804.6 MPa) than for S235 (541.9 MPa);
- DNV-RP-C208 recommendations represent a very low performance for S235.

In what concerns fatigue life behaviour, strain, stress-strain and strain-energy functions were implemented for each material. The following conclusion can be stated:

- Eiffel bridge material has considerably lower fatigue life when compared to structural steels and fatigue endurance of S355 is higher than S235;
- The transition between predominantly plastic and predominantly elastic regimes occurs for a significantly lower number of reversals for Eiffel bridge material compared to structural steels;
- DNV-RP-C208 recommendations for fatigue life behaviour are reasonable comparing to experimental results, however it does not distinguish material strength class leading to conservative results for S355;
- Normal distribution function led to characteristic fatigue life curves with good correlation with experimental evidences for both strain and SWT damage parameters.
- Using the maximum value of dislocation density obtained by XRD in Huffman model, a very good correlation with experimental results is obtained. Optimized values of dislocation density were found as: 4.20E15 m^{-2} for S235 and 6.42E15 m^{-2} for S355.

The assessment of FCG behaviour was based on new tests for structural steels as well as on a data collection from previous tests. The following conclusions can be stated:

- New tests allowed to assess the influence of stress ratio on FCG showing that higher velocity of propagation is obtained for higher values of stress ratio;
- Crack propagation is considerably faster in Eiffel bridge material compared to structural steels;
- S355 presented an improved FCG behaviour compared to S235 but only for stress ratio higher than 0.5;
- BS 7910 represent an unsafe prediction not only for puddled iron but also for S235 when stress ratio is lower than 0.5;
- The best approach to define characteristic curves was by shifting the mean curve by three times the standard deviation.

II.   FCG analytical model considering crack closure effects

Fatigue crack propagation on S235 and S355 was studied aiming to develop a FCG model that consider the effect of plasticity induced crack closure. The fundamental parameter that is used to consider this effect was the residual stress intensity factor whose determination was conducted based on experimental, analytical and numerical procedures. The crack opening force and the U parameter were measured during crack propagation on S355 CT specimens showing that:

- Crack closure effects are more significant for positive values of stress ratio closer to zero;
- The relation between effective and applied load is constant during crack propagation;
- There is a linear dependency between residual stress intensity factor and the applied stress intensity factor range.

Elastoplastic stress-strain field ahead of the crack tip formed during crack propagation was assessed considering SWT damage parameter for S235 and S355. The crack tip radius ρ^* is the fundamental parameter to conduct this procedure. It was found that:

- The accuracy of residual stress intensity factor is improved by adopting a smaller value for the crack tip radius;
- A good balance between computational effort and quality of results was achieved for $\rho^* = 1\text{E-7 m}$;
- Residual stress intensity factor is higher for S235 which is related to its lower value of yield stress;
- The numerical procedure used to assess the residual stress intensity factor for S355 was efficient.

The prediction of FCG rates considering crack closure effects using the proposed FCG model presented reliable results. The process block size, δ_p, which is the key parameter to derive FCG rates, can be determined based on the cyclic yield strength of the material and the effective stress intensity factor range. Both mean and characteristic approaches to define FCG predictions presented good correlation with experimental results.

III.   Global and local approaches for fatigue predictions of bolt hole details

Fatigue behaviour of bolt hole details was investigated by means of global and local approaches. Experimental fatigue tests were conducted on S235 specimens composed of a plate with a central hole with 18 mm of diameter. The following conclusions can be stated:

- Deformation range is constant during the main part of the test;
- The final size of the fatigue crack is within the invisible area of the plate (under the bolt head / nut and washer) for most of the cases. When the crack overcomes this region, the remaining number of cycles is very reduced;
- A global approach was used and a S-N curve was defined for all the data leading to slope $m = 6.6$;
- Global predictions based on EN 1993-1-9 [15] are not adequate, mainly because the slope proposed in this standard ($m = 3.0$) lead to unsafe results for high stress range values and very conservative results for low stress range values;

A comparison with similar experimental results found in literature allowed to understand that:

- Galvanization produces an embrittlement of the detail and a rapid formation of cracks in the coating that weakens the fatigue life;
- The method used to execute the hole plays an important role in the fatigue life. Punching presented consistent reduction of fatigue endurance when compared to drilling;
- The material that composes the detail also influences the fatigue life. A comparison with results from S355 plates allowed to understand that an improved fatigue life is achieved, mainly in low-cycle region.

Local approaches to fatigue were applied considering initiation and propagation phases. The following conclusions can be stated:

- Damage parameters were assessed by means of numerical computations using mean and characteristic values of stabilized cyclic stress-strain curve of S235. The upper boundary of this curve should be implemented in damage models in which mean stress effect is considered to obtain the highest value of damage for a characteristic approach;
- Single side and double side crack approaches were studied by means of experimental and numerical approaches. It showed that if a crack emerges in both sides of the hole, 30% smaller fatigue life is obtained;

- Numerical computation of fatigue crack propagation phase led to a number of cycles within the mean and characteristic values found experimentally.
- Huffman damage model was the most efficient local model to predict the fatigue life of this bolt hole detail.

IV.   Resin based material assessment for shear connectors

Two resin-based materials for shear connectors were studied aiming to characterize their performance under compression confined conditions by means of experimental and numerical procedures. Bare resin specimens were compared with steel-reinforced resin specimens. The following conclusions can be stated:

- Unconfined compression tests were used to define uniaxial material properties – steel reinforced resin presented 1.8 times higher stiffness and a significant reduction of strain at failure was obtained when compared to bare resin specimens;
- After applying 10 cycles of load, the stiffness of the steel-reinforced specimen is 2.6 times higher than the stiffness for bare resin specimens in confined conditions;
- Viscoelastic and residual plastic strains are consistently reduced for steel-reinforced specimens;
- The behaviour of the two materials under confined conditions was successfully described using the linear Drucker-Prager plastic model.

The material model that was defined allow for future research, especially in what concerns numerical modelling of bolted shear connectors.

V.   Preloaded injection bolts for bridge strengthening

Fatigue performance of preloaded injection bolts was assessed by means of experimental tests establishing a comparison with preloaded standard bolts considering a metallic bridge strengthening scenario. The adhesive that surrounds the bolt shank induces an increase of stiffness in the connection, namely by reducing the slip displacement by 60% for single shear and 80% for double shear. Preloaded injection bolts also contribute to reduce significantly the scatter of results as it was evident from the coefficient of determination. The slope of the S-N curve for double shear connections was $m \approx 7$ which is very similar to the value obtained in chapter 5 for plates with hole. In the case of single shear connections, the slope is higher ($m \approx 5$) which is related to the eccentricity effects. While for double shear connections there was a clear

fatigue strength improvement for preloaded injection bolts in all fatigue regions, for single shear connections this beneficial effect is only visible for high cycle fatigue region. However, it was evident that the presence of the adhesive around the bolt shank contributed to decrease the stress concentration in the plate by distributing the load through all the area of the hole. Without the adhesive, the load transfer through the hole is more localized leading to high concentration of stresses and a higher susceptibility to start a crack. The improvement that injection bolts produced in the fatigue life of this connection was quantified as 9% (considering a logarithmic scale), on average. Finally, it was evident that S-N curves proposed in EN 1993-1-9 [15] are not adequate to predict the fatigue life of these details because: a) the slope $m = 3$ does not have a good correlation with experimental evidences; b) the beneficial effect of injection bolts is not considered.

8.3   Recommendations for future work

The scientific contributes presented in this thesis deserve to be further developed aiming to improve the knowledge related to fatigue performance of resin-injected bolted shear connections. In this sense recommendations for future developments within the subject of this thesis are here summarized:

- Since Huffman damage model was the best fatigue approach to predict the fatigue life of the studied detail, it is essential to continue with scientific investigation on dislocation density, namely by evaluating this parameter with pre-strained samples. Strain levels used in LCF tests can be used to evaluate the effect of cyclic deformation on the dislocation density of metallic materials.

- In what concerns the effect of plasticity induced crack closure on FCG, the experimental procedure to compute residual stress intensity factor was based on the relation between force and crack opening displacement. However, future investigations should be focused on finding different approaches to compute the stress-strain field ahead of the crack tip, namely by considering digital image correlation, to further validate the expression proposed to define the process block size.

- It should be invested on study the effect of plasticity induced crack closure during FCG on bolt hole details.

- The experimental setup used to define mechanical material parameters of steel and steel-reinforced resins was successful in achieving confined conditions, as the cylinder did

not yield. However, the geometry of (steel-reinforced) resin body in a shear connector will result in a more complex stress distribution due to the possibility of the injection material to flow around the bolt shank, when in service, which requires additional investigation. Furthermore, future research should be focused also on the long-term behaviour of these materials, especially in what concerns its creep performance.

- It is essential to investigate the beneficial effect of using injection bolts in bolted shear connections composed only by non-alloy structural steels aiming to avoid the scatter effect of puddled iron and to be representative of new constructions.

- It is proposed to study the fatigue performance of resin-injected bolted connections under cyclic alternative loading (R_σ=-1).

REFERENCES

[1]   Akesson B. Fatigue Life of Riveted Steel Bridges. 1st ed. CRC Press, Taylor & Francis Group; 2010.

[2]   Jesus A, Fernandes A, Silva A, Correia J. Retrofitting of Old Riveted Portuguese Bridges: Past and Current Remnant Life Assessment Research. ICEM15 – 15th Int. Conf. Exp. Mech. Porto, 2012.

[3]   Oehme P. Schäden an Stahltragwerken – eine Analyse. Damage Analysis of Steel Structures. IABSE Proc. P-139/89, 1989.

[4]   Geissler K. Assessment of Old Steel Bridges. Struct Eng Int 2002;12:258–63.

[5]   Larsson T. Fatigue assessment of riveted bridges. PhD Thesis. Department of Civil and Environmental Engineering, Lulea University of Technology, 2009.

[6]   Imam B, Chryssanthopoulos M. A review of metallic bridge failure statistics. IABMAS, Philadelphia: 2010.

[7]   Pedrosa B, Rebelo C, Gervásio H, da Silva LS. Modal Identification and Strengthening Techniques on Centenary Portela Bridge. Struct Eng Int 2019;29. https://doi.org/10.1080/10168664.2019.1612314.

[8]   Pipinato A, Rebelo C, Pedrosa B, Gervásio H. Assessment Procedure and Rehabilitation Criteria for Riveted Road Bridges. Struct Eng Int 2020;30. https://doi.org/10.1080/10168664.2019.1615855.

[9]   Pedrosa B, Rebelo C, Gervásio H, Silva L, Correia J. Fatigue of Preloaded Bolted Connections with Injection Bolts. Struct Eng Int 2020;30.

[10]   Ivanov S, Geier R, Rebelo C, Pedrosa B. Innovative Strengthening Method for Steel Truss Nodes—Experimental Results. Struct Eng Int 2019;29. https://doi.org/10.1080/10168664.2019.1613945.

[11]   Lukic M, Al-Emrani M, Aygul M, Bokesjo M, Urushadze S, Fryba L, et al. Bridge fatigue guidance - meeting sustainable design and assessment (BRiFaG). EU Publications, Research Fund for Coal and Steel: 2013.

[12]   Cremona C, Eichler B, Johansson B, Larsson T. Improved Assessment Methods for Static and Fatigue Resistance of Old Metallic Railway Bridges. J Bridg Eng 2013;18.

[13]   Jorge R, Riberio A, De Jesus A, Figueiredo M, Castro M, Fernandes A. Ponte Eiffel - Viana do Castelo. Avaliação de Resultados de Programa Experimental (Eiffel bridge - Viana do Castelo. Experimental results evaluation). IDMEC/FEUP: Faculdade de Engenharia, Universidade Do Porto: 2006.

[14]   EU FP6. Sustainable Bridges - Background document D4.6: Improved assessment methods for static and fatigue resistance of old steel railway bridges. Goteborg: 2007.

[15]   CEN. EN 1993-1-9: Eurocode 3, Design of steel structures – Part 1-9: Fatigue. Brussels: European Committee for Standardization; 2005.

[16]   AASHTO. AASHTO LRFD: bridge design specification. American Association of State Highway and Transportation Officials; 2012.

[17]   JSSC. Fatigue Design Recommendations For Steel Structures 1995.

[18]   Correia J, Pedrosa B, Raposo P, Jesus A, Rebelo C, Gervásio H, et al. Fatigue strength evaluation of resin-injected bolted connections using statistical analysis. Engineering 2017;3 (6):795–805.

[19]   ECCS. European Recommendations for Bolted Connections with Injection Bolts. 1st ed. Publication No 79; 1994.

[20] Gresnigt A, Sedlacek G, Paschen M. Injection Bolts To Repair Old Bridges. Proc. Connect. Steel Struct. IV, 2000.

[21] Mattes J. Substituição de Rebites por Parafusos Injectados com Resina (Replacement of Rivets by Resin Injection Bolts). MSc Thesis, IST, University of Lisbon, Portugal, 2007.

[22] Jesus A, Silva J, Figueiredo M, Ribeiro A, Fernandes A, Correia J, et al. Fatigue Behaviour of Resin-Injected Bolts: An Experimental Approach. Iber. Conf. Fract. Struct. Integr., Porto: 2010.

[23] Schijve J. Fatigue of Structures and Materials. 2nd ed. Springer Dordrecht; 2009. https://doi.org/https://doi.org/10.1007/978-1-4020-6808-9.

[24] Miner M. Cumulative damage in fatigue. Trans ASME Ser E J Appl Mech 1945;12:159–64.

[25] Coffin L. A study of the effects of the cyclic thermal stresses on a ductile metal. Transl ASME 1954;76:931–50.

[26] Manson S. Behaviour of materials under conditions of thermal stress. Natl Advis Comm Aeronaut 1954.

[27] Griffith A, Taylor G. The phenomena of rupture and flow in solids. Philos Trans R Soc London Ser A, Contain Pap a Math or Phys Character 1921;221:163–98. https://doi.org/10.1098/rsta.1921.0006.

[28] Zhu S, Ai Y, Liao D, Correia J, Jesus A, Wang Q. Recent advances on size effect in metal fatigue under defects: a review. Int J Fract 2022;234:21–43. https://doi.org/10.1007/s10704-021-00526-x.

[29] Bowman M. Fatigue design and retrofit of steel bridges. Prog Struct Eng Mater 1997;1:107–14. https://doi.org/10.1002/pse.2260010116.

[30] Benden S, Abdullah S, Ariffin A. Review of Fatigue Crack Propagation Models for Metallic Components. Eur J Sci Res 2009;28:364–97.

[31] Basquin O. The Exponential Law of Endurance Tests. Am Soc Test Mater Proc 1910;10:625–30.

[32] Taras A, Greiner R. Development and application of a fatigue class catalogue for riveted bridge components. Struct Eng Int J Int Assoc Bridg Struct Eng 2010;20:91–103.

[33] Morrow J. Cyclic plastic strain energy and fatigue of metals. Intern Frict Damping Cycl Plast 1965:45–8.

[34] American Society for Testing and Materials. ASTM E 606: Standard Practice for Strain Controlled Fatigue Testing. 1998.

[35] Ramberg W, Osgood W. Description of stress-strain curves by three parameters. NACA Technical Note 902: 1943.

[36] Socie D, Morrow J. Review of Contemporary Approaches to Fatigue Damage Analysis. In: Burke JJ, Weiss V, editors. Risk Fail. Anal. Improv. Perform. Reliab., Boston, MA: Springer US; 1980, p. 141–94. https://doi.org/10.1007/978-1-4684-7811-2_8.

[37] Smith K, Watson P, Topper T. A Stress-Strain Function for the Fatigue of Metals. J Mater 1970;5:767–78.

[38] Huffman P. A strain energy based damage model for fatigue crack initiation and growth. Int J Fatigue 2016;88:197–204. https://doi.org/https://doi.org/10.1016/j.ijfatigue.2016.03.032.

[39] Irwin G. Analysis of stresses and strains near the end of a crack traversing a plane. J Appl Mech 1957;24:361–4.

[40] Fernandes A, Tavares de Castro P, Branco C. Fadiga de Estruturas Soldadas. 1st ed. 1999.

[41] Rooke D, Cartwright D. Compendium of Stress Intensity Factors. 1st ed. Stationery

Office; 1976.

[42]   Tada H, Paris P, Irwin G. The Stress Analysis of Cracks Handbook. 3rd ed. Professional Engineering Publishing; 2000.

[43]   Sun C, Jin Z. Fracture Mechanics. Academic Press; 2012.

[44]   American Society for Testing and Materials. ASTM E 647: Standard Test Method for Measurement of Fatigue Crack Growth Rates. 2015.

[45]   Paris P, Erdogan F. A critical analysis of crack propagation laws. J Basic Eng 1963;85:528–33. https://doi.org/10.1115/1.3656900.

[46]   Dowling N, Begley J. Fatigue Crack Growth During Gross Plasticity and the J-integral. Mech Crack Growth 1976;18:82–105.

[47]   Wolf E. Fatigue crack closure under cyclic tension. Eng Fract Mech 1970;2:37–45.

[48]   Elber W. The Significance of Fatigue Crack Closure, 1971, p. 230–42. https://doi.org/10.1520/STP26680S.

[49]   Department of Defense - USA. Joint Service Specification Guide - Aircraft Structures 2006.

[50]   Gallagher J, Berens A, Engle J. USAF damage tolerant design handbook: guidelines for the analysis and design of damage tolerant aircraft structures. n.d.

[51]   Chen H, Grondin G, Driver R. Fatigue resistance of high performance steel. Structural Engineering Report No. 258. University of Alberta. 2005.

[52]   Jesus A, Silva A, Correia J. Fatigue of riveted and bolted joints made of puddle iron - A numerical approach. J Constr Steel Res 2014;102:164–77. https://doi.org/10.1016/j.jcsr.2014.06.012.

[53]   Forth S, Everett R, Newman J. A Novel Approach to Rotorcraft Damage Tolerance, 2002.

[54]   Liu Y, Mahadevan S. Probabilistic fatigue life prediction using an equivalent initial flaw size distribution. Int J Fatigue 2009;31:476–87. https://doi.org/https://doi.org/10.1016/j.ijfatigue.2008.06.005.

[55]   White P, Molent L, Barter S. Interpreting fatigue test results using a probabilistic fracture approach. Int J Fatigue 2005;27:752–67. https://doi.org/https://doi.org/10.1016/j.ijfatigue.2005.01.006.

[56]   Molent L, Sun Q, Green A. Characterisation of equivalent initial flaw sizes in 7050 aluminium alloy. Fatigue \& Fract Eng Mater \& Struct 2006;29:916–37. https://doi.org/https://doi.org/10.1111/j.1460-2695.2006.01050.x.

[57]   Savaidis G, Savaidis A, Zerres P, Vormwald M. Mode I fatigue crack growth at notches considering crack closure. Int J Fatigue 2010;32:1543–58. https://doi.org/https://doi.org/10.1016/j.ijfatigue.2010.02.010.

[58]   Moreira P, Matos P, Castro P. Fatigue striation spacing and equivalent initial flaw size in Al 2024-T3 riveted specimens. Theor Appl Fract Mech 2005;43:89–99. https://doi.org/https://doi.org/10.1016/j.tafmec.2004.12.005.

[59]   Ellyin F. Fatigue Damage, crack Growth and life prediction. 1st ed. 1997. https://doi.org/10.1007/978-94-009-1509-1_10.

[60]   Glinka G. A notch stress-strain analysis approach to fatigue crack growth. Eng Fract Mech 1985;21:245–61. https://doi.org/https://doi.org/10.1016/0013-7944(85)90014-1.

[61]   Peeker E, Niemi E. Fatigue crack propagation model based on a local strain approach. J Constr Steel Res 1999;49:139–55. https://doi.org/https://doi.org/10.1016/S0143-974X(98)00213-2.

[62]   Noroozi A, Glinka G, Lambert S. A two parameter driving force for fatigue crack growth analysis. Int J Fatigue 2005;27:1277–96.

https://doi.org/https://doi.org/10.1016/j.ijfatigue.2005.07.002.

[63] Noroozi A, Glinka G, Lambert S. A study of the stress ratio effects on fatigue crack growth using the unified two-parameter fatigue crack growth driving force. Int J Fatigue 2007;29:1616–33. https://doi.org/https://doi.org/10.1016/j.ijfatigue.2006.12.008.

[64] Noroozi A, Glinka G, Lambert S. Prediction of fatigue crack growth under constant amplitude loading and a single overload based on elasto-plastic crack tip stresses and strains. Eng Fract Mech 2008;75:188–206. https://doi.org/https://doi.org/10.1016/j.engfracmech.2007.03.024.

[65] Mikheevskiy S, Glinka G. Elastic–plastic fatigue crack growth analysis under variable amplitude loading spectra. Int J Fatigue 2009;31:1828–36. https://doi.org/https://doi.org/10.1016/j.ijfatigue.2009.02.035.

[66] Hurley P, Evans W. A methodology for predicting fatigue crack propagation rates in titanium based on damage accumulation. Scr Mater 2007;56:681–4. https://doi.org/https://doi.org/10.1016/j.scriptamat.2006.12.040.

[67] Ellyin F, Kujawski D. An Energy-based Fatigue Failure Criterion. Microstruct Mech Behav Mater 1986;II.

[68] Molski K, Glinka G. A method of elastic-plastic stress and strain calculation at a notch root. Mater Sci Eng 1981;50:93–100. https://doi.org/https://doi.org/10.1016/0025-5416(81)90089-6.

[69] Kulak G, Fisher J, Struik J. Guide to Design Criteria for Bolted and Riveted Joints. 2nd ed. Wiley-Interscience; 1987.

[70] Juoksukangas J, Lehtovaara A, Mäntylä A. Experimental and numerical investigation of fretting fatigue behavior in bolted joints. Tribol Int 2016;103:440–8.

[71] Jiménez-Peña C, H. Talemi R, Rossi B, Debruyne D. Investigations on the fretting fatigue failure mechanism of bolted joints in high strength steel subjected to different levels of pre-tension. Tribol Int 2017;108:128–40.

[72] Fernando U, Farrahi G, Brown M. Fretting fatigue crack growth behavior of BS L45 4 percent copper aluminium alloy under constant normal load. Frett Fatigue ESIS 18 1994:183–95.

[73] Albrecht P, Sahli A, Wattar F. Fatigue Strength of Bolted Joints. J Struct Eng 1987;113:1834–49.

[74] Chakherlou T, Oskouei R, Vogwell J. Experimental and numerical investigation of the effect of clamping force on the fatigue behaviour of bolted plates. Eng Fail Anal 2008;15:563–74.

[75] Novoselac S, Kozak D, Ergić T, Damjanović D. Fatigue Damage Assessment of Bolted Joint Under Different Preload Forces and Variable Amplitude Eccentric Forces for High Reliability BT - Fracture at all Scales. In: Pluvinage G, Milovic L, editors., Springer International Publishing; 2017, p. 239–68.

[76] Deutsche B., Geschäftsbereich N. DS 804. Vorschrift fur Eisenbahnbrucken und sonstige Ingenieurbauteile [Regulation for railway bridges and other engineered constructions] 2000.

[77] Jesus A, Silva A, Correia J. Fatigue of riveted and bolted joints made of puddle iron - An experimental approach. J Constr Steel Res 2015;104:81–90.

[78] CEN. EN 1090-2, Execution of steel structures and aluminium structures - Part 2: Technical requirements for steel structures. European Committee for Standardization; 2008.

[79] Gresnight A, Stark J. Design of bolted connection with injection bolts. Connect Steel Struct III Behav Strength Des 1996:77–87.

[80] CEN. EN 1993-1-8: Eurocode 3, Design of steel structures – Part 1-8: Design of joints. Brussels: European Committee for Standardization; 2005.

[81] CEN. EN 1993-2: Eurocode 3 - Design of steel structures - Part 2: Steel bridges. Brussels: European Committee for Standardization; 2006.

[82] International Organization for Standardization. ISO 12107: Metallic materials — Fatigue testing — Statistical planning and analysis of data. 2012.

[83] Witkovsky V. ToleranceFactor (https://www.mathworks.com/matlabcentral/fileexchange/24135-tolerancefactor). MATLAB Cent File Exch 2021.

[84] Weibull W. A Statistical Distribution Function of Wide Applicability. J Appl Mech 1951;18.

[85] Goglio L, Rossetto M. Comparison of fatigue data using the maximum likelihood method. Eng Fract Mech 2004;71:725–36. https://doi.org/https://doi.org/10.1016/S0013-7944(03)00009-2.

[86] Bolfarine H, Sandoval M. Introduction to the statistical inference (in Portuguese). Chicago, I. 2001.

[87] Ben-Israel A. A Newton-Raphson method for the solution of systems of equations. J Math Anal Appl 1966;15:243–52. https://doi.org/https://doi.org/10.1016/0022-247X(66)90115-6.

[88] Barbosa J, Júnior R, Correia J, Jesus A, Calçada R. Analysis of the fatigue life estimators of the materials using small samples. J Strain Anal Eng Des 2018;53:699–710. https://doi.org/10.1177/0309324718782245.

[89] Zhang L, Xie M, Tang L. On Weighted Least Squares Estimation for the Parameters of Weibull Distribution. Pham H Recent Adv Reliab Qual Des Springer Ser Reliab Eng 2008.

[90] Fothergill J. Estimating the cumulative probability of failure data points to be plotted on Weibull and other probability paper. IEEE Trans Electr Insul 1990;25:489–92. https://doi.org/10.1109/14.55721.

[91] Júnior R, Belísio A. Probabilistic S–N curves using exponential and power laws equations. Compos Part B Eng 2014;56:582–90. https://doi.org/https://doi.org/10.1016/j.compositesb.2013.08.036.

[92] Appleton J, Moura R. A utilização do aço inox na reabilitação das insfraestruturas da Ponte Eiffel sobre o Rio Lima , em Viana do Castelo Inspecção e Reabilitação (Rehabilitation of Eiffel bridge Infrastructures using stainless steel), ASCP'09 – 1º Congresso de Segurança e Conservação de Pontes ASCP - Lisbon: 2009, p. 3–10.

[93] Det Norske Veritas. DNV-RP-C208: Determination of Structural Capacity by Non-linear FE analysis Methods, 2013.

[94] BSI Standards Publication. Guide to methods for assessing the acceptability of flaws in metallic structures. 2015.

[95] Lesiuk G, Pedrosa B, Zięty A, Błażejewski W, Correia J, Jesus A, et al. Minimal Invasive Diagnostic Capabilities and Effectiveness of CFRP-Patches Repairs in Long-Term Operated Metals. Metals (Basel) 2020;10:984. https://doi.org/10.3390/met10070984.

[96] Helmerich R, Kühn B, Nussbaumer A. Assessment of existing steel structures. A guideline for estimation of the remaining fatigue life. Struct Infrastruct Eng 2007;3:245–55. https://doi.org/10.1080/15732470500365562.

[97] Neslušan M, Jurkovič M, Kalina T, Pitoňák M, Zgútová K. Monitoring of S235 steel over-stressing by the use of Barkhausen noise technique. Eng Fail Anal 2020;117:104843. https://doi.org/https://doi.org/10.1016/j.engfailanal.2020.104843.

[98]   American Society for Testing and Materials. ASTM E112-13: Standard Test Methods for Determining Average Grain Size. 2018.

[99]   Schneider C, Rasband W, Eliceiri K. NIH Image to ImageJ: 25 years of image analysis. Nat Methods 2012;9:671–5. https://doi.org/10.1038/nmeth.2089.

[100] Oliveira I. Caracterização das Propriedades Mecânicas e Microestruturas do Ferro Pudlado. MSc Thesis, Universidade Federal Fluminense, 2021.

[101] Callister W, Rethwisch D. Ciência e Engenharia de Materiais - Uma Introdrução. 9th ed. Translated by Sergio Soares; 2018.

[102] Callister W, Rethwisch D. Material Science and Engineering - An Introduction. 10th ed. 2018.

[103] He K, Chen N, Wang C, Wei L, Chen J. Method for Determining Crystal Grain Size by X-Ray Diffraction. Cryst Res Technol 2018;53:1700157. https://doi.org/https://doi.org/10.1002/crat.201700157.

[104] Jesus A, Silva A, Figueiredo M, Correia J, Ribeiro A, Fernandes A. Strain-life and crack propagation fatigue data from several Portuguese old metallic riveted bridges. Eng Fail Anal 2011;18:148–63. https://doi.org/10.1016/j.engfailanal.2010.08.016.

[105] BSi. EN 10025-2:2004 Hot rolled products of structural steels - Part 2: Technical delivery conditions for non-alloy structural steels. Brussels: 2004.

[106] Pinto Soares. Aços - Características e tratamentos. 2010.

[107] International Organization for Standardization. ISO 6892-1. Metallic materials — Tensile testing — Part 1: Method of test at room temperature. 2009.

[108] Carvalho D, Silva A, De Jesus A, Fernandes A. Fatigue behaviour of structural steels. Comparison of Strain-life and Fatigue Crack propagation data. Mecânica Exp 2015;25:67–78.

[109] Jesus A, Matos R, Fontoura B, Rebelo C, Silva L, Veljkovic M. A comparison of the fatigue behavior between S355 and S690 steel grades. J Constr Steel Res 2012;79:140–50. https://doi.org/10.1016/j.jcsr.2012.07.021.

[110] Carvalho D. Comportamento à fadiga de aços estruturais. MSc Thesis, Universidade de Trás-os-Montes e Alto Douro, 2014.

[111] Ferreira S, Castro J, Meggiolaro M. Using the strip-yield mechanics to model fatigue crack growth by damage accumulation ahead of the crack tip. Int J Fatigue 2017;103:557–75. https://doi.org/https://doi.org/10.1016/j.ijfatigue.2017.06.039.

[112] Correia J, de Jesus A, Fernández-Canteli A. A procedure to derive probabilistic fatigue crack propagation data. Int J Struct Integr 2012;3:158–83. https://doi.org/10.1108/17579861211235183.

[113] Hadi Hafezi M, Nik Abdullah N, Correia J, Jesus A. An assessment of a strain-life approach for fatigue crack growth. vol. 3. 2012. https://doi.org/10.1108/17579861211281173.

[114] Jesus A, Correia J. Critical assessment of a local strain-based fatigue crack growth model using experimental data available for P355NL1 steel. J Press Vessel Technol 2013;135.

[115] Correia J, Jesus A, Fernández-Canteli A, Calçada R. Modelling probabilistic fatigue crack propagation rates for a mild structural steel. Frat Ed Integrita Strutt 2015;31:80–96. https://doi.org/10.3221/IGF-ESIS.31.07.

[116] Bogdanov S, Mikheevskiy S, Glinka G. Probabilistic Analysis of the Fatigue Crack Growth Based on the Application of the Monte-Carlo Method to Unigrow Model. Mater Perform Charact 2014;3:20130066. https://doi.org/10.1520/MPC20130066.

[117] Correia J, De Jesus A, Fernández-Canteli A. Local unified probabilistic model for fatigue crack initiation and propagation: Application to a notched geometry. Eng Struct

2013;52:394–407. https://doi.org/10.1016/j.engstruct.2013.03.009.

[118] Correia J, Apetre N, Arcari A, Jesus A, Muñiz-Calvente M, Calçada R, et al. Generalized probabilistic model allowing for various fatigue damage variables. Int J Fatigue 2017;100:187–94.

[119] Bang D, Ince A, Tang L. A modification of UniGrow 2-parameter driving force model for short fatigue crack growth. Fatigue \& Fract Eng Mater \& Struct 2019;42:45–60. https://doi.org/https://doi.org/10.1111/ffe.12865.

[120] Bang DJ, Ince A, Noban M. Modeling approach for a unified crack growth model in short and long fatigue crack regimes. Int J Fatigue 2019;128:105182. https://doi.org/https://doi.org/10.1016/j.ijfatigue.2019.06.042.

[121] Bang DJ, Ince A. A short and long crack growth model based on 2-parameter driving force and crack growth thresholds. Int J Fatigue 2020;141:105870. https://doi.org/https://doi.org/10.1016/j.ijfatigue.2020.105870.

[122] Kujawski D. An estimation of elastic–plastic strain and stress ahead of a fatigue crack in Mode I. Theor Appl Fract Mech 2021;115:103070. https://doi.org/https://doi.org/10.1016/j.tafmec.2021.103070.

[123] Kujawski D. A damaging function ΔKd for analyzing FCG and R-ratios in metallic materials. Theor Appl Fract Mech 2021;116:103091. https://doi.org/https://doi.org/10.1016/j.tafmec.2021.103091.

[124] Kujawski D. Correlating R-ratio effects on FCG behavior using ΔKd function. Theor Appl Fract Mech 2022;118:103244. https://doi.org/https://doi.org/10.1016/j.tafmec.2021.103244.

[125] Hutchinson J. Singular behaviour at the end of a tensile crack in a hardening material. J Mech Phys Solids 1968;16:13–31.

[126] Lal DN, Weiss V. A notch analysis of fracture approach to fatigue crack propagation. Metall Trans A 1978;9:413–26. https://doi.org/10.1007/BF02646393.

[127] Neuber H. Theory of Stress Concentration for Shear-Strain Prismatic Bodies with Arbitrary Nonlinear Stress-Strain Law. J Appl Mech 1961;28:544–50.

[128] Creager M, Paris PC. Elastic field equations for blunt cracks with reference to stress corrosion cracking. Int J Fract Mech 1967;3:247–52. https://doi.org/10.1007/BF00182890.

[129] Moftakhar A, Buczynski A, Glinka G. Calculations of elasto-plastic strains and stresses in notches under multiaxial loading. Int J Fract 1995;70:357–73.

[130] Valtinat G. Bolted Connections with Hot Dip Galvanized Steel Members With Punched Holes, 2004.

[131] Sun M, Packer JA. Hot-dip galvanizing of cold-formed steel hollow sections: a state-of-the-art review. Front Struct Civ Eng 2019;13:49–65. https://doi.org/10.1007/s11709-017-0448-0.

[132] Vogt J-B, Boussac O, Foct J. Prediction of fatigue resistance of a hot-dip galvanized steel. Fatigue \& Fract Eng Mater \& Struct 2001;24:33–9. https://doi.org/https://doi.org/10.1046/j.1460-2695.2001.00365.x.

[133] Aden-Ali S, Chamat A, Gilgert J, Petit EJ, Dominiak S, Schmitt L, et al. Fatigue Resistance of Hot-dip Galvanized Hot-rolled and High- Silicon TRIP Steel, 2013.

[134] Jiménez-Peña C, Goulas C, Rossi B, Debruyne D. Influence of hole-making procedures on fatigue behaviour of high strength steel plates. J Constr Steel Res 2019;158:1–14. https://doi.org/https://doi.org/10.1016/j.jcsr.2019.03.005.

[135] Berto F, Mutignani F, Tisalvi M. Notch Effect on the Fatigue Behavior of a Hot-Dip Galvanized Structural Steel. Strength Mater 2015;47:719–27.

https://doi.org/10.1007/s11223-015-9709-0.

[136] Berto F, Mutignani F, Tisalvi M. Notch Effect on the Fatigue Behavior of a Hot-Dip Galvanized Structural Steel. Strength Mater 2015;47:719–27. https://doi.org/10.1007/s11223-015-9709-0.

[137] Shih CF, Moran B, Nakamura T. Energy release rate along a three-dimensional crack front in a thermally stressed body. Int J Fract 1986;30:79–102. https://doi.org/10.1007/BF00034019.

[138] Dassault Systèmes Simulia Corp. ABAQUS/Theory Manual, Version 6.6. n.d.

[139] Kortiš I. The numerical solution of the bolted connection with the low-quality injected bolts. Proc. 9th Int. Conf. new trends statics Dyn. Build., Bratislava: 2011, p. 20–1.

[140] Rijkswaterstaat Steunpunt Opdrachtgeversschap. Eisen voor voegovergangen, Tech. Rep. 2007.

[141] Gresnigt A, Beg D. Design bearing stresses for injection bolts with short and long duration high loads. Int Conf Struct Eng Mech Comput 2013:1317–22.

[142] Olivier G, Csillag F, Tromp E, Pavlović M. Conventional vs. reinforced resin injected connectors' behaviour in static, fatigue and creep experiments on slip-resistant steel-FRP joints. Eng Struct 2021;236:112089.

[143] Olivier G, Csillag F, Tromp E, Pavlović M. Static, fatigue and creep performance of blind-bolted connectors in shear experiments on steel-FRP joints. Eng Struct 2021;230:111713.

[144] Csillag F, Pavlović M. Push-out behaviour of demountable injected vs. blind-bolted connectors in FRP decks. Compos Struct 2021;270:114043.

[145] Pedrosa B, Correia J, Rebelo C, Veljkovic M, Gervásio H. Fatigue experimental characterization of preloaded injection bolts in a metallic bridge strengthening scenario. Eng Struct 2021;234:112005.

[146] van Wingerde AM, van Delft DR V, Knudsen ES. Fatigue behaviour of bolted connections in pultruded FRP profiles. Plast Rubber Compos 2003;32:71–6.

[147] Nijgh M, Veljkovic M. Requirements for oversized holes for reusable steel-concrete composite floor systems. Structures 2020;24:489–98.

[148] Nijgh M, Girbacea I, Veljkovic M. Elastic behaviour of a tapered steel-concrete composite beam optimized for reuse. Eng Struct 2019;183:366–74. https://doi.org/10.1016/j.engstruct.2019.01.022.

[149] Nijgh M. New Materials for Injected Bolted Connections - A Feasibility Study for Demountable Connections. MSc Thesis, Delft University of Technology, 2017.

[150] Nijgh M. A Multi-Scale Approach Towards Reusable Steel-Concrete Composite Floor Systems. PhD Thesis, Delft University of Technology, 2021.

[151] Nijgh M, Xin H, Veljkovic M. Non-linear hybrid homogenization method for steel-reinforced resin. Constr Build Mater 2018;182:324–33.

[152] Xin H, Nijgh M, Veljkovic M. Computational homogenization simulation on steel reinforced resin used in the injected bolted connections. Compos Struct 2019;210:942–57.

[153] Drucker DC, Prager W. Soil mechanics and plastic analysis or limit design. Q Appl Math 1952;10:157–65.

[154] Hibbit D, Karlsson B, Sorensen P. ABAQUS/Standard User's Manual, Ver. 6.10. Pawtucket, Rhode Island: 2004.

[155] SAE. J444 - Cast Shot and Grit Size Specifications for Peening and Cleaning. 2012.

[156] Ravi-Chandar K, Ma Z. Inelastic Deformation in Polymers under Multiaxial Compression. Mech Time-Dependent Mater 2000;4:333–57.

[157] CZL Tilburg bv. https://www.czltilburg.nl/nl/processen/dicronite-dry-lubrication\ n.d.

[158] Ghafoori E, Motavalli M. A Retrofit Theory to Prevent Fatigue Crack Initiation in Aging Riveted Bridges Using Carbon Fiber-Reinforced Polymer Materials. Polymers (Basel) 2016;8:308. https://doi.org/10.3390/polym8080308.

[159] Ghafoori E, Prinz G, Mayor E, Nussbaumer A, Motavalli M, Herwig A, et al. Finite Element Analysis for Fatigue Damage Reduction in Metallic Riveted Bridges Using Pre-Stressed CFRP Plates. Polymers (Basel) 2014;6:1096–118.

[160] Ghafoori E, Motavalli M, Nussbaumer A, Herwig A, Prinz GS, Fontana M. Design criterion for fatigue strengthening of riveted beams in a 120-year-old railway metallic bridge using pre-stressed CFRP plates. Compos Part B Eng 2015;68:1–13. https://doi.org/https://doi.org/10.1016/j.compositesb.2014.08.026.

[161] Ghafoori E, Hosseini A, Al-Mahaidi R, Zhao X-L, Motavalli M. Prestressed CFRP-strengthening and long-term wireless monitoring of an old roadway metallic bridge. Eng Struct 2018;176:585–605. https://doi.org/https://doi.org/10.1016/j.engstruct.2018.09.042.

[162] Hosseini S, Mamun M, Mirza O, Mashiri F. Behaviour of blind bolt shear connectors subjected to static and fatigue loading. Eng Struct 2020;214:110584.

[163] Qiu B, Yang X, Zhou Z, Lei H. Experimental study on fatigue performance of M30 high-strength bolts in bolted spherical joints of grid structures. Eng Struct 2020;205:110123.

[164] Leonetti D, Maljaars J, Snijder H. Fatigue life prediction of hot-riveted shear connections using system reliability. Eng Struct 2019;186:471–83.

[165] Akyel A, Kolstein M, Bijlaard F. Fatigue strength of repaired welded connections made of very high strength steels. Eng Struct 2018;161:28–40.

[166] Liu N, Cui X, Xiao J, Lua J, Phan N. A simplified continuum damage mechanics based modeling strategy for cumulative fatigue damage assessment of metallic bolted joints. Int J Fatigue 2020;131:105302.

[167] Carpinteri A, Ronchei C, Scorza D, Vantadori S. Fracture mechanics based approach to fatigue analysis of welded joints. Eng Fail Anal 2015;49:67–78. https://doi.org/https://doi.org/10.1016/j.engfailanal.2014.12.021.

[168] Carpinteri A, Boaretto J, Fortese G, Giordani F, Iturrioz I, Ronchei C, et al. Fatigue life estimation of fillet-welded tubular T-joints subjected to multiaxial loading. Int J Fatigue 2017;101:263–70. https://doi.org/https://doi.org/10.1016/j.ijfatigue.2016.10.012.

[169] Zafari B, Qureshi J, Mottram JT, Rusev R. Static and fatigue performance of resin injected bolts for a slip and fatigue resistant connection in FRP bridge engineering. Structures 2016;7:71–84.

[170] Rodrigues M, Correia J, Jesus A, Moreira P, Calçada R, Xavier J, et al. Static and Fatigue Behaviour of Sikadur®-30 and Sikadur®-52 Structural Resins/Adhesives. Int. Conf. Struct. Integr., 2017.

[171] Koper A. Assessment of Epoxy Resins for Injected Bolted Shear Connections. MSc Thesis, Delft University of Technology, 2017.

[172] Kolstein H, Li J, Koper A, Gard W, Nijgh M, Veljkovic M. Behaviour of double shear connections with injection bolts. Steel Constr 2017;10:287–94.

[173] Russo F, Mertz D, Frank K, Wilson K. Design and Evaluation of Steel Bridges for Fatigue and Fracture – Reference Manual. Publication No. FHWA-NHI-16-016, Federal Highway Administration: 2016.

[174] Wang C, Wang Y, Duan L, Wang S, Zhai M. Fatigue Performance Evaluation and Cold Reinforcement for Old Steel Bridges. Struct Eng Int 2019;29:563–9.

[175] Di Battista J, Adamson D, Kulak G. Fatigue Strength of Riveted Connections. J Struct

Eng 1998.

[176] Sika Portugal. Sikadur®-52. Product Data Sheet. Https://PrtSikaCom/Dms/GetdocumentGet/99182134-32ad-37e2-A2ca-33bc83235a54/76%20Sikadur%2052%20Injection_07608Pdf (June 19th, 2016) 2016.

[177] Inter-composite@. Gelcoat Resin: Araldite SW 404 Resin with HY 2404 Hardener [online] Available: http://inter-composite.com/wp-content/uploads/2012/12/Araldite-SW-404-a-HY-2404.pdf. 2016.

[178] Sika Portugal. Sikadur®-30. https://gbr.sika.com/dms/getdocument.get/0a9f54be-6c6d-351e-a4a4-b56e9c98d49d/Sikadur+30+PDS+(CE).pdf, 2016.

[179] CEN. EN 1993-1-1: Eurocode 3, Design of steel structures – Part 1-1: General rules and rules for buildings. Brussels: European Committee for Standardization; 2005.

[180] American Society for Testing and Materials. ASTM D 7791: Standard Test Method for Uniaxial Fatigue Properties of Plastics. 2012.

[181] Pedrosa B, Correia JAFO, Rebelo C, Lesiuk G, De Jesus AMP, Fernandes AA, et al. Fatigue resistance curves for single and double shear riveted joints from old portuguese metallic bridges. Eng Fail Anal 2019;96. https://doi.org/10.1016/j.engfailanal.2018.10.009.

[182] Taras A, Greiner G. Statistical Background to the Proposed Fatigue Class Catalogue for Riveted Components. Report: Contribution to WG6.1 – Assessment of Existing Steel Structures, ECCS TC6, Spring Meeting – Lausanne – March 22-23,. 2010.

LIST OF OUTPUTS

JOURNAL PAPERS

1. **B. Pedrosa**, J. Correia, G. Lesiuk, C. Rebelo and M. Veljkovic, *Fatigue Crack Growth Modelling for S355 Structural Steel Considering Plasticity-Induced Crack-Closure By Means of Unigrow Model*, International Journal of Fatigue, vol. 164, 107120 (2022), https://doi.org/10.1016/j.ijfatigue.2022.107120

2. **B. Pedrosa**, L. Bücking and M. Veljkovic, *Steel-Reinforced Resin for Bolted Shear Connectors: Confined Behaviour Under Quasi-Static Cyclic Loading*, Engineering Structures, vol 256, 114023 (2022), https://doi.org/10.1016/j.engstruct.2022.114023

3. **B. Pedrosa**, J. Correia, C. Rebelo, M. Veljkovic and H. Gervásio, *Fatigue Experimental Characterization of Preloaded Injection Bolts in a Metallic Bridge Strengthening Scenario*, Engineering Structures, vol. 234, 112005 (2021), https://doi.org/10.1016/j.engstruct.2021.112005

4. **B. Pedrosa**, J. Correia, C. Rebelo and M. Veljkovic, *Reliability of Fatigue Strength Curves for Riveted Connections Using Normal and Weibull Distribution Functions*, ASCE-ASME Journal of Risk and Uncertainty in Engineering Systems, Part A: Civil Engineering, vol. 6, no. 3, (2020), https://doi.org/10.1061/AJRUA6.0001081

5. G. Lesiuk, **B. Pedrosa**, A. Zięty, W. Błażejewski, J. Correia, A. Jesus and C. Fragassa, *Minimal Invasive Diagnostic Capabilities and Effectiveness of CFRP-Patches Repairs in Long-Term Operated Metals*, Metals, vol. 10, no. 984 (2020), https://doi.org/10.3390/met10070984

6. A. Silva, J. Correia, A. Jesus, M. Figueiredo, **B. Pedrosa**, A. Mendes, C. Rebelo and F. Berto, *Fatigue Characterization of a Beam-To-Column Riveted Joint*, Engineering Failure Analysis, vol. 103, pp. 95-123 (2019), https://doi.org/10.1016/j.engfailanal.2019.04.073

7. **B. Pedrosa**, C. Rebelo, H. Gervásio and L. Silva, *Modal Identification and Strengthening Techniques on Centenary Portela Bridge*, Structural Engineering International, vol. 29, pp. 586-594 (2019), https://doi.org/10.1080/10168664.2019.1612314

8. A. Pipinato, C. Rebelo, **B. Pedrosa** and H. Gervásio, *Assessment Procedure and Rehabilitation Criteria for Riveted Road Bridges*, Structural Engineering International, vol 30, pp. 109-118 (2019), https://doi.org/10.1080/10168664.2019.1615855

9. **B. Pedrosa**, C. Rebelo, H. Gervásio, L. Silva and J. Correira, *Fatigue of Preloaded Bolted Connections with Injection Bolts*, Structural Engineering International, vol. 30, pp. 102-108 (2019), https://doi.org/10.1080/10168664.2019.1615398

10. S. Ivanov, R. Geier, C. Rebelo and **B. Pedrosa**, *Innovative Strengthening Method for Steel Truss Nodes - Experimental Results*, Structural Engineering International, vol. 29, pp. 542-546 (2019), https://doi.org/10.1080/10168664.2019.1613945

11. **B. Pedrosa**, J. Correia, C. Rebelo, G. Lesiuk, A. Jesus, A. Fernandes, M. Duda, R. Calçada and M. Veljkovic, *Fatigue Resistance Curves for Single and Double Shear Riveted Joints from Old Portuguese Metallic Bridges*, Engineering Failure Analysis, vol. 96, pp. 255-273 (2019), https://doi.org/10.1016/j.engfailanal.2018.10.009

12. J. Correia, A. Jesus, A. Silva, **B. Pedrosa**, C. Rebelo and R. Calçada, *FE Simulation of S-N Curves for a Riveted Connection Using Two-Stage Fatigue Models*, Advances in Computational Design, vol. 2, no. 4, pp. 333-348 (2017), https://doi.org/10.12989/acd.2017.2.4.333

13. J. Correia, A. Jesus, R. Calçada, **B. Pedrosa**, C. Rebelo, L. Silva and G. Lesiuk, *Statistical Analysis of Fatigue Crack Propagation Data of Materials from Ancient Portuguese Metallic Bridges*, Frattura ed Integrità Strutturale, vol. 42, pp. 136-146 (2017), https://doi.org/10.3221/IGF-ESIS.42.15

14. J. Correia, **B. Pedrosa**, P. Robalo, A. Jesus, H. Gervásio, G. Lesiuk, C. Rebelo, R. Calçada and L. Silva, *Fatigue Strength Evaluation of Resin-Injected Bolted Connections Using Statistical Analysis*, Engineering, vol. 3, no. 6, pp. 795-805 (2017), https://doi.org/10.1016/j.eng.2017.12.001

15. M. Rodrigues, J. Correia, **B. Pedrosa**, A. Jesus, B. Carvalho, C. Rebelo, J. Xavier and R. Calçada, *Numerical Analysis of a Double Shear Standard Bolted Connection Considering Monotonic Loadings*, Engineering Structures and Technologies, vol. 9, no. 4 (2017), pp. 183-194 (2017), https://doi.org/10.3846/2029882X.2017.1414638

CONFERENCE PAPERS

1. **B. Pedrosa**, L. Bücking, M. Veljkovic, *Resina Reforçada com Esferas de Aço para Parafusos Injetados: Comportamento em Condições de Confinamento Lateral*, XII Congresso Construção Metálica e Mista, Coimbra, Portugal, 2021

2. **B. Pedrosa**, C. Rebelo, J. Correia, M. Veljkovic and L. Silva, *Fatigue Life of Preloaded Injection Bolts in a Bridge Strengthening Scenario – Sensitivity Analysis of Fatigue Life Estimators*, EUROSTEEL 2021, Sheffield, United Kingdon, ce/papers, vol. 4, no. 2-4, pp. 125-130, 2021, https://doi.org/10.1002/cepa.1271

3. **B. Pedrosa**, J. Correia, G. Lesiuk, C. Rebelo, A. Jesus, R. Calçada, *Mode I Fatigue Crack Growth Tests on Puddled Iron Strengthened with CFRP Plates*, IABSE Symposium Wrocław, Poland, 2020

4. **B. Pedrosa**, J. Correia, G. Lesiuk, C. Rebelo, P. Huffman, A. Jesus, *Probabilistic fields of fatigue crack growth rates of puddled iron based on Huffman local approach*, IABSE Symposium Wrocław, Poland, 2020

5. **B. Pedrosa**, C. Rebelo, J. Correia, M. Veljkovic, L. Silva. *Enhanced Fatigue Life of Old Metallic Bridges—Application of Preloaded Injection Bolts*. Proceedings of the 3rd RILEM Spring Convention and Conference - RSCC 2020. RILEM Book series, vol 34. Springer, https://doi.org/10.1007/978-3-030-76465-4_18

6. **B. Pedrosa**, J. Correia, C. Rebelo, M. Veljkovic, L. Silva, *Análise experimental e numérica do comportamento à fadiga de ligações metálicas com parafusos injetados*, XII Congresso de Construção Metálica e Mista, Portugal, 2019

7. **B. Pedrosa**, G. Lesiuk, J. Correia, C. Rebelo, S. Sire, M. Veljkovic, L. Silva, R. Calçada, *Taxa de Propagação de Fendas em Metais Reforçados com Placas CFRP*, XII Congresso de Construção Metálica e Mista, Portugal, 2019

8. G. Lesiuk, S. Sire, M. Ragueneau, J. Correia, **B. Pedrosa,** A. Jesus, *Mean stress effect and crack closure in material from old bridge erected in the late 19th*, Procedia Structural Integrity 17 (2019) 198–205, https://doi.org/10.1016/j.prostr.2019.08.027

9. I. Stoyan, R. Geier, C. Rebelo, **B. Pedrosa**, *Experimental results of steel truss nodes strengthen by high strength concrete encasement*, IOP Conference Series: Materials

Science and Engineering, Volume 419, 9th International Symposium on Steel Bridges 10-11 September, Prague, Czech Republic, 2018

10. **B. Pedrosa**, J. Correia, C. Rebelo, A. Jesus, M. Veljkovic, L. Silva, *Fatigue resistance of single shear preloaded bolted connections – experimental tests on standard and resin injected bolts*, 19th International Colloquium on Mechanical Fatigue of Metals – ICMFM, 5-7 September 2018, Faculty of Engineering of the University of Porto, Porto, Portugal

11. **B. Pedrosa**, P. Raposo, J. Correia, C. Rebelo, H. Gervásio, A. Jesus, R. Calçada, L. Silva, *Fatigue resistance ofreinforced and unreinforced steel connections*, XI Congresso de Construção Metálica e Mista, Coimbra, Portugal, 2017

12. M. Rodrigues, P. Raposo, **B. Pedrosa**, J. Correia, S. Blasón, M. Calvente, A. Jesus. *Fatigue Characterization of Structural Resins used InReinforcement Of Old Steel Bridges*, XI Congresso de Construção Metálica e Mista, Coimbra, Portugal, 2017

13. J. Correia, A. Jesus, J. Pinto, R. Calçada, **B. Pedrosa**, C. Rebelo, H. Gervásio, L. Silva, *Fatigue behaviour of single and double shear connections with resin-injected preloaded bolts*, IABSE Congress Stockholm, Sweden, 21-23 September 2016, published in Challenges in Design and Construction of an Innovative and Sustainable Built Environment, pp. 327-339, https://doi.org/10.2749/stockholm.2016.0304

CONFERENCE ABSTRACTS

1. **B. Pedrosa**, J. Correia, C. Rebelo, G. Lesiuk, A. Jesus, M. Veljkovic, *Fatigue life prediction of S235 based on a strain energy model*, International Congress on Structural Integrity and Maintenance - SIM 2021 (virtual format), 8 - 9 April 2021

2. **B. Pedrosa**, J. Correia, C. Rebelo, M. Veljkovic, *Fatigue assessment of metallic details based on statistical analysis of material data*, Virtual Conference on Mechanical Fatigue - VCMF 2020 (virtual format), 9 - 11 September 2020

3. **B. Pedrosa**, J. Correia, C. Rebelo, A. Jesus, M. Veljkovic, *Statistical analysis of monotonic and cyclic experimental data from centenary bridge material*, Virtual

Conference on Mechanical Fatigue - VCMF 2020 (virtual format), 9 - 11 September 2020

4. **B. Pedrosa**, J. Correia, C. Rebelo, A. Jesus, M. Veljkovic, *Fatigue behaviour of shear connections with preloaded injection bolts in a bridge strengthening scenario*, First International Symposium on Risk Analysis and Safety of Complex Structures and Components - IRAS 2019, 1 - 2 July, Porto, Portugal, 2019.

5. **B. Pedrosa**, J. Correia, G. Lesiuk, C. Rebelo, S. Sire, M. Veljkovic, A. Jesus, R. Calçada, *Fatigue crack growth in long term operated bridge metallic materials and strengthening solutions*, First International Symposium on Risk Analysis and Safety of Complex Structures and Components - IRAS 2019, 1 - 2 July, Porto, Portugal, 2019.

6. **B. Pedrosa**, J. Correia, G. Lesiuk, C. Rebelo, M. Veljkovic, P. Montenegro, A. Jesus, R. Calçada. *Fatigue behaviour of double shear connections with preloaded injection bolts in a bridge strengthening scenario*, 29th Colloquium on Fatigue Mechanisms, 21 – 22 March, Brno, Czech Republic, 2019

7. M. Rodrigues, J. Correia, A. Jesus, P. Moreira, R. Calçada, J. Xavier, **B. Pedrosa**, *Static and fatigue behaviour of sikadur®-30 and sikadur®-52 structural resins/adhesives*, 2nd International Conference on Structural Integrity - ICSI 2017, 4 - 7 September, Funchal, Portugal, 2017

SCIENTIFIC PROJECT REPORT

1. European Commission, Directorate-General for Research and Innovation, P. Collin, R. Hällmark, K. Habermehl-Cwirzen, C. Rebelo, J. Correia, **B. Pedrosa** *et al*., Prolonging lifetime of old steel and steel-concrete bridges (PROLIFE) – Final report, Publications Office, 2020, https://data.europa.eu/doi/10.2777/561807

PRESENTATIONS IN MEETINGS

1. PROLIFE, **B. Pedrosa**, C. Rebelo, J. Correia, L. Silva, H. Gervásio, *WP 3.6 - Experimental tests on fatigue resistance of epoxy injected bolts replacing rivets or connecting new-old steel*, Luleå University of Technology, Sweden, 16 March 2018

2. PROLIFE, **B. Pedrosa**, C. Rebelo, J. Correia, L. Silva, H. Gervásio, *WP 4: Life-cycle considerations and assessment of durability aspects of the developed strengthening methods*, Luleå University of Technology, Sweden, 16 March 2018

3. PROLIFE, **B. Pedrosa**, C. Rebelo, J. Correia, L. Silva, H. Gervásio, *WP 3.6: Experimental tests on fatigue resistance of epoxy injected bolts replacing existing rivets or connecting new-old steel*, ArcelorMittal Belval & Differdange SA, Luxembourg, 5-6 October 2017

4. PROLIFE, **B. Pedrosa**, C. Rebelo, J. Correia, L. Silva, H. Gervásio, *WP 4: Life-cycle considerations and assessment of durability aspects of the developed strengthening methods*, ArcelorMittal Belval & Differdange SA, Luxembourg, 5-6 October 2017

COMPUTATIONAL TOOLS

1. Bruno Pedrosa (2023). Unigrow_Pedrosa (https://www.mathworks.com/matlabcentral/fileexchange/128569-unigrow_pedrosa), MATLAB Central File Exchange. Retrieved April 26, 2023.

2. Bruno Pedrosa (2023). ISO12107 (https://www.mathworks.com/matlabcentral/fileexchange/129479-iso12107), MATLAB Central File Exchange. Retrieved May 12, 2023.

3. Bruno Pedrosa (2023). Fatigue data analysis with Weibull distribution function (https://www.mathworks.com/matlabcentral/fileexchange/129489-fatigue-data-analysis-with-weibull-distribution-function), MATLAB Central File Exchange. Retrieved May 12, 2023.